STANFORD
U N I V E R S I T Y
MEDICAL CENTER

Hospital & Clinics · School of Medicine

GARY M. GLAZER, M.D.
*Emma Pfeiffer Merner Professor
in the Medical Sciences
Professor and Chairman
Department of Radiology*

October 2, 2004

The year 2004 has been a historic one for the Department of Radiology and the Richard M. Lucas Center. The Department is celebrating its 100 year anniversary and the Lucas Center is now a dozen years old. Both the Department and the Lucas Center exemplify the spirit of Stanford and the West in being adventurous and open to new ideas. Over time, we have been pioneers in a number of areas that have provided great benefit to medicine and society. By its 60th birthday the Department was well on its way to leading the world in creating major advances for the treatment of cancer using radiation therapy. Today, many people around the world, cured of Hodgkin disease, serve as a legacy to the efforts originated by this Department many years ago. In the late 1980's the original Department of Radiology divided into 2 units that today operate independently as the Department of Radiology and the Department of Radiation Oncology. I was recruited to Stanford in 1989 with a mandate to develop a department with a focus on Radiology and medical imaging which would make Stanford proud. Creation of the Lucas Center was the important and decisive step to catapult Stanford into the top tier of institutions pursuing fundamental advances in medical imaging.

A hundred years from now, in the year 2104, I believe historians will recognize today as a time in which enormous transformational steps were taken to strategically position the Department and Stanford to trailblaze many new paths in medicine and radiology. In addition to pursuing new avenues in biomedical imaging dependent on physics and engineering excellence, we have already completed major steps in bringing to the Department and Stanford exceptional talent in molecular biology and chemistry.

The most visible manifestation of our transformation will be the completion of the new Lucas expansion later this year. The Lucas expansion is a metaphor for our discipline in that both seek to make visible that which would otherwise be invisible. The constraint we faced in building the expansion was that the construction needed to be below ground to comply with the University master plan. Accepting this restriction, we designed the building so that the underground expansion would be quite visible, with its south wall looking to the sky through two stories of glass. A pedestrian walkway forms a bridge over the light wall giving the Stanford community a glimpse of the magic we hope to create within our laboratories. In this new space, the plan is to make visible those inner workings of the body, which are invisible to both the naked eye and to current methods of imaging.

Well-designed buildings and other infrastructure permit us to recruit outstanding students and faculty. We now serve as the home department to 40 graduate students and over 40 postdoctoral research and clinical scholars. I am also delighted to report that we have doubled our research faculty over the last two years as we expand our programs to extend imaging from the macroscopic to the microscopic and functional levels. It still amazes me that our non-invasive methods have yielded such powerful insights into so many areas, including brain function and imaging gene expression.

To the members of the Lucas Foundation I offer my deepest gratitude for starting us on our way in modern times and nurturing us as we move into our second century.

Gary M. Glazer, MD

LUCAS ANNUAL REPORT 2004

Acknowledgements

With the 2004 Lucas Report we celebrate and reflect on another year of remarkable achievements and gratefully acknowledge the continued support of all our sponsors and collaborators.

Special thanks to:

The Richard M. Lucas Cancer Foundation

and

The National Institutes of Health
NIH/NCRR P41 RR09784

And many thanks to Kevin Murphy for the many hours of hard work and dedication in preparing this Annual Report for publication.

Pictured on cover from the left: Gary Glazer, Norbert Pelc, Don Lucas, Gary Glover

Lucas Center 2004 Annual Report

TABLE OF CONTENTS

MAJOR GROWTH IN 2004

CONSTRUCTION

The groundbreaking of the expansion project for the Richard M. Lucas MRI(S) Center has set the stage for continued success for research in radiology. Construction is nearing completion and the new building will be open by early 2005. Dedication of the new building will coincide with the Department's 100th anniversary celebration in May.

The latest Lucas expansion is a two-story underground building with entry from a street-level plaza and hallway access from the basement of the existing Lucas Center. The building features an innovative light court constructed completely of Italian glass to bring sunlight below ground, creating an entry for both floors.

Approximately 20,000 square feet of space will more than double the size of the current Lucas Center and house state-of-the-art imaging research and educational facilities. Major installations include the 7T magnet, cyclotron, molecular imaging laboratories, and an education center equipped with the latest technology for fully interactive imaging seminars. With the new building we will maintain a central core for MR research in one facility, while providing space for equipment, labs and offices for the rapidly growing molecular imaging program (MIPS) .

Before beginning this expansion project, we needed to overcome several obstacles. The University requires that any new building near the Lucas Center should not impede the pedestrian walkways from Campus Drive to Welch Road and should have minimal impact on the medical school campus environment. An

Plaza level entry featuring Italian glass light wall

above ground structure would not be possible. The only option remaining was to go underground; we chose to go down not one but two stories to resolve our space and growing research needs.

Before beginning such a project, planners addressed issues that had arisen over the years with the current building. The existing Lucas Center consists of two floors above ground and one in the basement. When the first expansion took place in 1997, efforts were made to improve the environment in the basement where postdoctoral, graduate students and some faculty have their offices. Skylights were installed in the basement and other parts of the Center where windows were not possible.

When the idea of building two underground floors was decided, lighting and atmosphere were considered essential elements in the design. The concept of a light court was proposed, with windows extending the entire depth and width of the fa ade. The result is intended to bring natural light to researchers and scholars who come to work and study in this underground building. This unique feature will add architectural warmth to the overall project and the surrounding plaza will add an elegant terminus at the Welch Road end of the medical campus mall.

While the primary purpose of this new expansion is to provide space for researchers, facilities, and education, the overall goal is to make that space a stimulating and comfortable environment conducive to collaboration and creativity.

LEARNING CENTER

An important feature of the expansion will be the state-of-the-art education center which will advance radiology education and foster changes in the nature of learning and teaching. The learning center will serve as the setting for all resident and medical student conferences. The unique environment will also become a showsite for the Department's achievements and a desirable teaching space for our faculty.

The room is being designed to support interactive, collaborative group learning. It will be a technology-intensive learning space that will seat approximately 40 students and can easily be reconfigured to facilitate various seating styles. The technology includes multiple projectors, large dual screens, six flat panel monitors, program audio and speech reinforcement, wireless high performance networks, collaboration software, touchscreen control system, capture/streaming/archiving capabilities and more. The new facility will create a learning environment that will draw students to Stanford for their education and serve as a hub for faculty and visiting scholars.

1

SPACE

Our needs for space, people, funding and facilities continue to evolve as we meet established goals and identify new objectives and directions. The Lucas expansion provides much needed space to continue and expand our efforts in MRI (7T), MIPS (cyclotron and labs) and the learning center. This newly expanded Lucas Center will allow our research and clinical scientists to move benchtop concepts ahead and to accelerate the transition of diagnostic, management, and therapy tools to the clinic. This year's Annual Report will demonstrate how we have spent 2004 setting the stage for occupancy of this new facility.

State-of-the-art learning center will also be a showsite for the Department's achievements as well as a highly desirable teaching space for our faculty.

Much of our basic research continues to be carried out in the Lucas Center and, more recently, the Clark Center. With the addition of new faculty and support staff in MR and MI research, it has been necessary to find research space in many different locations within the School of Medicine. MRI research continues in the Lucas Center, with Volumetric CT development and Systems Biology. The newly opened CT flat panel angio research suite is located in the basement of the Grant building. MI research is carried out primarily in the Clark Center but also in four separate labs in the Edwards building and one additional lab in the basement of the hospital building. This list does not include areas used for clinical research. Radiology basic and clinical research faculty, with all scientific and administrative staff, now occupy more than 10 different areas on and off campus. With the opening of the Lucas expansion, we will consolidate three of these locations to bring together and form an interdisciplinary MRI/MI research center.

PEOPLE

The Radiology Department has a history of attracting talented and dedicated individuals. This tradition of excellence continues. To support growing clinical needs; to continue developing core competencies in physics and engineering, and to continue ramping up MIPS, we have added 7 new faculty to our radiology family. With continued focus on MRI, and new emphasis on MI, small animal imaging, and systems biology of cancer, our research group has grown from 50 basic science people to more than 100 people. We are pleased to announce that we have already outgrown the Lucas expansion.

FUNDING

The effort to expand our research portfolio this year has been outstanding. Faculty have worked relentlessy to meet goals related to research fundraising, including the submission of numerous applications for federal grants, foundation grants, and industry sponsored projects. Total proposed dollars from all faculty exceed $ 69M, a record-breaking total and a sound predictor for an explosive and rewarding 2005. Faculty in Radiology received 38 sponsored project awards in 2004, bringing our funded projects to 67. Federal dollars account for 89% of all dollars awarded for sponsored projects (see page 31 for detail).

FACILITIES

The 7T magnet will provide unique opportunity for new approaches to basic research in biology, physiology and morphology of humans and animals. In addition to the full body 7T system, we will also be siting a 7T small-bore system in the small animal imaging lab in the Clark Building. The cyclotron suite and radiopharmaceutical labs in the Lucas expansion will be critical to the success of our MIPS efforts to design new molecular imaging probes and develop biomarkers for disease.

NEW DIRECTION

Radiology is also venturing out along a new path, that of Systems Biology of Cancer (SBC). This highly competitive program, recently funded as a developmental project by NIH, has attracted established investigators from many different disciplines, both on and off campus. Those involved in this program include scientists in radiology, cancer biology, computer science, biomedical informatics, molecular imaging, genome technology and systems biology. The SBC program will receive funding by the end of October (See page 18 for added detail).

VISION

The vision and planning by The Richard M. Lucas Foundation to develop this important facility will dramatically affect our research efforts. The newly expanded Lucas Center will become an important locus for our widespread department. The Learning Center will have an impact on how we come together and share our work with one another, on how we educate on campus, and how we attract others from outside to visit this state-of-the-art facility.

LUCAS OVERVIEW & UPDATES

Lucas Center, Radiological Sciences Laboratory and the Center for Advanced MR Technology

Gary H. Glover

Director, Radiological Sciences Laboratory

The Lucas Center is home to the Radiological Sciences Laboratory (RSL), a section of the Radiology Department, and in conjunction with the Electrical Engineering Department, is host to the *Center for Advanced MR Technology*, an NIH-funded National Research Resource. Its state of the art imaging facilities support hundreds of on-campus and extramural researchers as a core facility.

The RSL comprises 10 faculty, approximately 60 graduate and postdoctoral students, 27 scientific staff and 7 administrative assistants, as well as the Lucas Center/RSL Administrative Director, Donna Cronister.

The faculty serve in a wide variety of advisory roles to government and foundation agencies such as the NIH and Whitaker Foundation and in policy-making positions for international scientific societies such as the ISMRM and RSNA. A number of our faculty, scientific staff and students have garnered prestigious awards for their exceptional research achievements. Some of the Lab's honors of the past year are reviewed here.

Roland Bammer received an NIH R01 grant entitled "Improving SENSE MRI for Spiral and Echo-planar Imaging", with Greg Albers (Neurology) as co-PI. He received a second grant for a Sponsored Clinical Trial - "A Multi-Center Study to Evaluate the Effect of Minimally invasive Versus Open Posterolateral Lumbar Fusion on the Paraspinal Musculature Using High Resolution Structural and Quantitative MR Imaging', with Co-PI **Kate Stevens**.

Kim Butts was awarded both an NIH RO1 and NIH R21 (as PI). She was also elected to the ISMRM Board of Trustees.

Annabel Chen, a postdoc of John Desmond's, obtained a faculty position at National Taiwan University and plans to continue working on brain imaging of cognition in normal and patient populations.

John Desmond was awarded an R01 from NIH/NIA for the project: "fMRI Analysis of Aging and Awareness In Conditioning." The goal of this project is to study how aging and stimulus contingency awareness affects medial temporal and cerebellar activation in classical eyeblink conditioning.

Rebecca Fahrig received an award for Translational Research from the Baxter Foundation for Lung Nodule detection work.

William Kennedy (Pediatrics) and **Rebecca Fahrig** were granted a 2003-2004 OTL Research Incentive Fund award for their proposal: "MRI Voiding Cystography in Children: Quality Improvement and Radiation Elimination".

Matt Kirschen received an award from the Ethical Dimensions of Neuroscience Research, Stanford BioX Interdisciplinary Initiatives Program (2003-2004) to support his graduate research in "Ethical issues in the clinical application of functional neuroimaging data". He also received Second Place for his poster presentation - Stanford Medical Student Research Symposium (May 2003).

Sam Mazin was granted a predoctoral fellowship from the American Heart Association for a project titled: "Fast Volumetric Cardiovascular CT Scanner" (Norbert Pelc, sponsor).

Mike Moseley was his usual productive self. 3 NIH Grants as PI: 2 R01's as competitive renewal and new award as well as a shared instrument grant for a new 7T animal magnet. Co-Organizer: Update on DTI Cognitive Neuroscience NSF conference, NYC August 2004. Service on 4 ad hoc NIH study section in addition to his normal service as a full member of the CDN1 NIH Study section. Past President of the ISMRM, and continuing member of the society's Executive and numerous other committees.

Norbert Pelc was appointed Associate Chair of Research for the Radiology Department. In addition, he was elected chair of the Strategic Planning Subcommittee of the NIH's National Advisory Council for Biomedical Imaging and Bioengineering (NACBIB). Norbert already serves on the Advisory Council of NIBIB. Furthermore, he was selected to the Advisory Committee of the Stanford High Resolution Electron Microscope Facility (An NCRR funded research resource).

Angel Pineda was granted a Senior Research Training Fellowship from the American Lung Association.

Shreyas Vasanawala has won the President's Award from the American Roentgen Ray Society for 2004 in the annual Resident's in Radiology Awards competition. Working with MRSRL in Electrical Engineering and the Musculoskeletal

Section, he developed a new MRI technique and applied it to musculoskeletal imaging. His paper is entitled: Rapid Musculoskeletal MR Imaging with Phase-Sensitive Steady-State Free Precession, **Shreyas S. Vasanawala, Brian A. Hargreaves, John M. Pauly, Dwight G. Nishimura, Christopher F. Beaulieu, Garry E. Gold.**

Zhifei Wen won the 2004 Association for the Advancement of Medical Instrumentation (AAMI) Young Investigator Competition for his paper ' Hybrid Interventional X-ray/MR System'. Co-authors were **Rebecca Fahrig, Arundhuti Ganguly, Stephen Kee, Bruce Daniel, Kim Butts, Huanzhou Yu** and **Norbert Pelc.**

RSL Faculty Recruitment

Last year the RSL added two faculty to enhance basic science developments in pediatric radiology, in concert with Richard Barth, Associate Chair of Pediatric Radiology. **Roland Bammer** and **Samira Guccione** were the successful candidates for these recruitments. Prior to accepting their faculty positions, Roland was a research associate working with Mike Moseley on a wide variety of basic MR imaging developments, while Samira was a research associate working with Mark Bednarski on molecular imaging methods.

In addition, the RSL is in the process of recruiting two additional faculty to develop novel imaging approaches for high field MRI, in anticipation of the soon-to-be installed 7T magnet (see below), and for advancements in the science of body MRI.

The National Center for Advanced MR Technology at Stanford (CAMRT)

The Center is now in its ninth year of operation as a National Research Resource of the NIH's National Center for Research Resources. Outstanding progress has been made in all six of the core technology development areas that include reconstruction methods (Dwight Nishimura, EE Department, core director), imaging of brain activation (Gary Glover, core director and PI), diffusion and perfusion weighted imaging methods (Mike Moseley, core director), imaging of cardiovascular structure and function (Norbert Pelc, core director and CAMRT co-PI), spectroscopic imaging development (Dan Spielman, core director) and interventional MRI technique development (Kim Butts, core director). Some of this research is chronicled in the scientific reports that follow. The Center faculty recently submitted the competing renewal P41 grant application for the next five years of support from the NCRR. A site visit will be held by the NIH in October to evaluate the application.

Lucas Center Facilities

The Center's major expansion is continuing, and completion is expected near the beginning of 2005. The new addition will nearly double laboratory and office space, and includes a new whole body 7T magnet, cyclotron, wet labs, hot labs, a 1000 sq. foot learning center and offices for faculty and students as well as visiting scholars. The 7T program is a research partnership with General Electric, which represents a particularly exciting opportunity. The radiolabeling facilities will augment the Molecular Imaging Program, directed by Sam Gambhir. In addition, plans are underway to remodel the animal magnet suite for installation of a second 3T magnet.

Scene from second floor office in August 2003 (left) and July 2004 (right) showing Southeast corner, where atrium is located.

July 2004: Cyclotron vault, with motor operated, heavily shielded door in place.

Left: March 2004 - Some of the 300 tons of steel are being welded in place for shielding the 7T magnet. Right: July 2004 - Magnet room shielding in place as seen from control room. Magnet arrives in early November.
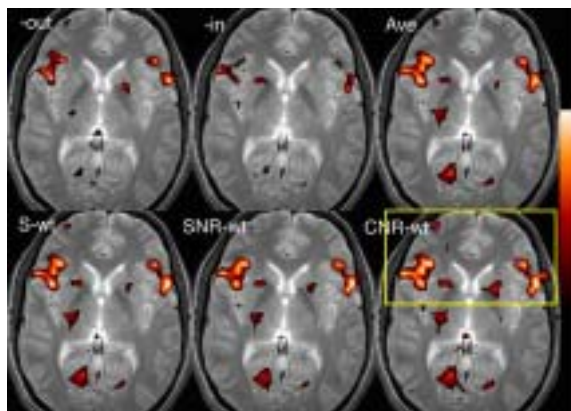
Neuroimaging

## Imaging of Brain Activation
Gary Glover

Left to right, front row, seated: Christine Law, Chardonnay Vance; standing: Yanle Hu, Sean Mackey, Gary Glover, David Ress, Jung-Jiin Hsu, Moriah Thomason, Gaurav Srivastava; back row: Nadine Gaab, Laura Pisani, Rebecca Rakow-Penner. Not shown: Lara Foland (now a grad student in Neurosciences at UCLA).

The functional MRI group has made good progress on methods for acquisition of functional data. Projects include improved methods of combining spiral-in/out timeseries, development of a pulse sequence analogous to spiral-in/out using EPI trajectory, continuation of the high resolution fMRI methods, 3D fMRI acquisitions, calibration of fMRI using breathholding and hemodynamic response measurements, and real-time fMRI with emphasis on therapeutic intervention using biofeedback. The Center has also been active in the FIRST BIRN schizophrenia testbed funded by the NCRR.

An optimized method has been developed and published for combining the spiral-in/out image timeseries, with grad student Moriah Thomason (see figure left, which compares several techniques: Glover, GH; Thomason, ME. Improved combination of spiral-in/out images for BOLD fMRI. Magn. Reson. Med 51:863-868 (2004).

An EPI-in/out sequence is under development, by student Christine Law (page 53). This method is similar to the spiral-in/out technique in that two timeseries are obtained. In this case the acquisition is conventional. The Hermitian symmetry property of k-space is utilized to generate an "EPI-in" and an "EPI-out" image from each conventional image using the top
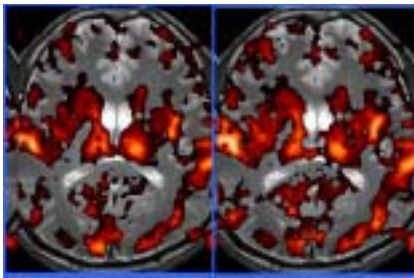
Comparison of conventional method (left) and EPI-in/out (right) for a breathholding task, which activates all grey matter.

and bottom halves of k-space, respectively. Like spiral-in/out, Epi-in/out recovers signal in drop-out regions. The advantage of this method is that a special pulse sequence is not needed.

The real-time fMRI projects include a pain experiment, in which biofeedback is introduced by showing subjects a representation of the level of activation in rostral anterior cingulated and asking them to either increase or decrease the level during noxious thermal stimuli. It is found that subjects learn to control the activation level, and that this level is an excellent surrogate for their perception of pain (pg 54).

Graduate student Yanle Hu is studying the noise propagation in 3D spiral fMRI acquisitions. Theoretically, the 3D method should have improved BOLD CNR, but incoherent noise between the kz phase encodings is reducing the gains. We have found that the impact of the noise can be reduced by reducing the signal level in several ways (pg 55).

Jung Jiin (Jason) Hsu has been developing localized shim coils that improve the homogeneity of the magnetic field in the vicinity of the frotal orbital region of the brain, and a paper was recently submitted on his findings, which are very effective (pg 56).

EE graduate student Gaurav Srivastava is developing denoising methods for reducing the deleterious effects of the magnetic field and gradient switching waveforms on the acquisition of EEG/ERP data in the magnet. He is using an Independent Components method for resolving the cardiac noise, and an adaptive filter for the gradient noise.

Finally, Stanford has been active in the FIRST BIRN schizophrenia project as a P41 contributor. Our group heads the Calibration Working Group for the eleven-site consortium. Moriah Thomason and RA Lara Foland have been examining methods of using calibration data from breathholding to reduce intersite variability (pg 57).

Functional "Microvascular" Neuroimaging
Roland Bammer and Michael Moseley

INTRODUCTION

Magnetic resonance imaging (MRI) continues to advance the state-of-the-art in neuroimaging. Our understanding of new contrast mechanisms that occur in the brain has provided completely new radiographic pictures of neuroanatomy and function over the last decade. This last year has further advanced functional MRI which can map and measure brain tissue water diffusion rates and direction, perfusion of blood, and the brain's response to many functional activation tasks (such as vascular responses to mild reversible stresses). The rapid rate of new discoveries in neuroimaging has been brought about by a steady advance in high-speed MR imaging and by high-field magnets, such as the new 3 Tesla MRI system now at the Lucas Center. We fully expect that the 7 Tesla MRI scanner to be installed will be an even more powerful tool for neuroimaging. These new tools of high-field and high-speed MRI have redefined the horizons of neuroimaging. Our MR Neuroimaging program focuses on disease processes in "brain attacks" (cerebral stroke) using diffusion MRI (DWI), tissue perfusion mapping (PWI), as well as the new field of mapping the brain and white matter connectivity in both adults and in children (DTI).

Left to right: Michael Moseley, David Clayton, Roland Bammer, Chunlei Liu, Calvin Lew, Barak Acar.

PERSONNEL

Roland Bammer has become the newest faculty member at the Lucas Center, joining Radiology as an Assistant Professor imaging physicist for Pediatric Radiology, where he will create and drive new imaging projects within the Pediatric community here at Stanford. He has established several key collaborations with the Departments of Neurology and Pediatrics and has already initiated an active pediatric DTI program on the Lucile Packard Children's Hospital MRI scanner. Roland Bammer, Ph.D., has become a key individual on the research as well as the clinical side of the neuroimaging projects. Roland is also a "Docent" at the University of Graz, Austria and teaches there for 3 weeks per year. Roland has also recently submitted four peer-reviewed grants to the NIH, has had two such grants funded and has been named as "key personnel" on eight others.

Mike Moseley was the President of International Society of Magnetic Resonance in Medicine (ISMRM) over the last year and now as Past President, holds key positions within the ISMRM as Chair of the Awards and Governance Committee. Mike has had two key grants funded over the last year, including an NCRR grant for a $ 2M experimental GE 7T MRI scanner. He has also sat on 6 different NIH study sections and is currently organizing an international meeting on DTI funded by the NSF and the NY Academy of Sciences.

David Clayton has joined Roland as a Research Associate active in implementing the exciting area of parallel imaging in Neuroimaging.

Chunlei Liu together with Burak Acar (now faculty at the National University of Turkey) remains involved in white matter tensor "fiber-tracking" neuroimaging projects as well as building a collaborative program with several graduate student involved in building a "digital toolbox" for fiber tracking applications neuroimaging here at Stanford. Chunlei has had two new papers on the use of higher-order tensor DTI for the future DTI projects envisioned by our group.

CURRENT PROJECTS

During the past year we've made significant progress in developing functional imaging technologies in several key areas under the general title of "Microvascular" imaging. These include diffusion and perfusion techniques for both imaging of acute stroke and for imaging of white matter structure and integrity. By responding to the needs of our collaborators and colleagues here at Stanford and worldwide, we have found that diffusion and perfusion techniques have significantly advanced far beyond the experimental arena into everyday, routine clinical applications in a wide variety of fields where they are being actively and effectively used in numerous self-initiated and collaborative studies. In a review of what we have accomplished. We found that we have in essence developed an array of functional sequence design and reconstruction "toolboxes" for use in two general and broad areas that we will continue to focus on in this section. These can be classified as (1) improved quantitative assessment of tissue microperfusion (PWI) and proton diffusion (DWI) in stroke and (2) imaging of structural white matter integrity (DTI). We have developed a battery of tools geared for our active collaborations. As our list of collaborations grows with outside investigators the need for modifications and enhancements to our basic methods increased significantly, and the center responded accordingly by increasing its effort along the lines of providing sequencing for DTI, together with fast and powerful off-line reconstruction and display algorithms ("Tensorcalc"). The result has been very successful bilateral interactions that have resulted in new pulse sequences and reconstruction programs on the Lucas Center's side, and a large number of DTI-oriented research projects resulting in new understanding in the neurosciences, as documented with papers and a number of new R01's funded by our collaborators.

Using our expertise in developing and applying high speed imaging, we proposed, in part, to develop corresponding diffusion and perfusion techniques on our inpatient and research whole body systems.

TOOLS DEVELOPED WITHIN THE MICROVASCULAR GROUP

Dwi_ epi	DWI Ssh-SE-EPI sequence for diffusion-weighted imaging.
Pwi_ epi	PWI Ssh-GRE-EPI sequence for bolus-tracking applications.
Dti_ epi	DTI sequence for tensor mapping, adds flexible table lookup for gradient axes.
Tensorcalc ("T1")	DWI/DTI recon toolbox with powerful built-in image registration tools. http://rsl.stanford.edu/research/software.html
Tensorcalc ("T2")	DTI recon built for linux platforms, added flexible recon strategies.
Tensorcalc ("T3")	DTI recon built for all platforms with DICOM visualization capabilities.
MRPac	PWI IDL-based software package for quantitative PWI from AIF data.
AutoAIF	PWI IDL-automatic AIF detection module, AutoAIF for MRPac.
FiT	DTI fiber-tracking tool (Matlab-based) for algorithm testing.

This effort has had a parts in numerous peer-reviewed publications, abstracts, and other dissemination (Lucas Reports, for example). A partial list of peer-reviewed publication resulting from the last one-year period (2003-2004) includes:

R Bammer, AM Herneth, SE Maier, K Butts, RW Prokesch, HM Do, SW Atlas, ME Moseley. Line Scan Diffusion Imaging Of The Spine. *AJNR Am J Neuroradiol.* 2003 Jan; 24(1):5-12.

R Bammer, B Acar, ME Moseley. In vivo MR tractography using diffusion imaging. Eur J Radiol. 2003 Mar; 45:223-34.

C Liu, R Bammer, ME Moseley. Generalized Diffusion Tensor Imaging (GDTI): A Method for Characterizing and Imaging Diffusion Anisotropy Caused by Non-Gaussian Diffusion. Israel J Chemistry 2003, 43: 145-154.

M Markl, R Bammer, MT Alley, CJ Elkins, MT Draney, A Barnett, ME Moseley, GH Glover, NJ Pelc. Generalized reconstruction of phase contrast MRI: analysis and correction of the effect of gradient field distortions. Magn Reson Med. 2003 Oct; 50:791-801.

R Bammer, M Markl, A Barnett, B Acar, MT Alley, NJ Pelc, GH Glover, ME Moseley. Analysis and generalized correction of the effect of spatial gradient field distortions in diffusion-weighted imaging. Magn Reson Med. 2003 Sep; 50:560-9.

C Liu, R Bammer, ME Moseley. Characterizing Non-Gaussian Diffusion by Using Generalized Diffusion Tensors. Magnetic Resonance in Medicine 2004, In Press.

M Mlynash, I Eyngorn, R Bammer, ME Moseley, D Tong. An Automated Method For Generating The Arterial Input Function In Perfusion Weighted Magnetic Resonance Imaging: Validation In Stroke Patients. In Review, 2004.

C Liu, R Bammer, ME Moseley. Self-navigated Interleaved Variable Density Spiral Diffusion Tensor Imaging. Magnetic Resonance in Medicine 2004, Submitted.

MORE TO COME

The coming year will advance our MR imaging tools and sharpen our focus on the critical clinical issues of detecting brain attacks with new experimental and clinical MR methods to predict eventual brain injury from attacks that may be reversible, to further map how the brain and spine are "wired", to understand the complex physiological stresses and changes that the brain experiences during stroke, and to extend these tools to better evaluate neuroprotective drugs that can reverse a brain attack.

Desmond Laboratory: Neural Correlates of Behavior
JOHN DESMOND

Our group consists of Matt Kirschen, graduate student in the M.D./Ph.D. program; Jenea Boshart, M.A., laboratory coordinator; Nikhil Jagtiani, graduate student in Computer Science; Marlys LeSene, administrative associate, and Dr. John Desmond, Assistant Professor and Principal Investigator. Dr. Annabel Chen, who was a postdoctoral fellow in the lab, has recently accepted a faculty position at the National Taiwan University, where she plans to continue research on neural correlates of cognition using brain imaging methods.

Our work focuses on the neural correlates of behavior using functional magnetic resonance imaging (fMRI) and transcranial magnetic stimulation (TMS) methods. Specific areas of interest and recent accomplishments include:

The contributions of the cerebellum, and cerebro-cerebellar circuits, to cognition. The cerebellum has traditionally been viewed as a structure involved in motor coordination. However, neuroimaging and patient studies have revealed unexpected cerebellar involvement in cognitive performance beyond motor behavior. We are specifically interested in cerebellar contributions to verbal working memory performance, and have been working on this topic under a grant from the NIH. "Verbal working memory" is the type of memory that one would use to hold a phone number in mind long enough to go to the telephone and dial it. In the past year we have investigated how brain activation in the cerebellum could be linked to phonological storage processes required by working memory. As predicted by our model of cerebro-cerebellar circuitry in verbal working memory, the right inferior cerebellum and left parietal lobule exhibited greater activation when letters to remember were phonologically similar. This increased activation in these regions occurred during the maintenance phase of the task in which the subject covertly rehearses the letters to keep them in mind. This investigation was presented at the Cognitive Neuroscience Society annual meeting.

Integration of transcranial magnetic stimulation (TMS) with functional MRI. TMS and fMRI are complementary methods, because fMRI can reveal which regions of the brain activate during a cognitive task, whereas TMS can assess which of those activations are necessary for performance. Our preliminary results indicate that TMS applied to the cerebellum affects working memory performance by slowing down response time. Additional controls have demonstrated that this effect is not due to motor impairment, or general distraction. We believe that the behavioral slowing occurs because TMS interferes with the internal brain circuitry that holds the information in mind.

Clinical applications of functional MRI, including characterization of altered brain activation due to disease, surgical planning, and diagnosis. An important aspect of fMRI for clinical purposes is that it is powerful enough to assess brain activations at the level of the individual patient as well as at the group level. The installation of an automated fMRI system

Left to right: Courtnea Rainey, Matt Kirschen, John Desmond, Jenea Boshart, Marlys Lesene

at Blake Wilbur hospital devoted to clinical fMRI studies is now in regular use for presurgical planning purposes. This system can be used to map sensorimotor, and language function in patients who are about to undergo neurosurgery. The system automates a number of steps required for fMRI data analysis and ends with automatic uploading of brain sections and rendered cortical surface (with functional activity superimposed) to a web site accessible to physicians and surgeons. The promises and challenges of clinical fMRI were recently described in symposium presentations by Dr. Desmond at the European Congress of Epilepsy in Vienna, Austria, and at the American Society of Neuroradiology in Seattle.

New Project: fMRI Analysis of Aging and Awareness in Conditioning. This 5-year RO1 research project was just awarded to Dr. Desmond by the NIH/NIA. The overall goal of this research is to elucidate how aging in humans affects neural systems that are important for associative memory, including two systems particularly important for classical conditioning, the medial temporal lobe and the cerebellum. Age-related changes will be studied in terms of eyeblink conditioning because (a) the neural circuitry underlying such conditioning is better delineated than any other form of mammalian learning and (b) there are well documented age-related declines in eyeblink conditioning. Remarkably, little is known from functional neuroimaging about why such associative learning declines with age. We postulate that changes in both cerebellar and medial temporal lobe systems, as well as changes in network dynamics, occur during normal aging and account for the overall pattern of eyeblink conditioning in older subjects. Upon successful completion of this project, we will achieve a better understanding of the age-related changes that occur in these neural systems. The clinical implications of this research are that simple eyeblink conditioning procedures may provide reliable indications of the integrity of cerebellar and medial temporal lobe structures, as well as network performance involved in the awareness of stimulus contingencies, that are essential for both non-declarative and declarative forms of learning and memory.

Cardiovascular Imaging

Norbert Pelc

Dynamic 3D imaging, including time resolved 3D (i.e. 4-D) velocity imaging, continues to be a major area of work, and a source of a great deal of collaboration. This year, we continued to make improvements in the acquisition methods, and our ability to correct for system imperfections (pg. 103). Our collaborators are using the method to study a number of disorders, including pulmonary arterial abnormalities (pg. 104-105) and congenital diseases. We have also begun a project to improve imaging of myocardial perfusion by using a 3D SSFP sequence (106).

Our project on robust separation of the signals from fat and water gained a great deal of momentum this year (pgs. 107-114). Improvements in the reconstruction method, and in the choice of echo delays made the method much more robust. Using a formal theoretical formalism (Cramér-Rao bound) we studied the impact of various choices in sequence parameters and also showed that our reconstruction methods are extracting all the information available in the data. We're applying the technique to a number of clinical applications, including cardiac and musculoskeletal imaging, and we've developed a faster (single measurement point) technique that may be useful for dynamic imaging. GE has now installed the more general method in a number of sites to further evaluate its clinical impact.
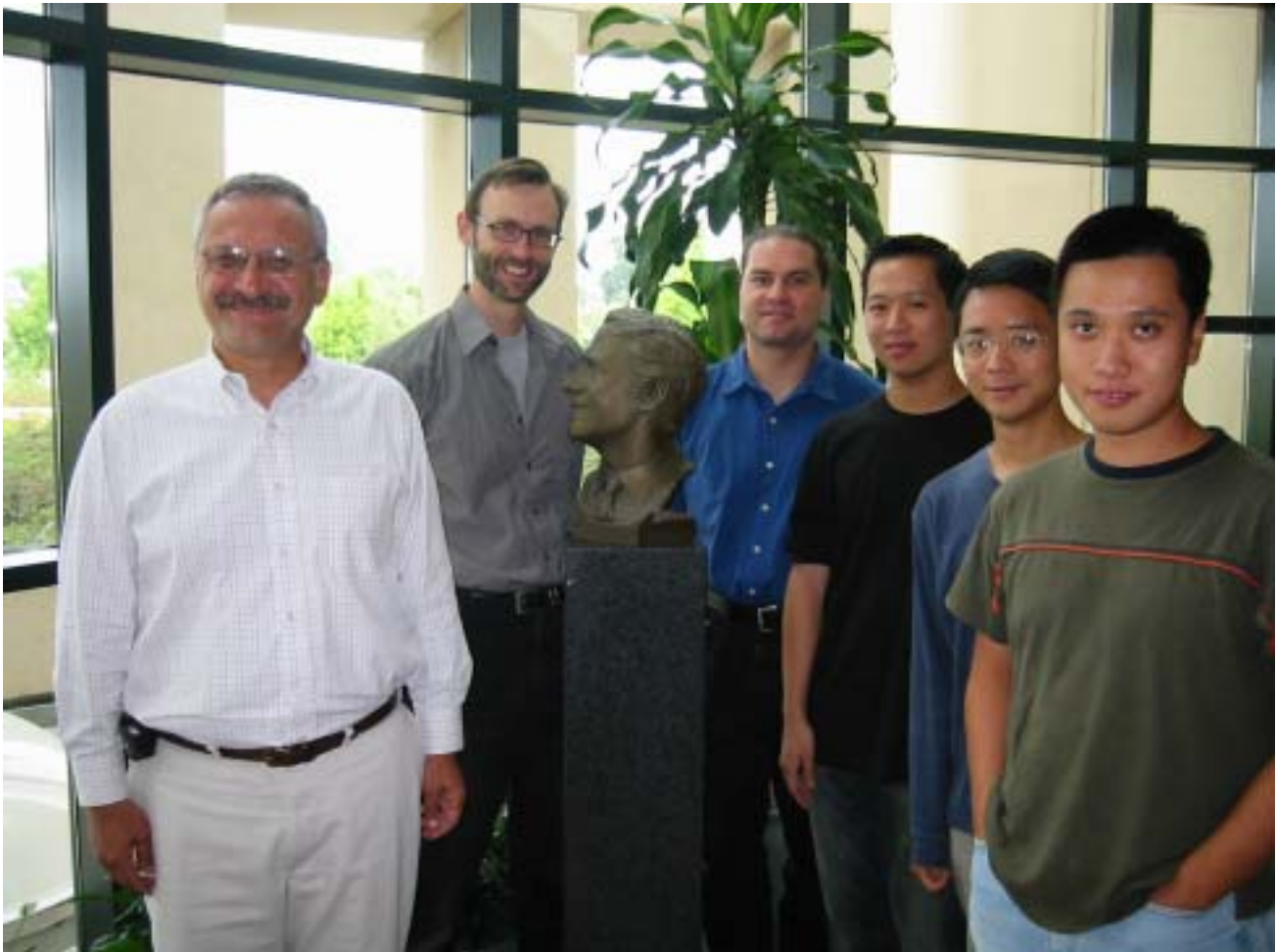
Left to Right: Norbert Pelc, Mark Alley, Michael Markl, Calvin Lew, Zhifei Wen, Huanzhou Yu.

MR Spectroscopy

Daniel Spielman

The MR Spectroscopy Group has continued to focus on the important technical challenges that arise when spectroscopic imaging is performed at high field. Increased information becomes available with the stronger field as the signal-to-noise ratio increases and coupling patterns are simplified, but optimal shimming is the corner stone of successful data acquisition.

The detection of citrate with proton spectroscopy has important implications for prostate cancer management. The resonances due to citrate show coupling patterns that are nicely resolved with 2D J-resolved spectroscopy at 3T, and as Dong-Hyun Kim demonstrates in his work, can be used with in vivo to measure both citrate and choline. We anticipate that further work on this project will lead to volumetric prostate imaging of the prostate with robust detection and separation of these key metabolites.

The suppression of undesired lipid signals provides one of the fundamental constraints in proton spectroscopy. Two of the abstracts in this report address the problem of lipid suppression. At very short echo times we demonstrate that efficient spatial encoding with spiral CSI can be effectively used to avoid within-voxel contamination by the severe out-of-voxel lipids (pg. 117-119). Further, at 3T it becomes feasible to take advantage of the spectral separation of lipids and the metabolites of interest to implement multi-inversion suppression techniques that provide robust lipid nulling across a range of T1s, while maintaining full signal from the desired metabolites (pg. 119). To maximize the information content of the proton spectrum at 3T, Dirk Mayer has combined powerful 2D constant-time spectroscopy with efficient spatial encoding of spiral CSI to acquire, in vivo, spatially resolved spectra where coupling patterns collapse into easily resolved singlets. With this technique, sampling of glutamate and myoinositol becomes feasible (pg. 120).

Dong-Hyun Kim built on prior shimming work by incorporating current constraints of the power supply into the solution for optimal field. This work is particularly important for shimming in regions with the most severe inhomogeneities (pg 121).

As for personnel, a new graduate student, Meng Gu, joined the group to work on spectroscopic imaging techniques. Dirk Mayer became a research associate as he continues his developmental work on increasing the information content of in vivo spectroscopy. Dave Clayton joined Roland Bammer's new group at the Lucas Center as a research associate, and Elfar Adalsteinsson leaves the Lucas Center for a faculty position at Massachusetts Institute of Technology with a joint appointment in the department of electrical engineering & computer science and the Harvard-MIT division of health sciences and technology.
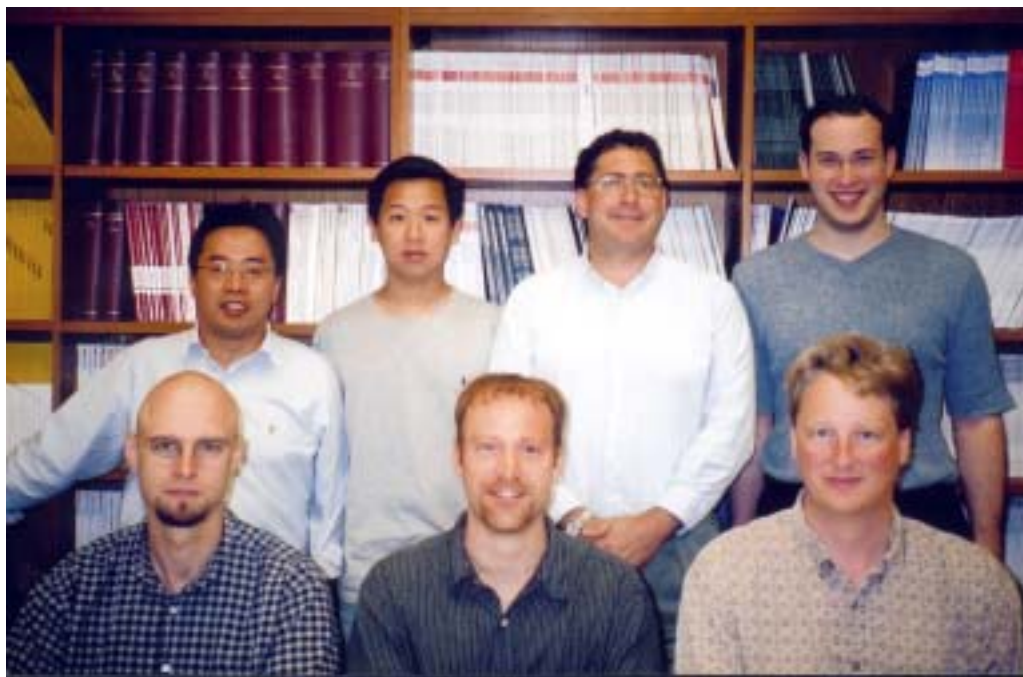
Standing: Donghyun Kim, Calvin Lew, Dan Spielman, Yakir Levin. Seated: Dirk Mayer, David Clayton, Elfar Adalsteinsson. Not pictured: Meng Gu

Interventional MRI
Kim Butts

Prostate, breast, and liver cancer continue to be a focus for the interventional MRI group. We published several papers on high intensity ultrasound ablation of the prostate with Chris Diederich and his group at UCSF (pg. 125). Together we worked on a resubmission of Graham Sommer's R33 grant, which received a favorable score. Viola Rieke continued to refine referenceless MR thermometry for this application (pg. 126), while Laura Pisani optimized the spatial resolution for these kinds of procedures (pg. 127). Sonal Josan continued to refine frozen tissue imaging and temperature quantitation for prostate cryoablation. We started a project with Blaine Chronik at the University of Western Ontario to make a gradient insert for breast interventions, and at our end, Jing Chen is using its specifications to optimize imaging performance for breast interventions. For liver applications, Karl Vigen validated his gated, navigated, multibaseline imaging method for temperature quantitation in vivo (pg. 128). We were sad to see him leave our group, but hope he will be happy at the University of Wisconsin where he took a staff scientist position. Viola Rieke developed an X-ray compatible MR phased array receive coil, for use with the integrated X-ray/MR system (pg. 130). Kim rotated off the ISMRM scientific program committee and onto the ISMRM Board of Trustees. All in all, it has been a very busy and productive year for this group.

Standing Sonal Josan, Jing Chin, Laura Pisani; seated Karl Vigen, Kim Butts, Viola Reike

Image Analysis

Sandy Napel

Bottom row left to right: *Barghav Raman, Cindy Shi, Burak Acar, Padma Sundaram, Ender Konukoglu, Joyoni Dey, Shauhua Sun, Evan Daniel.* ***Top row left to right:*** *Johann Won, David Paik, Tony Sherbondy, Feng Zhuge, Misung Han, Sandy Napel* ***Absent:*** *Tejas Rakshe, Markus Kukuk*

Sandy Napel's group addresses the field of image analysis, which has become increasingly important because the number of images per patient scan has increased dramatically and now numbers in the thousands. The group focuses on volumetric visualization, structure segmentation, quantitative analysis, and computer-aided detection of lesions. His group works with many colleagues in the Radiology Department, notably Chris Beaulieu, Dominik Fleischman, and Geoff Rubin who are active participants in the group's endeavors. This year saw the successful competitive renewal of their NIH CT Colonography project, which seeks to combine advanced visualization with computer-aided detection to improve the efficiency with which these examinations are interpreted. They continued work on existing projects, namely *Efficient Interpretation of Vascular Images,* funded by the NIH, *Computer-aided Detection of Lung Nodules,* funded by R2 Technology Inc., and the *Interventional Room of the Future,* funded by Siemens Medical Solutions, Inc., Four new papers are in press, eight abstracts have been submitted to RSNA 2004, and 3 abstracts have been submitted to Virtual Colonoscopy 2004. The group's move to the James H. Clark Center has already borne fruit in the form of a well-scoring NIH BISTI grant, which leverages the multidisciplinary nature of the Bio-X program to increase the utility and applicability of biocomputation techniques to all forms of biomedicine, including radiology.

Advanced X-ray Imaging Techniques

Rebecca Fahrig and Norbert Pelc

Standing: Sung-Won Yoon, Taly Gilat Schmidt, Sam Mazin, Norbert Strobel, Rebecca Fahrig, Norbert Pelc, Marcus Golstein (behind), Marlys Lesene (in front), Lei Zhu, Arun Ganguly. Kneeling: Jeff Dormo, Robert Bennett, Jared Starman, Zhifei Wen

The *Advanced X-ray Imaging Techniques* Group, led by Drs. Fahrig and Pelc, is involved in several ongoing investigations into the design, implementation and applications of digital detectors to diagnostic imaging and interventional guidance.

The X-ray/MR project (pgs. 155-156, 130) investigates the integration of a digital flat panel fluoroscopy system into the bore of an interventional MR system. In the past year, we completed the first comprehensive patient study demonstrating that use of the hybrid system increases the accuracy of the TIPS procedure. We have also started to investigate hybrid contrast agents that could be used to provide enhanced image contrast in both modalities, as well as expanding the possible applications for the system. Development of x-ray compatible MR coils provides artifact-free x-ray imaging while maintaining MR image quality. A presentation on aspects of this work (first author Wen) was awarded First Place Young Investigator's Award at the Association for the Advancement of Medical Instrumentation Annual meeting in June 2004. The next phase of this project, adding x-ray bi-plane capabilities, is now in the planning phase. This project has benefited from a close collaboration with GE Medical Systems.

Several projects using unique technology from the Scanning Beam Digital X-ray System (NexRay, Inc.) are also continuing (pgs.157-161). We are investigating the use of the system for lung nodule detection, and have built and verified numerical models that will allow us to optimize the system geometry for this imaging task. To avoid lengthy and complicated observer studies, we are also building digital observer models that will streamline the optimization process. We are also investigating the use of the NexRay technology for advanced volumetric CT systems. The design uses a large area scanned x-ray source and a fast, small area detector. We have obtained our first experimental images with the system. The data confirms theoretical predictions and the concept has great promise. The use of multiple small-area detectors are being investigated as a means to reduce the total required scanning time. The work on the CT scanner geometries has also benefited from collaboration with GE Medical Systems as well as from the collaboration with NexRay.

In other CT work, an investigation of the noise properties of digital x-ray detectors (pg. 162) has shown that binning of detector data prior to reconstruction reduces SNR as compared with appropriate filtering during reconstruction. Another project is developing techniques to experimentally identify the transition from quantum noise limited to electronic noise limited performance in CT (pg. 162).

The Axiom Lab with state-of-art C-arm faclity for phantom and animal experiments. Supported by Siemens AX.

The new state-of-the-art C-arm facility for phantom and animal experiments, the Axiom Lab, was completed in February 2004. Several pre-clinical experiments using the flat panel for 3D imaging have already been undertaken, and the reconstructed images are very encouraging. Investigations to improve image quality of the 3D reconstructions are underway (pgs. 163-164) including correction algorithms for scatter and for truncated projections. This project is supported by and benefits greatly from the collaboration with Siemens AX.

Model-Based Outcomes Analysis of Screening

Sylvia K. Plevritis

Sylvia Plevritis' multidisciplinary research group develops mathematical and statistical model toward advancing the understanding of the natural history of breast cancer and evaluating the impact of screening interventions (i.e. mammography, MRI) on cancer mortality. Over the past four years, we have been working in an NCI collaborative program entitled Cancer Intervention and Surveillance Modeling Network (CISNET) with NCI staff and six other research centers to quantify the relative contributions of screening mammography and adjuvant therapy on the recent decline in US breast cancer mortality. We have been a key contributor to the soon-to-be-released CISNET consortium summary statement on the impact of mammography, a hotly debated public health topic. Our group was also given supplemental funds by the DHHS to apply our CISNET model to predict future breast cancer trends and assess whether national targets for breast cancer mortality will be met (pgs. 167-168, 170-171).

Our research portfolio is expanding to include a study on the effectiveness and cost-effectiveness of lung cancer screening (pg. 168). We were recently awarded NIH R01 funding to transfer the methods that we developed in our breast cancer screening work to lung cancer. We will be modeling the natural history of lung cancer and evaluating screening for lung cancer with CT. The NCI CISNET program in lung cancer has invited to join work collaboratively with the NCI and three other NIH funded groups who are modeling on lung cancer screening.

We are expanding our research mission into the broader field of biocomputation. Our work in screening has revealed numerous fundamental questions about cancer progression that can not be addressed from an epidemiological perspective, but may be answered with the recent explosion of data and methods at the molecular level. For more details on this new program, see section entitled "Biocomputation."

17

Systems Biology of Cancer

Sylvia K. Plevritis

OVERVIEW

We have launched a campus-wide research initiative in Systems Biology of Cancer (SBC). Our mission is to bring together talented researchers to tackle complex computational modeling problems of cancer biology. We aim to elucidate the genetic, metabolic and signaling pathways underlying cancer initiation and progression through the seamless integration of experimentation and computational modeling. Revealing underlying molecular pathways will not only advance our understanding of cancer biology but may lead to the development of molecularly targeted therapies that will ultimately reduce cancer mortality.

We have been awarded an NIH P20 Planning Grant from the NCI's "Integrative Cancer Biology Program" (ICBP) to develop a Center for Systems Biology of Cancer at Stanford University. We have 18 Stanford faculty collaborators and 4 external affiliates whose collective expertise spans cancer biology, biochemistry, oncology, radiology, pathology, genetics, epidemiology, bioinformatics, engineering, computer science, statistics and mathematics.

P20 DEVELOPMENTAL PROJECT

Our NIH/P20 funded research program, entitled "Computational Modeling of Cancer Biology" aims to identify processes underlying the transformation from low grade to high grade lymphoma. Gene expression microarrays on disease pre- and post-transformation are available and promise to reveal new insights in this process. However, the analysis and interpretation of such vast amounts of data poses challenges that require new computational tools and direct communication between experimentalists and modelers. We aim to provide an environment that will produce computational tools needed by "wet lab" experimentalists to identify key regulatory networks and signaling pathways. Our study of malignant transformation will be done on humans and mice. In humans, we will focus on the transformation of follicular lymphoma to high grade lymphoma using gene expression data derived from tissue that is correlated to clinical events of disease progression and patient outcomes. Our study in mice will focus on the transformation of tumors from dependence to independence of MYC, the initiating oncogene, using gene and protein expression data, as well as molecular imaging studies. The mouse model gives us a valuable experimental system for validation and focuses us on a specific oncogene that has been highly implicated in the transformation of human follicular lymphoma. We aim to identify key gene regulatory networks through probabilistic modeling, signaling pathways through logical inference of experimental studies with highly curated databases, and kinetic models of specific gene-protein and/or protein-protein interactions driving the transformation process. The computational tools and experimental methods developed here should have broad applicability to the study of other cancers and other disease processes.

Left to right: Sylvia Plevritis, Slava Sigal, Jarrett Rosenberg, YenLin Chia, Peter Salzman

Molecular Imaging Program at Stanford (MIPS)

Sanjiv Sam Gambhir

Director, MIPS

The MIPS is an interdepartmental program (http://mips.stanford.edu) that has rapidly grown over the last 12 months. This program brings together faculty from many different disciplines for the purpose of advancing the field of molecular imaging. Development of new molecular probes, novel instrumentation, assays for living subjects, and translation of strategies for clinical imaging are all goals of the MIPS.

Many new faculty have been recruited to the program in the last year, primarily through the Department of Radiology. Over 60 faculty, research scientists, postdoctoral fellows are now in place as part of the MIPS. A full list of faculty may be found on the MIPS web site, but the recent accomplishments of MIPS faculty with Radiology as their primary Department are described next.

Sandip Biswal, M.D., is helping to bridge clinical musculoskeletal imaging with the MIPS. He was awarded the Donald E. and Delia B. Baxter Foundation Research Scholar Award for the project entitled "Can't you see the pain I'm in?: Using molecular imaging technologies to develop objective ways to diagnose and manage pain and nociception." He is also co-PI on a Office of Technology and Licensing Research Incentive Fund Award for the project: "Spatiotemporal analysis of hematopoietic stem cell trafficking in response to hematopoietic stress using a novel bone graft model".

Francis Blankenberg, M.D., Ph.D.., continues to advance validation of radiolabeled Annexin as well as study other new radiolabeled tracers. He has recently received one NIH R01 on "Imaging Apoptosis In Vivo with Technetium 99m Annexin V" and is Co-PI on a second grant with Jonathan F. Tait on "Membrane Binding and Imaging Applications of Annexins".

Xiaoyuan (Shawn) Chen, Ph.D., was recently recruited from University of Southern California as an Assistant Professor. He trained with the group at Washington University as a postdoctoral fellow prior to going to USC. He has significant experience in PET radiochemistry including peptide-based tracers. Several of his grants are being transferred from NIBIB, DOD, and American Lung Association. His recent paper entitled "MicroPET and Autoradiographic Imaging of GRP Receptor Expression with 64Cu-DOTA-[Lys3]Bombesin in Human Prostate Adenocarcinoma Xenografts" was featured on the cover of Journal of Nuclear Medicine.

Sam Gambhir, M.D., Ph.D., received two RO1's from the NIH including one on multimodality cardiovascular imaging and a second on imaging protein-protein interactions. He received a $ 1,000,000 gift from the Listwin/Canary Foundation to advance early detection of cancer through new imaging strategies. He also received a $ 300,000 equipment grant from the Department of Energy towards the purchase of a new microPET. Dr. Gambhir received the Academy of Molecular Imaging Scientist of the Year Award and is now President Elect of the Academy. Dr. Gambhir also received the 2003 Holst Medal from Philips Research and TU Eindhoven. Research Articles from the Gambhir lab were featured on the covers of FASEB, Human Gene Therapy, Circulation, and Protein Design and Engineering. Ian Chen, a Medical Scientist Training Program (MSTP) student in the Gambhir lab received the American Heart Association Pre-doctoral Fellowship Award. In addition, Shahriar Yaghoubi a postdoctoral fellow received the RSNA Research and Education Award. Christophe DeRoose, a postdoc in the lab received the Young Scientist Award for the Best Abstract at the AMI meeting in Madrid, Spain. Dr. Gambhir will serve on the NIH Medical Imaging Study Section for the next 4 years and has been selected to serve on the NIBIB Blue Ribbon Panel to advise the Director of the NIBIB.

Samira Guccione, Ph.D., was recently recruited to the Pediatric Radiology Division and to MIPS. She has recently received a grant from Varian Medical on "Localized Drug Delivery Using External Beam Radiation" with Susan Knox (Radiation Oncology) as co-PI.

Craig Levin, Ph.D., was recently recruited from University of California San Diego. He was awarded a R13 grant from NCI and NIBIB to put together a workshop on the Nuclear Radiology of Breast Cancer. Jin Zhang in his lab was awarded the 2004 Stanford University School of Medicine Dean's Fellowship.

Mike Moseley, Ph.D., is a great asset to the MIPS and brings significant expertise in small animal MRI to the group. He has recently received two RO1's and was awarded a $ 2,000,000 NIH shared instrument grant for a MRI. His many additional accomplishments are described in the RSL section.

Jianghong Rao, Ph.D., was recruited from UCLA as an Assistant Professor. He trained in Chemistry at Harvard and did a post-doc in cell imaging at UCSD. He transferred the highly competitive Burroughs Welcome Award with him. He was also awarded an NIH R21 for his project: "A Unified reporter gene for multi-modality imaging". Xinrui Yan, a postdoc in his lab was selected as one of three McCormick Scholars by the Katherine McCormick Fund for Women.

Joseph Wu, M.D., Ph.D., is a cardiologist and molecular pharmacologist who was recruited from UCLA. He will serve as bridge between the Departments of Radiology and Medicine in order to advance Cardiovascular Molecular Imaging. He was awarded a NIH/NHLBI K08 Clinical Scientist grant and a cardiovascular grant from the American Society of Nuclear Cardiology.

The MIPS now has a very active small animal imaging resource (http://mips.stanford.edu/public/sci3.adp) with multiple small animal imaging instruments located in the Clark Center. These technologies are playing critical roles in helping to validate new molecular imaging probes and many different types of pre-clinical models. The imaging instruments are described below.

MicroPET Imaging System (Concorde Microsystems, Inc. microPET R4)
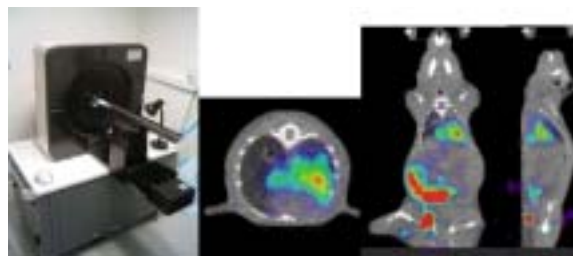
The center owns a Concorde Microsystems Rodent 4 ring microPET tomography, capable of acquiring list mode data and sorting the results to arbitrary (sub-second) frame durations. Non-invasive functional imaging of radiotracers may be performed on this instrument with an absolute system sensitivity of ~ 2.3% (at center) and spatial resolution of ~ 2 mm isotropic within the central 5 cm of the FOV. The system has 20 cm transverse field of view (FOV), and 8 cm axial FOV.

Left: Concorde Microsystems microPET R4. Middle and Right: Fused microPET/CT image of melanoma cancer cell animal model. The cancer cells are marked with HSV1-sr39tk and have metastasized to lungs allowing ^{18}FHBG imaging.

MicroCT Imaging System (GE Medical, eXplore RS)

The eXplore RS (Locus) Micro CT Scanner is designed to image small laboratory animals, such as mice and rats. It is an ideal instrument for molecular imaging research laboratories to non-invasively acquire 3-D images of both in vivo and in vitro specimens. The eXplore RS images whole-body small animals at resolutions of 45 or 90μm and in vitro specimens at 27μm. All eXplore micro CT systems use Volumetric Conebeam CT technology which, unlike conventional CT, allows the entire volume of a sample to be imaged in one rotation, rather than slice-by-slice. This method is significantly faster than conventional single slice or multi-slice CT. Volumetric Conebeam CT provides exceptional image quality with short scan times with a greater signal to noise ratio. With appropriate fiducial reference markers, microCT and microPET images acquired on each of these instruments may be superimposed.

GE Medical Systems eXplore RS MicroCT System.

In Vivo Optical Bioluminescence and Fluorescence Imaging Systems (Xenogen Inc. IVIS[a])

At the core of the facility are four Xenogen In Vivo Imaging Systems (IVIS), which allow non-invasive detection of luciferase-tagged cells or reporter gene expression in small animals. The light emitted from the cells expressing the bioluminescent reporter is detected at the surface of the living animal by an extremely sensitive integrating cooled charged-couple device (CCD) mounted on a light-tight imaging chamber. The acquisition of this bioluminescence signal in the IVIS system is controlled by the Living Image software, which allows quantitative analysis of the signal, which correlates directly to the number of cells expressing the luciferase gene, or the degree of induction of the reporter. Typically, transgenic animals expressing the luciferase gene under the control of a specific promoter, or animals injected with cells (tumor or pathogen) tagged with the luciferase gene under the control of a constitutive promoter are imaged over time with these systems. Three of the IVIS systems allow imaging of up to five animals simultaneously, with two having the option of fluorescence imaging by including

Xenogen bioluminescence imaging systems. Left, IVIS100 (2D) and right, IVIS 3D.
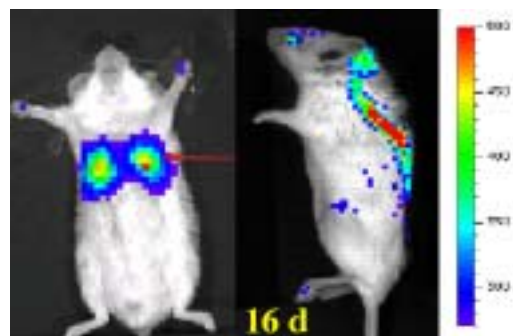

Image examples.

20

an illumination source and rotating emission band filter wheel. The fourth IVIS system is a prototype 3D instrument, which can be used to automatically image a single animal from multiple views.

MicroSPECT/CT Systems (Gamma Medica A-SPECT)

Gamma-Medica A-SPECT single photon emission computer tomography (microSPECT-CT) system is available for sub-millimeter radionuclide imaging in small animals. The camera comprises two flat panel heads, each which uses an array of 2 mm x 2 mm x 6 mm NaI(Tl) pixels coupled to a position sensitive photomultiplier tube readout. Each head has a 130 mm x 130 mm field of view. Pinhole collimators are available with interchangeable apertures of 0.5, 1, 2, and 3 mm. The two gamma camera heads attach to separate linear translation stages allowing the focal distance of the cameras to be varied easily and independently. Images are reconstructed with an ordered sets expectation maximization (OSEM) algorithm. This A-SPECT system incorporates an integrated microCT capability with the CT perpendicular to the FOV of the radionuclide system in the gantry. The microCT system is implemented in a cone-beam geometry to utilize the limited x-ray flux from a microfocus tube efficiently with a high resolution GOS/CMOS detector (2048 by 2048 readout of 50_ m by 50 _ m pixels). Using this detector along with this microfocus x-ray tube rated at 50 KV and 1.0 mA, the CT system achieves high-resolution (better than 100 μm) imaging with cone beam image reconstruction. This integrated x-ray CT system gives hybrid, co-registered CT/SPECT images. Animal movement includes a vertical translation stage and a rotational stage for full angle tomography. Animals can be imaged while anesthetized and/or catheterized. The cameras can be adjusted to facilitate anterior/posterior planar scintigraphy with pinhole or parallel hole collimators. The gantry is compact in size, requiring just 40 inches by 25 inches of floor space. The gantry is on a wheeled platform incorporating a backup power supply allowing it to be moved between laboratories. Currently located at the Nuclear Medicine Department. This instrument is to be moved to the SCI3 in December 2004.
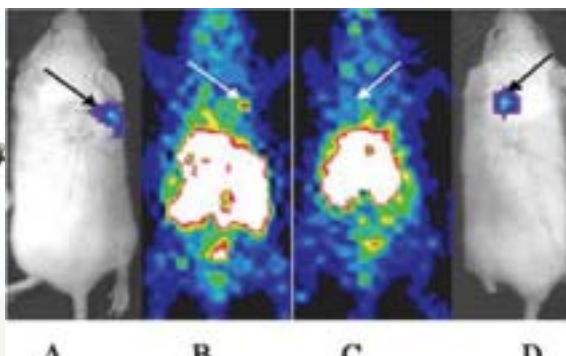
Far left:Gamma Medica A-SPECT system available for small animal imaging. Figures A-D: Radionuclide and bioluminescent imaging of small subcutaneous tumors with VEGF-driven assembled complexes. The images show co-localization of in vivo *bioluminescent and targeted radionuclide images. Two groups of tumor bearing mice (n= 5, 99mTc-HuS/ Hu-P4G7 antibody; n= 10, 99mTc-HuS/Hu-VEGF) were anesthetized for planar whole body BLI and radionuclide imaging 10 days after implantation of 4T1gfp/luc cells into the shoulder region.* Panel A, *BLI of a mouse with right shoulder tumor,* Panel B, *radionuclide image of the same mouse one hour after injection with 99mTc-HuS/Hu-VEGF,* Panel C, *radionuclide image of a mouse with left shoulder tumor after injection with 99mTc-HuS/Hu-P4G7, and* Panel D, *BLI of the same mouse. Black arrows in panels A and D mark tumor locations as observed by BLI. White arrows in panels B and C mark location of tumor on radionuclide images.*

## In Vivo Fluorescence Tomograph (GE-ART eXplore Optix)

ART's preclinical optical molecular imager, eXplore Optix, is based on time domain (TD) optical imaging technology. With the use of specialized laser sources and sensitive detectors, TD optical imaging allows the distinct separation of light scatter and light absorption in tissue. TD optical technology measures significantly more information than other optical imaging technologies and is not limited to surface structures. In addition, TD optical imaging obtains fluorescence lifetime information– an important parameter in the measurement of tissue environment. The system has been designed with multi-wavelength capabilities to examine exogenous fluorescence and absorption as well as endogenous contrast. A computer, monitor, and accessories are included with the system, as well as software for data acquisition and analysis. As soon as the animal is positioned, the operator can select a region of interest (ROI) and a desired resolution within a maximum scan area of 20 by 9 cm. Scan-

GE eXplore Optix Fluorescence Tomograph.

ning time depends on the scan area and resolution, and ranges from 1 to 20 minutes. The system is self-calibrated. Fast image processing is done automatically after the scanning phase is complete. One can select fluorescence lifetime, fluorescence intensity, and absorption images and superimpose on the visible image. The illumination wavelength occurs via a single fixed near-infrared wavelength in the range of 660 to 780 nm. Detection wavelengths occur in the range of 680 to 860 nm: one at the illumination wavelength (absorption measurement) and one at the emission wavelength. The choice of wavelengths can be defined in the near-infrared wavelength region and visible, if required.

HIGH-RESOLUTION ULTRASOUND (VISUALSONICS, VEVO)

Ultrasound imaging of small animals is also available using the VisualSonics Vevo 660 high-resolution ultrasound micro-imaging system. This instrument was designed specifically for non-invasive small animal imaging, and allows resolution down to 30μm. This high-resolution ultrasound imaging system enables in vivo visualization, assessment, and measurement of anatomical structures and hemodynamic function in longitudinal imaging of small animals. Real-time images can be acquired in B-mode, Pulsed-wave Doppler Mode, and M-mode at a frame rate of 30Hz. Real-time microvisualization (RMV) scanheads of different centering frequencies (40 MHz, 35 MHz, 25 MHz) can be used to optimally image structures at resolutions down to 30 microns for efficient viewing of small physiological structures and imaging living tissue and blood flow with near-microscopic resolution. The system can be used to guide injection of genes or cells into mouse embryo, mouse heart, and rat heart, respectively or to measure tumor volumes. The built-in Vevo Software allows myriads of measurements including placental diameter and depth, left ventricular volumes, and velocity time integral across all major valves. Using a rail-mounted needle injection system, quick alignment and adjustment of RMV probe and the associated injection system are possible for real-time image-guided injections and extractions to be performed. This allows targeted injection of cells, drugs or genetic material for small embryo to adult.
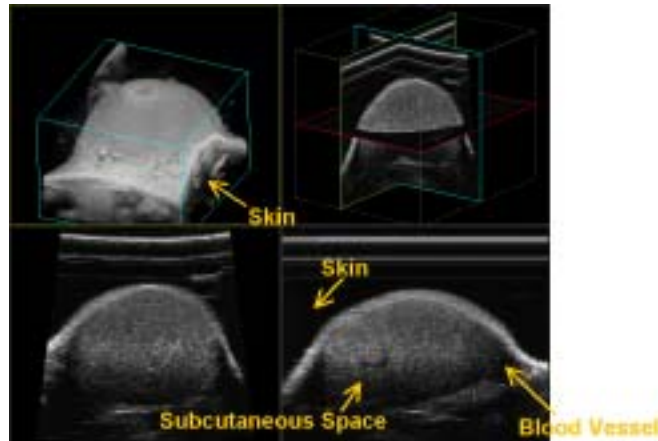
Left: VisualSonics Vevo 660 high-resolution ultrasound micro-imaging system. Right: Ultrasound Imaging of Mouse B16 Melanoma Xenograft A nu/nu mouse was subcutaneously inoculated with 5 million B16 melanoma cells on the right flank. The tumor xenograft was imaged 7 days later with a high-resolution small-animal ultrasound system (VisualSonics Inc., Vevo660) using a motor-controlled RMV (Real-time Microvisualization) scanhead (center frequency=40MHz, focal length=6mm, FOV=17.9mm). 3D reconstruction followed by surface rendering of the 2D image dataset reveals an ellipsoidal tumor beneath the skin (top left panel). Close-up examination of tumor volume in two of the three orthogonal planes (red, green, and blue planes; top right panel) with respect to the scan head reveals anatomical details both surrounding (skin, subcutaneous space; bottom left panel) and within tumor (blood vessel, bottom right).
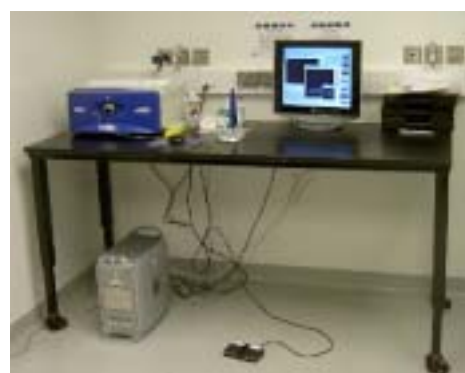
MICROMR SYSTEMS (VARIAN MEDICAL, INC. UNITY INOVA AND GE MEDICAL, INC. MICROSIGNA 7.0)

The presently available small-animal MRI system has a Varian Unity Inova console coupled to an Oxford MarkII 4.7 Tesla (horizontal) bore magnet with shielded GE Acustar[a] gradients for small animal and in vitro research (15cm bore, 12Gauss/cm gradient strength, with a slew rate of 800mT/m/ms). This system uses Varian 30mm and 80mm volume RF coils and has MR microscopy capabilities with 20-50_ m resolution. A MacG4-based data acquisition system is available for real-time physiologic monitoring, as is a computer controlled pump that can produce physiologically relevant flow waveforms, and a flexible, PC controlled stepper-motor system having 3 axes of motion for phantom development. The system is equipped with both cardiac and respiratory gating capabilities and uses a quadrature, transmit/receive RF coil for rat imaging. MRVision software is specifically used for region of interest (ROI) analysis and derivation of T1 and T2/T2* maps.

New MRI system for small animal imaging: Mike Moseley has been recently been awarded a shared instrument grant from NIH to purchase a 7T MRI system dedicated to small animal imaging. The scanner is the newly-announced GE Medical Systems "microSigna 7.0", a new high-field 7Tesla, small bore (310mm) horizontal scanner that brings the best in clinical consoles (the GE LX 11, EXCITE 2, multi-coil platform) and all GE and Stanford-derived LX pulse sequences together with a new design in high-speed gradients (25cm, 500mT/m) with 8-channel multi-coil RF arrays. The microSigna 7T is similar in RF, electronic, and hardware/software design and inventory to the whole-body 7T currently being offered by GE commercially, with the main exceptions of much faster gradients (25cm, 500mT/m), smaller bore (310mm vs. 900mm), and RF coil sizes (the microSigna7T comes with a 18cm whole-body RF coil) making it suitable for rodents, nonhuman primates and rabbit cardiovascular studies. This system will be delivered in 2005.

HIGH-RESOLUTION CONFOCAL MICROSCOPE (MAUNA KEA TECHNOLOGIES, CELL-VIZIO)

The Cell-viZio from Mauna Kea Technologies is a fiber coupled confocal imaging device specifically designed for in vivo animal imaging in real time at the cellular level. The Cell-viZio is a flexible probe capable of confocal reflectance and fluorescence imaging. For reflectance imaging, a red or infrared light is shone onto a tissue and focused several tens of microns below its surface. The photons composing the laser beam are reflected by the various components of the tissue. Delicate filtering allows the device to optically section the tissue, thus making high resolution images (2.5-5.0 μm lateral and 15-20 μm axial) of thin layers at distinct depths. The resulting images have exquisitely fine resolution, showing the cells in their natural environment. The reflectance images are obtained by placing the probe on the surface of the tissue and by focusing the laser beam about 40 microns

Mauna Kea Technologies' high-resolution confocal microscope.

below the surface. No physical sectioning on the tissue is required. In order to research molecular processes in vivo, it is possible to mark the tissue under observation with fluorescent contrast agents. Excited at a given wavelength, these agents will reemit fluorescent light. The Cell-viZio enables high-resolution in vivo confocal fluorescence imaging with a variety of contrast agents. As in the reflectance case, light is focused at a certain depth in the tissue and illuminates its components. This time, only components which have been marked by the fluorophore will react to the illumination. Depending on the nature of the marker, one can thus obtain an image of various essential cellular components, such as nuclei or cytoplasmic membranes.

FLUORESCENCE MICROENDOSCOPY (BUILT IN-HOUSE)

A group led by Mark Schnitzer (Applied Physics and Bio-X) has developed two forms of minimally invasive fluorescence microendoscopy and tested their abilities to image cells in live animals. Both one- and two-photon fluorescence microendoscopy are based on doublet and triplet compound gradient refractive index (GRIN) lenses that are 350-1000 mm in diameter and provide resolution of about 0.85 ± 0.05 μm and fields of view of 122-1000 μm. One-photon microendoscopy allows full frame images to be viewed by eye or with a camera. Two-photon microendoscopy is a laser-scanning modality that provides optical sectioning deep within tissue. The lengths of the endoscopes can be up to several centimeters, allowing one for example, to access brain tissue at any depth within the rodent cerebrum. As these devices become more mature, they will be available to the MIPS.

DIGITAL WHOLE-BODY AUTORADIOGRAPHY (DWBA)

Digital whole body autoradiography (DWBA) is a powerful invasive tool to obtain very high resolution images of tracer distribution. MicroPET/microSPECT permits repeated, non-invasive radionuclide imaging of mice, with good resolution. When very high resolution of trapped radioactivity is required, DWBA with beta- or positron-emitting probes offers imaging resolution at 25-200 microns. The autoradiography facilities available to the SCI3 include both a Leica cryostat for whole-body sectioning of small animals and a Molecular Dynamics phosphor imaging system which produces autoradio-

Figure. *Cryostat and Digital Phosphor imaging system for performing Digital Whole-Body Autoradiography (DWBA). Left panel shows the Leica Systems macrotome with cryostat and tissue sectioning capabilities. Middle panel shows the Molecular Dynamics PhosphorImager system with re-usable digital plates blanked by an eraser. A workstation can be used to view and quantitate images. Right: The final quantitative DWBA can be directly compared to the anatomical cross-section (a mouse injected with ^{14}C-ganciclovir is shown).*
Figure. *Photon imaging microscope built in-house for high resolution cell culture studies.*

grams with a resolution as high as 50 microns. Mice injected with a tracer are sacrificed, frozen in carboxymethylcellulose and whole-body sectioned at 25-50 micron thickness. Tissue slices are exposed for 4-72 hours to digital plates, which are then scanned in a phosphor imager. The Amersham Biosciences (Molecular Dynamics) PhosphorImager SI is a scanning instrument that is a compact laser-optical imager that uses innovative storage phosphor technology to detect and quantify radioactivity. It is connected to a Windows NT operating system. The system uses the ImageQuant and Scanner Control software from Molecular Dynamics. The system allows one to acquire accurate data quickly from any sample traditionally visualized using X-ray film.

The PhosphorImager SI takes the place of film in dozens of applications. A full 20Σ25 cm sample scan @200 microns will complete in 4 minutes. Photographs of whole-body sections can be compared with autoradiograms to correlate anatomy and probe localization. Using radioactive standards, full quantitation is possible. Animals scanned by microPET can subsequently be sacrificed and used for high-resolution tracer distribution analysis by DWBA. Animals scanned optically can also be sectioned for comparison of optical signal with anatomy.

The space plans for the MIPS include the Clark Center, Edwards Building, and the soon to finish Lucas Expansion. The Lucas Expansion will house the new cyclotron, radiochemistry labs, and synthetic organic chemistry labs. It is currently expected that students/staff for Drs. Rao, Chen, Biswal, and Guccione will all be housed in the Lucas Expansion in a shared laboratory environment. The cyclotron will help to produce both clinical tracers (e.g., FDG) and research tracers for the MIPS. A new cyclotron facility head is expected to be hired in the next few months. Radioactive Tracers will move from the Lucas Expansion to the Clark and the Stanford hospital via an underground pneumatic tube. Nuclear Medicine will undergo significant space renovations over the next three years and will be a key component of MIPS for pilot testing of new radiopharmaceuticals.

Lucas Center Faculty, Staff & Students

FACULTY

Gary M. Glazer, M.D.
Gary H. Glover, Ph.D.
Roland Bammer, Ph.D.
Mark Bednarski, M.D., Ph.D.
Kim Butts, Ph.D.

John E. Desmond, Ph.D.
Rebecca Fahrig, Ph.D.
Samira Guccione, Ph.D.
Robert J. Herfkens, M.D.
Michael E. Moseley, Ph.D.

Sandy Napel, Ph.D.
Norbert J. Pelc, Sc.D.
Sylvia K. Plevritis, Ph.D.
Daniel M. Spielman, Ph.D.

SCIENTIFIC STAFF

Elfar Adalsteinsson, Ph.D.
Marcus Alley, Ph.D.
Wendy Baumgardner, RVT, LATg
Robert Bennett, M.S.
Jenea Boshart, M.A.
Thomas Brosnan, Ph.D.
Steven Choi, B.S.
David Clayton, Ph.D.

Mary Draney, Ph.D.
Arundhuti Ganguly, Ph.D.
Diane Howard, RVT, LATg
Hsi-An (Sean) Lee, R.T.
Laura Logan, B.S., R.T.
Linda Novello, R.T.
Ruminder Samra, R,T,

Anne Sawyer-Glover, B.S., R.T. (R)(MR)
Pamela Schraedley, Ph.D.
Bronislava Sigal, Ph.D.
Marc Sofilos, R.T.
Yingyun Wang, B.S.
Yishan Yang, Ph.D.
Marowan Zakhour, M.D.

ADMINISTRATIVE AND SUPPORT STAFF

Mary Bobel
Maggie Bos
Nancy Bucy
Michelle Christierson
Donna Cronister
Debra Frank

Susan Kopiwoda
Marlys Lesene
Kevin Murphy
Sharon Pollio
Kala Raman

John Reuling
Flor Reyes
Lanzie Rivera
Susie Spielman
Lakeesha Winston

POSTDOCTORAL FELLOWS

Joyoni Dey, Ph.D.
Jung-Jin (Jason) Hsu, Ph.D.
Dong Hyun Kim, Ph.D.
Daniel Margolis, M.D.

Rex Neubold, Ph.D.
David Paik, Ph.D.
Angel Pineda, Ph.D.

Laura Pisani, Ph.D.
Raghav Raman, M.D.
Scott Reeder, M.D.

GRADUATE STUDENTS

Jean Chen, M.S.
Yen-Lin Chia, M.S.
Jamie Dermon, M.D.
Jeff Dormo, M.D.
Taly Gilat, M.S.
Joan Greve, M.S.
Anjia Gu, M.S.
Meng Gu, M.S.
Michael Hope, M.D.
Yanle Hu, M.S.
Matthew Kirschen, M.D.
Sonal Josan, M.S.

Christine Law, M.S.
Yakir Levin, M.S.
Calvin Lew, M.S.
Sam Mazin, M.S.
Michael Padilla, M.S.
Julia Po, A.B.
Rebecca Rakow, M.S.
Tejas Rakshe, M.S.
Viola Rieke, M.S.
Anthony Sherbondy, M.S.
Cindy Shi, Ph.D.

Gaurav Srivastra, M.S.
Jared Starman
Shaohua Sun, M.S.
Padma Sundaram, M.S.
Moriah Thomason, M.S.
Chardonnay Vance, M.S.
Zhifei Wen, M.S.
Jung Ho Won, M.S.
Sung-Won Yoon, M.S.
Huanzhou Yu, M.S.
Lei Zhu, M.S.

VISITING RESEARCHERS AND SCHOLARS

Markus Goldstein, M.S.

UNDERGRADUATES

Klaus Aichelen
Courtney Rainey

Lucas Center Collaborators

COLLABORATING STANFORD DEPARTMENTS

Almost three hundred faculty, postdoctoral fellows, students and research staff from across the university are affiliated with research programs at the Lucas Center representing the following departments:

Applied Physics

Cancer Biology

Cardiovascular Medicine

Computer Sciences

Electrical Engineering

ENT

Functional Restoration

Infectious Diseases

Mechanical Engineering

Medical Informatics

Medicine/Oncology

Nephrology

Neurobiology

Neurology

Neurosurgery

OB/GYN

Orthopedics/Orthopedic Surgery

Pediatrics/Neonatology

Psychiatry

Psychology

Stroke Center

Surgery

Urology

Vascular Surgery

OUTSIDE COLLABORATORS

Active collaborations are in place with researchers from outside Stanford representing the following institutions:

Aneurex

Bresagen

Chiron

Cordis

Elbit

Endius

Ethicon

FeRx, Inc.

Galil Medical

Genentech, Inc.

Genetics

GE Medical Systems

Lunar Corporation

NexRay

Novartis

Nycomed

R2 Technology, Inc.

Siemens Medical Systems

Smith Kettlewell Eye Institute

SRI International

Stanford Center for Biomedical Ethics

Sterling

University of California, Berkeley

University of California, Davis

University of California, Irvine

University of California, San Francisco

University of California, San Diego

New Faculty, Staff, Research Fellows and Visitors at the Lucas Center and Throughout the Department

We welcome new faculty, staff, fellows and visitors from institutions locally, around the country and abroad.

FACULTY

Roland Bammer, Ph.D.
Assistant Professor

Samira Guccione, Ph.D.
Assistant Professor

Craig Levin, Ph.D.
Associate Professor

Xiaoyuan Chen, Ph.D.
Assistant Professor

Jianhong Rao, Ph.D.
Assistant Professor

STAFF

Robert Bennett, M.S.
Mary Bobel
Steven Choi
David Clayton, Ph.D.

Debra Frank
Arundhuti Ganguly, Ph.D.
Sharon Pollio

POSTDOCTORAL FELLOWS

Karen Ayotte
Pediatric Imaging

Shane Ball
Body Imaging

Carmel Chan
Molecular Imaging

Kirk Chottanapund
Neuroimaging

Donna D D'Alessio
Mammography

Abhijit De
Molecular Imaging

Samuel Edward Fuller
Musculoskeletal Imaging

Nadine Gaab
RSL

Olivier Gehysens
Molecular Imaging

Adam Gittleman
Neuroimaging

Frezghi Habte
Molecular Imaging

Richard Hallett
Cardiovascular Imaging

Sumi Hasegawa
Molecular Imaging

Eric Herget
Cardiovascular Interventional
Radiology

Mark Hiatt
Cardiovascular Imaging

Aya Kamaya
Body Imaging

Marcus Kukuk
3D Laboratory

Ray Lertvaranuk
Molecular Imaging

Jelena Levi
Molecular Imaging

Stanley Lim
Body Imaging

Stanley Lu
Neuroimaging

Sanjay Mohindra
Cardiovascular Interventional
Radiology

Rexford Newbould
RSL

Para Padmanabhan
Molecular Imaging

Steven Poplaw
Body Imaging

Pritha Ray
Molecular Imaging

Scott Reeder
Body Imaging

Adrienne Sage-el
Nuclear Medicine

Meike Schipper
Molecular Imaging

Cindy Shi
3D Laboratory

Jeffrey Tseng
Nuclear Medicine/Molecular Imaging

Roy Vaid
Neuroimaging

Vikas Vij
Neuroimaging

John Wahlen
Body Imaging

Jason Wong
Cardiovascular Interventional
Radiology

Yan Wu
Molecular Imaging

Ben Xing
Molecular Imaging

Shariar Yaghoubi
Molecular Imaging

Doris Yip
Neuroimaging

Jin Zhang
Molecular Imaging

GRADUATE STUDENTS

Ian Chen
Molecular Imaging

Jeff Dormo, M.S.
RSL

Angela Foudray, M.S.
Molecular Imaging

Markus Goldstein, M.S.
RSL

Joan Greve, M.S.
RSL

Anjiu Gu, M.S.
RSL

Thomas Hope, M.S.
RSL

Andy Loening, M.S.
Molecular Imaging

Sam Mazin, M.S.
RSL

Manish Patel, M.S.
Molecular Imaging

Julia Po, A.B.
RSL

Sunetra Ray, M.S.
Molecular Imaging

Cesar Rodriguez, M.S.
Molecular Imaging

Gaurav Srivastava, M.S.
RSL

Jared Starman, M.S.
RSL

Zac Walls, M.S.
Molecular Imaging

Jung Ho Won, M.S.
RSL

Farewells

In the past year we have bid farewell to the following people. We send our best wishes with them for happiness and success in their new positions.

SCIENTIFIC STAFF

Elfar Addelsteinsson, Ph.D.
Massachusetts Institute of Technology

Lara Foland, B.A.
University of California, Los Angeles Graduate School

Michael Markl, Ph.D.
University of Frieberg, Germany,
Faculty

Karl Vigen, Ph.D.
University of Wisconsin

POSTDOCTORAL FELLOWS

Annabel Chen, Ph.D.
University of Taiwan, Faculty

Walter Hundt, Ph.D.
Practicing Radiology

Jon Levin, M.D., Ph.D.
Radiologist and Clinical Instructor
St. Luke's Medical Center, Minneapolis, MN

Laura Stables, Ph.D.
University of California, San Francisco, Faculty

GRADUATE STUDENTS

Michael Hope, M.D.
University of Michigan, Residency

Peter Salzman, Ph.D.
University of Rochester, Postdoctoral Fellow

Congratulations

It is a mark of particular pride that some of our students remain with us after their training to continue the outstanding work that they have begun here. We would like to congratulate the following people for their promotions in our program.

RESEARCH STAFF FROM POSTDOCTORAL FELLOWS

David Clayton, Ph.D.

Arundhuti Ganguly, Ph.D.

FACULTY FROM RESEARCH STAFF

Roland Bammer, Ph.D.

Samira Guccione, Ph.D.

Awards and Honors

SANDIP BISWALL

The Baxter Foundation award for using molecular imaging to diagnose andmanage pain and nociception

CHRIS CONTAG, SANDIP BISWALL

Office of Technology Licensing (OTL) Research Incentive Fund Award. Spatiotemporal Analysis of Hematopoietic Stem Cell Trafficking in Response to Hematopoietic Stress Using a Novel Bone Graft Model

REBECCA FAHRIG

The Baxter Foundation award for Tranlational research in lung nodule detection.

SANJIV SAM GAMBHIR

Distinguished Basic Scientist of the Year Award, *Academy of Molecular Imaging,*.Multimodality Molecular Imaging: Emerging Strategies for the Interrogation of Diseased Cell. March 2004.

Holst Medal, *Philips Corporation and TU/e, Netherlands.* For significant innovations in a field of applied science. Imaging Diseases with Molecular Detectives, Holst Memorial Lecture and Symposium on Molecular Imaging. Eindhoven, Netherlands. November, 2003.

Listwin/Canary Foundation award to advance early detection of cancer

Molecular Imaging, Bavaria Lectureship, *V. Munchner Nuclearmedizin-Symposium*. Munich, Germany. September 2003.

National Blue Ribbon Panel, *National Institute of Biolagicl Imaging and Bioengineering (NIBIB)* to advise Director of NIBIB

GARY GOLD

Cum Laude Award for Outstanding Paper, *Society of Computed Body Tomography and Magnetic Resonance Imaging.* Garry Gold, Bryan Hargreaves, Han, John Pauly, Grant Wright, Robert J. Herfkens, Jean Brittain, Christopher Beaulieu. Rapid Measurement of Early Articular Cartilage Degeneration at 3T. March 2004

MICHAEL HOPE

Lauterbur Award, *Society of Computed Body Tomography and Magnetic Resonance Imaging.* Michael Hope, Jonathan Levin, Michael Markl, Mary T. Draney, N Wilson, Robert Herfkens. Four-Dimensional Magnetic Resonance Velocity Mapping: Velocity Profile of Blood-Flow through the Thoracic Aorta in 10 Healthy Volunteers. March 2004

JUDY ILLES

Special Ethics Panel, *Society for Neuroscience*
Member, Advisory Council, *Canadian Institutes of Health Research, Neurosciences, Mental Health and Addiction Institute*

WILLIAM KENNEDY, REBECCA FAHRIG

Office of Technology Licensing (OTL) Research Incentive Fund Award. MRI Voiding Cystography in Children: Quality Improvement and Radiation Elimination

MATTHEW KIRSCHEN

Student Grant, *Stanford BioX Interdisciplinary Initiatives Program,*Investigation of the effects of different analytic strategies on the outcome of clinical fMRI studies. 2003.

BARTON LANE

Stanford B. Rossiter Senior Faculty Award, *Stanford University Department of Radiology.* 2004.

SAM MAZIN

Pre-doctoral fellowship. *American Heart Association Sam Mazin.* Fast Volumetric Cardiovascular CT Scanner

MICHAEL MOSELEY

President, *International Society of Magnetic Resonance in Medicine*, 2003-2004

NORBERT PELC

Advisory Committee, *Stanford High Resolution Electron Microscope Facility (An NCRR funded research resource)*
Chair of the Strategic Planning Subcommittee, *National Advisory Council for Biomedical Imaging and Bioengineering (NACBIB)*

ANGEL PINEDA

Research Training Fellowship, *American Lung Association.*

LAURA PISANI

Student Stipend, *International Society of Magnetic Resonance in Medicine.*Optimizing Spatial Resolution for MR Thermal Imaging of Transurethral Ultrasound Prostate Ablation May 2004

F. GRAHAM SOMMER

Second Place Paper Award, *Society of Uroradiology.* F. Graham Sommer, Larry Chow, Norbert Pelc. Measurement of renal extraction fraction using contrast enhanced CT.

SHREYAS S. VASANAWALA

President's Award, *The American Roentgen Ray Society* Shreyas S. Vasanawala, Brian A. Hargreaves, John M. Pauly, Dwight G. Nishimura, Christopher F. Beaulieu, Garry E. Gold. Rapid musculoskeletal MR imaging with phase-sensitive steady-state free precession

XINRUI YAN

McCormick Scholar. *Katherine McCormick Fund for Women*

ZHIFEI WEN

Young Investigator Award, *Association for the Advancement of Medical Instrumentation.* Zhifei Wen, Rebecca Fahrig, Arundhuti Ganguly, Stephen T. Kee, Bruce L. Daniel, Kim Butts, Huanzhou Yu, and Norbert J. Pelc.Hybrid Interventional X-ray/MR System

Strategic Research Development

Susan Kopiwoda

The Stanford University Department of Radiology has had a remarkable year in terms of research activity during 2004. NIH awards for 2004 increased from $ 8M to $ 12M. Based on the number and dollar value of NIH proposals during 2004 we anticipate another surge in award activity for 2005.

The Radiology Department' s research activity is coordinated through the Strategic Research Development Office, which provides a resource for funding opportunities, assists in developing strategic funding plans, and aids faculty to reach departmental and individual research goals. We work with established investigators on a variety of levels to provide a wide range of assistance to facilitate the smooth transition of applications as they move from concept to final submission. For recently appointed faculty just beginning to write federal grants, the Strategic Research Office can help make an overwhelming process seem less intimidating and more approachable.

RESEARCH FUNDING FOR 2004

More than 95% of Department sponsored research funding is received from various NIH Institutes. This year has been a tremendously active year with a total of $ 68M in proposals. More than 80% of this amount can be attributed to NIH proposals. Awards in 2004 have also increased by $ 4M over the previous year. Based on the $ 68M in proposals for 2004 we look forward to an even more successful 2005 and nearly a doubling in NIH awards. (Figure 1)
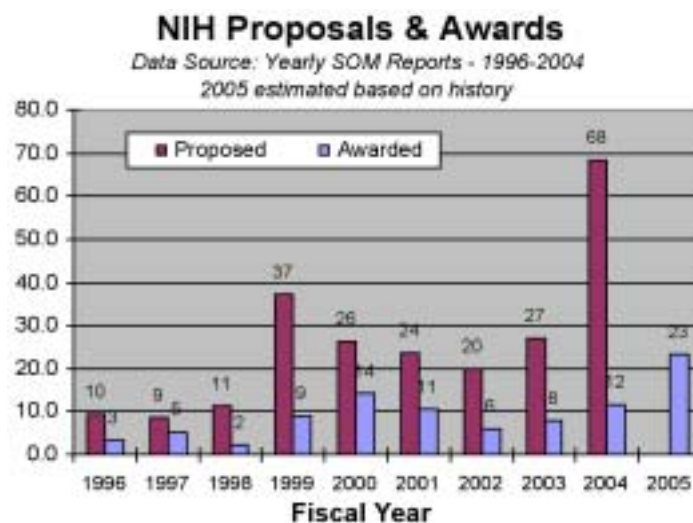
The enormous growth in NIH proposals this year reflects increased activity in many areas in the department. However, a significant fraction can be attributed to a few major applications, each representing an important focus area for the department:

1. Systems Biology in Cancer Program (SBC-P20)
2. High Field GE Experimental MR Scanner (NIH HEI Program)
3. In Vivo Cancer Molecular Imaging Center (ICMIC-P50)
4. Center for Advanced Magnetic Resonance Technology (CAMRT-P41)

History of NIH proposals and awards to Stanford Radiology department. Numbers represent dollars in millions.

As of this publication the Systems Biology in Cancer Program (P20) and the High Field Experimental Scanner (NIH HEI Program) have both been approved and funding will be available before the end of this calendar year. Both are important programs and fit well with the CAMRT and the ICMIC@Stanford Programs. The High Field MR Scanner will add yet another dimension to Stanford's growing molecular imaging program (MIPS). The Systems BiologyProgram establishes an exciting new direction for the department and will surely bring an added layer of important research. We expect to hear about the ICMIC by the end of this calendar year and the CAMRT continuation soon thereafter.

In addition to these major programs there are many more outstanding applications that were submitted and awarded during this past year. We look forward to an exciting 2005 with the opening of the newly expanded Lucas Facility with the ultra high field 7 Tesla MR imaging system and the cyclotron facility for radiopharmaceutical production. This new facility, with all that it has to offer, will very directly impact our research efforts. The research planned for the Lucas Expansion will provide new basic knowledge about human health and disease, and also promises to impact clinical care through improvements in how we diagnose, treat and monitor patients.

The following list represents all funded and proposed Sponsored Projects from Radiology faculty in the past year.

Active Awards FY 2004

Government Sponsored Projects

PI	Agency	Title	Type
Adalsteinsson	NIH	MR Spectroscopic Imaging in Alzheimer's Disease	R01
Bammer	NIH	Improving SENSE MRI for Spiral and Echo-Planar Imaging	R01
Beaulieu	NIH	Three-Dimensional CT Colonography	R01
Blankenberg	NIH	Imaging Apoptosis in vivo with Technetium 99m Annexin	R01
Butts	NIH	iMRI Methods for Cancer Diagnosis and Treatment	R01
Butts	NIH	Improved Open MRI for Image-Guided Breast Procedure	R21
Daniel	NIH	Magnetic Resonance Imaging of Breast Cancer	R01
Daniel	NIH	MR-Guided Radiofrequency Ablation of Breast Cancer	R21
Daniel	NIH	Techniques for MRI-Guided Cryosurgery of Prostate Cancer	R01
Desmond	NIH	fMRI and TMS Analysis of Cerebellar Cognitive Function	R01
Desmond	NIH	fMRI Analysis of Aging and Awareness in Conditioning	R01
Fahrig	NIH	Improved C-Arm CT for Interventional Procedures	R01
Fahrig (prev. Pelc)	NIH	Hybrid X-Ray/MR Systems for Image-Guided Procedures	R01
Gabrieli	NIH	Cognitive Analysis of Working Memory Development	R01
Gambhir	NIH	Correlative Imaging of Tumor Angiogenesis	R21
Gambhir	NIH	Reporter Imaging of Protein-Protein Interactions	R01
Gambhir, Sam	NIH	Multimodality Imaging of Cell Mediated Gene Transfer	R01
Glover	NIH	Center for Advanced Magnetic Resonance Technology at Stanford	P41
Gold	NIH	Rapid MRI for Evaluation of Osteoarthritis	R01
Levin	NIH	Nuclear Radiology Workshop of Breast Cancer	R13
Moseley	NIH	DWI Assessment of Clinical Acute Stroke	R01
Moseley	NIH	Improved PWI Methodology in Acute Clinical Stroke	R01
Moseley	NIH	High Field GE Experimental MR Scanner	RR
Napel	NIH	Efficient Implementation of 3D Vascular Image Data	R01
Pelc	NIH	Advanced Techniques for Cancer Imaging	T32
Plevritis	NIH	Cost Effectiveness Analysis of Breast Cancer Screening	R01
Plevritis	NIH	Breast Cancer Trend Analysis Using Stochastic Simulation	U01
Plevritis, Sylvia	NIH	Cost Effectiveness Analysis of Lung Cancer Screening	R01
Plevritis, Sylvia	NIH	Computational Modeling of Cancer Biology	P20
Rao	NIH	Unified Reporter Gene for Multi-Modality Imaging	R21
Rubin	NIH	Volumetric Analysis of the Aorta and Its Branches	R01
Sommer	NIH	MRI of Renal Anatomy and Function in Chronic Ischemia	R01
Sommer	NIH	Precise MRI-Directed Sonic Ablation of Prostate Cancer	R33
Spielman	NIH	Magnetic Resonance Spectrosopic Neoplasm Imaging	R01
Wu	NIH	Clinical Scientist with Focus on Cardiovascular Molecular Imaging	K08
Glover	NIH/ UC San Diego/ UC Irvine	Functional Imaging Research in Schizophrenia Testbed	M01
Chen	Dept. of Army	Alpha-v Integrin Targeted PET Imaging of Breast Cancer Angiogenesis and Low-Dose Metronomic Anti-Angiogenic Chemotherapy Efficacy	
Gambhir	Dept of Energy	Molecular Imaging of Stem Cell Survival, Apoptosis, and Differentiation in Myocardium	
Pelc	NASA	Non-invasive Investigation of Bone Adaptation in Humans to Cumulative Daily Mechanical Loading	
Glazer	Veterans Affairs	Department of Veteran Affairs Mammography Screening Contract	
Glazer	Veterans Affairs	Solicitation Agreement	
Glazer	Veterans Affairs	Solicitation Agreement for IR and Cardiovascular Imaging	
Glazer	Veterans Affairs	Solicitation Agreement for Musculoskeletal Services	

Non-government Funding

PI	Sponsor	Title
Atlas	Greenwall Foundation	Ethical Challenges in Neuroimaging
Bammer	Endius, Inc.	A Multi-Center Study to Evaluate the Effect of Minimally Invasive Versus Open Posterolateral Lumbar Fusion on the Paraspinal Musculature Using High Resolution Structured and Quantitative MR Imaging
Biswal	OTL Research Incentive	Spatiotemporal Analysis of Hematopoetic Stem Cell Trafficking
Chan	The Whitaker Foundation	Optimized Four-Dimensional Magnet Resonance Flow Imaging for Congenital Heart Disease
Chen/Gambhir	American Heart Association	Multimodality Imaging of Cardiac Therapy
Dake	Cook Incorporated	Zilver Vascular Stent in the Iliac Arteries
Dake	W.L. Gore & Associates	A Clinical Study Evaluating the Use of the Thoracic EXCLUDER Endprostheis in the Treatment of Descending Thoracic Aortic Diseases
DeRoose	American Molecular Imaging Society	Young Scientist Award
Desmond	Stanford OTL	Neuroimaging Investigations of Cognitive Impairment After Concussion Injury
Do	Parallax Medical, Inc.	A Controlled Trial Investigating Vertebroplasty Efficacy
Fahrig	The Whitaker Foundation	Ultrafast Tomosynthesis for the Detection of Lung Cancer
Frisoli	W.L. Gore & Associates	A Feasibility Study Using a Transluminally Placed Self-Expanding Stentgraft (PTAG) for Treatment of Descending Thoracis Aortic Aneurysms
Frisoli	W.L. Gore & Associates	A Clinical Study Comparing Use of the Thoracic EXCLUDER Endoprosthesis to Open Surgical Repair in the Primary Treatment of Descending Thoracic Aneurysms (TAG)
Frisoli	W.L. Gore & Associates	Evaluation of the GORE TAG Thoracic Endoprothesis for Treatment of Descending Thoracic Aneurysms
Frisoli	W.L. Gore & Associates	Treatment IDE for Use of the GORE TAG Thoracic Endoprosthesis in Subjects with Descending Thoracic Aortic Aneurysms Requiring Surgical Repair
Gambhir	Pfizer Central Research	Molecular Imaging of the Effects of New Anti-Tumor Pharmaceuticals
Glazer	General Electric	Magnetic Resonance Imaging (MRI) Systems
Glazer	General Electric	GE PACS System
Glover	SRI International	CVD Risk Factors and Brain Morphology in Twins
Gold	The Whitaker Foundation	MR Imaging of Joints with Intra-Articular Coils
Gold	Interdisciplinary Initiatives Program	Modeling Muscles in Contact
Goris	Eli Lilly and Company	Annexin V Imaging of Fas-Mediated Cell Death
Goris	Glaxco, Inc.	Preceptorship Agreement
Goris	Segami Co	Standardizing Myocardial Perfusion SPECT Images
Herfkens	National Marfan Foundation	Assessment of Mechanical Properties of the Aortic Arch in Patients with Marfan Syndrome by Means of Magnetic Resonance Imaging (MRI)
Ikeda	Susan G. Komen Breast Cancer Foundation	Do K21, Parametric Mapping or Tumor Morphology on Contrast-Enhanced Breast MRI Predict Tumor Response to Chemotherapy
Marks	Concentric Medical, Inc.	Multi-center Controlled Clinical Trial to Evaluate the Concentric Retriever System (MERCI)
Marks	Concentric Medical, Inc.	A Multinational Controlled Registry to Evaluate the Concentric Merci Retriever System
Marks	Endovasix, Inc.	A Non-Randomized, Feasibility Study to Evaluate the Safety and Performance of the EPAR Laser System in the Treatment of Endovascular Blood Clots
Marks	Diversified Diagnostic Products, Inc.	A Prospective Collection of Safety Data Related to Respiratory Slowing and Apnea for Xenon-CT Imaging for the Purpose of Measuring Cerebral Blood Flow (CBF) in Patients with a Spectrum of Neurological Conditions
Mazin	American Heart Association	Fast Volumetric Cardiovascular CT Scanner (Fellowship)
Moseley	Nihon Medi-Physics	Comparison of Fast Imaging Techniques for MRI of H20-17

Napel	R2 Technology, Inc.	Computer Aided Tracking and Analysis of Pulmonary Nodules Over Time
Napel	Siemens Corporate Resear	Interventional Room of the Future
Pelc	The Whitaker Foundation	Special Opportunity Award: Department of Bioengineering-Graduate and Postdoctoral Education
Pelc	GE Med Systems	CT XRAY
Pelc	General Electric	High Resolution Volumetric Computed Tomography (VCT) for Thoracic Imaging using Digital Flat-Panel Technology
Pineda/Fahrig	American Lung Association	Task-Based Reconstruction of Ultrafast Tomosynthesis for Guidance of Lung-Nodule Biopsy
Rao	The Burroughs Wellcome Foundation	Career Award at the Scientific Interface
Razavi	Boston Scientific Corporation	Uterine Artery Embolization Study
Razavi	The Medicine Company	APPROVE: A Study to assess the safety of replacing heparin with Angiomax in patients undergoing percutaneous peripheral (non-cardiac) interventional procedures
Razavi	W.L. Gore & Associates	M-CTAA A Clinical Study Comparing Use of the Bifurcated EXCLUDER Endovascular Prosthesis to Open Surgical Repair in the Primary Treatment of Infrarenal Abdominal Arotic Aneurysms (AAA) (Protocal AAA-98-03)
Rubin	Stanford VPUE	Faculty grant for undergraduate research (to fund Emily Lu for summer quarter)
Rubin	Medtronic AneuRx	-M-CTAA Medtronic-Aneurex Thoracic Aorta Stent-graft Trial
Spielman	SRI International	In Vivo Diffusion and Spectroscopic Brain Imaging in Alcoholism
Sze	W.L. Gore & Associates	A Clinical Study comparing the Use of the Modified Bifurcated EXCLUDER Endoprosthesis to Open Surgical Repair in the Primary Treatment of Infrarenal Abdominal Aortic-Aneurysms (AAA)
Wu	American Soc of Nuclear Cardiology	Clinical Scientist Award
Yaghoubi	RSNA	Research and Education Award

Submitted Proposals FY 2004

Proposals to Government

PI	Source	Title	Type
Bammer	NIH	Cortical MR9S) in MS Patients with Cognitive Impairment	R21
Blankenberg	NIH	Annexin V Imaging and Therapeutic Outcome in Lung Cancer	R01
Butts	NIH	Handheld MR-Guided Focused Ultrasound Cancer Therapies	BRP
Chan	NIH	MR Pressure-Flow Assessment of Pulmonary Stenosis Repair	R01
Chen	NIH	MicroPET and NIR Fluorescence Imaging of Tumor Angiogenesis	R21
Chen	DOA	Alpha-v Integrin Targeted PET Imaging of Breast Cancer…	
Desmond	NIH	fMRI Analysis of Aging and Awareness in Conditioning	R01
Desmond	NIH	fMRI and TMS Analysis of Cerebellar Cognitive Function	RO1
Fahrig	NIH	Hybrid Biplane Xray/MR System	R01
Gambhir	NIH	In Vivo Cellular Imaging Center at Stanford	P50
Glover	NIH	Center for Advanced MR Technology at Stanford	P41
Glover	NIH	Functional Imaging Research in Schizophrenia Testbed	
Gold	NIH/UCSF	Data Coordinating Center for Osteoarthritis Initiative	
Goris	DOE	Optimizing Radiotherapy of Tumors with Novel Gene Based Therapies for Validation of Radio-Gene Therapy	
Herfkens	NIH	MR Imaging of Aortic Mechanics in Marfan Syndrome	R01
Levin	NIH	Feasibility of In-Vivo Bioluminescence Tomography	R21
Levin	NIH	A new Photon Sensor to Improve Molecular Cancer Imaging	R21
Levin	NIH	New Scintillation Light Detection Concepts for PET	R21
Pelc	NIH	Dose Efficient Volumetric CT Using Inverse Geometries	R01
Plevritis	NIH	Cost Effectiveness Analysis of Lung Cancer Screening	R01
Plevritis	NIH	Breast Cancer Trend Analysis Using Stochastic SimulationU01	
Rao	NIH	A Unified Reporter Gene for Multi-Modality Imaging	R01
Spielman	NIH	Magnetic Resonance Spectroscopic Neoplasm Imaging	R01

Proposals for Non-government Funding

PI	Sponsor	Title
Bammer	Endius, Inc.	A Multi-Center Study to Evaluate the Effect of Minimally Invasive Versus Open Posterolateral Lumbar Fusion on the Paraspinal Musculature Using High Resolution Structured and Quantitative MR Imaging
Biswal	Roche	MRI of Treated and Control Non-Stanford Murine Models of Rhematoid Arthritis
Biswal	Damon Runyon Cancer Research Center	Development of Mesenchymal Stem Cell-Based Gene Therapy for Primary or Metastatic Malignant Osseous Tumors with the Aid of Molecular Imaging Technologies
Blankenberg	SibTech, Inc	VEGF-driven PET Imaging of Tumor Vasculature
Chan	Whitaker Foundation	Optimized Four-Dimensional Magnet Resonance Flaw Imaging for Congenital Heart Disease
Chen	Susan G. Komen Breast Cancer Foundation	Tumor Specific Chemotherapy Using Integrin Targeted Drug Delivery
Frisoli	W.L. Gore	Treatment IDE for the Gore TAG Thoracic Endoprothesis
Gambhir	Doris Duke Distinguished Clinical Scientist Award -2004	Molecular Imaging of Cancer with a Voltage Sensor
Kee	W.L. Gore	TAG 99-01 Amendment
Kee	Vivant Medical Inc.	Feasibility Study on Microwave Ablation of Metastatic Bone Tumors for Palliation of Pain
Levin	Susan G. Komen Breast Cancer Foundation	Workshop on the Nuclear Radiology of Breast Cancer
Marks	Concentric Medical, Inc	Protocol INT-TR-001 A multinational Controlled Registry to Evaluate the Concentric Merci Retriever System
Pineda/Fahrig	American Lung Association of New York (Fellowship)	Task-Based Reconstruction of Ultrafast Tomosynthesis for Guidance of Lung Nodule Biopsy
Rao	Burroughs Wellcome Fund	Career Award at the Scientific Interface
Razavi	Abbott	Catheter-Directed Intrathrombus Thrombolysis with Urokinase and Anticoagulation versus Anticoagulation alone for Acute Iliofemoral Venous Thrombosis: A Multicenter, Randomized Trial
Sze	Cook, Inc.	Zenith TX2 Thoracic TAA Endovascular Graft

NCI Training Program in Cancer Imaging

Donna Cronister

Our twefth year of training began on February 1, 2004. We have graduated 18 trainees from our program, Advanced Techniques in Cancer Imaging, thus far. A specific aim of this training program is to position our trainees for a career in academic radiology. Ten of the postdoctoral fellows who have completed the program are actively performing research as faculty or academic staff in major universities. Our trainees continue to be extremely productive and we often collaborate with them in their new positions both locally and throughout the country. Dr. Jon Levin completed his two year fellowship in 2004. Dr. Levin has moved to St. Luke's Medical Center where he is a practicing radiologist and clinical instructor.

We have two fellows participating in the project, Dr. Laura Pisani is working with Drs. Gary Glover and R. Kim Butts and will finish her appointment in December 2004. Dr. Daniel Margolis is working on a number of projects and will finish up his training on June 30, 2005. We have two new Ph.D. fellows who will begin in Autumn 2004. We have 4 open positions available during this year's funding period. Advertisements have been placed in major radiological journals to attract outstanding fellows for our program. A new clinical fellow has been selected and will begin his appointment in July 1, 2005.

Ms. Lanzie Rivera has assumed the program administration role for this program. She is eager to learn the ropes and will be a tremendous asset to the project.

TRAINEES SUPPORTED ON NCI TRAINING GRANT

GRADUATED TRAINEES

John Strang, M.D.
09/01/93 - 08/31/95
from Harbor - UCLA, Los Angeles, CA
Robert Herfkens, M.D. – preceptor
Current Position: Assistant Professor
University of Rochester, Rochester, NY

Ian Ch'en, M.D.
07/1/94 - 06/30/96
from University of Colorado, Denver, CO
King Li, M.D.-preceptor
Current position: Staff Radiologist
Southwest Washington Medical Center
Vancouver, WA

Susan Lemieux, Ph.D.
10/16/93 - 08/31/96
from Siemens Gammasonics, Knoxville, KY
Gary H. Glover, Ph.D. – preceptor
Current position: Assistant Professor
Diagnostic Imaging, University of
Western Virginia

Bruce Daniel, M.D.
07/01/95 - 06/30/97
from University of Michigan
Robert Herfkens, M.D. – preceptor
Current position: Assistant Professor
Stanford University

Garry Gold, M.D.
07/01/95 - 06/30/97
from Stanford University
Albert Macovski, Ph.D. – preceptor
Current position: Assistant Professor:
Stanford University

Yi-Fen Yen, Ph.D.
09/01/95 - 08/31/97
from Los Alamos Nat'l Lab, Los Alamos, NM
Gary H. Glover, PhD – preceptor
Current position: Assistant Professor
University of Western Ontario, London , Ontario Canada

Esther Yuh, Ph.D.
05/01/97 – 09/30/98
from Heartport, Inc., San Mateo, CA
King Li, M.D. – preceptor
Sandy Napel, Ph.D. – preceptor
Current position: Medical Student
Stanford University

Roger Shifrin, M.D.
07/01/96 - 06/30/98
from Bowman Gray Univ., Winston-Salem, NC
Norbert J. Pelc, Sc.D. – preceptor
Robert Herfkens, M.D. – preceptor
Current position: Private Practice
Radiology Associates, Daytona Beach, FL

Steven G. Heiss, M.D.
07/01/97 – 06/30/99
from University of California, Los Angeles, CA
King Li, M.D. – preceptor
Current position: Radiology Imaging Associates
Denver, Colorado

Martin Blum, M.D.
07/01/98 - 06/30/2000
from The Cleveland Clinic
Brooke Jeffrey, M.D. – preceptor
Current Postion: PET/Nuclear Med Research
Palo Alto VA Health Care System

Curtis Coulam, M.D.
07/01/99 - 06/30/01
from: Duke Univesrity
Graham Sommer, M.D. – preceptor
Research topic: Prostate cancer imaging
Current Position: Gems State Radiology Group
Boise, Idaho

Samira Guccione, Ph.D.
01/31/00 - 01/30/02
from: Johns Hopkins
Mark Bednarski, M.D., Ph.D. – preceptor
Research topic: Molecular Imaging
Current Position: Research Associate
Stanford University

Yishan Yang, Ph.D.
12/01/00 - 04/30/02
From: Stanford University
Mark Bednarski, M.D., Ph.D. – preceptor
Research topic: Molecular Imaging
Current Position: Research Associate
Stanford University

Lawrence Chow, M.D.
07/01/00 - 06/30/02
from: Stanford University
Graham Sommer, M.D. – preceptor
Research topics: Prostate cancer imaging
Current Position: Assistant Professor
Stanford University

Karl Vigen, Ph.D.
01/29/01 - 01/28/03
from: Univesity of Wisconsin, Madison
R. Kim Butts, Ph.D. – preceptor
Research topic: Thermal treatment of cancer, liver
Current Position: Research Associate
Stanford University

Susan Hobbs, M.D., Ph.D.
02/12/01 - 02/11/03
from: University of Minnesota
Mark Bednarski, M.D., Ph.D. – preceptor
Research topic: Molecular Imaging
Current Position: Resident
University of Minnesota

Charles Liu, M.D.
07/01/01 - 06/30/03
from: University of San Diego
Robert Herfkens, M.D., Graham Sommer, M.D. – preceptors
Research Topic: Cardiac Function Analysis: Breath-Hold
and Free Breathing Techniques
Current Position: Radiologist
La Jolla Radiology

Jon Levin, M.D.
07/01/02 - 06/30/04
from University of California, Los Angeles
Robert Herfkens, M.D., Graham Sommer, M.D. preceptors
Research Topic: Cardiac and Prostate Imaging using
multiple imaging modalities
Current Position: Radiologist and Clinical Instructor
St. Luke's Medical Center, Minneapolis, MN

Postgraduate Education

Susie Spielman

The Department's Continuing Medical Education program has just concluded another year of extraordinary growth with over 2300 registrants, a 10% increase vs. 2003. With ten courses and 154 speakers, the program excels as the leading Radiology CME program in the country.

Many factors helped to differentiate our program and lead to our sustained growth. We carefully develop premiere courses on new technologies and identify topics which directly meet the accreditation needs of our registrants. We have strict criteria for site selection and timing of our meetings and have now established a strong history for many of our courses.

When our program first began we selected "resort" destinations with content covering broad topics. Today, we have added meetings which are singly focused and the first to educate the medical imaging community about impending transitions to new and emerging technologies. Breast MRI is a perfect example of a new technology that resulted in a high demand for education. Our "How to set-up Breast MRI in Your Practice" course has had glowing reviews and over 400 attendees each of the past two years.

It is also our priority to offer the highest quality experience for both the faculty and registrants. We have been experimenting with the best uses of technology for increasing the interactivity of our meetings and providing important tools to help enhance the educational experience for our registrants. For example, we offered wireless access, hands on workstation training and interactive case CDs in 2004.

Workstation Face-off at the 6th Annual International Symposium on MDCT in San Francisco, June 2005.

Our International Symposium on Multidetector Row CT (MDCT) is now in its sixth year and, with over 700 attendees and innovative content, this year's program surpassed our earlier efforts. We have received feedback from registrants and industry alike that its reputation as the premier meeting on MDCT has again been validated.° The program included the second annual Workstation Face-off in which five workstation vendors demonstrated the capabilities of their equipment. These sessions provided a unique chance for our registrants to view and compare how each major workstation can be used for visualization of the same five 3D data sets. It was a rare opportunity for the vendors to showcase their products and an extraordinary experience for our attendees to evaluate the quality of the images and the usability of each product.

The inclusion of world renowned speakers at our courses has also been a key element of differentiation. We are able to bring together multiple leading experts in a single forum on a focused topic. It is a rare opportunity for our registrants, industry supporters and even our own faculty to learn, network and discuss the key issues in our field.

Additionally, we have meetings that are co-hosted by strategic partners in Japan and Europe which build international relationships for our faculty and grow our international reach and reputation. We are currently planning for a program in Barcelona Spain for 2005 and China in 2006.

We look forward to continued growth and innovation in years ahead.

MR Systems, Education and Systems Support

Anne Marie Sawyer-Glover, B.S., R.T.(R)(MR)
Romi Kaur Samra, R.T.(R)

SYSTEMS UPDATES 2003 - 2004

The 1.5 Tesla G.E. Medical Systems Echospeed LX CV/i MR system was upgraded to the 11.0 M4 systems revision software and the Excite II hardware that provides the capability of 8-channel/receiver imaging with phased array coils. These improvements will allow faster imaging, shorter echo times, and the capacity to remain on the leading edge of functional brain imaging and cardiovascular applications, and provides capabilities such as increased sensitivities for Diffusion Weighted Echo Planar Imaging used in the detection and treatment of stroke. The maximum gradient strength now being utilized is 50 mT/m. The software upgrade provided additional imaging sequences and enhancements to existing acquisition capabilities. Advantages include faster scanning, greater coverage, and higher temporal and spatial resolution. New imaging software allows the visualization of white matter tracks in the central nervous system and provides information on the molecular diffusion of biological tissues.

Currently plans are underway to upgrade the 3.0 Tesla G.E. Medical Systems Echospeed LX NV/i MR system to the Excite II platform with 8-channel/receiver capability. Multi-Nuclear Spectroscopy is available and phosphorus imaging is under current development. A multitude of functional brain imaging studies (fMRI) investigating diseases, conditions and congenital disorders are being conducted in adults and children as well as studies focused on advancing neuroscientific knowledge. Body and musculoskeletal imaging applications are in development at the 3.0T including knee, ankle/foot, wrist, elbow, shoulder, breast, abdomen, pelvis, prostate, and cervical spine.

Alison Adcock, Ph.D., a neuroscientist from the Department of Psychology, prepares a subject enrolled in a research protocol studying brain functions through the use of Functional MR imaging (fMRI) at the 3.0T MR system.

MR research studies in the detection and characterization of breast disease and prostate cancer continue at both 1.5T and 3.0T as well as stroke, cardiovascular disease, kidney disease, cystic fibrosis, muscle damage, cartilage of the knee, cancer of the head and neck, aging, Alzheimer's disease, schizophrenia, depression, obesity, post traumatic stress disorder, bipolar disorder, attention deficit hyperactive disorder, dyslexia, memory and language disorders, vision, mood disorders, psychotic disorders, concussion, autism, chronic and intractable pain, alcoholism, Fragile X syndrome, obsessive compulsive disease, mental retardation, Williams syndrome, uterine leiomyomata, Lumbar spine fusion, AIDS and HIV.

Planning is underway for research studies to be conducted at the 7.0 Tesla magnet being installed this fall in the new extension of the Lucas Center currently under construction.

Thick slabs of steel line the new magnet room under construction for the 7.0 Tesla magnet being installed in the fall of 2004.

RADIO FREQUENCY COIL UPDATES

2003 - 2004

The investigation and testing of new designs and concepts in RF imaging coils for use in MR imaging and spectroscopy is on-going at the Lucas Center whole body scanners, both 1.5 Tesla and 3.0 Tesla. Of primary focus currently is improved imaging in the brain, knee, foot/ankle, wrist, breast, abdomen, and prostate at 3.0T. We are working with coil manufacturers and independent researchers building coils at the Lucas Center and at other academic research facilities. As part of the Excite II upgrade to the 1.5T MR system, new multiple channel RF coils higher signal-to-noise ratio that allows higher resolution imaging were added including an eight channel head coil and an eight channel neurovascular coil.

Eight channel phased array coils (left) for high resolution imaging of the brain at 1.5T (T. Schubert, MRI Devices Corporation, Waukesha, WI, USA). Axial (below left) and coronal oblique (below right) images of the brain acquired using the eight-channel phased array head coil.
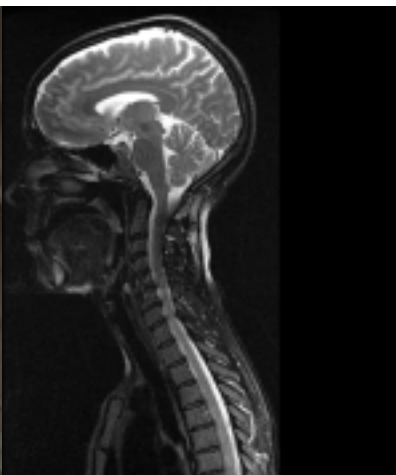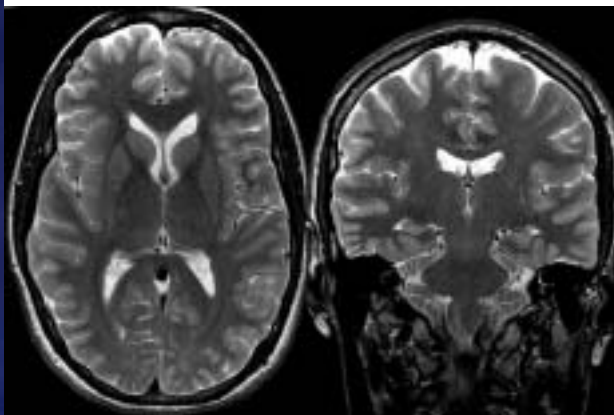
Eight channel phased array coils (far left) for high resolution imaging and extended coverage of the brain and major vessels arising from the aortic arch at 1.5T (T. Schubert, MRI Devices Corporation, Waukesha, WI, USA). Sagittal view (near left) of the brain and cervical spinal cord acquired using the eight-channel neurovascular radiofrequency coil.

A new birdcage design head coil has recently been added to the 1.5T (R. Hashoian, Clinical MR Solutions, Brookfield, WI, USA) to provide increased signal-to-noise ratio and improved image quality for functional imaging of the brain (fMRI), quantification of different tissues of the brain from 3D volume imaging, and spectroscopy.
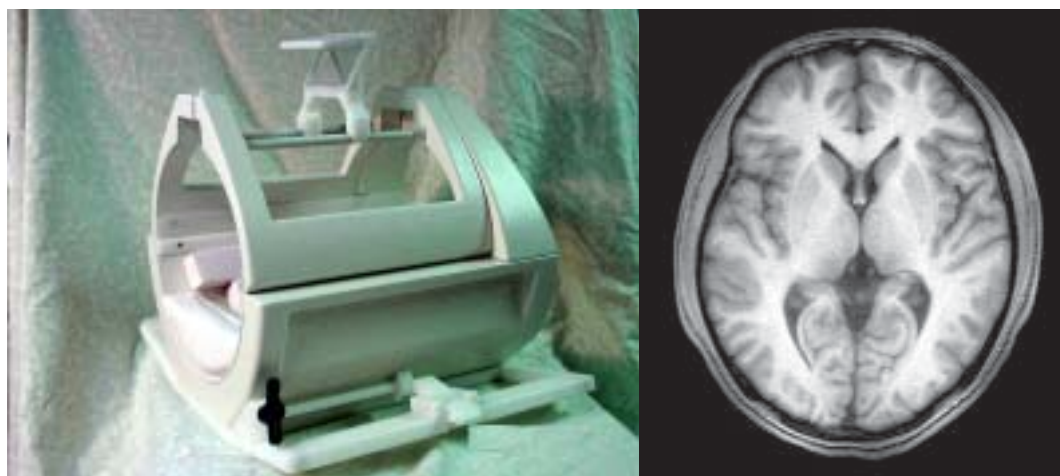
1.5T Brain coil (left) for functional imaging, 3D volume acquisitions for quantification of brain tissues, and spectroscopy (R. Hashoian, Clinical MR Solutions, Brookfield, WI, USA). Right: Axial image of the brain acquired with the Clinical MR Solutions radiofrequency head coil.

A recent addition to the 3.0T MR system is a receive-only posterior head coil (Nova Medical, Inc., Wilmington, MA, USA) providing more homogeneous signal in imaging of the occipital lobe of the brain for functional brain imaging of vision.
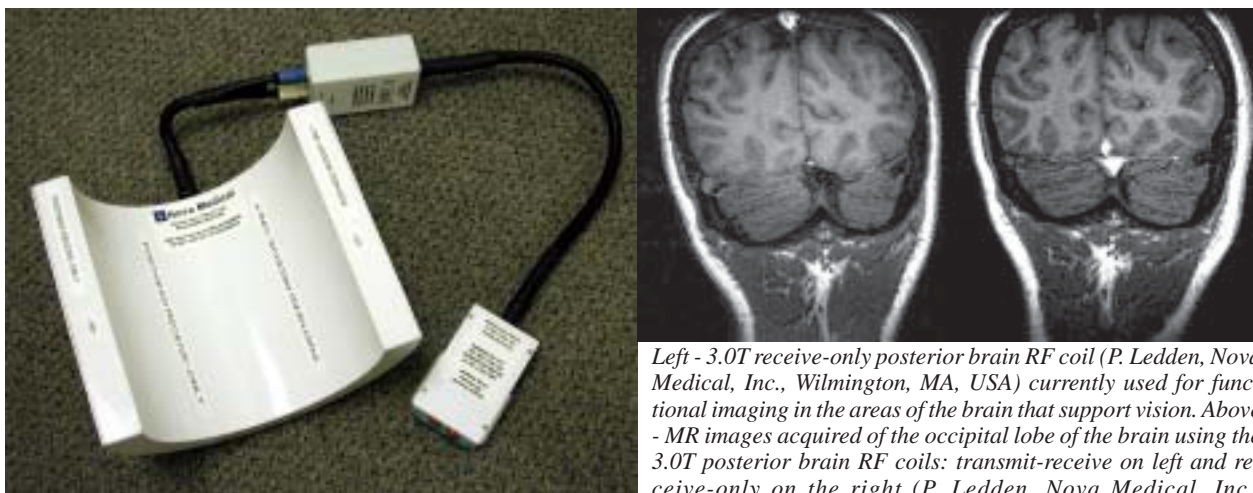
Left - 3.0T receive-only posterior brain RF coil (P. Ledden, Nova Medical, Inc., Wilmington, MA, USA) currently used for functional imaging in the areas of the brain that support vision. Above - MR images acquired of the occipital lobe of the brain using the 3.0T posterior brain RF coils: transmit-receive on left and receive-only on the right (P. Ledden, Nova Medical, Inc., Wilmington, MA, USA).

Research by Sean Mackey, M.D. and his laboratory continues at the 3.0T MR system in functional imaging of the cervical spinal cord using a receive-only cervical spine coil (Nova Medical, Inc., Wilmington, MA, USA) to provide information about human subjects in chronic pain.
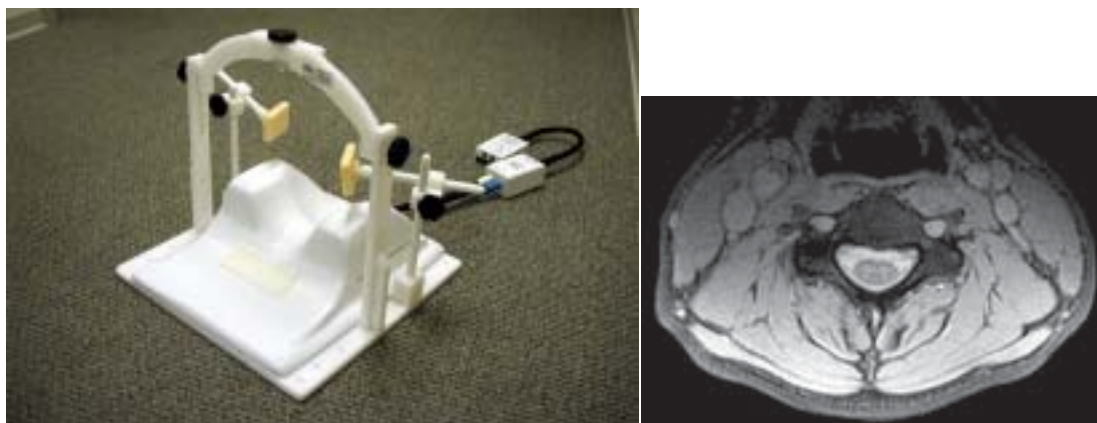
Left - 3.0T Cervical spine RF coil (P. Ledden, Nova Medical, Inc.) currently used for functional imaging in the spinal cord to evaluate chronic and intractable pain in human subjects (S. Mackey, M.D., Anesthesiology, Stanford University). Right - Axial oblique MR image of the cervical spine demonstrating the spinal cord acquired at 3.0T acquired using the RF coil .

MR imaging of the prostate is being conducted at the 3.0T MR system using a rigid endorectal coil provided by Charles Dumoulin and Ronald Watkins at G.E. Global Research Center.

Left - 3.0T RF coil for imaging of the prostate (C. Dumoulin and R. Watkins, G.E. Global Research Center, Niskayuna, NY, USA). Right - Examples of high resolution axial (left) and coronal (right) prostate MR images acquired at the 3.0T using a fast spin echo sequence.

Initial work is being conducted to develop scan protocols and imaging accessories to image the abdomen, pelvis and chest at the 3.0T MR system using a four channel phased array RF coil (G.E. Healthcare, Waukesha, WI, USA)
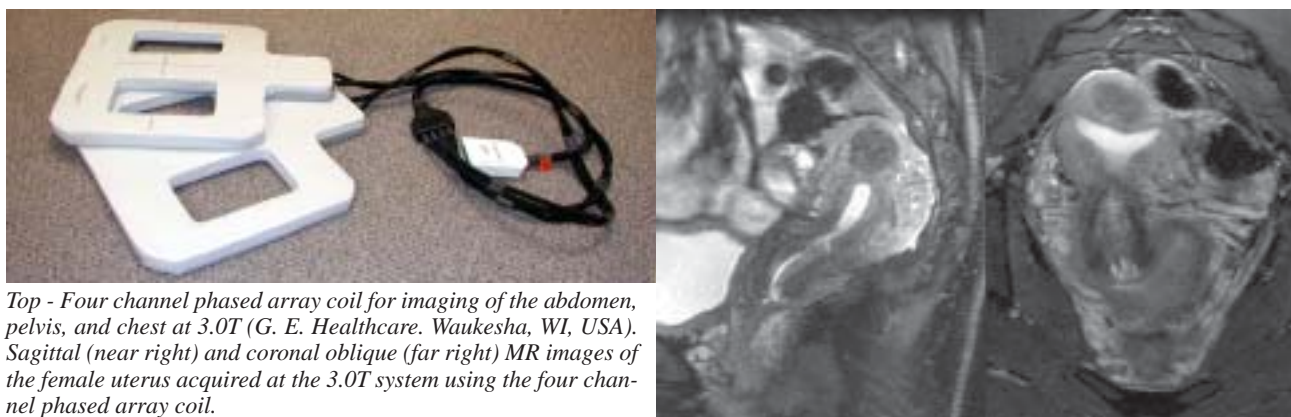
Top - Four channel phased array coil for imaging of the abdomen, pelvis, and chest at 3.0T (G. E. Healthcare. Waukesha, WI, USA). Sagittal (near right) and coronal oblique (far right) MR images of the female uterus acquired at the 3.0T system using the four channel phased array coil.

Protocol development continues on musculoskeletal imaging at the 3.0T MR system including the knee, ankle, shoulder and wrist.
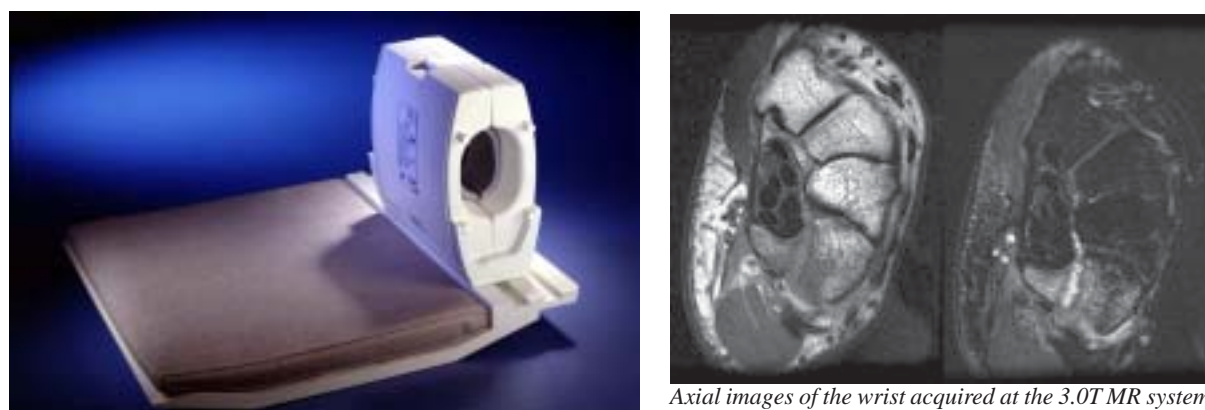
Four channel phased array RF coil for imaging of the wrist at 3.0T (T. Schubert, MRI Devices Corporation., Waukesha, WI, USA).

Axial images of the wrist acquired at the 3.0T MR system using the RF coil.

EQUIPMENT UPDATES 2003 - 2004

Several new imaging devices and accessories have been added over the last year including an eye tracker for use at 3.0T for functional brain studies (B. Krasnow, Mag Concepts). A tiny video camera (P. Goldin, Department of Psychology) has been implemented to monitor human subjects' reactions to visual stimulus for functional brain imaging of social phobias.

Currently, there are two monitoring systems that provide heart rate, cardiac waveform, pulse oximetry (saturated oxygen), end-tidal carbon dioxide, and blood pressure (non-invasive and invasive). These monitoring systems can also synchronize the MR image acquisition to various types of motion generated by the subject such as breathing, the beating heart and blood
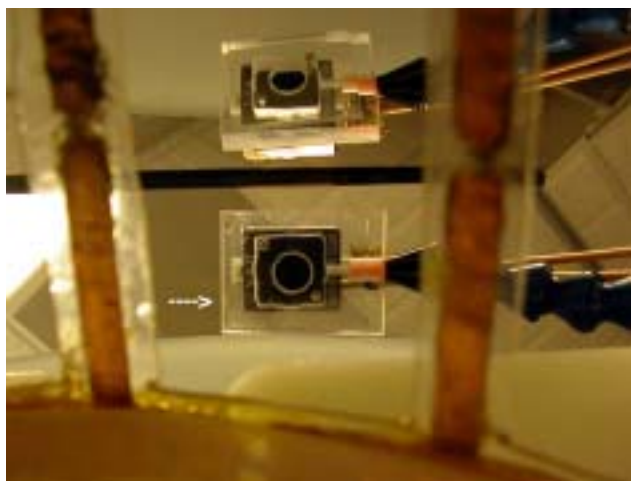
Above - A tiny video camera (white arrow) is mounted on a RF imaging head coil. The picture is taken from within the coil looking up towards the camera and its reflection in a viewing mirror also mounted on the coil. Below - A still image taken from a video taping of a subject (P. Goldin, Department of Psychology) during the MR scan in the RF imaging head coil.

Eye tracker device in development for use at 3.0T MR System (B. Krasnow, Mag Concepts).

flow. These improve image quality and improve the accuracy of collected MR data. In addition, these systems are used to monitor the status of animal models while being imaged in the magnet under the affects of anesthesia and often on a respirator.

SAFETY TRAINING AND SYSTEM INSTRUCTION 2003 - 2004

Safety training and system instruction have been provided to ninety-two new researchers conducting experimental MR studies at the Lucas Center. Magnet safety training is provided twice a month and is a requirement for all researchers assisting or conducting studies on any of the magnet systems at the Lucas Center. Safety training is a yearly requirement for all researchers. A magnet safety refresher course is currently being provided to 127 researchers. This ensures that all users and assistants are qualified to operate the system and satisfies Lucas Center and University requirements for safety. System and safety support is provided to the researchers 7 days a week, 24 hours a day to ensure that research endeavors are successful, generate valuable data, and, above all, are safe for the researchers, the human subjects and the MR system and its components. Magnet safety is an on-going concern as the MR environment can be a potentially lethal setting without continuing education and persevering support. The research environment generates many new yet prototype designs in RF imaging coils, imaging accessories, monitoring and response devices such as button boxes, eye trackers, and electroencephalogram (EEG) recorders, and sensory devices. Evaluation of these new devices is on-going to ensure that neither the image data, the safety of the human subject, nor the integrity of the MR system is compromised by the presence of these devices in the magnet room, in the bore of the magnet, or in the presence of an RF coil.

MR SYSTEMS SUPPORT 2003 - 2004

Daily support is provided to all researchers including faculty, post-doctoral fellows, graduate students, and visiting scholars in the Lucas Center and Department of Radiology; researchers from other University departments such as Psychology, Psychiatry, Neurology, Neurosurgery, and Nephrology; and service center users from outside of the University.

Scan support was provided for multiple research studies including:μ

- MR Imaging of Breast Disease and Cancer; R. Herfkens, B. Daniel, D. Ikeda, R. Birdwell, G. Glover, and L. Stables (Radiology)
- Identification of Ductal Atypia with MR Galactography of the Breast; A. Hartmann, (Oncology), B. Daniel (Radiology)
- MRI/MRS of Prostate at 3.0T; B. Daniel, G. Sommer (Radiology)
- MRI of Renal Anatomy and Function in Chronic Ischemia; G. Sommer and N. Pelc (Radiology); B. Myers (Nephrology)
- A Model for Hypercortisolism for Major Depression; Functional MRI of the Brain; HPA Axis/Dopamine Interactions in Psychotic Depression; D. Lyons and A. Schatzberg (Psychiatry)
- Computer Modeling and MRI of Hemodynamic Conditions in the Aorta; Blood Flow in a Porcine
- Thoracic Aortic Bypass Graft Measured In Vivo using MR Imaging; Hemodynamic Determinants of AAA Disease

43

Following Spinal Cord Injury; C. Taylor, C. Zarins (Vascular Surgery); N. Pelc, R. Herfkens (Radiology)
- Cortical Processing of Visual Motion in Primates; W. Newsome (Neurobiology)
- Fat Redistribution and Metabolic Change in HIV; A. Zolopa (Infectious Diseases)
- Diabetes Therapy to Improve Muscle Mass and Clinical Status in Cystic Fibrosis Patients with Abnormal Glucose Tolerance; R. Moss (Pediatrics)
- Image Based Computational Blood Flow Modeling of the Pulmonary Tree as Applied to Problems in Congenital Heart Disease; J. Feinstein (Pediatric Cardiology), C. Taylor (Vascular Surgery)
- Cortical Processing of Arm Movements (Primates); K. Shenoy (Neurobiology)
- MRI Study to Measure Operative Muscle Damage; T. Alamin (Orthopedic Surgery), R. Bammer, K. Stevens (Radiology)
- Trial on Efficacy and Safety of Long Term Treatment with ICL670 in Comparison with Deferoxamine in B-thalassmeia Patients with Transfusional Hemosiderosis; M. Jeng (Pediatric Oncology)
- Indirect MR Lymphangiography of Head/Neck using Gadolinium contrast agent; Q-T. Le (Radiation Oncology)
- Phase III Double Blind Study to Evaluate Efficacy and Safety of Two Doses of J867 vs. Placebo in Subjects with Uterine Leiomyomata; L. Swiersz (Obstetrics and Gynecology)

Experimental Model Management

Diane Howard, RVT, LATg

Wendy Baumgardner, RVT, LATg

In our continuing efforts to provide support to the Radiology investigative staff, we are entrusted with the responsibility of overseeing all animal protocols within our department and all other departments carrying on work at the Lucas Center. Two experienced California Licensed Veterinary Nurses (RVT) each with over 20 years in the field, attend all animal studies making the health and welfare of the animals always our most important priority. Diligent care is taken during all procedures involving animal subjects; they are treated with the utmost respect, compassion, and professional care. Animal studies at the Lucas Center enhance both treatment and diagnostic abilities, and are never taken lightly.

A licensed veterinary nurse attends to anesthesia and imaging equipment in a non-aseptic study.

All personnel working with animals under IACUC (Institutional Animal Care and Use Committee) approved protocols have attended "required" seminars from the University's Department of Comparative Medicine. Further specifically tailored "one on one" training for more advanced techniques are taught by either Diane or Wendy here at the Lucas Center.

Vital signs are recorded by a licensed RVT using a multifunctional monitoring system, in conjunction with arterial blood gases and activated clotting times to maintain homeostasis.

We realize the necessity of living subjects in advancing our knowledge, and ensure proper respect for life is part of all protocols. Work at the Lucas Center produces advancement of invasive and non-invasive procedures such as magnetic resonance imaging, fluoroscopy, focused ultrasound, computed topography, as well as magnetic resonance therapy. In addition, studies currently being done involve the study of alcoholism, stroke, liver and prostate cancers, neuroimaging of the brain, and stent/graft implantation. The techniques currently being explored at the Lucas Center all contribute to more efficient and effective medical treatment for illness and disease.

CURRENT IACUC APPROVED PROTOCOLS FOR THE LUCAS CENTER

- Magnetic Resonance Imaging of Experimental Rabbit Atherosclerosis
- Minimally Invasive Therapies with Fluoroscopy and C-arm CT Guidance
- Cortical Processing of Visual Motion
- Magnetic Resonance Imaging Sequence Development on the 4.7T Magnet
- Prefrontal Brain Growth and Psychosocial Development
- Cortical Processing of Arm Movements
- Image Based Computational Blood Flow Modeling of the Pulmonary Tree as Applied to Problems in Congenital Heart Disease
- Integrative Neuroscience Initiative on Alcoholism: Imaging Core
- Cerebral Perfusion During Heart Surgery
- Eudragit for Embolization of a AVM Model
- Prostate Ablation Using Acoustic Applicators and MRI Guidance
- Control of Gene Expression Using Focused Ultrasound
- Molecular Imaging of Tumor and Vascular Receptors
- Genetic Analysis of Tumorigenesis Using Mouse Knockout Transgenic Models
- Characterization of Biomedical and Biochemical Tissue Properties of Pig Aortas
- Delivery of Protein Kinase C Isozyme Regulators as Therapeutic Agents in Stroke using a Rat Model
- Catheter-based Cardiovascular Magnetic Resonance Imaging
- Novel Therapies for the Treatment of Cardiomyopathy
- Stent Coating to Decrease in Stent Restenosis after Deployment in the Rabbit Iliac Artery
- Magnetic Resonance Guided Prostate Cryosurgery
- Gene Expression Changes and Protein Profile Pattern in Tumor Ablation Using Focused Ultrasound
- Minimally Invasive MR-guided Thermal Therapies
- Squirrel Monkey Neuroimaging
- Imaging Apoptosis During Cancer Therapy Using Annexin V
- To Determine the Efficacy of Intramyocardial Delivery for Treatment of Cardiomyopathy
- Model of Hypercortisolism for Depression-phase 2
- Evaluation of Endovascular Devices Using Fluoroscopy MRI or Ultrasound
- Techniques of Stent/Graft Implantation and Liver Ablation with Radiofrequency
- Relationship of CT Dose to Scan Resolution for Volumetric CT Imaging Utilizing a 16 Detector CT Scanner
- The Effects of Antioxidant Supplementation on the Aging Mammalian Brain in Vivo Magnetic Resonance Spectroscopy of Energy Metabolism
- CT Angiography Using PH-50 in Atherosclerotic Watanabe Rabbits
- Study of Anti-tumor Efficacy of Novel Radio Immunotherapy agents
- MR-Guided Prostate Cryosurgery
- Somatic Gene Therapy for Vascular Restenosis
- Controlled Release Systems for Low Dose Adenoviral-mediated Gene delivery to the Arterial Wall in Vivo
- Adenoviral Mediated Gene Delivery to Engineer a Thrombo-resistant Vein Graft
- Blood Flow in a Porcine Thoracic Aortic Bypass Graft Measured in Vivo using MR Imaging
- Regeneration of Infarcted Myocardium with Stem Cells
- Cardiac Molecular Imaging
- Molecular Mechanisms of Restenosis after Angioplasty
- Proteomic Analysis of Blood Components in Autoimmune Disease
- Vascular Biology and Neural Stem Cells
- Elucidating the Functional Differences between b1 and b2 Adrenergic Receptors in the Murine Heart
- Hematopoietic Cell Transplantation for Altering Immune Responses in Mice

3-D Visualization and Quantitation: Clinical Applications

Laura J. Logan, BA, R.T. (R) (CT) and Geoffrey D. Rubin, M.D.

MISSION AND GOALS

The mission of the Stanford 3-D medical imaging laboratory is to develop and apply innovative techniques for efficient analysis and display of medical imaging data through interdisciplinary collaboration. Our clinical goal is to deliver these advances as rapidly as possible following validation as services to the Stanford and worldwide healthcare communities. Our education goal is to disseminate knowledge and duplicate our 3-D services at other institutions by providing training for physicians and technologists locally and worldwide in the latest developments in 3-D imaging.

PROGRESS

Over the past year, the 3-D laboratory has expanded operations and settled into two locations: the first floor of the Lucas Center as well as the third floor of the James H. Clark Center, a new building dedicated to interdisciplinary science. Both labs include space for two to four 3-D technologists, a software engineer, and an administrative assistant, as well 6-10 students, post-docs and visiting MDs and scholars. With our expansion, opportunities for increased interactions between radiologists, technologists, clinicians, and researchers have grown. Projects are not limited to radiology personnel—other biomedical science departments who seek to extend volumetric analyses into their practices and research programs collaborate with our technologists and researchers. For example, this past year neurosurgeons devised a method for teaching surgical approaches to the lumbar spine using 3-D imaging for displaying anatomical variants (*Fig 1*).

Figure 1. Volume rendered image of lumbar spine.

Infrastructure

In both labs, a central area table accommodates eight advanced workstations for processing clinical cases, and for research and development. A 50-inch wall mounted plasma display television monitor, with 1280 x 768 XGA resolution, aids in teaching and display of our work. Four General Electric Advantage Windows workstations are used to process 80% of the clinical cases. The remainder of the clinical exams are processed on two Windows XP workstations running Vitrea2 software (Vital Images, Inc.), a W2K Aquarius 3-D workstation (TeraRecon, Inc.), and another W2K workstation running software for grading coronary calcification studies (AccuImage, Inc.). Real-time volume rendering is available to physicians within the school of medicine via the network with our two AquariusNet servers (TeraRecon, Inc.). All workstations are linked to and supported by a 10/100 Mb/s switched network. This year we upgraded two of our GE Advantage Windows workstations to the new 4.2 software, designed for speed and efficiency on the HP x4000 Linux based platform. We also upgraded our Vital Images Vitrea2 workstations to V3.4.5, running efficiently on Dell Precision 530 with twin Xeon processors. These upgrades contain software to speed up the 3-D process by providing automation of some operator-dependent tasks, such as tissue segmentation and tracking and quantifying blood vessels (*Fig 2*). They also contain specialized 3-D software packages for performing virtual colonoscopy, CT brain perfusion, and automated lung nodule detection.

Figure 2. Automated curved planar reformation of right posterior tibial artery.

Clinical

The clinical arm of the laboratory is staffed by our experienced, full-time 3-D technologists (Laura Logan, 3-D lab manager, Marc Sofilos Linda Novello, and Sean Lee), an administrative assistant (Lakeesha Winston), and a software engineer (Kala Raman) and is attended by a rotation of radiology body fellows and residents. New processing techniques have been introduced into clinical practice this past year, including automatic bone removal and segmentation as mentioned above, and cardiac functional analysis.
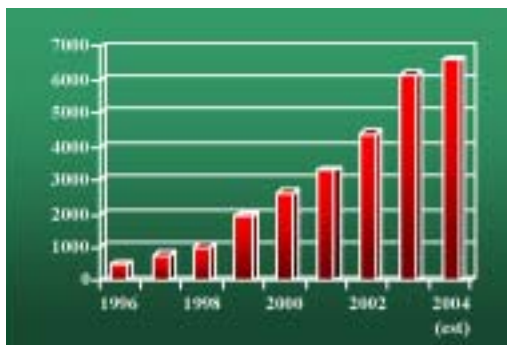
Figure 3. Case volume since inception. 2004 volume is estimated, and amounts to an average of 550 cases/month.

The modern multidetector-row CT scanners at the medical center, as well as faster MR scanning sequences, continue to contribute to an increase in the number of exams processed by the lab (*Fig. 3*). 90% of our referrals are from CT, and the remainder are from MRI.

We provide this service for every clinical department at the Stanford Medical Center. The majority of our referrals come from vascular surgery, cardiothoracic surgery, gastroenterology, cardiology, urology, and neurosurgery (see sample, figure 4). Outside referrals come not only from physicians at other Bay Area hospitals, but also from hospitals in other states. While we process these studies and provide their physicians with 3-D reports, we encourage these hospitals to send their technologists and MDs to us for training, so that they can implement this technology at their own institution.

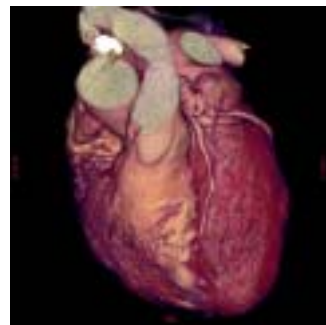Following 3-D analysis, we provide dedicated 3-D reports, including color images and the results of quantitative analyses (diameters, angles, tissue volume, path lengths, vessel flow, ejection fraction). These reports are commonly preferred by the referring physicians, compared to viewing the hundreds or thousands of cross-sectional images generated by the scanners. In addition, all 3-D renderings are stored on Radiology's central PACS server and/or on the Web so that they can be accessed with the standard images and reports. Results of quantitation are stored in databases for future reference and statistical analyses. Referring physicians are quite appreciative of our prompt service and the quality of the 3-D images. They share the images in clinics with their patients, and many will not operate without the 3-D images in the surgical suite.

Figure 4. Coronary artery CT angiogram referred by cardiology.

Education

Our laboratory continues to set international standards for 3-D interpretation and communication in radiology departments. We regularly receive visits from radiologists and technologists from the US and other countries, who wish to understand and duplicate our operations within their own departments. Many stay for several days of intensive hands-on training from our enthusiastic technologists. The exchange of ideas is mutually beneficial to our lab, as we also learn from our visitors.

Industry Partnerships

In addition, we have excellent relationships with corporate developers of 3-D workstations (*e.g.,* General Electric, TeraRecon, and Vital Images) who site their hardware and software here in anticipation of our valuable feedback. These relationships ensure that we are able to provide the latest technology available to our patients.

We also work with medical device developers who use our expertise to evaluate their current and future products. These companies include Medtronic AneuRx, Biosense Webster, and Corazón Technologies, manufacturers of chest and abdominal aorta stent-grafts, ablation catheters, and drug therapies. We provide them with images as well as quantitation for clinical trials, in anticipation of FDA approval for their new products.

Conclusions

The 3-D Medical Imaging Lab continues to function as a major clinical, teaching, and research facility and to advance the Department and the Lucas Center as leaders in this aspect of medical imaging science. The confluence of talented clinical, medical, and engineering expertise as well as the most up-to-date 3-D equipment has resulted in a steady stream of innovation and new developments of diagnostic and treatment planning approaches. Looking forward, we anticipate the arrival of even more multidetector-row channels in CT (up to 64 compared with our present 16) that will provide us with images that will make cardiac gated CT a contender for diagnosis and screening of heart disease (*Fig 5*). We hope to develop more efficient and cost-effective methods to post-process CT and MRI exams and to provide results more quickly to referring physicians in order to assist in medical decision-making. Accomplishment of these goals will ensure that this exciting technology becomes available globally.

Figure 5. Glimpse of a 3-d image from a future 64 multidetector-row dataset. Source images courtesy of Axel Kuettner, Ebingen, Germany.

Psychologists Offer Proof of Brain's Ability to Suppress Memories

Lisa Trei

Stanford News Service

This article appeared on January 8, 2004 in the Stanford Report. This study was performed at the Lucas Imaging Center. The article, published in Science, was also reported in the New York Times and Palo Alto Weekly.

For the first time, researchers at Stanford University and the University of Oregon have shown that a biological mechanism exists in the human brain to block unwanted memories.

The findings, published Jan. 9 in the journal *Science*, reinforce Sigmund Freud's controversial century-old thesis about the existence of voluntary memory suppression.

"The big news is that we've shown how the human brain blocks an unwanted memory, that there is such a mechanism and it has a biological basis," said Stanford psychology Professor John Gabrieli, a co-author of the paper titled "Neural Systems Underlying the Suppression of Unwanted Memories." "It gets you past the possibility that there's nothing in the brain that would suppress a memory —that it was all a misunderstood fiction."

The experiment showed that people are capable of repeatedly blocking thoughts of experiences they don't want to remember until they can no longer retrieve the memory, even if they want to, Gabrieli explained.

Michael Anderson, a psychology associate professor at the University of Oregon and the paper's lead author, conducted the experiment with Gabrieli and other researchers during a sabbatical at Stanford last year.

"It's amazing to think that we've broken new ground on this ... that there is a clear neurobiological basis for motivated forgetting," Anderson said. "Repression has been a vague and controversial construct for over a century, in part because it has been unclear how such a mechanism could be implemented in the brain. The study provides a clear model for how this occurs by grounding it firmly in an essential human ability —the ability to control behavior."

In recent years, the question of repressed memory has attracted considerable public attention concerning cases involving childhood sexual abuse. "That was very controversial because it went through two pendulum swings," Gabrieli said. "The first swing was that people thought, ' What a horrible thing.' The second was that people said, ' How many of these might be false memories?' Then people started asking does repressed memory even exist, and can you show that experimentally or scientifically?"

Anderson first revealed the existence of such a suppression mechanism in the brain in a 2001 paper published in *Nature* titled "Suppressing Unwanted Memories by Executive Control." He took the research a step further at Stanford by using brain imaging scans to identify the neural systems involved in actively suppressing memory. The core findings showed that controlling unwanted memories was associated with increased activation of the left and right frontal cortex (the part of the brain used to repress memory), which in turn led to reduced activation of the hippocampus (the part of the brain used to remember experiences). In addition, the researchers found that the more subjects activated their frontal cortex during the experiment, the better they were at suppressing unwanted memories.

"For the first time we see some mechanism that could play a role in active forgetting," Gabrieli said. "That's where the greatest interest is in terms of practical applications regarding emotionally disturbing and traumatic experiences, and the toxic effect of repressing memory." The Freudian idea is that even though someone is able to block an unpleasant memory, Gabrieli said, "it's lurking in them somewhere, and it has consequences even though they don't know why in terms of their attitudes and relationships."
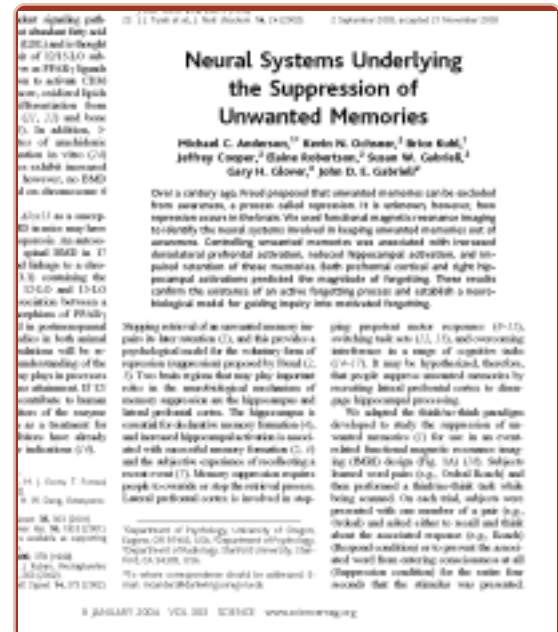
The Experiment

Twenty-four people, aged 19 to 31, volunteered for the experiment. Participants were given 36 pairs of unrelated nouns, such as "ordeal-roach," "steam-train" and "jaw-gum," and asked to remember them at 5-second intervals. The subjects were tested on memorizing the word pairs until they got about three-quarters of them right —a process that took one or two tries, Anderson said.

The participants then were tested while having their brains scanned using functional magnetic resonance imaging (fMRI) at Stanford's Lucas Center for Magnetic Resonance Spectroscopy. The researchers randomly divided the 36 word pairs into three sets of 12. In the first set, volunteers were asked to look at the first word in the pair (presented by itself) and recall and think about the second word. In the second set, volunteers were asked to look at the first word of the pair and *not* recall or think of the second word. The third set of 12 word pairs served as a baseline and was not used during the brain scanning part of the experiment. The subjects were given four seconds to look at the first word of each pair 16 times during a 30-minute period.

After the scanning finished, the subjects were retested on all 36 word pairs. The researchers found that the participants remembered fewer of the word pairs they had actively tried to *not* think of than the baseline pairs, even though they had not been exposed to the baseline group for a half-hour.

"People's memory gets worse the more they try to avoid thinking about it," Anderson said. "If you consistently expose people to a reminder of a memory that they don't want to think about, and they try not to think about it, they actually don't remember it as well as memories where they were not presented with any reminders at all."

Implications of the Study

Gabrieli said the findings contradict human intuition. "What's funny about that, from a psychological viewpoint, is that mostly people are quite the opposite in life —a very unpleasant thing intrudes into their thinking," he said. "They ruminate, it bothers them, and it comes up when they don't want to think about it. Mostly, if you say, ' Don't think about a pink elephant or a white bear,' people flash onto it immediately."

Anderson likened the brain's ability to control memory to an individual's reflexive ability to halt an unwanted action. For example, Anderson recalled once standing at an open window and noticing a potted plant starting to fall. He quickly tried to catch the plant until he realized it was a cactus that could have injured him. "Our ability to stop action is so ubiquitous we don't know we're doing it," Anderson said. "This idea is that the neurobiological mechanism that we have evolved to control overt behavior might be recruited to control internal actions such as memory retrieval as well."

Anderson said the findings about the brain's ability to suppress memory could be used as a tool to better understand addiction and the ability of people to suppress unwanted thoughts related to craving. It might also help provide a model to assess individuals at risk from suffering post-traumatic stress disorder, he said.

In addition to Anderson and Gabrieli, the paper was written by Kevin N. Ochsner, a former Stanford postdoctoral fellow now at Columbia University; and other Stanford researchers including graduate student Brice Kuhl; social science research assistants Jeffrey Cooper and Elaine Robertson; science and engineering associate Susan W. Gabrieli; and radiology Professor Gary H. Glover. The research was supported by grants from the National Institute of Mental Health.

NEUROIMAGING

Statistical Combinations of Partial k-space EPI for BOLD fMRI

Christine S. Law and Gary H. Glover

Department of Radiology

INTRODUCTION

The spiral-in/out technique has been proposed recently for the improved detection of BOLD fMRI [1]. Activation volumes are increased over simple averaging using a statistically weighted combination of two activation maps each separately derived from the spiral-in and spiral-out images [2]. We propose application of the same concept to EPI: The upper half k-space in EPI (pre-TE) is analogous to spiral-in, the lower half to spiral-out. From each half we then form a complete image using homodyne reconstruction [3]. These two EPI images are combined using their individual activation map as weights. While thermal noise in the two half-images is uncorrelated except near the k-space origin, physiological fluctuations can cause correlated noise to appear across the entire readout. Thus combination of two magnitude images, each containing noise uncorrelated with the other, may result in less noise than conventional EPI and can improve contrast-to-noise ratio (CNR) and fMRI activation. Further, susceptibility dropout may be lower overall in the combined image due to adaptive combination [1].

MATERIALS AND METHODS

A conventional single shot EPI is used for breathholding fMRI scans. Raw data is gridded on a 64x64 matrix to account for nonuniform spacing during k-space acquisition [4]. A conventional EPI image is first reconstructed by Fourier transformation of the raw data. Then upper and lower k-space images are reconstructed separately by homodyne technique.

The breathholding experiment was carried out at 3T (GE Signa, Cv/Nv gradients). This task consists of 15s normal breathing and 15s breathholding after inspiration, visually cued and repeated for 8 cycles. This causes a systemic hypoxia and results in BOLD signal modulation, independent of cognition, having a trough during breathholding epochs [5]. Six axial slices are gathered using an fMRI head coil (TR/TE/a /TH/FOV = 1s, 30ms, 70˚, 4mm, 22cm). Correlation coefficient maps are formed by cross-correlating image time-series for each pixel with sine and cosine functions at the fundamental task frequency. This correlation analysis is performed using full k-space data, and then again using upper and lower k-space data. A *sigma filter* is used to cluster pixels in a 3x3 region thereby reducing single-voxel false

(a)

(b)
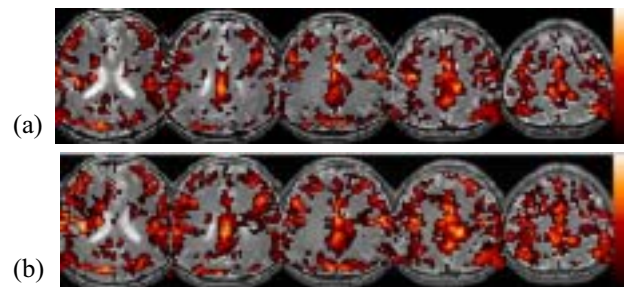
(a) Breath holding activation maps in five slices using conventional EPI reconstruction. (b) Same slices as (a) but with activation maps calculated by combining two upper/lower EPI images.

positives [2,6]. Finally, the upper and lower k-space images are combined, weighted by their correlation coefficient maps.

RESULTS

Figure (a) illustrates the correlation coefficient maps using conventional EPI reconstruction overlaid on five T2-weighted images. Figure (b) shows data from the same acquisition but processed using our new upper/lower k-space EPI technique to generate the correlation overlays

CONCLUSION

We developed a technique to enhance EPI fMRI data by performing homodyne reconstruction to make upper and lower EPI images then combined; weighted by their individual correlation coefficient maps. The combined upper/lower EPI activation maps shown in Fig. 2 has significant activation improvement over the conventional EPI image. Unlike spiral in/out where the improved CNR comes from lengthening the readout duration, noise reduction in combined upper/lower EPI originates from the elimination of correlated noise between the two halves. Since breathholding induces robust global activation [5], higher activation volumes indicate superior reconstruction technique indeed. While the homodyne technique is suitable for this image slice, scans near air/tissue interface regions cause rapid phase variations and k-space DC-component shift. In that situation, other partial k-space reconstruction techniques such as POCS may perform better. This method, nevertheless, may offer significant improvements for fMRI in analogy to the spiral-in/out technique.

REFERENCES

1. Glover GH, Law CS, Magn Reson Med. 2001; 46:515-22.
2. Glover GH, Thomason ME, Magn Reson Med. 2004; 51:863-868.
3. Noll DC, et al, IEEE Trans. Med. Imag. 1991; 10:154-163.
4. Jackson J, et al, IEEE Trans. Med. Imag. 1991; 10:473-478.
5. Kastrup A, et al, Magn. Reson. Med. 1999; 42:608-611.
6. Glover GH, Lai S, Magn. Reson. Med. 1998; 39:361-368.

Learned Explicit Control Over Brain Activation and Pain Using Real Time fMRI

R. Christopher deCharms[1], Fumiko Maeda[2], Gary H. Glover[3], David Ludlow[5], John M. Pauly[4], Deepak Soneji[2], John D. E. Gabrieli[2], Sean C. Mackey[5]

[1]Neurion, [2]Dept of Psychology, [3]Dept of Radiology, [4]Dept of Electrical Engineering, [5]Dept of Anesthesia, Division of Pain Management

INTRODUCTION

Control over specific neuronal processes is of central importance to neurology, psychiatry, pharmacology, and neurostimulation. Brain processes mediate behavior and cognition, so in order to perform behaviors subjects exercise implicit, unknowing control over the brain processes that form the basis of their actions. However, it is not known whether subjects can learn to take explicit control over the many localized processes taking place within the brain, potentially impacting behavior, cognition, or associated disease.

MATERIALS AND METHODS

A target region of interest (ROI) in the rACC was individually defined for each subject based upon anatomical landmarks and physiological activation using a pain attention task. Subjects then began training inside a 3T MRI scanner while continuously viewing the level of fMRI activation in the target ROI in the form of a scrolling line graph. Subjects underwent 3 training scans of 13 minutes, and a final test run. These consisted of 5 repetitions of a 30s rest period, a 60s period during which subjects were instructed to learn to increase the level of rACC activation, and a 60s period during which subjects were instructed to learn to decrease rACC activation.

RESULTS

Here, we demonstrate that using real time fMRI (rtfMRI) feedback(6-9) to guide training, subjects can learn increased explicit control over a specific brain mechanism, activation in the rostral anterior cingulate cortex (rACC), a region putatively involved in pain perception and regulation(10). This in turn leads to changes in pain, a behavioral function that this brain area may take part in mediating. When subjects deliberately induced increases or decreases in rACC activation, there was a corresponding change in pain caused by noxious thermal stimuli.

CONCLUSION

Previous work has shown that subjects can learn to control a number of physiological measures. However, these may all reflect common endpoints downstream from generalized, nonspecific central regulatory mechanisms such as relaxation. Using real time neuroimaging, it is now possible to explore the extent to which subjects can learn conscious control over much more specific, localized neural mechanisms and their associated cognitive process such as pain perception. The present study demonstrates that such region-specific control
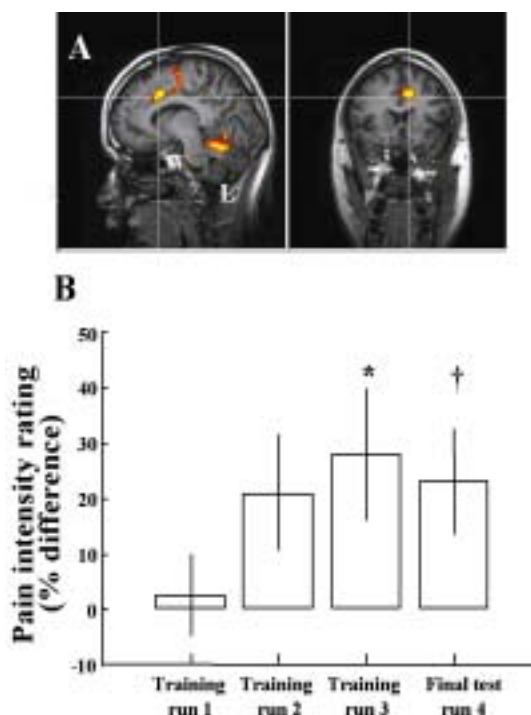
Learned control over rACC activation and pain. (A) Spatial pattern of changes in activation through the course of training. The most significant change in forebrain activation was in rACC, the targeted brain region (crosshairs). (B) Control over pain increased significantly through the course of training in the experimental subject group (* p<0.05, linear regression, p<0.05, ° t-test run 3/4 vs. run 1).

of neural processes can be learned, and that such learning can alter associated behavior (Fig. 1). Learned control over rACC activation and pain. (A) Spatial pattern of changes in activation through the course of training. The most significant change in forebrain activation was in rACC, the targeted brain region (crosshairs). (B) Control over pain increased significantly through the course of training in the experimental subject group (* p<0.05, linear regression, p<0.05, † t-test run 3/4 vs. run 1).

REFERENCES

1. Kumar K, Toth C, Nath RK. Neurosurgery 1997; 40:736-46; discussion 746-7.
2. Fields HL. *Pain*. 1987. McGraw-Hill Book Co, New York
3. Rainville P. Curr Opin Neurobiol 2002; 12:195-204.
4. Petrovic P, Ingvar M. Pain 2002; 95:1-5.
5. Jones AK, Kulkarni B, Derbyshire SW. Br Med Bull 2003; 65:83-93.
6. deCharms RC, Christoff K, Glover GH, Pauly JM, Whitfield S, Gabrieli JDE. Neuroimage 2004; 21:436-43.
7. Cox RW, Jesmanowicz A, Hyde JS. Magn Reson Med 1995; 33:230-6.
8. Weiskopf N, Veit R, Erb M, Mathiak K, Grodd W, Goebel R, Birbaumer N. Neuroimage 2003; 19:577-86.
9. Posse S, Fitzgerald D, Gao K, Habel U, Rosenberg D, Moore GJ, Schneider F. Neuroimage 2003; 18:760-8.
10. Rainville P, Duncan GH, Price DD, Carrier B, Bushnell MC. Science 1997; 277:968-71.

Navigated 3D fMRI vs. 2D fMRI

Yanle Hu[1, 2], Gary H. Glover[2]

[1]Department of Physics and [2]Department of Radiology

INTRODUCTION

In functional MR imaging, methods which can achieve higher Signal to Fluctuation Noise Ratio (SFNR) are always desirable. Such methods can increase the temporal resolution or enhance our capability to detect even subtle BOLD signal changes. In principle 3D stack of spirals methods can achieve higher SNR than the 2D spiral method [1]. However, incoherence across the k_z direction causes increased fluctuation noise in 3D method. Here we examine the use of navigation [2] to increase SFNR in 3D method.

MATERIALS AND METHODS

The 3D spiral acquisition method excites the whole FOV in the slab select direction, adds phase encoding in the same direction and then performs 2D spiral acquisition for each phase encoding step to acquire the 3D k-space data. Experiments were performed on a normal subject using a 1.5 Tesla whole-body scanner (Signa, GE Medical Systems, Milwaukee, WI) with normal head coil. Imaging parameters are TR/TE/FA/MAT/NSLC = 100ms/40ms/27/64*64/16. Additional data collected before the phase encoding gradient was applied were used to perform the phase correction along the slab select direction. Functional activation data was obtained with an auditory task in which subject heard tones at 3Hz during a 20-s "on" block and no tones during a 20-s "off" block. Six complete cycles were used for a total scan time of 4 minutes. Activation maps were overlaid on the T_2 images for visual inspection. SFNR is given by the ratio of average signal to the signal standard deviation across the time frames for a given pixel. The region of interest for the noise analysis is an 8*8 matrix located in a region near auditory cortex but avoiding susceptibility-dephasing and CSF.

RESULTS

Representative results are shown below. Fig. 1 gives the comparison of auditory activations between 2D, 3D and navigated 3D acquisition methods. For thinner slices (4mm), the navigated 3D fMRI demonstrates greater volume and intensity of activations. For 6mm slices, the navigated 3D fMRI is not clearly an advantage over 3D or 2D fMRI. Detailed SFNR and fluctuation noise analyses for different slice thicknesses are given in Fig. 2. Patterns of percent of fluctuation are nearly independent of slice thickness. However, the advantage of 3D acquisition methods in SFNR vanishes gradually as the slice thickness increases. Fig. 2 also shows that the navigation correction is more important for thicker slices.
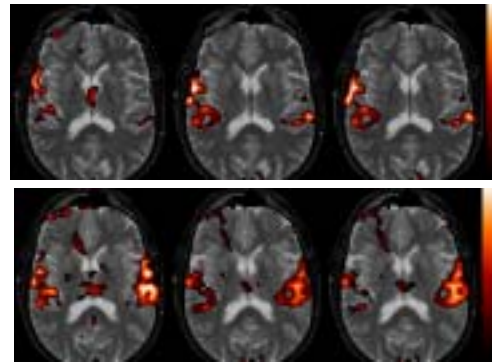

Figure 1. Comparison of auditory activations between 2D (first column), 3D (second column) and navigated 3D (third column) acquisition methods. The slice thickness is 4mm for first row and 6mm for second row.
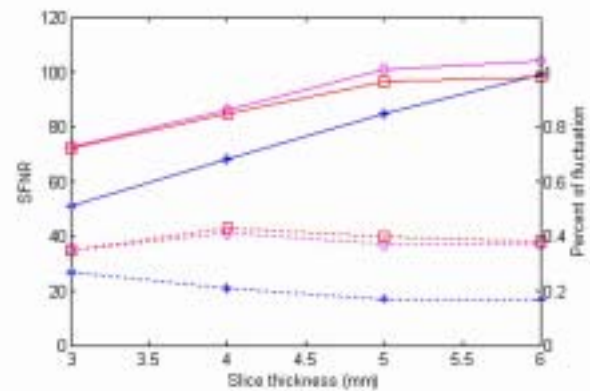

Figure 2. Comparison of SFNR (solid lines) and percent of fluctuation (dotted lines) between different slice thicknesses. Stars, squares and diamonds correspond to 2D, 3D and navigated 3D acquisition methods respectively.

CONCLUSION

Results show that navigation correction can reduce fluctuation noise and increase SFNR in 3D acquisitions especially with thicker slices. However, for thicker slices, 3D acquisition methods lose SFNR advantage over 2D. Since the percent of fluctuation doesn't change, the results indicate that 3D acquisition methods suffer more signal loss than 2D as the slice thickness increases. This may be caused by intravoxel dephasing across the slab select direction because the signal in 3D methods is more sensitive to susceptibility-induced gradients.

REFERENCES

1. Lai S, Glover GH. Three-Dimensional Spiral fMRI technique: a comparison with 2D spiral acquisition. Magn Reson Med 1998; 39:68-78

2. Hu X, Kim SG. Reduction of Signal Fluctuation in Functional MRI Using Navigator Echoes. Magn Reson Med 1994; 31:495-503

Localized Active Shimming for fMRI Signal Recovery

Jung-Jiin Hsu, Gary H. Glover

*Lucas Magnetic Resonance Spectroscopy and Imaging Center*

INTRODUCTION

In mapping brain neuronal activity by fMRI, obtaining accurate data in the inferior portion of the frontal lobe (IFL) is difficult because the imaging magnetic field (B0) in this region is seriously distorted [1]. Existing field shimming methods use shim coils that are basis functions ideal for overall symmetrical or homogeneous imaged objects. But this design is inefficient for imaging the human brain because the field inhomogeneity created by local structures in the human head has much smaller scale that requires shim coils of very high orders. A magnetic field generated to shim local structures is therefore desirable. Previously we had shown [2] that the localized shimming field can be actively and conveniently generated by free electronic currents in coils placed in the mouth; the shimming is efficient, and the advantages are that the currents can easily be adjusted in size and shape for optimal results and can be determined in situ on a patient-by-patient basis. In this work [3], we further examine the effect of the active shim coils in signal recovery in fMRI.

MATERIALS AND METHODS

The mouth shim coil is composed of three circular coils (channels); each is wound with gauge 32 magnet wire and of 1.6 cm in diameter and 60 turns. The current of each channel can be adjusted individually. The size is designed to be small for comfort but still efficient in generating needed field strength with reasonable amount of currents. To determine the shim currents, a test current is input to one of the channels and a B0 map is acquired; then the procedure is repeated for the other channels. The B0 maps are subtracted by a background B0 map obtained without any current so each subtracted map represents the shimming field generated by the test current. Then the required shim currents are solved by least-square fitting to eliminate the third B0 map.
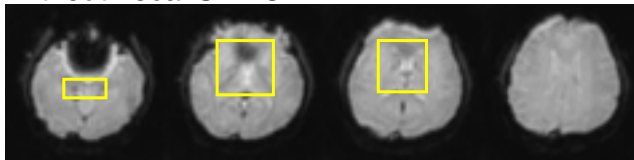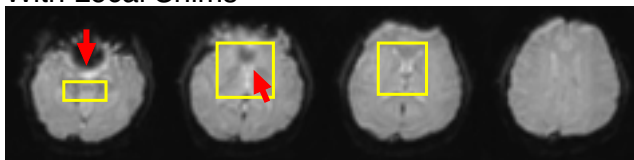
In the fMRI experiment, the subject is visually cued to perform a breath-holding (15 s) and normal-breathing (15 s) interleaved task (eight periods total), which is expected to result in blood-oxygen-level-dependent (BOLD) signal globally in the brain. The change of the signals in the ROI as well as other areas less affected by the inhomogeneity can be observed and compared. A spiral pulse sequence is used for the data acquisition.

RESULTS

Shown in Fig. 1 are the images obtained by averaging all the time-course images from which the fMRI activation maps are derived; TE = 40 ms. The boxes indicate the ROI which the shimming field was optimized for. Signal recovery by the mouth shim can be seen in the ROI and its vicinity, in particular in regions pointed to by the arrows. This improves the accuracy of the fMRI analysis.

Shown in Fig. 2 are the activation maps. In the ROI and its vicinity, the use of the mouth shim has allowed more activation to be detected. In the ROI, the number of pixels above the lower threshold has increased by 12 %. The areas of improved activation signal agree with that of improved field homogeneity in the average images of Fig. 1; this affirms the contribution of the mouth shim.

CONCLUSION

Our localized active shim coil and the algorithm to determine the shim currents can effectively improve the field homogeneity and fMRI data accuracy. The method is easy and convenient to implement. It has adjustable parameters that can be optimized in situ patient by patient and the shimming procedure can be completed in a very short period of time.

REFERENCES

1. S Li, et al., Magn Reson Med 34, 268 (1995); S Li, et al., ibid. 36, 705 (1996); and references therein.
2. J-J Hsu and GH Glover, Proc Intl Soc Mag Reson Med 11, 734 (2003).
3. J-J Hsu and GH Glover, Proc Intl Soc Mag Reson Med 12, 994 (2004).
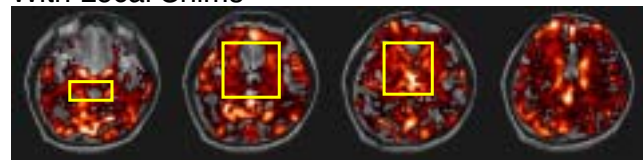
Without Local Shims

With Local Shims

Figure 1 Images acquired during an fMRI experiment (TE = 40 ms).

Without Local Shims
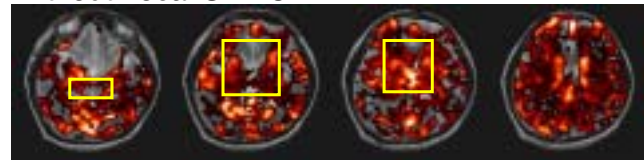
With Local Shims

Figure 2 BOLD signal recovery using the localized active shimming.

Calibration of fMRI Activation for the FIRST BIRN Project

M. E. Thomason[1], L. Foland[2], F. BIRN[3], G. H. Glover[1,2]

*[1]Neurosciences, [2]Radiology, Stanford University;
[3]Biomedical Informatics Research Network, NIH NCRR, Bethesda, MD*

INTRODUCTION

The FIRST (Functional Imaging Research Schizophrenia Testbed) Biomedical Informatics Research Network (fBIRN) program is the first-ever large scale, multi-center fMRI study of schizophrenia (http://www.nbirn.net). The fBIRN goal is to scan 60 subjects at each of the 11 participating sites to enable the acquisition of a large and diverse study population in a modest time period. To be able to pool fMRI scan data across sites, a calibration series was performed utilizing a protocol in which 5 normal volunteers were scanned at each of the 11 sites. The concept was to examine whether activation from a sensorimotor and/or hypoxic challenge could be used to eventually normalize data from the cognitive tasks associated with the schizophrenia evaluation across sites. This abstract presents initial results for comparison of sensorimotor and breathholding activation from scans conducted at Stanford University, one of the 11 sites.

MATERIALS AND METHODS

The calibration protocol comprised 2D and 3D anatomic scans and 8 fMRI scans that were performed in one session for each subject and repeated the next day. Three of the five subjects began the fBIRN study at Stanford University and returned approximately 1.5 months later for repeat scans. The other two subjects were scanned during one 2-day visit. Thus, a total of 16 scan sessions was utilized in the analysis presented here. The functional portion of the calibration scan protocol included 4 sensorimotor (SM) tasks, 2 breathholding (BH) tasks and 2 resting state (R) scans.

During the 15s experimental condition of the SM task, the subject viewed a contrast-reversing checkerboard pattern while performing bilateral finger tapping on button boxes and hearing frequency modulated auditory tones, all synchronized at 3Hz. The control condition was a 15s fixation cross; 8 on-off blocks were collected. The BH task consisted of 15s of normal breathing and 15s of breathholding after inspiration, visually cued and repeated for 8 cycles. This caused systemic hypoxia and resulted in global BOLD signal modulation not dependent on cognition. The signal significantly decreased during breathholding epochs, as has been demonstrated previously (1). The resting state scans are not discussed here.

After giving informed consent, the volunteers were scanned at 3T (GE Signa, Cv/Nv gradients) using a spiral-in/out sequence (2). The fBIRN acquisition parameters were 35 axial
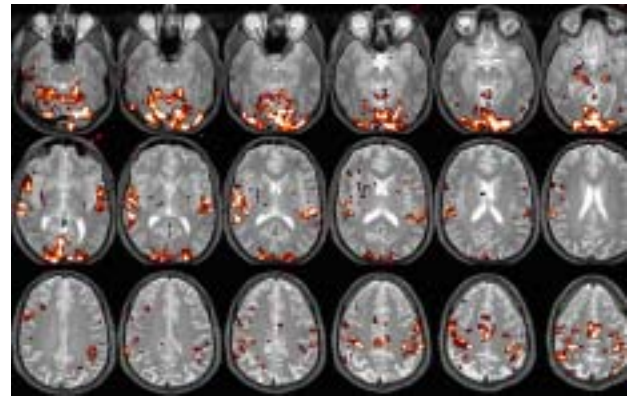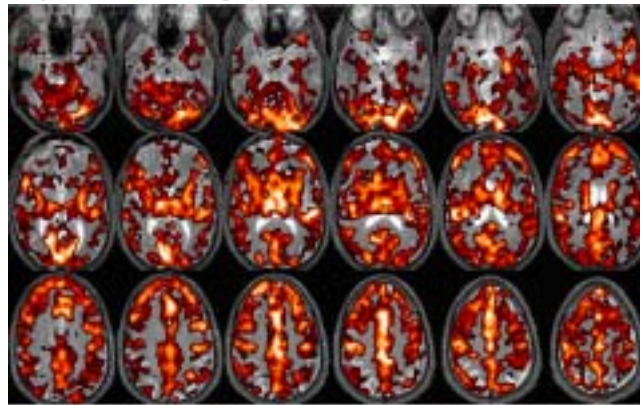

Fig. 1: Activation maps for SM task

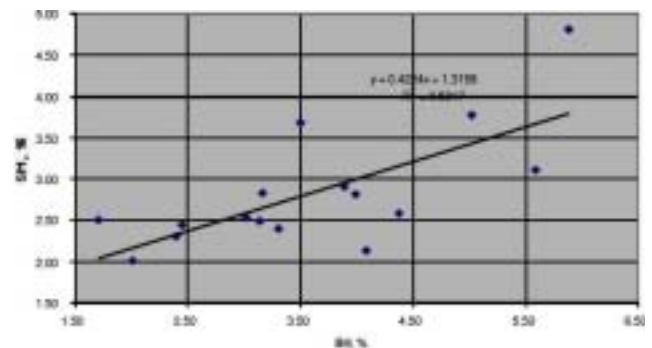*Fig. 2: Activation maps for BH task*

Fig. 3: BOLD signal for SM vs. BH.

4 mm contiguous slices, 22 cm FOV, 64x64 matrix, TE 30ms, TR 3000ms, 87 time frames (2 discards). After 2 cognitive tasks (Sternberg and mismatched negativity), functional calibration scans were obtained in the following order: SM1, R1, SM2, BH1, SM3, BH2, R2, SM4. The image timeseries were analyzed with ROIs in visual, auditory and motor cortices defined using activation maps from SM4.

Percent BOLD signal in the SM and BH scans was obtained with Fourier analysis of the timeseries signal by averaging over all activated voxels.

These values were averaged over the session (4 SM and 2 BH scans), to give one (SM-BH) data pair for that session and ROI. These results were plotted to determine degree of correlation between SM and BH.

RESULTS

The figures show typical activation maps for SM and BH as well as quantitative BOLD signal comparisons for auditory cortex. The latter resulted in a grouped linear regression R2 value of 0.50 and slope of 0.42 for SM vs. BH (Fig. 3). Similar results were obtained in motor and visual cortices with R2 values of 0.62 and 0.47, respectively, suggesting a good correlation between the non-cognitive BH task and the sensorimotor task.

Global variations in the BH BOLD signal during repeated scans in the same and subsequent days were observed. These variations may result from differences in inspiration level.

CONCLUSION

The observed correlation between BOLD signal in the BH task and SM task suggests that BH is an effective calibration metric, because it is a measure of vascular reactivity (i.e. is a systemically caused O2 state change) intrinsically devoid of neuronal processes and is therefore not modulated by attentional variations. In addition, while SM provides activation only in sensory regions, BH results in global BOLD modulation in gray matter (Fig. 2), so that all active voxels in the brain can be characterized. This is an important consideration for calibrating between-group or in multicenter studies of higher cognitive function. For greatest reliability it may be important to control the level of inspiration during BH.

Enhanced BOLD Response in Breast Tumors Induced by Breath Holding

R. Rakow-Penner, B. Daniel, L. Stables, G. Glover

Departmen of Radiology

INTRODUCTION

Current protocols for tumor imaging, specifically applied with breast cancer candidates, call for the use of pharmaceutical contrast agents. These agents require intravenous injection causing additional discomfort to the patient while also requiring qualified personnel to start the IV. The cost of the enhancing agents (both the chemical itself and the process of injection) drives up the cost of MRI, making MRI less accessible to both patients and doctors as a standard method for investigating breast cancer. An alternative that allows for a totally non-invasive procedure, by simply exploiting the innate physiology of tumors, is ideal. A defining property of tumors is their high affinity for oxygen, causing regionally altered perfusion characteristics.

MATERIALS AND METHODS

The scan protocol used a 3D "stack of spirals" imaging sequence with a spectral-spatial pulse for fat suppression. Scan parameters included: TE = 24 ms, TR = 62.5 ms, 2 interleaves per slice, and flip angle of 40. The resolution was 100 x 100 x 32 with a FOV of 20 cm x 20 cm x 8 cm. Partial k-space acquisition in the slice direction acquired 20 of 32 lines. Two healthy volunteers (both age 24) and one breast tumor patient (age 36) participated in the study. The healthy volunteers were scanned on a 1.5T Signa GE scanner, while the patient was scanned on a 1.5T Twin GE scanner, all with designated breast coils made by MRI Devices. Each participant held their breath for 15 s intervals followed by 15 s of regular breathing, for 7 cycles. For each slice, 12 time frames/period were collected. In the case of the patient, a routine Gadolinium (Gd) enhanced protocol directly followed.

Data analysis of BOLD results applied a time course correlation method established by Adrian Lee et al.[1] The method correlates the breath holding cycle to sinusoidal functions, providing results in which both magnitude and phase of the BOLD signal variation can be observed.

RESULTS

Figure 1 shows a Gd enhanced image from the patient. Cancer was diagnosed and confirmed by biopsy, finding a malignant tumor 1.2 x 1 cm in the lower inner quadrant, as well as adjacent ductal carcinoma in situ to the left of the round tumor (arrows). The BOLD data (collected before acquisition of the Gd enhanced data) is shown in Figs. 2. The left image of Fig. 2 represents the BOLD response with a correlation phase of 7.5 s later than that of the image to its right. Note that arrows 1 and 2 (Fig. 2) correspond to the enhanced regions in the Gd image (Fig. 1). This indicates that the carcinogenic regions responded more quickly to variation in oxygen intake then the rest of the tissue, as is consistent with tumor physiology and conventional dynamic contrast enhanced studies. The results in normal volunteers demonstrated no focal regions of
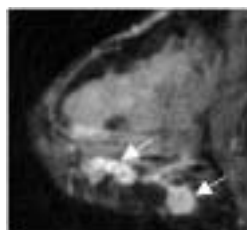

Figure 1. Gadolinium enhanced breast. Note the large round mass on the bottom right and the adjacent enhanced region to the left – biopsies found these regions to be malignant.
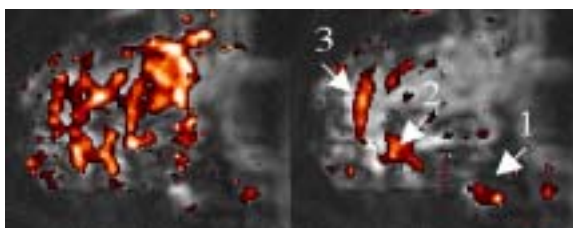

Figure 2: BOLD response in tumor patient. The left-side half is the response with a 7.5 s delay to the right-side image on the right.

rapid response such as those seen in the patient (Fig. 2, right), and were consistent with the delayed response in the non-tumor regions of the patient (Fig. 2, left). Arrow 3 marks a region of apparent BOLD contrast at the border of fat and glandular tissue that may result from motion correlated with the breath holding task. Indeed, a correlation of 24% was found between the BOLD response in the breast and bulk breast motion, measured from the image time series. Such potential motion artifacts were also noted in regions near the chest wall in several slices of the healthy volunteers, where there is otherwise no BOLD response.

CONCLUSION

Malignant regions present in Gd enhanced images paralleled regions observed in early response BOLD images stimulated by hypoxia. As expected, carcinogenic regions responded earlier than healthy regions under hypoxic conditions, with re-

sults indicating a 7.5 s time delay between the malignant verses healthy tissue. This study demonstrates how BOLD images can identify tumor regions without contrast agents, with the potential of providing additional diagnostic information. Future studies include correlating BOLD signal with specific tumor types, studying differentiation between malignant and benign response, filtering out motion artifact, and optimizing the BOLD sequence timing and imaging parameters.

REFERENCES

1 Taylor, N. Jane, et al. Journal of Magnetic Resonance Imaging (14):156-163, 2001.
2 Kastrup, Andreas, et al. Magnetic Resonance in Medicine (42):608-611, 1999.
3 Lee, Adrian T., et al. Magnetic Resonance in Medicine (33):745-754, 1995.

In Vivo Phosphorus Spectroscopy at 3 Tesla: Hardware Development and Study Goals

Chardonnay J. Vance[1,2], Dan Spielman[3], Bruce Ames[1,2], Gary Glover[3]

[1]Department of Molecular and Cell Biology at UC Berkeley, [2]Children's Hospital Oakland Research Institute, [3]Department of Radiology at Stanford

INTRODUCTION

Accumulation of oxidative damage to mitochondria in tissues and organs, including the human brain, can impair the cellular processes of detoxification, DNA replication and repair, osmotic balance, and the capacity to generate ATP. Several anti-oxidants and respiratory chain metabolites have been found to significantly decrease with age, with neurodegenerative diseases and with mitochondrial dysfunction. Current research in the Ames lab has shown that oral supplementation of these metabolites can delay or reverse age related mitochondrial decay in tissue models and can improve memory and locomotion in old rats.[1] Our goal is to develop an assay which can longitudinally judge mitochondrial function and objectively observe the effectiveness of the supplementation regimen as non-invasively as possible in the brains of healthy humans. This will be accomplished through *in vivo* [31]P nuclear magnetic resonance spectroscopy at the Lucas Center, first in old and young rat brains and then in human brains. Further subjects may include specific strains of mice and/or humans who have genetic mitochondrial dysfunction.

MATERIALS AND METHODS

We built a dual-tuned low pass phosphorus-proton quadrature birdcage coil for acquiring spectroscopic images from the rat brain at 3 Tesla.[2] Each channel of the coil was tuned to within 50 kHz, matched to approximately 50 with minimal reactance, with attenuation of at least -18dB between channels. A B_1 field map of the entire volume of the dual tuned rat coil shows an adequate working volume throughout the coil, and a uniform (+/- 5% field strength with a 90° pulse) working volume of 5 cm³ at both frequencies in the

Axial proton localizer image of rat head. Both data sets acquired at 3 Tesla with the dual tuned $^1H/^{31}P$ volume coil.
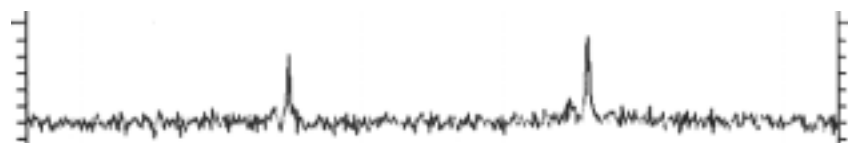
Spectrum acquired from 25 min. FID CSI scan of a phantom containing 10 millimolar each Phoshocreatine (right peak) and Hexamethylphosphorus tiramide (left peak)

center of the coil. A dual tuned head coil of a similar design will be built for the human studies at 3 Tesla, with expected qualitatively similar performance.

Currently, we are investigating different outer volume suppression paradigms and chemical shift imaging routines on rat brains. Most promising is a $1cm^3$ voxel encompassing most of the brain, as is outlined in yellow in the image at right, excited by a single slice of a FID CSI routine. This sequence applied on a rat-emulating phantom containing physiological concentrations of phosphorus metabolites has yielded a signal to noise ratio of 6:1 after a 25 min. acquisition, as is shown by the spectrum at right.

The first subjects scanned will be male Fisher 344 rats. All will be fed a standard purified diet with or without the addition of supplements. The supplement regimen will include alpha-lipoic acid and acetyl-l-carnitine. Two age ranges will be studied: young-adults, aged 3 to 12 months, and old-adults, aged 20 + months. During the beginning of supplementation, the individual rats will be scanned once a week on a rotating schedule, so that the response to supplementation can be measured on a day by day basis. After the first month of supplementation, the rats will be scanned once a month, again on a rotating schedule.

CONCLUSIONS

The dual tuned volume coil and various spectroscopic and CSI pulse sequences have been thoroughly tested for broadband functionality and practicality for rat brain studies at the 3 Tesla system at the Lucas Center. We are now ready to begin our study on the rat brain.

REFERENCE

1. J. Liu et al., *PNAS* 2002, 99:2356-2361

Laminar Activation Profiles in Early Visual Cortex
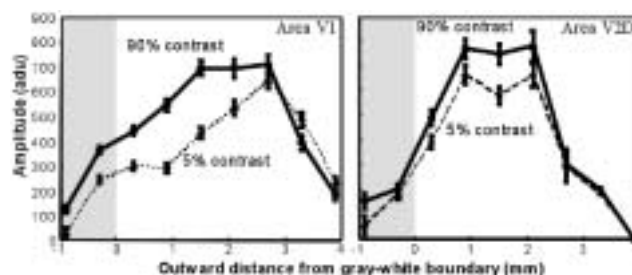
David Ress, Brian A. Wandell, G. H. Glover

Departments of Psychology and Radiology, Stanford University

INTRODUCTION

Human neocortex has a well-known laminar structure consisting of six layers designated I—VI going from pia to white matter. These layers are distinguished cytoarchitecturally and by their specialized anatomical projections. In particular, Layer IV neurons receive their inputs from the thalamus. The anatomical profiles of these laminae vary between different areas of visual cortex. Specifically, layer IV in Area V1 is thicker and elaborately specialized for its connections with the thalamus. By contrast, extrastriate visual cortex, such as areas V2D and V3D, are thinner than V1 and have a much less elaborate layer IV. We used high-resolution fMRI to investivate whether different conditions of visual contrast and attention would affect the laminar activation profiles if several areas of early visual cortex.

MATERIALS AND METHODS

Subjects performed a sequence of 1.5-s contrast-discrimination tasks, each consisting of a 0.75-s stimulus presentation followed by response period. Stimuli were 4-Hz flickering checkerboards presented in an annular aperture around a fixation mark. The stimulus aperture varied between a small annulus (0.5—1.25I) and a larger annulus (1.75—2.5I) to create an 18-s alternation period. Eight 4-min-duration scans each were performed, half with low (<5%) and half with high (~90%) contrast stimuli. Functional images were obtained while the subject performed this task using a 3T GE scanner. Eight 1-mm-thick slices with 0.6-mm pixels were obtained every 2 s along an axis perpendicular to the calcarine sulcus near the occipital pole of left hemisphere. The high resolution was enabled by using a 6-cm-diam surface coil, a 10-cm FOV, and a 3-shot spiral readout. The activation time series was fit with sinusoid and the resulting amplitude data was interpolated into a coaligned T1 reference anatomy (0.6-mm isotropic voxels) to enable determination of laminar ROIs in early visual areas predefined by a separate retinotopy scanning sessions.

Laminar profiles of functional activity in visual areas V1 and V2.

RESULTS

Good quality functional activations were obtained from each scan. Activation was almost entirely confined to the gray matter, as seen in the laminar activation patterns shown in the Figure. The profile in V1 is substantially broader than in V2D. Also in V1, but not in V2D, the high-contrast stimuli produces a differential increase in activity near the center of the profile, possibly reflecting the increase in Layer IV input.

CONCLUSION

Laminar activity profiles can be measured in human visual cortex using high-resolution fMRI.

Diffusion Tensor Imaging Using SENSE-Single-Shot EPI

Roland Bammer, M. Moseley, David Clayton, G. Albers

Lucas Center, Departments of Radiology and Neurology

INTRODUCTION

Single-shot EPI (ssh-EPI) is the most frequently used method for DTI because of its robustness against motion artifacts and its fast image acquisition capability. However, it is sensitive to field inhomogeneities, chemical shift, and image blurring all of which distort DTI. It has recently been shown that the increased *k*-space velocity (intrinsic to parallel imaging techniques such as SENSE) can be used to strongly improve image quality of diffusion-weighted images and fMRI scans.

METHODS AND RESULTS

Eight healthy volunteers and 4 patients with stroke were imaged at 1.5T with two distinct SENSE-sshEPI sequences using a dedicated multi-element head array and were compared with regular DTI scan. Both SENSE scans were conducted with a reduction of 3. One of the SENSE scans was performed with an acquisition matrix of 128x128, the second with 256x128.

Aside from the improved image quality for DTI (Fig.1) we could demonstrate that lesion conspicuity and detection rate of microemboli improves significantly with SENSE-DWI scanning when applied to stroke patients (Fig.2). Moreover, T2* induced blurring, chemical shift and susceptibility artifacts could be dramatically reduced.

CONCLUSION

This study clearly demonstrated that SENSE sshEPI improves the quality of DTI maps significantly with respect to resolution enhancement and off-resonance artifact suppression. Corresponding FA maps allowed an excellent delineation of white matter tracts. Exploiting the advantages of a single-shot technique, we obtained images with markedly improved quality and with a spatial resolution that has not been possible with EPI thus far. These artifact reduction capabilities are especially important at higher fields where increased off-resonance artifacts could otherwise impair image quality.
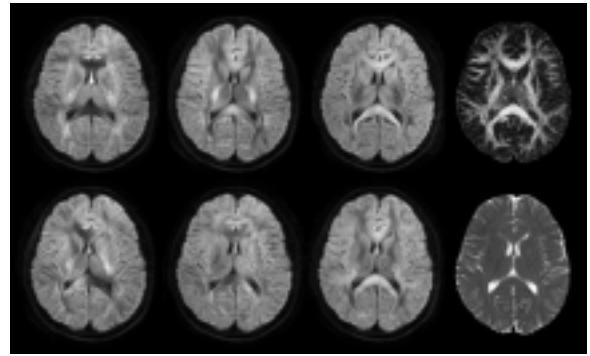

Fig. 1 - DTI using SENSE-EPI (128x128, R=3). Three left-most columns: Intermediate DW images with diffusion encoding in L/R, A/P, C/C direction. Right: FA (top) and trace (bottom). The shorter EPI readout allowed shorter echo times and, thus, reduced the SNR-loss due to missing profiles. Since SENSE-EPI is still a single-shot technique, excessive averaging is an option and keeps the total acquisition time in a reasonable range.
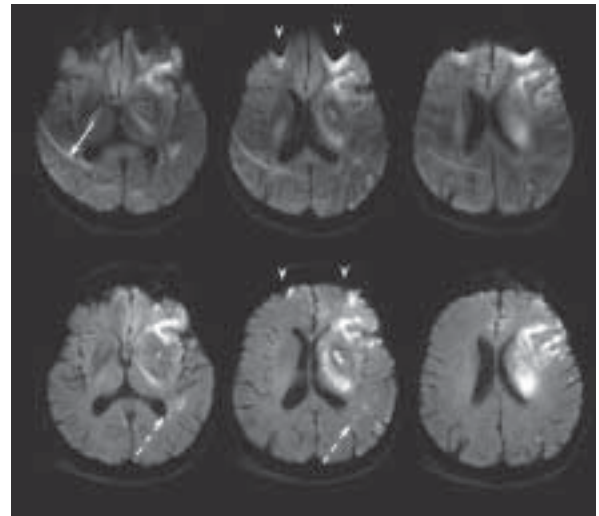

Fig. 2 - Patient that suffered from an ischemic stroke. Top row: conventional diffusion-weighted single-shot EPI. Bottom row: high-resolution dw-SENSE-EPI DTI was performed in volunteers using a standard DTI-EPI sequence with SENSE reduction factor of 3.0 and with either 128x128 or 128x256 acquisition matrices. Since the unfolding process can be ill-conditioned, principles of matrix regularization were employed. Moreover, to minimize deviations of measured coil sensitivities from the real B1-modulations, a coil sensitivity estimation algorithm based on calculus of variations was used.

Given the larger baseline SNR and the more distinctive coil sensitivity profiles, we anticipate that even higher reduction factors can be used at 3T and our new 7T magnet.

Self-Navigated Interleaved Variable Density Spiral Diffusion Tensor Imaging.

Chunlei Liu, Roland Bammer, M. Moseley

*Department of Radiology*

INTRODUCTION

With DTI maturing ever further, there is an increased demand for higher spatial resolution and diminished artifacts in diffusion-weighted imaging. This will provide better lesion delineation in acute ischemic stroke and high fidelity data for diffusion tensor–based tractography. Thus far, single-shot EPI is most frequently used for DTI because it has the advantage of rapid image acquisition and insensitivity to phase errors caused by subject motion. Despite the rapid image formation, however, T2*-decay impairs image resolution and off-resonant spins can cause deleterious image degradation. To speed up k-space traversal and, hence, minimize k-space velocity related artifacts, multi-shot sequences can be used; however, multi-shot methods generally suffer from view-to-view phase variations caused by motion in the presence of diffusion-encoding. One approach to correct for these variations is to acquire additional navigator data that can be used to resolve the phase error.

METHODS AND RESULTS

For navigated image reconstruction the data acquired on the interleaved spiral trajectories are first resampled onto a Cartesian grid of size 2N x 2N using a standard gridding algorithm with density precompensation. After the gridding step, phase correction is performed in image space for each interleaf. Here, the phase error is estimated from individual VD spiral interleaves using the fully sampled part at the center portion of the k-space. The low-resolution phase is then removed from the aliased high-resolution image. Similar to POCS reconstructions, this phase correction procedure is iterated several times until the relative error norm converges. We found already satisfying convergence after two iterations in our study. The image-based phase correction also corrects nonlinear phase that exists in the low resolution phase estimate. Since these k-space shifts are usually on a continuous scale they are easier to correct for using the low resolution navigator images. In other words, nonlinear phase correction in the image space is equivalent to convolving the k-space data with a kernel that is not an impulse function. As a result, the intensity of the k-space data can be modified after phase correction.
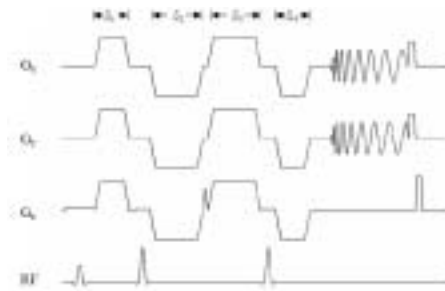
Variable density spiral diffusion-weighted TRSE sequence.
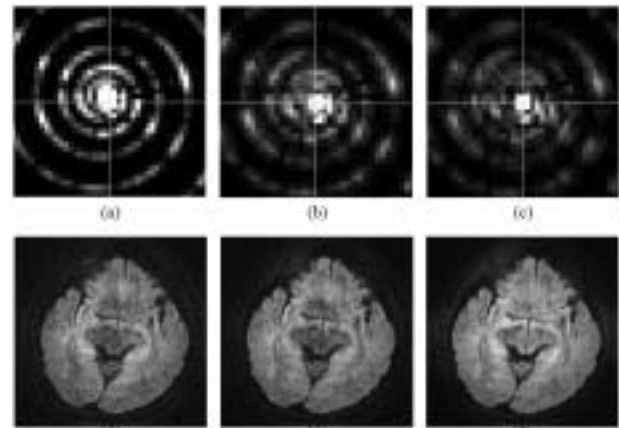
Comparison of the k-space data of one interleaf (a-c) and corresponding reconstructed images (d-f) before and after phase correction. Two white lines in (a-c) indicate the coordinate system. (a & d) Before correction. The k-space data is displaced due to motion during the diffusion sensitizing gradients and signal cancellation occurs in the image. (b & e) After one iteration of correction. (c & f) After two iterations of correction. The peak has been shifted back to the origin of the k-space and signal loss in the image space has been restored.

CONCLUSION

Compared to single-shot EPI, these images provide a great level of detail and a much better delineation of neuroanatomic structures. Unlike in single-shot diffusion weighted EPI, the signal averaging is performed in the k-space. One great advantage of the interleaved spiral readout is the remarkable reduction of geometrical distortions in the DW images. Due to the high bandwidth per pixel and the TRSE approach the sequence is virtually immune to image warping caused by eddy currents; a severe problem for single-shot EPI DWI.

The Effect of Gaussian Noise on Generalized Diffusion Tensor Imaging

Chunlei Liu[1, 2], Roland Bammer[2], Michael E. Moseley[2]

[1]*Dept of Electrical Engineering,* [2]*Lucas Center, Dept of Radiology, Stanford University*

INTRODUCTION

Recently a generalized diffusion tensor imaging (GDTI) method was introduced to characterize non-Gaussian diffusion (1,2). It has been shown that non-Gaussian properties of a diffusion process can be characterized by a series of generalized higher order diffusion tensors. In this report, the effect of Gaussian noise on the HOTs and the reconstructed PDF is investigated by using random walk simulation. Gaussian noise with two levels of standard deviation was added to the signal. The estimated HOTs and the reconstructed PDF are compared to that of the noiseless situation.

MATERIALS AND METHODS

Random walk simulation was performed on two phantoms: two perpendicularly crossing tubes (Phantom 1), and a Y-shaped tube (Phantom 2).

The particle motion is represented as a stochastic process, denoted by $\mathbf{x}(t)$. The process behaves in the interior of the phantoms like a standard Brownian motion. At the boundary $\mathbf{x}(t)$ reflects elastically. The particle motion is represented as a sequence of small random displacement: $\mathbf{x}(t+t) = \mathbf{x}(t) + \mathbf{x}$.

For a spin echo sequence, the simulated spin phase at TE for a single spin n is given by (3)

$$m(k) = m(0)\exp\left[\sum_{n=2}^{\infty} j^n D^{(n)}_{i_1 i_2 \cdots i_n} b^{(n)}_{i_1 i_2 \cdots i_n}\right], \qquad [1]$$

where $\mathbf{x}_n(t)$ is the position vector of spin n at time t. The generalized higher order diffusion tensors were estimated according to the following signal equation (1, 2),

$$\Phi_n = \gamma\mathbf{G}\cdot\left[\sum_{t=0}^{\delta}\mathbf{x}_n(t) - \sum_{t=\Delta}^{\delta+\Delta}\mathbf{x}_n(t)\right]\Delta t \qquad [2]$$

A total of 2.5×10^5 spin trajectories with uniformly distributed starting positions were simulated. The following parameters were used: t = 0.2 ms, = 30.0 ms, = 40.0 ms, TE = 80.0 ms, G_{max} = 40 mT/m, and D = 2.02 x 10^{-3} mm^2/s. Gaussian noise with different variance is added to the signal in order to assess the effect of noise. The PDF can be computed by using the Gram-Charlier series (1, 2).

RESULTS

Fig. 1 shows the reconstructed PDF skewness map and iso-surface map for both Phantoms. Here red indicates negative value and green represents positive value. Column (a) is the result in the absence of noise. Column (b) and (c) are results obtained under two different noise levels. The percentage error in the estimated tensor elements introduced by the additive Gaussian noise is given in table 1.

CONCLUSION

When the PDF is reconstructed by using the HOTs measured in the noisy situation, its quality will be degraded as illustrated in Fig. 1. Nevertheless, for a reasonably high SNR, for example, when SNR = 4.6 at b = 3126 s/mm^2, the PDF is not significantly distorted.

REFERENCES

Chunlei Liu, et al. Proceedings of the 12th Annual Meeting of ISMRM, 2003.
Chunlei Liu, et al. Israel J. Chem. 2003, 43: 145-154.
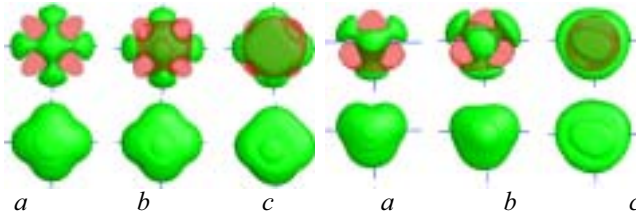Andrej Duh, et al. J Magn Reson 2001, 148:257-266.

Fig. 1 – *The three columns on the left are results for Phantom 1. The other three columns on the right are for Phantom 2. The first row is skewness map and the second row is PDF iso-surface. (a) noiseless; (b) SNR = 31.5 when b = 313 s/mm², and SNR = 4.6 when b = 3126 s/mm²; (c) SNR = 15.9 when b = 313 s/mm², and SNR = 2.4 when b = 3126 s/mm².*

% error		$D^{(2)}_{i_1 i_2}$	$D^{(3)}_{i_1 i_2 i_3}$	$D^{(4)}_{i_1 i_2 i_3 i_4}$
Phantom 1	SNR (b)	1.1%	N/A	2.2%
	SNR (c)	3.0%	N/A	6.9%
Phantom 2	SNR (b)	2.4%	12%	8.6%
	SNR (c)	4.1%	16%	12%

Table 1 – *Percentage of error of the measured HOT elements. For each tensor-order, the error is computed as the average of the absolute value of the errors over all the elements.*

Improvements for Pediatric MRI: The Optimized Pediatric DTI Exam.

Roland Bammer, Ron Ariagno, Allan White, Pat Barnes, Scott Atlas

Departments of Pediatrics and Radiology

INTRODUCTION

The DTI portion of an imaging protocol for scanning pre-term babies at term age comprises faster scanning of raw DTI data to minimize motion artifacts and reduce overall examination time. Using this new acquisition approach, a full set of raw DTI data that covers the entire brain takes now 1 min and 50 seconds, instead of 3 minutes and 25 seconds per average. Additional averages can be acquired by simply continuously repeating the DTI acquisition w/o the need of further preparation or prescanning. Although reliable quantitative tensor information can already be obtained from the initial tensor scan, these additional averages are paramount to a high quality estimation of the diffusion tensor elements, specifically the fractional anisotropy (FA). These separated acquisitions also allows us to identify examinations with motion better and reject perturbed acquisitions while still being able to restore the whole tensor information and minimizing the need to reject an entire DTI scan as technically inadequate. We have performed all our preliminary experiments with a quadrature birdcage coil that has been specifically built for neonates. The inner diameter of the coil is 16cm and provides restraining tapes and motion restricting head rest with sufficient padding for the baby.

METHODS AND RESULTS

Initial experience with the coil showed that the supine position is not the most wanted position because of aspiration problems. Upon our request, the company assured us to modify the coil so that we can place the baby in either left or right side position. Initial measurements revealed a SNR benefit factor of ~2.3 over the standard GE Head coil. This elevation in baseline SNR is of great importance and essentially reduces scan time to a fourth; thus, further minimizing the likelihood of motion compared to a regular head coil. We capitalized from the increased SNR by improving both in-plane and trough-plane resolution.

Fig. 1: This photo shows the neonate head coil that was used for the new high-resolution DTI The inner diameter (birdcage end ring) was 16cm. A standard size soda can was placed in the coil for better assessment of the dimensions of the coil
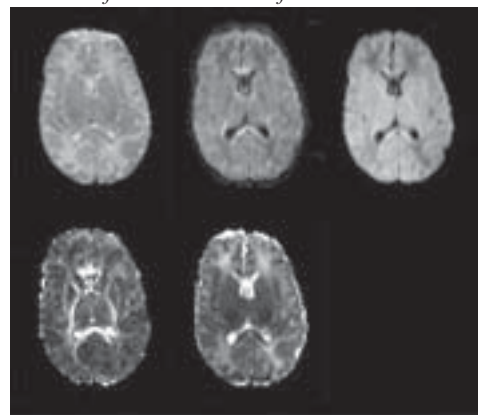

Fig. 2: Improved high-resolution DTI using the Neonate birdcage coil. By reducing the FOV to 18cm and the slice thickness to 2.5 mm, the image quality could be further improved. Despite the decrease in voxel size, there is still an SNR advantage of 1.44 over the regular protocol with this kind of scanning approach.

CONCLUSION

DTI offers valuable information about the structural integrity of white matter in pre-term babies. Although ssshEPI DTI is amongst the fastest scanning methods in our portfolio, reliable tensor computation is challenged by involuntary patient motion, hesitation to use sedative drugs to prevent kids from moving, and the small size of the babies. All of these issues required a rethinking of the conventional DTI scanning. Currently, our approach is to scan the kids as fast as possible to reduce the likelihood of motion. Here, dedicated coils and an optimized pulse sequence lead to a significant quality improvement.

Diffusion Weighted Imaging in the Assessment of Renal Dysfunction

Lawrence C. Chow, Ruby Chang, Roland Bammer

Department of Radiology

INTRODUCTION

While diffusion-weighted imaging (DWI) has been predominantly applied in the CNS, recent studies have begun to explore the feasibility of DWI MRI in the abdomen and its use in detecting and characterizing abdominal abnormalities. Until recently, attempts at abdominal DWI have been thwarted by the presence of physiologic motion including respiration, peristalsis and blood flow, which are orders of magnitude greater in amplitude than diffusional motion and can easily overwhelm the effects of diffusion. Newer, more powerful gradients yielding reductions in diffusion-encoding and EPI readout times, have allowed breath-held full-organ coverage DWI in the abdomen with improved image quality. In this study, the relationship between ADC values and renal failure was evaluated by comparing renal ADC values with serum creatinine levels in patients with normal and abnormal renal function.

MATERIALS AND METHODS

Breath-held abdominal DWI was performed in 15 patients referred for abdominal MRI. All MR scans were performed on 1.5T, commercially available MRI units (Signa CV/I and TwinSpeed, GE Medical Systems, Waukesha, WI) fitted with high performance gradients (40 mT/m, trise = 268ms) and the body coil. All procedures performed were approved by the institutional review board at Stanford University. SE-DW-sshEPI sequences were performed: FOV = 30 x 30 cm to 40 x 40 cm, TR of 2600– 3200 ms, TE of 45.3 – 55.1 ms, matrix 128 x 128, bandwidth +125 kHz. Tetrahedral diffusion encoding was utilized to allow for the determination of directionally invariant D (trace) at minimum TE for a given b-value. The b-value was 300-s/mm2 (2 averages). Values of D obtained from ROIs drawn within the renal parenchyma on D maps were retrospectively correlated with serum creatinine levels (Cr), findings from conventional T1 and T2-weighted SE and FSE images, contrast-enhanced 3D fast spoiled-gradient echo MRI images and clinical information.

RESULTS

6 out of 15 patients had abnormally elevated (>1.6 mg/dL) Cr levels. These patients demonstrated significantly decreased D values for the kidneys, when compared with renal D values obtained in patients with normal Cr<1.6 mg/dL (*Fig. 1*) (p=0.0005) using a two-tailed t-test with a linear correlation between D and Cr (r=-.741, p<0.001). Image quality was deemed excellent in all cases and in no case did susceptibility or other artifact obscure the kidneys (*Fig.* 2). Two patients with borderline elevation of Cr (1.5 and 1.7) had unilateral renal disease (right renal obstruction and left renal artery stenosis, respectively). Renal D values were markedly asymmetric in these patients with a 23-24% reduction in D in
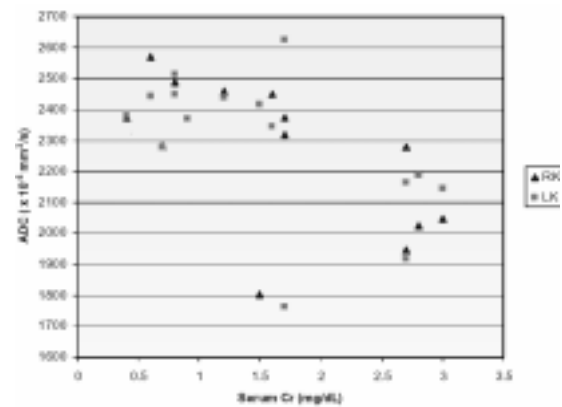

Figure 1. Scatterplot showing the relationship between serum creatinine levels and renal D. Patients with elevated serum creatinine had statistically significantly lower renal Ds. Two patients had unilateral renal disease, which was reflected as markedly decreased Ds on the affected side despite only borderline elevation of Cr and normal contralateral renal Ds.
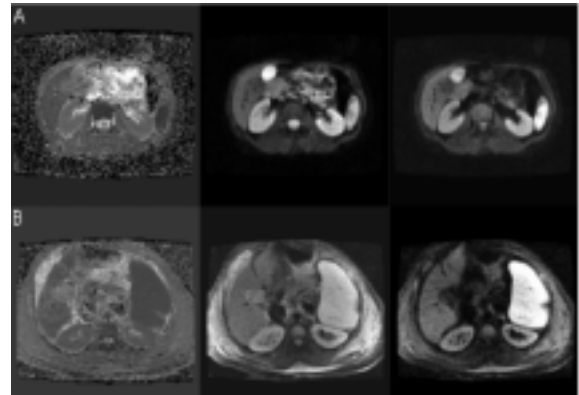

Figure 2. D map, b=0 reference images, and b=300 DWI scans in patients with normal (A) and elevated (B) Cr.

the affected kidney and normal Ds in the contralateral kidney. In patients with unilateral disease, Ds of the affected kidneys were even lower than those of kidneys with bilateral disease. Excluding the patients with unilateral disease, the average Ds obtained in the renal parenchyma of patients with normal Cr was $2437\pm111 \times 10^{-6}$mm^2/s. Average Ds obtained in the renal parenchyma of patients with elevated Cr was $2171\pm214 \times 10^{-6}$mm^2/s. Differences in D between the right and left kidneys ranged from 3×10^{-6} to 266.5×10^{-6} with a mean of $100.9\pm90 \times 10^{-6}$, excluding the two patients with unilateral disease and one patient who had only one kidney. D values for the 8 patients with Cr<1.6 and symmetric kidneys correlated well with normal values established in prior work.

CONCLUSION

There is a significant decrease in renal D in patients with renal insufficiency and a linear correlation between renal D and Cr in patients without unilateral disease. There was a striking difference in Ds between normal and compromised kidneys in patients with unilateral renal disease. This technique has great potential for the evaluation of patients with renal disease, particularly those with unilateral disease such as renal artery stenosis and congenital hydronephrosis which may not be reflected in cruder measures of renal function such as Cr.

Sensitivity Encoding for Diffusion-Weighted Breast MRI

Julia Po, Roland Bammer, Rebecca Rakow-Penner, Bruce Daniel

Department of Radiology

Purpose

To evaluate the potential of sensitivity encoding (SENSE) parallel imaging to reduce artifacts and improve image quality in diffusion-weighted (DW) breast MRI.

Materials and Methods

A comparative evaluation of DW breast MRI was performed in six subjects. Subjects were imaged with a 1.5-T magnet using a 4-element phased-array breast surface coil, two elements per breast. DW echo-planar imaging was performed with and without SENSE. Diffusion gradients in six directions were applied with maximum b value of 500 s/mm2. Aside from SENSE, the twice-refocused approach was taken to reduce geometric distortions due to eddy currents. The field of view was 24 cm, slice thickness 8 mm with 0 gap, TE 73.1 ms, and TR 3000 ms. Overall scan time was 2 min. DW scan magnitudes were averaged over all six directions to produce isotropic DWI scans. Maps of the apparent diffusion coefficient (ADC) were calculated from the averaged isotropic images for each slice.

Quality assessment was done by presenting the isotropic DWI scans and the ADC maps with and without SENSE in a randomized fashion to three blinded radiologists. The radiologists judged the images when produced with and without SENSE in terms of image clarity and presence of artifacts.

Results

In total 48 images were judged. Image quality was significantly improved with SENSE (p=0.041): Isotropic DWI scans were superior 17/36 times, while images made without SENSE were superior 7/36 times. Image quality of ADC maps with SENSE was also significantly improved over those without (p=0.003): ADC maps with SENSE data were superior 14/36 times, while maps without SENSE were selected 2/36 times.

Conclusion

Overall image quality in DW breast MRI was superior with SENSE. The improvement in image quality arises from less blurring from T2* decay because of shorter EPI readout, less misregistration from eddy currents, and fewer susceptibility artifacts in the inframammary crease and nipple region. Residual artifacts due to SENSE processing could be removed by using an improved off-line reconstruction. There were no artifacts due to SENSE processing. The inherent loss of SNR with SENSE can be compensated for by adding additional averages, without significantly increasing scan time.

Review of Parallel Imaging of the Abdomen

Daniel J. A. Margolis, Lawrence Chow, Roland Bammer

Department of Radiology

Introduction

Parallel imaging is a relatively new technique for rapid magnetic resonance imaging. Using sensitivity information from a multi-channel phased-array system, MRI sequences can be performed in half the time or faster, by acquiring spatial data from multiple coils simultaneously which is subsequently "unfolded" using the sensitivity data. Great benefits for abdominal imaging can be anticipated from parallel imaging, specifically in techniques with high baseline SNR, such as CE-MRA, 3D MRI, and 3T scanning. Moreover, parallel MRI makes more studies possible which would have been otherwise not feasible. This comes at the cost of some reduction in signal-to-noise, but with numerous advantages.

Materials and Methods

Experimental subjects were evaluated using a 1.5 Tesla MRI (GE Medical Systems) with parallel imaging capabilities. Conventional and parallelized sequences were performed through the abdomen including fast spin echo, single-shot fast spin echo, fast gradient echo in- and out-of-phase, and FAME (Fast Acquisition with Multiphase Efgre3D) using a

combination of free breathing, incomplete breath-holding, and complete breath-holding. Images were reviewed by two experienced radiologists (LC, DM) for overall image quality, the degree of motion and reconstruction artifact, image noise, and overall diagnostic adequacy. Informed consent was obtained from each subject in accordance with the investigational review board.

Results

There was no significant difference in image quality or motion artifact between the parallel and conventional data during the free-breathing and complete breath-hold sequences with experimental subjects. However, there was significant motion artifact in the conventional but not the
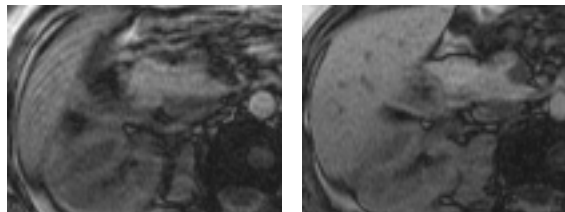

The first image acquired with a 20-second scan, but only a 15-second breath hold has motion artifact. The second image acquired in 11 seconds with parallel imaging but otherwise identical parameters has no motion artifact and little overall increased noise.

parallel sequences during incomplete breath-holding. Likewise, significant motion artifact degraded image quality on conventional but not otherwise identical parallel sequences on many clinical cases.

Also, although parallel reconstruction artifacts were evident with the first iteration of the software, these did not significantly degrade diagnostic quality, and the only sequences judged clearly inferior to their conventionally-acquired counterparts were the thin-section T2-weighted coronal images used in MRCP which had lower SNR that compromised MIP creation.

CONCLUSION

Parallel imaging, by virtue of collecting the same volume of data with half or fewer phase-encodes, reduces the time required for a specific sequence. This can be used to reduce overall scan time with resultant reduction in motion artifact, increase spatial resolution within the same scan time, or add additional parameters such as fat suppression which would otherwise make scan times too long for a single breath-hold. In addition, parallel imaging has the added advantages of a shorter echo-train resulting in less T2-blurring and spatial distortion and susceptibility with echo-planar sequences. Indeed, the parallel technique can be applied to almost any pulse sequence. The sensitivity map, when acquired with the quadrature body coil as well as the individual phased array coils, also allows for correction of spatial intensity heterogeneity correction. This has application for static as well as functional dynamic imaging of the abdominal organs.
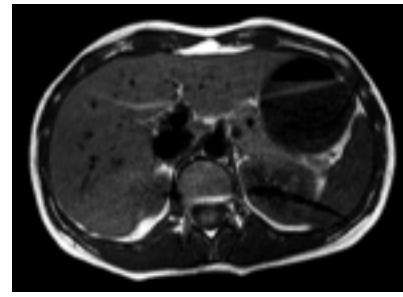
Residual Aliasing artifacts from incomplete SENSE reconstruction. These artifacts are most apparent if bright tissue signal (e.g. fat in T1w) is close to the receive coils and the corresponding coil sensitivity estimation is wrong for this voxel (i.e. due to motion, chemical or geometric shift or too large voxel sizes).

Parallel imaging is not without its drawbacks. There is a necessary increase in noise, and the additional noise is non-uniform and structured, giving rise to unfamiliar artifacts. Moreover, incomplete unfolding may occur if coil sensitivity information is used for image reconstruction that differs from the true encoding coil sensitivity of the receive coil. These kind of new reconstruction artifacts have to be recognized by radiologist when interpreting a case.

REFERENCES

1. Margolis DJA, Bammer R, Chow LC. *Parallel Imaging of the Abdomen*, Topics in Magnetic Resonance Imaging, *publication pending*.

Interleaved Dual-Echo Spiral-out-Spiral-In DSC Imaging with Generalized SENSE.

Roland Bammer, Michael Moseley

Lucas Center, Department of Radiology

INTRODUCTION

Dynamic susceptibility contrast (DSC)-based PWI is frequently challenged by technical difficulties that are associated with single-shot EPI: Besides the strong geometric distortions and poor resolution of EPI scans, there are considerable problems in determining accurately an arterial input function (AIF). The latter is mandatory for deconvolving the tissue response signal in PWI. Using single-shot EPI, large feeding vessels, such as the internal carotid arteries (ICA) or branches of the major cerebral arteries, are frequently difficult to depict and can be contaminated by tissue partial volume averaging. This is mainly due to (i) strong T2*-induced blurring, (ii) susceptibility gradients emanating from the sinuses and the auditory canals adjacent to the brain, and (iii) the high concentration of contrast material during bolus passage that causes clipping of the bolus maximum due to the lack of dynamic range and low SNR. We have minimized these problems by using a dual-echo acquisition in combination with a multi-shot sensitivity-encoded variable-density interleaved spiral imaging approach.

MATERIALS AND METHODS

A multi-slice DSC-PWI pulse sequence was implemented with interleaved variable-density spiral readout gradients where the center of k-space was sampled with sufficient density for estimation of the coil sensitivities and for phase-navigation. For high scan efficiency, a spiral-out/in trajectory was used. This design gives a minimum TE for the early echo (TE_1=6ms) (spiral-out) while producing enough T2*-effect in the feeding arteries without severe geometric distortions or saturation effects. The spiral-in trajectory guarantees that the image formation is finished at the late echo time (TE_2=55ms), providing the most effective readout while still sufficiently sensitive to detect the subtle contrast passage in deep white matter. The dual-echo spiral sequence was implemented using the following parameters: FOV=22cm, 5mm/1mm section thickness/gap, 20 slices, $TR/TE_1/TE_2$/a=500ms/6ms/55ms/45°, recon matrix 128 x 128, bandwidth ±100 kHz, four interleaves, dynamic scan resolution = 2 s, and 80 time points. To reduce geometric distortions from off-resonant spins, a SENSE reduction factor of 2.0 was introduced along the radial dimension of the trajectory. An iterative generalized SENSE (GSENSE) algorithm was used to reconstruct the undersampled spiral trajectories. Coil sensitivity information was retrieved from the center portion of each interleave.
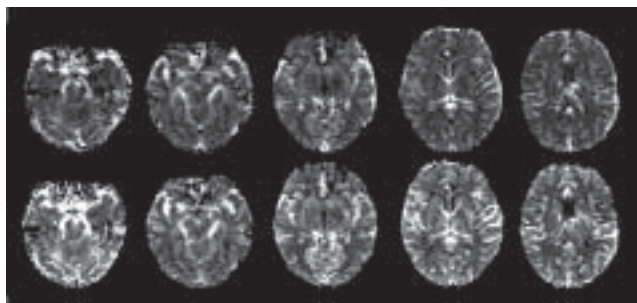
67

Figure 1 – Unfiltered maps of cerebral blood volume (CBV, top row) and cerebral blood flow (CBF, bottom row) computed from the dual-echo spiral DSC scans. The artifact reduction is clearly apparent.

Results

The variable density approach uses increased sampling near to the k-space origin, which enables phase navigation and auto-calibration (GSENSE) capabilities; this minimizes motion sensitivity of the sequence and the SENSE reconstruction process. When compared to conventional single-shot EPI, the interleaved spiral approach combined with GSENSE allowed a significant reduction of distortions from off-resonant spins. Specifically, the regions adjacent to sinuses and the auditory canals were well preserved. The large feeding vessels can be clearly delineated and the typical T2*-"blooming" effect during bolus passage can be avoided. In contrast to single-shot EPI, where pixel shifts (of voxels containing large amounts of Gd) along the phase-encode direction due to the low bandwidth per pixel can be quite significant and may lead to perturbed AIF shapes, the interleaved spiral approach is much more immune against such distortions. Due to the short readouts and the fact that the acquisition is finished almost immediately after the second echo, the sequence is very efficient and allows full brain coverage.

Conclusion

The interleaved dual-echo spiral-out-spiral-in approach combined with GSENSE provides significantly improved image quality, better spatial resolution, and, hence, better vessel conspicuity. These improvements allow one to perform more reliable measurements of the AIF, while still being sufficiently sensitive to small T2*-changes in white matter.

An Automated Method for Generating the Arterial Input Function in Perfusion Weighted MR Imaging: Validation in Stroke Patients

Michael Mlynash[1], Irina Eyngorn[1], Roland Bammer[3], Michael Moseley[3], David Tong[1,3]

[1]Stanford Stroke Center, [2]Department of Neurology and Neurological Sciences, and [3]Department of Radiology

Introduction

The choice of arterial input function (AIF) can have a profound effect on the blood flow maps generated by perfusion weighted MR imaging (PWI). However, current analytical techniques use an AIF subjectively chosen by the investigator. This can lead to substantial variation in the AIFs used with resultant variability in the blood flow maps derived. Automation of this process could eliminate operator dependency, increase consistency, and accelerate PWI analysis. In this study, we created an automated AIF identification program (auto-AIF) and validated its performance against conventional manual methods.

Materials and Methods

We compared the auto-AIF against manually derived AIFs from multi-slice PWI images of 16 stroke patients. Time to peak, curve width, curve height, and voxel location determined by both techniques were then compared. A smaller time to peak was considered as an earlier bolus arrival time combined with faster local flow dynamic; a narrower AIF curve - less corrupted by dispersion of the bolus from the site of injection to the site of measurement; a higher peak - to indicate less partial-volume averaging. The time to maximum of the tissue residue function (Tmax) was also computed on a per pixel basis for each AIF. Spatial patterns of Tmax maps were compared by computing Pearson correlation coefficients between maps generated by each method.

Results

The anatomical locations of the optimized AIF in all cases were considered to be appropriate and always within the middle cerebral artery territory. All automatically derived AIF parameters, including bolus time to peak, width, and height were consistently superior to manually derived ones. Reproducibility of the auto-AIF based Tmax maps was excellent (r=1.0). Paired Tmax maps from both techniques correlated well (r=0.8). Time to identify the-AIF was significantly shorter using the auto-AIF method compared with the manual technique (mean difference 81 sec., 95% CI: 54-108 sec.).

Conclusion

An automated program that identifies the AIF is feasible and can create reliably reproducible and accurate Tmax maps. Automation of this process could reduce PWI analysis time, increase consistency, and may allow for the more effective use of PWI in acute stroke evaluation. Supported by NIH grants 2R01NS34866, 1R01EB002771, 1R01NS35959, and 1R01NS39325.

References

1. Kucharczyk J, Mintorovitch J, Asgari H, Moseley M. Diffusion/perfusion MR imaging of acute cerebral ischemia. Magn Reson Med. 1991; 19:311–315.
2. Warach S, Li W, Ronthal M, Edelman RR. Acute cerebral

ischemia: evaluation with dynamic contrast-enhanced MR imaging and MR angiography. Radiology. 1992; 182:41–47.

3. Ostergaard L, Weisskoff RM, Chesler DA, Gyldensted C, Rosen BR. High resolution measurement of cerebral blood flow using intravascular tracer bolus passages. Parts I and II: Mathematical approach and statistical analysis. Magn Reson Med. 1996; 36:715–736.

4. Wirestam R, Andersson L, Ostergaard L, et al. Assessment of regional cerebral blood flow by dynamic susceptibility contrast MRI using different deconvolution techniques. Magn Reson Med. 2000; 43:691–700.

5. Calamante F, Gadian DG, Connelly A. Quantification of Perfusion Using Bolus Tracking Magnetic Resonance Imaging in Stroke: Assumptions, Limitations, and Potential Implications for Clinical Use. Stroke. 2002; 33:1146-1151.

6. Carroll TJ, Rowley HA, Haughton VM. Automatic Calculation of the Arterial Input Function for Cerebral Perfusion Imaging with MR Imaging. Radiology. 2003; 227:593–600.

7. Morris ED, VanMeter JW, Tasciyan TA, Zeffiro TA. Automated Determination of the Arterial Input Function for Quantitative MR Perfusion Analysis. ISMRM 8th Scientific Meeting. Denver, Colorado, USA, April 3-7 2000.

8. Reishofer G, Bammer R, Moseley ME, Stollberger R. Automatic Arterial Input Function Detection from Dynamic Contrast Enhanced MRI Data. ISMRM 11th Scientific Meeting. Toronto, Ontario, Canada, July 10-16 2003.

9. Alsop DC, Wedmid A, Schlaug G. Defining a Local Input Function for Perfusion Quantification with Bolus Contrast MRI. ISMRM 10th Scientific Meeting. Honolulu, Hawaii, USA, May 18-24 2002.

Quantitation of Perfusion from Bolus Tracking MRI. The Stanford PWI Toolboxes

Roland Bammer[1], M. Moseley[1], G. Albers[2], D. Tong[2], M. Lansberg[2], J. Alger[3], C. Kidwell[3], V. Thijs[2]

Departments of [1]Radiology (Lucas Center) and [2]Neurology (Stroke Center), [3]UCLA Stroke Center

INTRODUCTION

We built a robust and flexible toolbox to allow us to explore new approaches and algorithms to map CBV, MTT, and CBF from arterial-input function selections. Within a voxel the amount of injected tracer that inputs into a feeding artery (AIF) and the amount of absorbed tracer in the tissue (C_{tissue}) are related by a mathematical convolution. There are several new approaches and algorithms to map CBV, MTT, and CBF from arterial-input function selections. These fall into two broad deconvolution methods that are based either in the time-domain or the Fourier domain.

METHODS

We built an IDL-based software package ("MRPac") that allows us to simulate and analyze the reliability and accuracy of various deconvolution approaches and to evaluate these methods in the setting of acute stroke patients. Into this rapid prototyping perfusion mapping package we have incorporated variations of each of the time-domain and Fourier domain approaches. This tool allows us to objectively compare and evaluate existing and new methods as well as their performance over a wide range of parameters, such as SNR, CBV, MTT, and CBF. In addition, these routines can be applied to *in-vivo* data in concert with either single-AIF, multiple-AIF, or automated (AutoAIF) techniques. The incorporation of local input functions and a comparative evaluation with global AIF methods is currently underway.

In designing MRPac for acute stroke, we have added in-house approaches to a comprehensive PWI analysis environment. Specifically, for the deconvolution in the **time domain** we
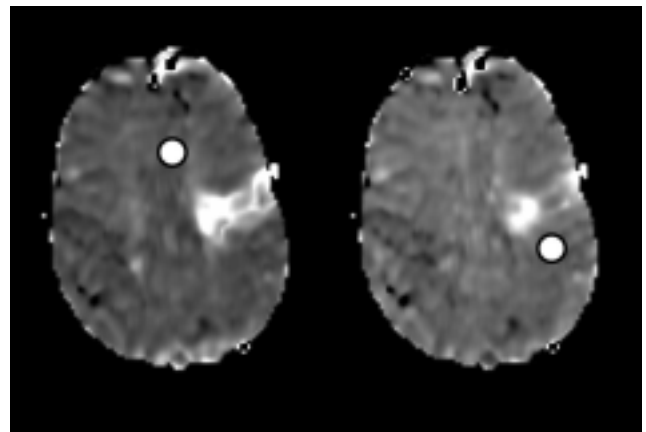

Fig. 1 - Effect of AIF Placement in the TSVD Method. Two MTT maps are shown with differing AIF sources. Notice that the size of the lesion appears much smaller in the right image than it does at the left in this TSVD deconvolution. If there is a time delay between arterial delivery and local tissue AIF as in this patient, placement of the AIF can cause large variations in the measured MTT and CBF values.
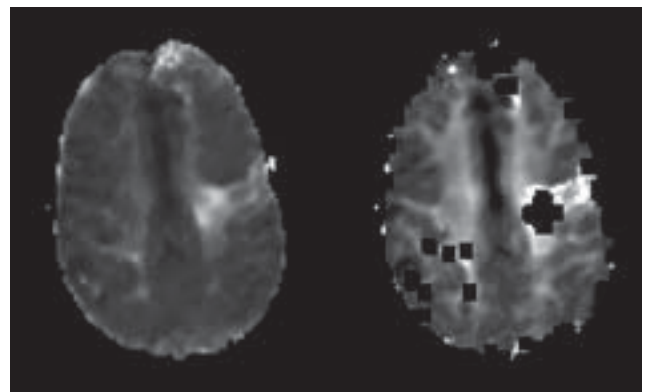

Fig. 2 – MTT maps obtain with circular deconvolution (left) and TSVD deconvolution of gamma-variate fits (right). The latter showed impressive arrival time differences between gray and white matter but suffered from severe quality loss in the stroke area and structures with little dynamic T2* effect.

have written a variation of the truncated SVD regularization (TSVD) with an improvement in the numeric integration part (Newton-Cote), circular deconvolution to address shift issues, and with adjustable threshold levels from the singular values. In addition, Tikhonov regularization and L-curve regularization optimization has been included. For deconvolution in the **Fourier domain** three approaches have been developed: first, the approach from Smith *et al*. adding gamma-variate fits of the measured *AIF* and C_{tissue} data to circumvent noise; second, analytic FT's or FFT's of the gamma-variate fits, and thirdly, from the FT'ed original data using an optimal filter (such as a Wiener Filter) to suppress high-frequency spectral components which otherwise would lead to oscillations in the solution for $R(t)$.

RESULTS

Results from this study supported existing evidence that the placement of the AIF strongly affects the outcome of size and magnitude of hemodynamically abnormal areas. Without corrective measures the tissue residue function $R(t)$ obtained with TSVD strongly depends on time delays between the C_{tissue} and *AIF* (Fig. 1). Both circular TSVD and Fourier-based deconvolution using a Wiener filter perform much better.

Using gamma-variate fits the influence of noise in the numeric deconvolution can be reduced dramatically. Moreover, influences from numeric instability can be reduced using an analytic expression for the deconvolution of these parametrized functions. However, fitting errors and breakdown of the gamma-variate model (such as in the stroke area) can cause severe problems.

In summary, reliable selection of the AID is important. Both circular TSVD and Fourier-based deconvolution using a Wiener filter were of comparable quality, which is also supported by theoretical considerations.

High Resolution MR Imaging of Paraspinal Muscle Injury Following Minimally Invasive and Conventional Open Posterolateral Lumbar Fusion.

Kathryn Stevens[1], Todd Alamin[2], Eugene Carragee[2], Garry Gold[1], Amy Forro[3], Roland Bammer[1]

*Department of [1]Radiology and [2]Surgery, Stanford; [3]Endius Inc., Plainville, MA*Introduction

Instrumented spinal fusions are performed for a variety of reasons in the lumbar spine. However, the outcome is not always satisfactory, and may result in persistent pain and disability. One of the reasons for the so-called "failed back syndrome" is postulated to be the dissection and retraction of the paraspinal muscles needed to perform a standard posterior instrumented spinal fusion. However, conventional MR scans of the lumbar spine show only limited detail of the paraspinal muscles, and there are very few MRI papers focusing specifically on the paraspinal muscles in the literature.

MATERIALS AND METHODS

Patients with a recent minimally invasive or open single level posterolateral spinal fusion were recruited at a single institution by 2 spinal surgeons. Eight patients (6 females, 2 males) with a mean age of 51.5 years were enrolled in the study. The average duration of symptoms prior to fusion was 7.4 years (range 1-20 yrs). Four had an endoscopic Atavi fusion and 4 had conventional open spinal fusion. The average operative procedure times for the Atavi and Open groups were 251 minutes (range 198-285 mins) and 221 minutes (range 140-262 mins) respectively. MRI scans were performed approximately 6 months post operatively (range 4-10 months). All subjects were imaged in a supine position using a 1.5 T Signa LX (General Electric, Milwaukee, WI) with a phased-array spine coil. Axial multi-slice T1-weighted spin echo (SE) and axial flow-compensated T2-weighted fast
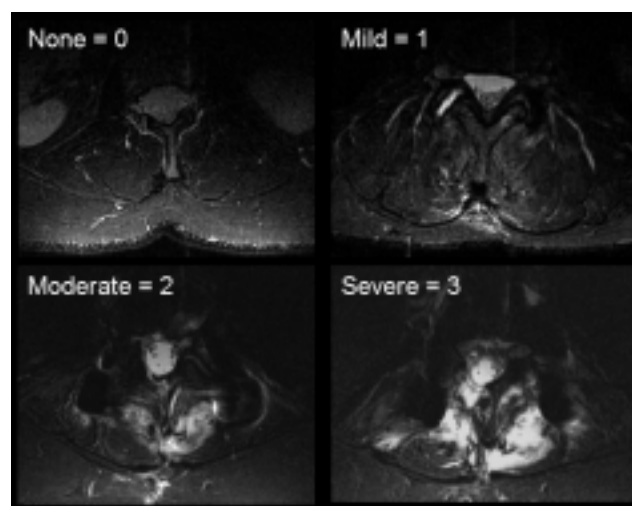

Figure 1: Edema scoring.

spin echo (FSE) sequences were used for high-resolution structural imaging. In order to differentiate between edema and fatty atrophy, a combination of axial STIR T2-weighted FSE and fat-saturated T2-weighted FSE sequences were used. An oblique coronal T2 FSE sequence was also performed for better assessment of overall extent of injury.

Edema and atrophy within the multifidus muscle was scored on a scale of 0 to 3 with 0 = none, 1= mild, 2= moderate, and 3 =severe (Fig.1). For quantitative T2-mapping, an axial dual spin echo sequence was performed, with multiple axial slices at the levels of the lumbar intervertebral discs. The T2 relaxation times were calculated on a per pixel basis using a monoexponential fit. A region of interest measuring a minimum of 10 mm^2 was placed on the individual bundles of the multifidus muscles bilaterally. In order to compare the 2 surgical groups, the average T2 relaxation time was also calculated in the multifidus muscles at the level of the fusion.
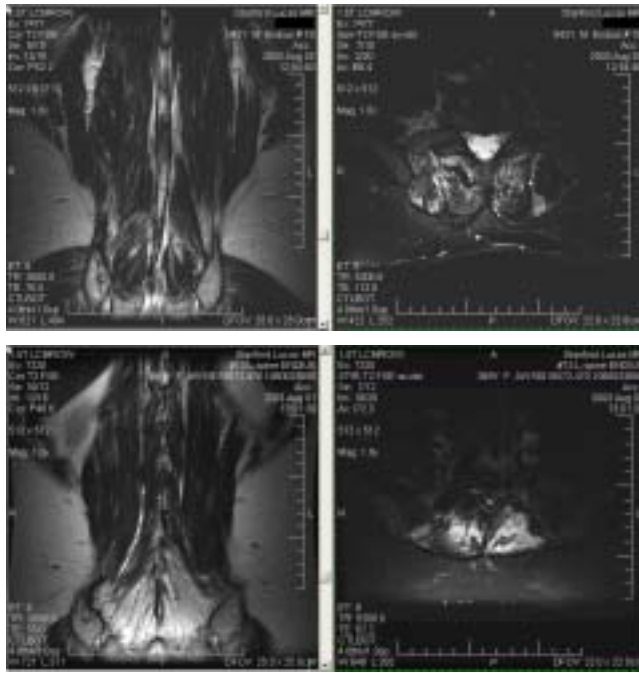
Figure 2: (Top) Open patient #13 with L4/5 fusion, 6 months post-surgery. Coronal T2w-FSE (left) and axial T2w-STIR (right). (Bottom) Atavi patient #18 with L3/4 fusion, 5 months post surgery. Coronal T2w-FSE (left) and axial T2w-STIR (right).

RESULTS

There was a striking difference in muscle edema between the Atavi and Open spinal groups (Figs 2 - 4). There was also a marked difference between the 2 groups in the T2 measurements measured in the multifidus muscle at the level of the fusion. The mean T2 relaxation time was 98 ms in the patients having open spinal fusion, compared with a mean of 47 ms in the minimally invasive fusion patients, which was statistically significant (p < 0.04). The T2 measurements correlated well with the visual estimation of muscle edema

CONCLUSION

The MRI protocol we developed in this study resulted in remarkable anatomical and functional detail of the paraspinal musculature. The preliminary results appear to indicate that less muscle damage occurs after the endoscopic spinal fusion when compared to the conventional open procedure. Larger prospective controlled studies are currently underway to confirm these results, evaluate the correlation between muscle damage and clinical outcome, and substantiate the long-term benefits of minimally invasive spinal surgery.

Cerebro-Cerebellar Circuitry of Verbal Working Memory

S.H. Annabel Chen[2] and John E. Desmond[1, 2]

Neuroscience Program[1] and Department of Radiology[2], Stanford University, Stanford, CA, USA

INTRODUCTION

Anatomical, neuropsychological, and neuroimaging studies have indicated cerebellar involvement in cognitive processing. Using a Sternberg working memory task with event-related fMRI (Chen & Desmond, 2003), we showed the left parietal region, which has been implicated in phonological storage, and the right inferior cerebellum, which is anatomically linked to parietal regions via cortico-pontine and pontocerebellar projections, to be activated in tandem during the maintenance phase of the task. In the present event-related fMRI study, we hypothesized that if this left-parietal/right inferior cerebellar circuit were involved in phonological storage, then tasks that challenge the phonological store would be expected to increase activation in these associated regions.

Figure 1: Participants performed 4 sessions of the Sternberg Verbal Working Memory Task and each session lasted about 11 minutes. Each session had 48 trials: with equal number of easy (3-letters) and hard (6-letters), and similar (B-C-D-G-P-T-V) and dissimilar (F-H-J-Q-R-S-W) trials.

METHODS AND MATERIALS

17 right-handed, healthy young adults (10 males), age 19-28 with 13-19 years of education, were presented a two alternative forced choice Sternberg paradigm in the Lucas 3T scanner.

RESULTS

Behavioral data showed Load and Phonological Similarity revealed only a significant (p < .0001) main effect for Load for both accuracy (High Load = 82.78%, Low Load = 90.56%) and reaction time (High Load = 856ms, Low Load = 779ms). For accuracy the Load x Similarity interaction approached significance (p = .14). The conjunction of functional activation for task phase with the high vs low load contrast replicated previous results from our laboratory (Chen & Desmond, 2003).

Figure 2: The Similar>dissimilar (red) emphasizes phonological processing, and dissimilar>similar (blue) emphasizes visual code processing.

CONCLUSIONS

The **similar > dissimilar** (**red** in fig 2) activabilateral cerebellar activations observed during retrieval reflect additional contributions of the cerebellum in responding to the probe under conditions of phonological similarity.

The **dissimilar > similar activations** (**blue** in fig 2) observed mainly observed during encoding and retrieval phases of the task, suggest increased processing related to translating the orthographic form of the letters into an articulatory trajectory during the dissimilar condition.

REFERENCE:

1. Chen SA & Desmond JE (2003). Cerebral-cerebellar circuitry of verbal working memory. **Society for Neuroscience Abstracts**.

ACKNOWLEDGMENTS

"Sparse Temporal Sampling" Improves Power in Auditory Experiments - An fMRI Study Comparing Event-related and Sparse Designs

Nadine Gaab[1,] John D.E.Gabrieli[1], Gary H. Glover[2]

[1] Department of Psychology [2] Department of Radiology

INTRODUCTION

Previous studies have discussed the influence of the scanner background noise (SBN) on auditory experiments using fMRI. The SBN may lead to differences in attention, may produce auditory activation itself and may suppress signal throughout the entire brain.

MATERIALS AND METHODS

Using a verbal auditory task and 3 experimental designs with varying TRs we examined the influence of the experimental design and degree of SBN on the functional anatomy as well as signal intensity within auditory and extratemporal areas. Subjects listened to a series of four one-syllable words (duration =4s) and had to decide whether two of the presented words were the same. This was contrasted with a no-stimulus control condition. The exp. designs had varying TRs but a constant duration of 17 min.: (A) a previously reported sparse temporal sampling technique (STsamp; Gaab et al. 2003) acquiring only 1 set of slices following each of the stimulations with a TR =16s and jittered delay times over 7s; (B) a clustered volume acquisition (CVA) design (TR=6s; 160 volumes), where stimuli were presented during the silent periods in between acquisitions; and (C) an event related design with continuous scanning (ERcont) using the stimulation design of STsamp but a TR =2s (516 volumes).
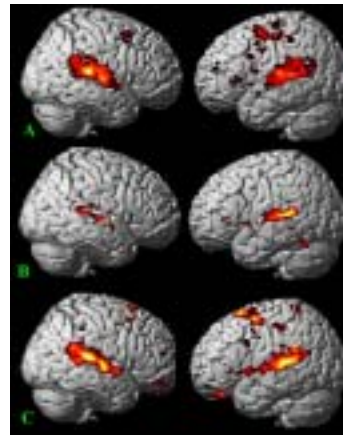
Results for the three experimental conditions (A) STsamp (B) CVA and (C) ERcont. All results are corrected for multiple comparisons (FDR) and are shown in radiological convention.

RESULTS

Preliminary results show increased signal within temporal and extratemporal areas for the STsamp technique in comparison to ERcont and especially CVA, although only 65 volumes were acquired during the 17 min. It was found that the functional anatomy of the verbal task differed between the 3 experimental designs resulting in e.g. varying degrees of hemispheric lateralization.

CONCLUSION

The full recovery of the stimulus-induced hrf signal and lack of signal suppression from SBN during our STsamp design makes this technique a powerful approach for conducting auditory experiments using fMRI.

REFERENCES

1.Gaab N, Gaser C, Zaehle T; Jancke L, Schlaug G. Functional anatomy of pitch memory-an fMRI study with sparse temporal sampling. Neuroimage 2003; 4:1417-26.

Examining the Neural Nases of Amusement and Sadness: A Comparison of Block Contrast and Dynamic Emotion Intensity Idiographic Regressor Approaches

Philippe R. Goldin, Cendri A.C. Hutcherson, Kevin N. Ochsner, Gary H. Glover, John D.E. Gabrieli, James J. Gross

Department of Psychology

Neuroimaging studies have made substantial progress in elucidating the neural bases of emotion. However, no study to date has taken into account the idiosyncratic, time-varying nature of emotional experience. In the present study, we employed functional magnetic resonance imaging to examine the neural bases of two common emotions: amusement and sadness using both (a) a conventional stimulus-based block contrast approach, and (b) a novel subject-specific, continuous, dynamic emotion intensity rating idiographic regressor approach. Thirteen women twice viewed a set of nine 2-minute amusing, sad, or neutral film clips. On first viewing, participants just watched the films. On second viewing, they made continuous dynamic ratings of amusement and sadness intensity experienced during the first film viewing. Whole-block and idiographic regressor approaches revealed in common that sad films were associated with activations in medial prefrontal cortex (PFC), precuneus, ventral occipital cortex, amygdala and thalamus, and that amusing films were associated predominantly with activations in left PFC and temporal lobes. While the idiographic regressor detected regions similarly identified by the block approach during sad films, it revealed more subcortical and medial PFC areas of activation than the block approach for amusing films. These results suggest a relationship between emotion-specific temporal dynamics and the sensitivity of different data analytic methods for identifying distinct cortical and subcortical regions of activation. These findings shed light on the neural bases of emotion, and suggest a new approach for examining the dynamic aspects of emotional responses that differ so dramatically across individuals.

Attentional Modulation of Neural Response to Emotional Films

C. A. Hutcherson*, P.R. Goldin, K.N Ochsner, E.R. Robertson, J. D. Gabrieli, J.J. Gross.

Department of Psychology

Research has shown that attention fundamentally influences what is observed and experienced. Furthermore, when attention is directed to an evaluation of internal emotional experience, this shift in focus may enhance subjective awareness of and reactivity to emotional stimuli. However, the interaction of the attentional and affective neural systems that support internally focused emotion evaluation is not well understood. To examine attentional modulation of emotion, we used fMRI to measure neural responses in 24 female participants while viewing a series of 2-minute sad, amusing and neutral films. Continuous psychophysiological indices (heart rate, skin conductance and respiration) were also collected. In the first viewing, 12 of the participants simply watched the films. The other 12 participants made continuous ratings of concurrent emotion experience during the initial film viewing. In order to assess initial emotional response for the subjects who did not make ratings in the first viewing, participants made continuous dynamic retrospective ratings of amusement and sadness experienced during the initial film presentation. These ratings were used to assess initial emotional response. Self-reported ratings indicated that the films successfully induced emotional responding. The attentional manipulation modulated neural activation for emotional compared to neutral film clips in insula, anterior and posterior cingulate, and superior frontal cortex, regions previously shown to be involved in emotion response. Additionally, functional connectivity analyses revealed different profiles of covariance in these regions under the varying attentional and emotional contexts. These results suggest that attention can reliably modulate the interaction between various components of an emotional response.

Exploring Emotion Coherence: Autonomic, Experiential, and Neural Responses During Amusement and Sadness

P. R. Goldin, C. A. Hutcherson, K. N. Ochsner, E. R. Robertson, J. D. Gabrieli, & J. J. Gross*.

Psychology Department

A central tenet of emotion theory is that emotions impose coherence across autonomic, experiential, and neural response systems. However, previous studies that have probed the neural bases of emotion have not assessed autonomic, experiential, and neural responses with a temporal resolution that makes it possible to discern the dynamic relations among these three systems as the emotion unfolds over time. In order to assess the degree of coherence across multiple indices of a temporally evolving emotional response, 24 participants were imaged while watching a series of 2-minute sad, amusing and neutral film clips. During film viewing, continuous measures of physiological arousal (skin conductance, heart rate and respiration) and dynamic subjective report of emotion experience were collected for all participants. Neural signal correlating with autonomic responses and the self-reported experience of sadness and amusement were found in regions in cingulate and superior frontal cortices, parietal cortex, as well as the insula and cerebellum, areas known to be sensitive both to emotional experience and autonomic changes. The level of coherence across neural signal, psychophysiological measures and emotion experience varied as a function both of the type and intensity of emotion evoked within each film. These findings further our understanding of how the interaction of psychophysiologic, behavioral and neural indices vary across time to construct the dynamic emotional responses that we experience in daily life.

Visual noise reduces the BOLD response to words in occipito-temporal sulcus

M. Ben-Shachar, R. F. Dougherty, G. K. Deutsch, and B. A. Wandell

Psychology Department, Stanford University

INTRODUCTION

There is a left ventral occipital temporal region that shows higher fMRI BOLD signal to words than to checkerboard patterns (Cohen et al. 2000, 2003). We identified this region in individual brains and measured the effect of increasing visual noise in the word stimuli. Noise sensitivity measurements provide a quantitative index of the ability to extract visual information about words in individual brains and may be a useful tool in studying reading development.

MATERIALS AND METHODS

Word stimuli (4-letter nouns) were presented in varying amounts of visual noise. The stimuli were mixtures of a high contrast word and a noise pattern created by randomizing the phase spectrum of the same word stimulus. In experimental trials, the weighted sum of signal and noise was parametrically controlled while subjects judged the color of a fixation cross in the center of the word stimuli. Thus, reading the word stimuli was incidental. Experimental conditions were presented in 12s blocks (6 words per block), alternating with fixation blocks. Measurements spanned twenty-six 3x3x3 mm axial slices (GE, 3T, spiral acquisition) covering occipital temporal cortex. Left ROIs were defined functionally by contrasting the word conditions against fixation and anatomically based on sulcal landmarks (Cohen et al., 2003).

RESULTS

BOLD activation in the left occipital temporal sulcus decreased with increasing noise, though residual activation was elicited by the pure noise stimulus. These effects were reliably present in individual subjects. The phenomenon was also present in right ventral occipital temporal cortex, but the anatomical variability of the right regions made it difficult to establish homology. Response decrease to added noise was not found in early visual areas (V1/2/3).

CONCLUSION

Responses decreased to added noise in ventral occipital temporal regions in both hemispheres of individual subjects, but not early visual areas. Preliminary data suggest that similar response functions may be present in 8-11y children.

Figure 1. Ventral surface of the brain showing activation for all word conditions (arrow points to left occipito-temporal ROI).

Figure 2. Average time course in the occipito-temporal ROI, showing activation increase with word visibility.

REFERENCES

1. Cohen, L., Lehericy, S. Chochon, et al., (2002). Language-specific tuning of visual cortex? Functional properties of the visual word form area. Brain, 125, 5, 1054-69.
2. Cohen, L., Martinaud, Lemer, C., et al., (2003). Visual word recognition in the left and right hemispheres: anatomical and functional correlates of peripheral alexias. Cerebral Cortex, 13, 1313-1333.

Human Ventral Occipitotemporal Cortex Contains Several Visual Field Maps With Differential Stimulus Selectivity

A A Brewer1, J Liu2, A R Wade4, B A Wandell1,3

1Neuroscience, 2 Applied Physics, 3Psychology, Stanford University, 4Smith-Kettlewell Eye Research Institute, San Francisco

INTRODUCTION

Human ventral occipitotemporal cortex (VOT) is important for many visual recognition processes, but the visual field maps in this region have not been determined precisely[1-4]. These maps occupy a fairly small cortical surface area, so that even modern fMRI techniques obtain only 1-2 dozen spatial samples/map. Thus, it is important to find additional sources of data, such as stimulus selectivity, that support the presence of a visual area. Here, we describe coordinated measurements of color, object and face responsivity coupled with visual field maps in VOT.

MATERIALS AND METHODS

We used fMRI and phase-encoded methods to measure retinotopic maps in VOT. The rotating wedge and expanding ring stimuli consisted of 3˚ and 16˚ black and white, drifting radial checkerboard patterns. The resulting temporal phase-encoded signals were transferred onto flattened views of visual cortex and analyzed with an automated, atlas-fitting algorithm. Color, face, and object-selective regions were found with localizer scans and compared to the visual field maps.

RESULTS

We identify two visual areas anterior to V3v (Fig. 1). Each area represents a hemifield heavily weighted towards central vision and spans about 3.5 x 2.5 cm2. One area (hV4) falls along the posterior fusiform gyrus, adjacent to V3v, and shares a foveal representation with the confluent V1/2/3 central field maps. The second area (VO-1) falls along the fusiform gyrus and collateral sulcus. This area is anterior to hV4 and has a distinct foveal representation with a detailed eccentricity map expanding medially. The two areas show distinct differential selectivity for faces, objects and/or color (Table 1).
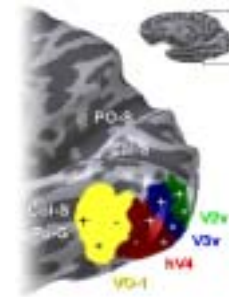
Fig. 1. Visual Areas in VOT. The positions of hV4, VO-1 and the established visual areas V2v/V3v as defined by 3 deg radius traveling wave stimuli are shown on the posterior part of a right hemisphere. Foveal representations (*), upper visual field maps (+), and lower visual field maps (-) are marked. The brain has been inflated for visualization. Dark gray depicts gyri, and light gray depicts sulci. (PO-S, parietal-occipital sulcus; Cal-S, calcarine sulcus; Col-S, collateral sulcus; Fu-G, fusiform gyrus.)

Area	Color	Faces	Objects
hV4, upper vf	+	-	-
hV4, lower vf	+	-	-
VO-1	+	-	+
Lateral to hV4	-	+	-
Anterior to VO-1	-	-	+
Lateral to VO-1	-	+	-

Table 1. Differential Stimulus Selectivity in VOT. Stimulus selectivity was measured in 3 mm radius disks placed at corresponding eccentricities in each of the listed regions. Significant selectivity for a stimulus type is indicated with a '+'.

CONCLUSION

Human VOT contains at least two hemifield representations with differential stimulus selectivity. This organization differs from current models of visual field maps beyond V3/VP in macaque.

REFERENCES

1. Wade, A.R., et al., Philos Trans R Soc Lond B Biol Sci, 2002. 357(1424): p. 963-73.
2. Bartels, A. and S. Zeki, Eur J Neurosci, 2000. 12(1): p. 172-93.
3. Hadjikhani, N., et al., Nature Neuroscience, 1998. 1(3): p. 235 - 241.
4. Malach, R., et al., Proc Natl Acad Sci U S A, 1995. 92(18): p. 8135-9.

White Matter Pathways Related to Reading

R.F. Dougherty[1], G.K. Deutsch[1], R. Bammer[2], A. Schwartzman[1], B.A. Wandell[1]

*[1]Psychology, [2]Radiology*

INTRODUCTION

There is a correlation between reading performance and white matter structure in a left temporoparietal region measured with diffusion tensor imaging (DTI). Here we analyze the major neural pathways coursing through this region.

MATERIALS AND METHODS

We used whole-brain DTI to measure the fractional anisotropy (FA) in normal and poor readers aged 7 to 13 (n=14). Groups were matched in age, SES and nonverbal IQ. We identified a region of interest (ROI) of about 200 mm3 in which the group FA values differed significantly (Deutsch in press; Klingberg 2000). We then used fiber tracing (Mori 2002) to identify the major pathways passing through this ROI.

RESULTS

We show that the ROI with reduced FA in poor readers is primarily within the posterior limb of the corona radiata (pCR), but overlaps the superior longitudinal fasciculus (SLF) and abuts projections from the posterior corpus callosum (pCC). The ROI position with respect to these pathways varies between the two groups- it is well within the pCR for normal readers but overlaps the SLF in poor readers. This pathway displacement can explain the observed FA differences.
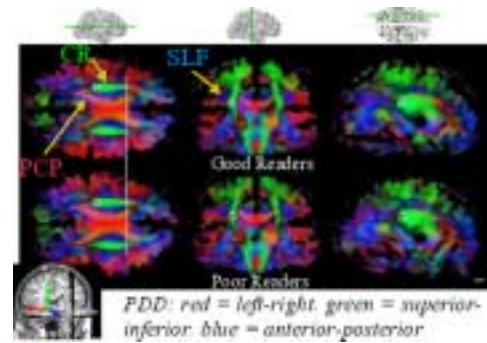
Major white matter structures are displaced in poor readers.

CONCLUSION

Two major left temporoparietal white matter pathways (pCR and SLF) are related to the acquisition of skilled reading. Our results suggest that the observed FA differences reflect a broad organizational difference between good and poor readers in these pathways (and perhaps the abutting pCC) rather than focal dysfunction within a pathway. However, the functional role of these pathways with respect to reading remains to be seen.

REFERENCES

1. Deutsch et al. (in press). Correlations between white matter microstructure and reading performance in children. Cortex.
2. Klingberg et al. (2000). Microstructure of temporal-parietal white matter as a basis for reading ability: Evidence from diffusion tensor magnetic resonance imaging. Neuron, 25:493-500.
3. Mori et al. (2002). Imaging cortical association tracts in the human brain using diffusion-tensor-based axonal tracking. MRM, 47:215-223.

What do you expect? – FMRI of Expected Utility

Brian Knutson[1], Matthew Kaufman[1], Richard Peterson[1], Jonathan Taylor[2], Gary Glover[3]

[1]Department of Psychology, [2]Department of Statistics, [3]Department of Radiology

INTRODUCTION

The concept of Expected Utility (EU) plays a central role in both economic and psychological theory, especially concerning appetitive behavior. EU can be calculated as a product of the scaled magnitude and probability of receipt of future gains or losses. In this study, we independently manipulated these variables within the context of a monetary incentive delay (MID) task where participants anticipated, made responses for, and received varying amounts of monetary gains and losses as they were scanned with FMRI (1, 2).

Hypothesizing that the mesial prefrontal cortex (MPFC), subcortical ventral striatum (VS), and ventral tegmental area (VTA) of the midbrain played essential roles in the calculation of EU, we localized brain areas in which activation correlated with a computational model of EU. We then examined which components of EU most potently modulated activity in those regions of interest.

MATERIALS AND METHODS

Probabilistic Monetary Incentive Delay Task: 11 healthy volunteers (7 women, right handed) participated. During each of 288 consecutive 8 second trials, subjects saw one of eighteen shapes (cue; 2000 ms), then waited a variable delay period (anticipation; 2000–2500 ms), and responded with a button press to the rapid presentation of a solid white square (target; 160-310 ms). Subsequent feedback then notified subjects whether they had won or lost money on that trial as well as their cumulative total (outcome; 2000 ms). Each of the eighteen shapes included information about how much money could be gained or lost on that trial, as well as the probability of success (20%, 50%, or 80%, manipulated by adaptive timing algorithm that varied the target presentation
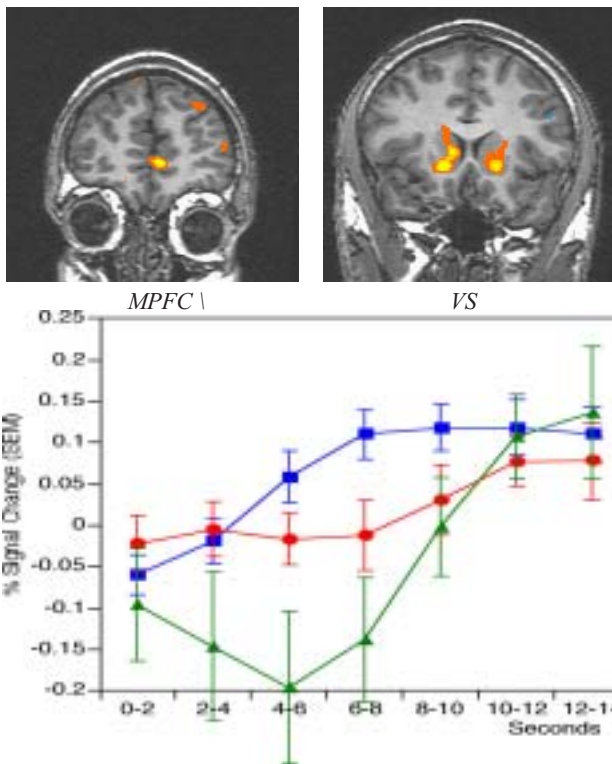
Top: Brain areas where activation correlated with a calculation of Expected Utility. Bottom: Averaged time series % signal change in the MPFC of trials where participants gained $5. The third time point corresponds to the anticipatory phase; green, red and blue are 20%, 50%, and 80% probability trials, respectively.

duration according to the participant's performance). Each trial type was presented 16 times in an individually randomized order.

Scan parameters: 24 4-mm-thick slices (in-plane resolution 3.75 X 3.75 mm, no gap) using a 1.5-T GE Signa; functional scans acquired every 2 sec with a T2*-sensitive in-/out- spiral pulse sequence.

RESULTS

As predicted, EU was significantly correlated with activation foci in the VTA, bilateral VS, and left MPFC (p<.00001, uncorrected. Anticipatory activation (6 sec lag) was submitted to 2 (valence) X 3 (magnitude) X 3 (probability) ANOVAs. VTA activation showed a main effect of magnitude (F(2,20)=10.78, p<.001). VS activation showed a main effect of magnitude (F(2,20)=17.67, p<.001), qualified by an interactions of magnitude by probability (F(4,40)=3.79, p<.01) and valence by magnitude by probability (F(4,40)=3.68, p<.01). MPFC activation yielded a main effect of probability only (F(2,12)=4.54, p<.05).

CONCLUSION

The present findings suggest that areas of the MPFC, VS, and VTA are prominently involved in the calculation of EU. VTA activation increased during anticipation of larger incentives, consistent with calculation of the magnitude component of EU only. VS activation increased when subjects anticipated improbable rather than probable large gains, consistent with computation of the valence and magnitude terms of EU. MPFC activation was higher during anticipation of probable versus improbable outcomes, consistent with the computation of the probability term of EU.

REFERENCES

1. Knutson, B., Adams, C. S., Fong, G. W. & Hommer, D. (2001). Anticipation of monetary reward selectively recruits nucleus accumbens. *Journal of Neuroscience*, 21:RC159.
2. Knutson, B., Fong, G. W., Bennett, S. M., Adams, C. S., & Hommer, D. (2003). A region of mesial prefrontal cortex tracks monetarily rewarding outcomes: Characterization with rapid event-related FMRI. *NeuroImage*, 18, 263-272.

---

fMRI Investigation of Size Representation across Human Visual Cortex

David Andresen, Kalanit Grill-Spector

Department of Psychology

INTRODUCTION

 One of the most fundamental aspects of human cognition is our ability to recognize familiar objects regardless of the particular viewing conditions. For example, one can recognize an object as a coffee cup nearly instantaneously and with little perceived effort whether it is very close and takes up much of our visual field, or far away and takes up very little of our visual field. However, the manner by which the brain represents and processes visual objects to afford such invariant object perception is not understood. In this study, we examined how invariance to object size develops across visual cortex, and whether the sensitivity to object size is a static or dynamic property of a visual area.

MATERIALS AND METHODS

We examined the representations underlying invariant object recognition using functional magnetic resonance imaging techniques in a 3.0 Tesla GE scanner. First, the boundaries of early retinotopic areas were defined using standard techniques. Next, object-selective areas were defined as those regions that responded higher to intact images of objects compared to scrambled versions of those objects. All analyses were performed on regions selected using these analyses.

Eight participants completed in ten runs in which they viewed centrally-presented line drawings of animals and cars in four sizes, extending into 3˚, 6˚, 9˚, and 12˚ of eccentricity. In

addition, participants were presented new objects from the same categories, scrambled images, and fixation-only trials that served as baseline.

Participants performed two tasks while viewing the images that directed their attention to certain aspects of the stimuli. During the Size Task, participants categorized each image as small, medium, or large. During the Object Task, participants categorized each image as an animal, vehicle, or neither (scrambled and fixation-only).

RESULTS

Figure 1 shows the average response across all subjects from regions that preferred large (12˚ eccentricity) images within each of four visual areas. Importantly, visual representations become more size invariant from early visual cortex (e.g., V1) to more high-level visual areas (e.g., fusiform gyrus).

Figure 2 shows the average response in the lateral occipital (LO) region, which is activates selectively to objects. Importantly, LO is more invariant to image size when subjects were performing the object task compared to when they were performing the size task.

CONCLUSION

Size invariance develops incrementally across the hierarchy of visual areas, but even high-level visual areas retain some degree of size-preference. Furthermore, size invariance is not a static property of a visual area, but can be modulated by task demands, becoming more or less invariant as needed.
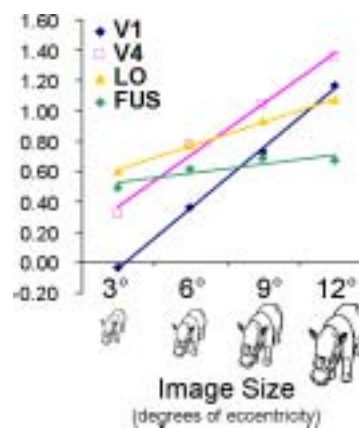
Figure 1. Selectivity to four sizes across four visual areas from cortical regions that preferred the largest size of image. (LO: lateral occipital, FUS: fusiform gyrus).
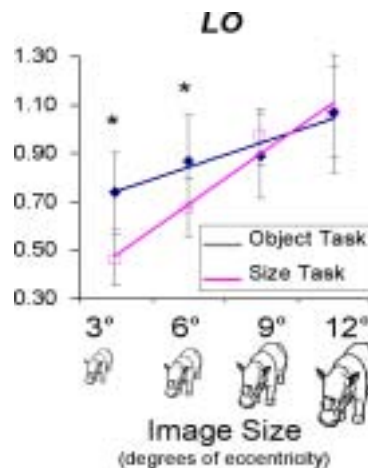
Figure 2. Size selectivity in LO to four sizes of image for the Object and Size tasks.

Object and Shape Processing in the Human Lateral Occipital Complex

Joakim Vinberg, Kalanit Grill-Spector, Sven Heinrich

Department of Psychology, Stanford University

INTRODUCTION

The human lateral occipital complex (LOC) has been characterized as involved in object perception (Malach, 1995, Grill-Spector et al. 2000), shape perception (Kourtzi & Kanwisher, 2001) and also in processing salient regions (Stanley & Rubin, 2003), despite informational differences in these types of stimuli. The differences in characterization may result from the usage of different experimental paradigms. Here we asked whether the LOC processes objects, shapes or salient surfaces?

MATERIALS AND METHODS

To answer this question we designed stimuli in which we could examine a perceptual dissociation between surfaces, shapes and objects. Conditions included: (a) an object above a surface; (b) a surface with a shaped aperture; (c) gratings; (d) two surfaces (without contours) and (e) random noise. Importantly, the shape contour was identical for the object and aperture conditions. Subjects participated in two ex-

periments with these conditions. In the first experiment, stimuli were created via random dot stereograms. Subjects were asked to fixate and decide if the fixation was on the front or back surface. In the second experiment, stimuli were created from moving dots. Subjects were asked to fixate and determine if the motion was to the left or to the right. We concurrently measured brain activation in 5 subjects (3T GE scanner) and performance.

RESULTS

We found in all subjects that the both the aperture condition and the object condition elicited a significantly higher response in LOC than either gratings, two surfaces or random noise, for both the motion and stereo experiments. In addition, we observed a hierarchical processing of shape along the ventral stream: the posterior regions (i.e. LO) responded to both objects and shaped apertures, whereas the anterior regions along the fusiform responded more strongly to objects than shaped apertures. These results provide critical insights for the role of subregions of the LOC for object and shape processing.

References

1. Grill-Spector K, Kushnir T, Hendler T, Malach R. Cue-invariant activation in object-related areas of the human occipital lobe. Neuron. 1998 Jul;21(1):191-202.

2. Kourtzi Z, Kanwisher N. Representation of perceived object shape by the human lateral occipital complex. Science. 2001 Aug 24;293(5534):1506-9.
3. Malach R, Reppas JB, Benson RR, Kwong KK, Jiang H, Kennedy WA, Ledden PJ, Brady TJ, Rosen BR, Tootell RB. Object-related activity revealed by functional magnetic resonance imaging in human occipital cortex. Proc Natl Acad Sci U S A. 1995 Aug 29;92(18):8135-9.
4. Stanley DA, Rubin N. fMRI activation in response to illusory contours and salient regions in the human lateral occipital complex. Neuron. 2003 Jan 23;37(2):323-31.

The Processing of Object Distance by Dorsal Stream Visual Areas

Janelle Weaver, Kalanit Grill-Spector

Department of Psychology

Introduction

To perceive an object's distance, we must reconstruct the third dimension from 2D retinal information. Many visual areas have been mapped out in 2D retinotopic space in humans, but relatively little is known about how 3D information is represented in the brain. Here we examined brain regions involved in computing object distance based on monocular depth cues (e.g., linear perspective, texture gradients) provided by the background scene.

Materials and Methods

In two studies, we acquired fMRI data from eight subjects with the 3T GE Signa scanner and the posthead transmit/receive surface coil. In the first study subjects viewed images of a railroad track scene that varied in two ways: 1) scene type: upright, inverted or scrambled, and 2) presence or absence of a novel object placed either above or below fixation within the scene. In alternating 40s blocks, subjects indicated either an object's distance compared to a fixation cross (near, far, same) or its 2D location (above, below, same), with the same images being presented in event-related fashion for both tasks. In an unrestricted search, regions of interest (ROIs) were selected based on a higher response during object distance judgments compared to 2D location judgments.

In the second study we used fMR-Adaptation[1] to assess the sensitivity of these ROIs to changes in either object position or perceived distance. Here subjects judged object distance for pairs of images. The second image of each trial was either identical to the first or different in one of these ways: 1) object 2D location changed (perceived distance changed); 2) background scene inverted (perceived distance changed); 3) both object 2D location changed and background scene inverted (no change in perceived distance).

Results

When contrasting brain activation during distance versus 2D location judgments, two consistent brain regions were evident: a region in the posterior middle temporal gyrus, just lateral to the transverse occipital sulcus (TOS); and a region at the superior parieto-occipital sulcus (POS). During the distance judgment task only, these ROIs responded more robustly to intact scenes containing objects compared to scenes without objects. Furthermore, the TOS and POS recovered from adaptation (i.e., were sensitive) to changes in object location and perceived distance.

Conclusion

The results indicate that the TOS and POS process scenes with objects to determine object position within a scene, forming a network of dorsal stream areas involved in computing object distance based on monocular depth cues from a background scene.

References

1. Grill-Spector, K, and Malach, R. (2001) fMR-adaptation: a tool for studying the functional properties of human cortical neurons. Acta Psychol (Amst) 107(1-3): 293-321.

Typical Brain Development: Neurofunctional Studies

Allan L. Reiss, Dean Mobbs, Michael Greicius, Vinod Menon, Tony Yang, Ian Gotlib, Sonia Crottaz-Herbette.

Stanford Psychiatry Neuroimaging Laboratory, Department of Psychiatry and Behavioral Science

INTRODUCTION

The Stanford Psychiatry Neuroimaging Laboratory (SPNL, http://www.spnl.stanford.edu/) is dedicated to structural and functional imaging of brain structure and function in typically developing individuals. This report summarizes three functional MRI studies conducted at the Lucas Center that illustrate how fMRI is an invaluable technology in understanding the neural functioning of the normal brain.

MATERIALS AND METHODS

Images in these studies were acquired at the Lucas Center on a 1.5-T GE Signa scanner with Echospeed gradients using a standard whole head coil.

RESULTS

HUMOR MODULATES BRAIN MESOLIMBIC REWARD CENTERS

Humor plays an essential role in psychological, social, and somatic functioning, and its most fundamental feature is reward; to date, however, researchers have failed to demonstrate the cortical correlates of the reward system. In this 3-T functional MRI study1, healthy volunteers viewed funny and non-funny cartoons during scans. As shown in Figure 1, humor engaged a network of subcortical regions including the nucleus accumbens, a key component of the mesolimbic dopaminergic reward system—the same reward circuits in the brain activated by rewards. We found that the degree of humor intensity correlated positively with BOLD signal intensity in these regions. This finding could help to diagnose the early stages of depression, or show whether antidepressants are taking effect, during which people's appreciation of humor is altered.
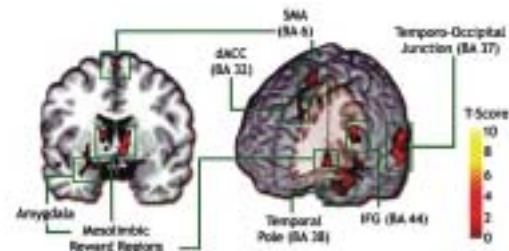
Fig 1. Functional Topographical Map of Funny Minus Nonfunny Cartoons. Activation clusters were superimposed on Talairach normalized brain using MRIcro. Significant clusters of activation were determined using the joint expected probability distribution with height and extent threshold corrected at the whole-brain level. Results revealed activation in the left temporo-occipital junction (Brodmann area [BA] 37), inferior frontal gyrus (BA 44/45) extending ventrally to include a subcluster in the temporal pole (BA 38), and supplementary motor area (BA 6/32) extending to the pre-SMA and dorsal anterior cingulate (dACC). A subcortical cluster also was observed encompassing the ventral striatum/NAcc, anterior thalamus, ventral tegmental area (VTA), hypothalamus, and amygdala

AMYGDALAR ACTIVATION ASSOCIATED WITH HAPPY FACIAL EXPRESSIONS

The amygdala has been extensively studied for its role in emotions and responses to facial expressions. Although the examination of the amygdalar response to the perception of different facial expressions is fairly limited in adults, it is virtually nonexistent in adolescents. In this study2, 12 healthy adolescent males and females underwent 3-T fMRI imaging while viewing pictures of happy, sad, and neutral facial expressions. Happy faces produced significant bilateral amygdalar activation when compared with neutral faces (p < .05). Sad faces relative to neutral did not produce significant amygdalar activation (Figure 2). These results extend the role of the amygdala in adolescents to include the recognition of happy facial expressions. This study demonstrates the feasibility of using happy facial expressions to noninvasively study amygdalar function in adolescents and establish a baseline against which the amygdalar response to emotional stimuli in several psychiatric conditions may be compared.
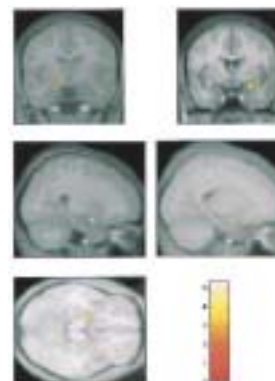

Fig. 2. Top: coronal views showing left and right amygdalar activation to happy faces compared with neutral. Middle: sagittal views of the same left and right amygdalar activations shown in the coronal images. Bottom: axial view showing the same bilateral amygdalar activations as seen in the coronal and sagittal slices. The color bar indicates the Z score of the activations seen in these images.

NEURAL BASES FOR VERBAL WORKING MEMORY

The neural bases of verbal (nonspatial) working memory (VWM) have been examined using visual stimuli, but few studies have investigated the neural bases of VWM using auditory stimuli, and fewer have explored modality differences in VWM. In this study3, we examined similarities and differences between visual VWM and auditory VWM in which stimuli were presented visually and aurally in a 1-back and 2-back test of working memory. Performance levels were similar in the two modalities and there was extensive overlap of activation bilaterally in the dorsolateral and ventrolateral prefrontal cortex (DLPFC and VLPFC), intra-parietal sulcus, supramarginal gyrus, and the basal ganglia. However, a statistical comparison revealed significant modality differences: the left posterior parietal cortex, primarily along the intraparietal sulcus, showed greater responses during vis-VWM whereas the left dorsolateral prefrontal cortex showed greater responses during aud-VWM (Figure 3). No such differences were observed in the right hemisphere. Other modality differences in VWM were also observed, but they were associated with relative decreases in activation. In particular, we detected bilateral suppression
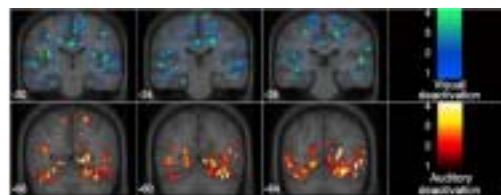
Fig 3. The superior and middle temporal gyri showed significant "deactivation" during visual WM, that is, greater activation during the control compared to the WM condition.
Bottom: The lingual, fusiform and inferior temporal gyri showed significant "deactivation" during auditory WM.

of the superior and middle temporal (auditory) cortex during vis-VWM, and of the occipital (visual) cortex during aud-VWM, thus suggesting that cross-modal inhibitory processes may help to provide preferential access to high-order heteromodal association areas. These findings suggest that although similar prefrontal and parietal regions are involved in aud-VWM and vis-VWM, there are important modality differences in the way neural signals are generated, processed, and routed during VWM.

CONCLUSION

These results illustrate the importance in functional MRI technology in understanding the neural underpinnings of brain functioning in humor, emotion, and working memory of typically developing individuals. This research provides a more complete picture of neural functioning in typically developing individuals that allows us to understand the deficits of brain functioning found in individuals with neurogenetic and neuropsychiatric disorders.

REFERENCES

1. Mobbs, D., Greicius, M.D., Abdel-Azim, E., Menon, V. & Reiss, A. L. Humor modulates the mesolimbic reward centers. Neuron, 40, 1041 - 1048, (2003).
2. Yang TT, Menon V, Reid AJ, Gotlib IH, Reiss AL: Amygdalar activation associated with happy facial expressions in adolescents: A 3T functional MRI study. Journal of the American Academy of Child and Adolescent Psychiatry 42(8):979-985, 2003.
3. Crottaz-Herbette S, Anagnoson R, Menon V. Modality effects in verbal working memory: differential prefrontal and parietal responses to auditory and visual stimuli. Neuroimage 21:340-351, 2004.

Atypical Brain Development : Neuroanatomical and Neurofunctional Studies

Allan L. Reiss, Vinod Menon, Kirk Neely, Jenny Dyer-Friedman, Mark Eckert, Shelli Kessler, Hower Kwon, Dean Mobbs, Amy Garrett, Jackie Leroux, Asya Karchemskiy, Melody Chang.

Stanford Psychiatry Neuroimaging Laboratory, Department of Psychiatry and Behavioral Science

INTRODUCTION

The Stanford Psychiatry Neuroimaging Laboratory (SPNL, http://www.spnl.stanford.edu/) is dedicated to structural and functional imaging of brain structure and function in individuals with neurogenetic and neuropsychiatric disorders. In this report, we summarize several recent structural and functional MRI studies conducted at the Lucas Center in individuals with Turner Syndrome, Williams syndrome, and fragile X syndrome that illustrate how magnetic resonance imaging has helped bridge our understanding between gene-brain-behavior relationships in atypical development,

MATERIALS AND METHODS

Images in these studies were acquired at the Lucas Center: for structural studies, images were acquired on the 1.5T GE scanner and analyzed using BrainImage (SPNL) and SPM99 software; functional studies were performed on the 3T GE-signa scanner.

RESULTS

TURNER SYNDROME (TS)

Turner syndrome (TS), a neurogenetic–neurodevelopmental disorder characterized by the absence of one X chromosome in a phenotypic female, is frequently associated with visuospatial impairments. We investigated1 the neural mechanisms underlying deficits in spatial orientation processing in TS. A total of 13 subjects with TS and 13 age-matched typically developing controls underwent neuropsychological assessments and were scanned using functional MRI while they performed easy and difficult versions of a judgment of line orientation (JLO) task. Controls and subjects with TS activated parietal-occipital regions involved in spatial orientation during the JLO task. However, activation was significantly less in the TS group. Control subjects responded to increased task difficulty by recruiting executive frontal areas whereas subjects with TS did not activate frontal brain regions to meet increased task demands. Subjects with TS
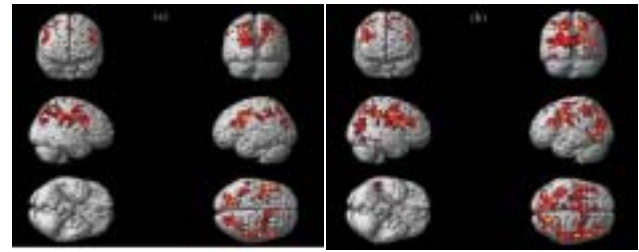
Fig 1. Between-group comparisons indicated that, during the difficult JLO task, (a) controls demonstrated significantly greater activation in IFG, SFG, MFG, cingulate, motor and sensory cortices, IPL, SPL, MOG and SOG; and (b) These differences remained even after covarying for JLO performance.

demonstrate activation deficits in parietal-occipital and frontal areas during the JLO task (Figure 1). Activation (and possibly deactivation) deficits in these areas may be responsible for the visuospatial deficits observed in females with TS.

WILLIAMS SYNDROME (WS)

Williams syndrome is a neurogenetic–neurodevelopmental disorder characterized by a highly variable and enigmatic profile of cognitive and behavioral features. Relative to overall intellect, affected individuals demonstrate disproportionately severe visual-spatial deficits as well as enhanced emotionality and face processing. In one study2, 43 individuals with WS and 40 age- and gender-match controls were studied by both volumetric analysis and voxel-based morphometry to provide convergent approaches for studying this profile. Participants with WS showed reduced thalamic and occipital lobe gray matter volumes and reduced gray matter density in subcortical and cortical regions comprising the human visual-spatial system compared with controls (Figure 2). Subjects with WS also showed disproportionate increases in volume and gray matter density in several areas known to participate in emotion and face processing, including the amygdala, orbital and medial prefrontal cortices, anterior cingulate, insular cortex, and superior temporal gyrus. Persons with WS may possess impairments in visual cortical regions, possibly disrupting global-coherence and visuospatial aspects of face and gaze processing. In a separate study3, we found patterns of activation in WS (compared with controls) suggesting a preservation of neural functioning within frontal and temporal regions during face and eye gaze processing tasks, which activated primary and secondary visual cortices (Figure 3).
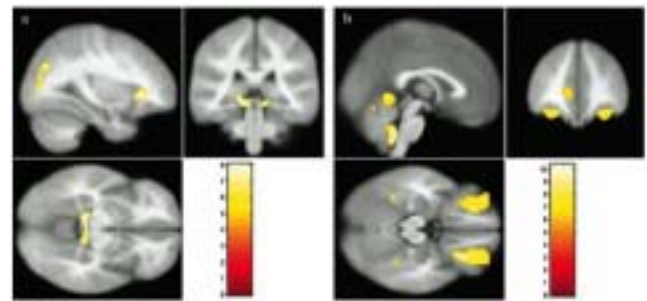

Fig 2. Results of voxel-based morphometry analyses. a, Regions where controls showed greater gray matter density compared with WS. b, Regions where WS participants showed greater gray matter density compared with controls
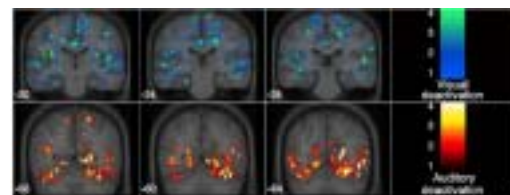

Fig. 3. Within-group t-maps for both typically developing controls (A) and individual with WS (B) showing significant regions of activation. Activation was superimposed on normalized brains of respective groups. Note the preserved right FuG activation in WS subject

FRAGILE X SYNDROME

Females with fragile X syndrome were studied by functional MRI with a Go/NoGo task to examine neural substrates of response inhibition[4]. Although performing similarly to control females in this task, females with fragile X showed abnormal activation patterns of several cortical and subcortical regions, with significantly reduced activation in the supplementary motor area, anterior cingulate and midcingulate cortex, basal ganglia, and hippocampus (Figure 4). One important finding from this study is that neural responses in the right ventrolateral prefrontal cortex (PFC) and the left and right striatum were correlated with the level of FMR1 expression, the gene that is disrupted in fragile X syndrome. These findings support previous work showing
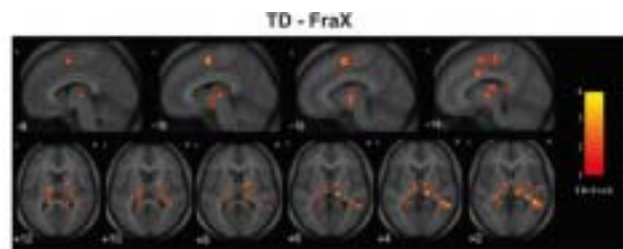
Fig. 4. Brain regions in which females with fragile X showed significantly reduced activation, compared with typically developing females, during the Go/NoGo task.

that frontalstriatial regions typically associated with response inhibition are disrupted in fragile X and illustrate a direct gene-brain linkage in this disorder.

CONCLUSION

These results illustrate how structural and functional MRI combined with genetic analyses and behavioral/cognitive measures, an approached called "behavioral neurogenetics" can provided insights into our understanding of how both genetic and environmental factors contribute to complex variations in atypical human development.

REFERENCES

1. Kesler SR, Haberecht MF, Menon V, Warsofsky IS, Dyer-Friedman J, Neely EK, Reiss AL. Functional neuroanatomy of spatial orientation processing in Turner syndrome. Cereb Cortex. 2004 Feb;14(2):174-80.
2. Reiss A, Eckert M, Rose F, Karchemskiy S, Kessler S, Chang M, Reynolds M, Kwon H, Galaburda A. An experiment of nature: brain anatomy parallels cognition and behavior in Williams syndrome J Neurosci 2004, 24(21):5009-5015.
3. Mobbs D, Garrett A, Menon V, Rose F, Bellugi U, Reiss A. Anomalous brain activation during face and gaze processing in Williams syndrome. Neurology 2004 62:2070-2076.
4. Menon V, Leroux J, White CD, Reiss AL. Frontostriatal deficits in fragile X syndrome: relation to FMR1 gene expression. PNAS 2004 101(10):3615-20.

DECREASED VENTRAL STRIATAL ACTIVATION RELATED TO SYMPTOMS OF DEPRESSION IN PEDIATRIC BIPOLAR DISORDER

A Garrett, K Chang, A Karchemskiy, M Chang, Menon, N Adleman, A. L. Reiss

Department of Psychiatry

INTRODUCTION

Children and adolescents with bipolar disorder (BD) experience changing mood states that have deleterious effects on academic and social development. Since brain function is likely to differ depending on whether an individual is experiencing a manic, depressive, or euthymic episode, investigations of the neural basis of BD have sought to distinguish between abnormalities related to current mood state and those related to the trait, or underlying diathesis, of bipolar illness. Previous functional magnetic resonance imaging (fMRI) studies of brain activation in adults with BD have begun to identify aberrant activation related to mood state, but little is know about mood state related activation in pediatric BD. Data is especially lacking for subclinical mood states and in paradigms using affective stimuli. In this study, we sought to identify abnormalities in brain activation related to the perception of affective facial expressions in children and adolescents with BD compared to healthy controls, and to determine whether these differences could be attributed to the current mood state of the subjects.º

MATERIALS AND METHODS

Twelve male children and adolescents with familial BD and twelve age, sex, and IQ matched control subjects underwent fMRI scanning while they identified the gender of faces with happy, sad, or neutral expressions. Whole brain activation was compared between groups. Based on between-group differences, specific brain regions were chosen for post-hoc correlation with scores on tests of depression (Childhood Depression Inventory, CDI) and mania (Young Manic Affect Rating Scale, YMARS).

RESULTS

There were no group differences in accuracy or response time on the gender identification task. Analysis of happy, sad, and combined (happy+sad) faces compared to baseline consistently showed that boys with BD had decreased activation in the ventral striatum, dorsal striatum, putamen, and thalamus compared with controls. Furthermore, a region of interest analysis showed a significant inverse correlation between ventral striatal activation and symptoms of depression, but not mania, within the BD group.

CONCLUSION

Compared with controls, male adolescents with familial BD have decreased ventral striatal, dorsal caudate, putamen, and thalamic activation in response to viewing affective facial expressions. Furthermore, decreasing ventral striatal activation is associated with increasing depression scores in sub-

jects with BD. These data demonstrate that the mood state of patients with BD, even at subclinical levels, is associated with specific neural abnormalities in response to affective stimuli. Since the ventral striatum is associated with the anticipation and experience of reward, reduced activation to affective stimuli may be related to the decreased motivation and loss of pleasure associated with depressed mood.

White Matter Tract Disruption by DTI in Pediatric Familial Bipolar Disorder

Kiki Chang, M.D., Naama Barnea-Goraly, M.D., Amy Garrett, Ph.D., Melody Chang, Allan L. Reiss, M.D.

Department of Psychiatry and Behavioral Sciences, Division of Child and Adolescent Psychiatry

INTRODUCTION

Increased amounts of white matter hyperintensities (WMH) on T2-weighted MRI images have been reported in many, but not all, studies of patients with bipolar disorder (BD), both adult and pediatric (Lyoo et al., 2002; Strakowski et al., 2000; Sassi et al., 2003). These findings raise the possibility that disruption of white matter contributes to the etiology of BD. However, it is also possible that adults with BD have higher cardiovascular risk factors, which may account for micro CNS events leading to WMH. Therefore, studying children with BD, who presumably have had less chance to develop such events, would help clarify the role of WMH in BD. The few such studies as yet have suffered from either small sample size, inconsistent methodologies, or combination of psychiatric samples. Another way of assessing white matter integrity is through diffusion tensor imaging (DTI) (Taylor et al., 2004), which can measure the relative degree of white matter anisotropy in patients with BD. However, no DTI studies have yet been published in BD. We sought to examine possible white matter disruption in BD by assessing patients with familial pediatric BD by DTI and MRI.

METHODS AND MATERIALS

Subjects were 13 bipolar offspring diagnosed with bipolar I disorder by the WASH-U-KSADS and12 healthy controls. Parents of bipolar offspring all had a diagnosis of bipolar I or II disorder by the SCID. Subjects had stimulants discontinued for at least 24 hours; other medications were continued. Magnetic resonance images were acquired using a GE-Signa 3-Tesla scanner. A DTI sequence was based on a single-shot spin-echo, echo-planar imaging (EPI) sequence with diffusion sensitizing gradients applied on either side of the 180° refocusing pulse. Imaging parameters were: field of view (FOV)= 24 cm, matrix size 128x128, TE/TR=106/6000 ms, 19 axial-oblique slices, slice thickness 5 mm/skip 1.5 mm. The scan was prescribed from the top of the brain and included only the most superior part of the cerebellum. Diffusion gradient duration was d = 32 ms, diffusion weighting was b = 900 s/mm2. In addition, T2 weighted image were acquired by removing the diffusion sensitizing gradients.

Diffusion was measured along six non-collinear directions: XY, XZ, YZ, -XY, -XZ and -YZ. This pattern was repeated four times for each slice with the sign of all diffusion gradients inverted for odd repetitions. Fractional anisotropy (FA) was calculated for each voxel according to Basser and Pierpaoli (Basser & Pierpaoli, 1996) to produce an FA image. FA images were further processed using Statistical Parametric Mapping software (SPM99; Wellcome, UK). A white matter mask was applied to the images to eliminate noise and edge effects. Smoothed images for controls and subjects with BD were compared using voxel-wise two-tailed t-tests and results were normalized to Z-scores. Finally, the joint expected probability distribution of the height and extent of Z-scores, with height (Z > 1.67; p < 0.05) and extent (p < 0.01) thresholds, was used to determine the presence of significant clusters of difference and correct for spatial correlation in the data. Further methods have been described elsewhere (Barnea-Goraly et al., 2004).

RESULTS

There were no significant differences between subjects with BD and controls in age, gender, handedness, or IQ. All subjects were males with bipolar I disorder. Mean age was 13.1+/- 3.3 years for subjects with BD, and 13.8 +/- 2.8 for controls. Controls did not have any areas of decreased white matter FA compared to subjects with BD. Subjects with BD had multiple areas of decreased white matter FA compared to controls (p < .01) (Figure 1). Peaks of major clusters were found in:

- Entire body of corpus callosum (CC): Posterior body of corpus callosum extending to anterior body, with extensions to posterior cingulate and optic radiations (Figure 2)
- Right ventro-medial prefrontal cortex and corpus callosum, extending to superior frontal gyrus (Figure 1)
- Left medial temporal gyrus/inferior temporal gyrus (Figure 3)
- Left deep parietal white matter extending into arcuate fasiculation and left optic radiations
- Midbrain

When a prefrontal mask was applied for post-hoc analysis, additional prefrontal areas of decreased FA were found in inferior prefrontal cortex, approaching subgenual cingulate

CONCLUSIONS

This is the first report, of which we are aware, of white matter anisotropy in pediatric patients with bipolar disorder. Notably, there were no regions of increased FA in the subjects with BD compared to controls. Thus, all areas of differences between groups found by DTI were due to decreased FA in bipolar subjects, signifying possible relative white matter disruption in pediatric familial BD.

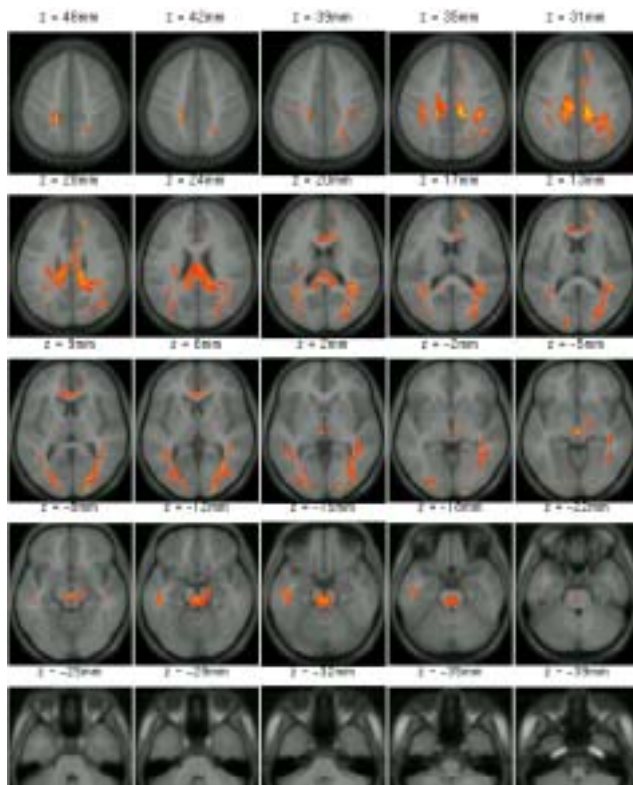White matter hyperintensities have been reported to be found

Figure 1: Areas of reduced FA in subjects with BD compared to healthy controls (p<.01)

in greater numbers in patients with BD compared to controls. These WMH, largely periventricular and in deep white matter, may also signify areas of white matter disruption. As hypothesized, we found decreased FA in areas of the prefrontal cortex, particularly ventromedial areas. Prefrontal white matter disruption may cause dysfunction of prefrontal-limbic circuitry involved in emotion regulation (Blumberg et al., 2003). These circuits may include white matter extending to inferior temporal regions, including amygdala, which we also found abnormal in this study. However, we also found decreased FA in corpus callosal, parietal, and occipital white matter of bipolar subjects. Parietal white matter disruption could be related to cognitive deficits observed in BD, including decreased visuospatial memory (Dickstein et al., 2004; Quraishi & Frangou et al., 2002). However, it is less clear what relevance decreased FA in occipital white matter has to the pathophysiology of BD. Similarly, although widespread disruption of corpus callosum was seen in bipolar subjects, the neurofunctional relevance of disruption of interhemispheric communication is unclear but deserves further study.

Limitations of this study include a relatively small sample size and presence of psychotropic medication exposure in subjects with BD. While further studies with larger numbers are needed, this study suggests that pediatric subjects with bipolar disorder have significant white matter disruption.

REFERENCES

1. Barnea-Goraly N, Kwon H, Menon V, Eliez S, Lotspeich L, Reiss AL (2004): White matter structure in autism: preliminary evidence from diffusion tensor imaging. Biol Psychiatry 55:323-6.
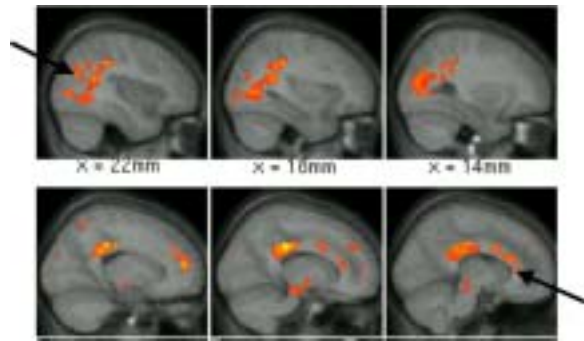
Figure 2: Decreased FA in bipolar subjects in body of CC, extending to superior parietal and occipital cortex.
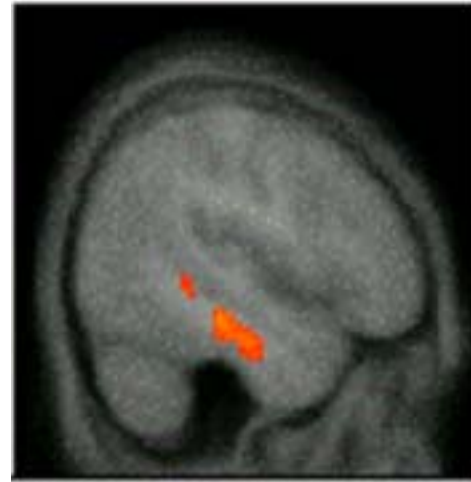
Figure 3: Saggital view of decreased FA in bipolar subjects in white matter extending to left inferior temporal gyrus

2. Basser PJ, Pierpaoli C (1996): Microstructural and physiological features of tissues elucidated by quantitative-diffusion-tensor MRI. J Magn Reson B 111:209-19.
3. Blumberg HP, Martin A, Kaufman J, et al (2003): Frontostriatal abnormalities in adolescents with bipolar disorder: preliminary observations from functional MRI. Am J Psychiatry 160:1345-7.
4. Dickstein DP, Treland JE, Snow J, et al (2004): Neuropsychological performance in pediatric bipolar disorder. Biol Psychiatry 55:32-9.
5. Lyoo IK, Lee HK, Jung JH, Noam GG, Renshaw PF (2002): White matter hyperintensities on magnetic resonance imaging of the brain in children with psychiatric disorders. Compr Psychiatry 43:361-8.
6. Quraishi S, Frangou S (2002): Neuropsychology of bipolar disorder: a review. J Affect Disord 72:209-26.
7. Sassi RB, Brambilla P, Nicoletti M, et al (2003): White matter hyperintensities in bipolar and unipolar patients with relatively mild-to-moderate illness severity. J Affect Disord 77:237-45.
8. Strakowski SM, DelBello MP, Adler C, Cecil DM, Sax KW (2000): Neuroimaging in bipolar disorder. Bipolar Disord 2:148-64.
9. Taylor WD, Hsu E, Krishnan KR, MacFall JR (2004): Diffusion tensor imaging: background, potential, and utility in psychiatric research. Biol Psychiatry 55:201-7.

Functional Disconnectivity During Speech Production in Schizophrenia

[1]Daniel H. Mathalon, [2]Susan L. Whitfield, [3]Judith M. Ford

[1]Department of Psychiatry, Yale University;
[2]Departments of Psychology and Psychiatry, Stanford University

INTRODUCTION

We are using fMRI and event-related potential (ERP) responses to auditory probes to assess hypothesized dysfunction in communication between the frontal lobes, where speech and verbal thoughts are generated, and the temporal lobes where they are processed that may underlie the phenomenon of hallucinations in schizophrenia. Below, we report on our progress with the study of fMRI activations to spoken sounds.

MATERIALS AND METHODS

FMRI data were collected while 16 patients with schizophrenia (DSM-IV) and 16 age- and gender-matched healthy adults uttered the syllable [a] aloud and then listened to it played back through headphones. Both talking and listening were timed to occur only during the silent periods of clustered acquisition sequences developed by Glover and colleagues at the Lucas Center. Event-related fMRI data were analyzed using SPM2, with the Psycho-Physiological Interaction (PPI) option. The covariates in the analysis were (1) the time series from a region in superior temporal gyrus identified in a conjunction analysis of the Talk-Rest condition with the Listen-Rest condition, collapsing across all 32 subjects, (2) a vector coding the Talk-Rest contrast and another coding for the Listen-Rest contrast (3) a term reflecting the interaction of (1) and (2). This analysis produced statistical parametric maps showing regions of the brain where activity was correlated (positively or negatively) with the activity in auditory cortex, significantly more during Talking than Rest, during Listening than Rest, and during Talking than Rest.

RESULTS

During Talking, the activity in many regions of the brain involved in speech production (Broca's area, cerebellum, Anterior Cingulate) was more negatively correlated with an ROI delineating the STG than during Rest. This was not seen in patients. Furthermore, there were more areas showing negative correlations with the STG during Talking than Listening in controls, but less so in patients. Initial analysis suggests that the lack of negative correlation during talking is greater in patients with more severe hallucinations.
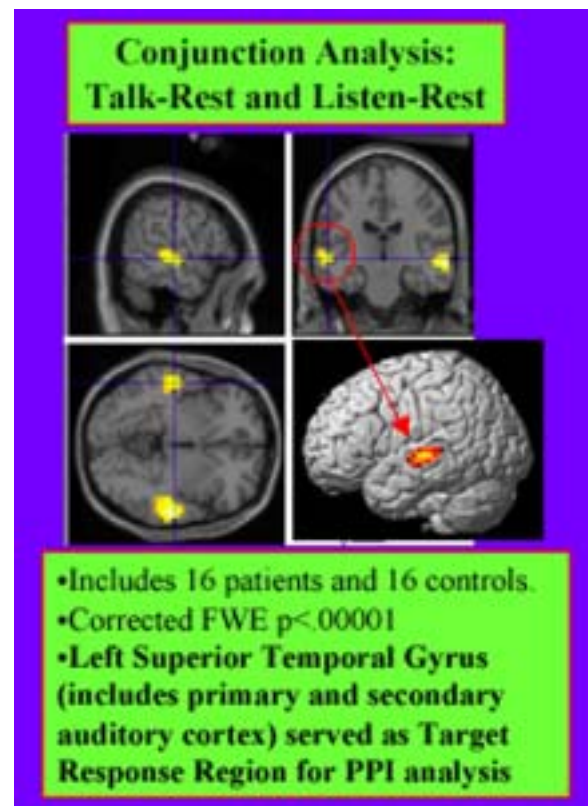
Controls   *Patients*
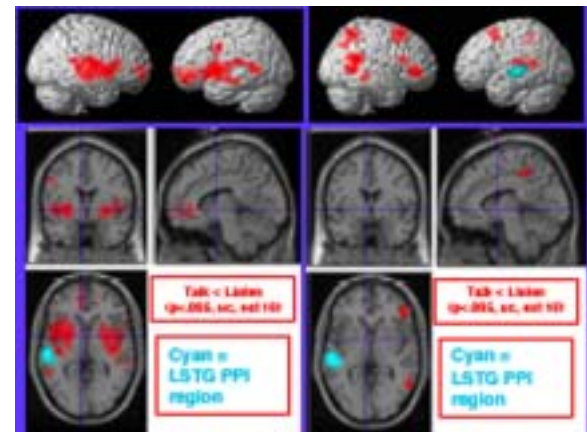
Talk – Listen:
Red = more negative correlation during Talk than during Listen.
Green = more positive correlation during Talk than during Listen (none showing in this picture.)

CONCLUSION

The results confirmed our hypothesis that an efference copy/corollary discharge mechanism suppresses auditory cortex during talking in controls more than in patients with schizophrenia.

Parallel Interhemispheric Processing in Aging and Alcoholism: Relation to Corpus Callosum Size

T. Schulte[1], A. Pfefferbaum[1,2] and E.V. Sullivan[1]

Department of Psychiatry & Behavioral Sciences, Stanford University and Neuroscience Program, SRI International, Menlo Park, CA

Introduction

Human lesion studies provide evidence that disruption of integrity of the corpus callosum (CC), the thick band of white matter fibers structurally and functionally connecting the two cerebral hemispheres, can contribute to impairment in sensory and cognitive integration. Simple RT tasks with targets presented in the same (uncrossed) or opposite (crossed) visual field have been used to assess interhemispheric transfer time (ITT). Uncrossed responses can be processed within the same hemisphere, whereas crossed responses require transfer of information between hemispheres via the corpus callosum. Thus the difference between crossed and uncrossed reaction times (CUD) can be taken as an index of ITT. Earlier studies have revealed significant callosal thinning in chronic alcoholics. We sought to determine whether alcoholics showed evidence of altered ITT and whether this was related to measures of the CC.

Materials and Methods

We tested parallel processing of visual information using the redundant targets effect (RTE) paradigm in 12 alcoholics and 13 matched controls. The paradigm was a simple reaction time task (RT) with targets presented in the same (uncrossed), opposite (crossed), or both (redundant) visual fields.

The corpus callosum was measured on the midsagittal slice of a T1-weighted 3D spoiled gradient recalled scan acquired with full-brain coverage. Measurements were made on a midline slice extracted from the native data after interpolation, alignment, and reslicing. For extraction of the aligned midline slice, the anterior commissure (AC) was identified on the native sagittal slice on which it was best visualized. The sagittal slices were then stacked and interpolated to high (1 mm) isotropic resolution. The left/right midline was determined from a coronal reconstruction passing through the AC. The AC and posterior commissure (PC) were identified on a resliced midline sagittal image. Head tilt angle was defined on a high-resolution coronal image and head rotation was defined on a high-resolution axial image using an interactive rotating cursor. The resultant landmarks and angles

Aligned, extracted, and rotated midsagittal slice of a manually outlined corpus callosum (anterior is left, posterior is right). Following outlining, the corpus callosum silhouette was rotated to a plane parallel to the inferior extremes of the rostrum anteriorly and splenium posteriorly. The midpoint along this plane between the anterior extreme of the genu and posterior extreme of the splenium was used as the center of a circle, and radii were projected at +30 degree and +150 degree angles from the plane, thus dividing the corpus callosum into genu+rostrum (medium gray), body (light gray), and splenium (dark gray).

were used to align the volume in a uniform space and orientation anchored on the AC. The midsagittal image was then extracted for semi-automated edge identification of the corpus callosum. Regional callosal areas genu+rostrum, body, splenium) were defined geometrically.

Results

In older alcoholics (>50 years) the RT gain invoked by redundant targets did not exceed probability measures, suggesting compromised interhemispheric processing of parallel information in this subgroup compared with controls or younger alcoholics. The difference between crossed and uncrossed RTs (CUD), an index of interhemispheric transfer time, was greater in older than younger subjects. Moreover, the CUD was negatively correlated with the CC total area and body in controls, supporting the concept of a structure-function relationship of interhemispheric transfer. This relationship was not found in alcoholics, although the midsagittal area of the CC, genu, and body but not intracranial volume, was significantly smaller in alcoholics than controls.

Conclusion

These results suggest that chronic alcohol abuse together with advancing age exert subtle disruption on parallel interhemispheric processing reliant on callosal connections (Schulte et al., 2003).

Reference

Schulte T, Pfefferbaum A, Sullivan EV: Parallel interhemispheric processing in aging and alcoholism: Relation to corpus callosum size. Neuropsychologia 2003; 42:257-271

Dissociation of Remote and Anterograde Memory Impairment and Neural Correlates in Alcoholic Korsakoff Syndrome

Rosemary Fama,[1] Laura Marsh,[2] and Edith V. Sullivan[3]

1Neuroscience Program, SRI International, Menlo Park; Department of Psychiatry and Behavioral Sciences, 2Johns Hopkins University School of Medicine, Baltimore; 3Department of Psychiatry and Behavioral Sciences, Stanford University.

INTRODUCTION

Alcoholic Korsakoff's syndrome (KS) is marked by remote memory impairment together with characteristic profound anterograde memory deficits. Despite previous studies of memory processes in KS, questions remain regarding the nature and severity of these impairments and identification of brain systems that underlie these different memory impairments.

MATERIALS AND METHODS

This study examined remote and anterograde memory function in five KS patients in comparison with eight patients with Alzheimer's disease (AD) and 24 normal control subjects (NC). In addition, relationships between memory performance and regional brain volumes were examined in the KS group.

Subjects underwent brain magnetic resonance imaging (MRI) including a dual-echo spin-echo axial sequence used for assessing white and gray matter volumes of cortical regions of interest, and a dual echo, coronally-acquired sequence with 3 mm contiguous slices used for assessing volumes of hippocampus.

RESULTS

Overall, the KS group showed severe impairment on both remote and anterograde memory measures, performing at the level of the AD group on most measures. Differences were observed on the pattern of temporal gradient for verbal recognition, with KS exhibiting a more steeply graded rate of decline over the most recent period examined. Severity of the remote memory deficit in KS was not associated with severity of anterograde memory deficit. Examination of brain structure-function relationships in the KS subjects revealed that photo naming of remote historical information was related to posterior cortical white matter volumes but not hippocampal volumes; sequencing was related to prefrontal but not hippocampal volumes. By contrast, a measure of anterograde memory for nonverbal visual material showed a relationship to hippocampal but not regional cortical white matter volumes.
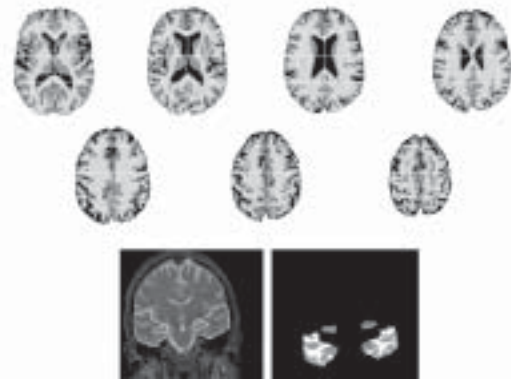
Upper: Axial MRI acquired using a dual-echo spin-echo sequence. Slices, were segmented into gray matter white matter, and cerebrospinal and divided into outer 45%, (cortical) regions, and inner regions. The cortical area was divided into regions that roughly corresponded to prefrontal, frontal, anterior superior temporal, posterior superior temporal, anterior parietal, and posterior parietal-occipital lobar anatomy: Lower: Early echo coronal MRI with hippocampi and temporal lobes outlined.
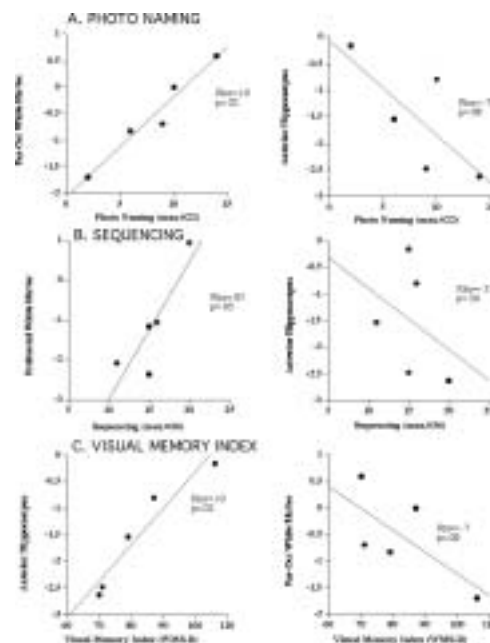
Scatterplots of the relationship between remote and anterograde memory measures and selected brain volumes in KS

CONCLUSION

This set of dissociations, which parallels that observed in our earlier study of AD, is now documented in KS and provides further evidence that these separate cortical and limbic brain systems are principal neural substrates of the remote and anterograde memory and sequencing deficits in KS. (Fama et al., 2004).

REFERENCES

1. Fama R, Marsh L, Sullivan EV: Dissociation of remote and anterograde memory impairment and neural correlates in alcoholic Korsakoff Syndrome. JINS 2004; 10:427-441

Hippocampal Volume Deficits Contribute Significantly to the Amnesia of Alcoholic Korsakoff's Syndrome

Edith V. Sullivan[1] and Laura Marsh[2]

[1]*Department of Psychiatry and Behavioral Sciences and Neuroscience Program, Stanford University,*
[2]*Department of Psychiatry and Behavioral Sciences, Johns Hopkins University School of Medicine, Baltimore, MD, U.S.A.*

INTRODUCTION

Persisting, dense, amnesia is the hallmark of alcoholic Korsakoff's Syndrome (KS). Decades of memory research and clinical assessment have proceeded on the assumption that the global amnesia characteristic of KS arises from severe pathology of the diencephalon and thalamus. The role of hippocampus, the brain structure essential for memory consolidation, however, has been diminished or dismissed altogether. We challenged this assumption with quantitative neuroimaging.

MATERIALS AND METHODS

The groups comprised 5 nondemented KS patients, 20 Alzheimer's disease (AD) patients with bilateral hippocampal volume loss, and 36 healthy controls. All were men, age 50 to 76 years, and underwent brain magnetic resonance imaging (MRI). The hippocampus and other comparison regions were quantified from dual echo, 3mm thick, coronally-acquired slices.

RESULTS

Relative to controls, both the KS and AD groups had equivalent and significant bilateral hippocampal volume deficits, which were on the order of 1 standard deviation. Extensive volume abnormalities were also present in both patient groups in temporal lobe cortical gray matter, temporal horns, and lateral and third ventricles. A memory deterioration index was related to the extent of the hippocampal but not temporal cortical volume shrinkage in KS patients.
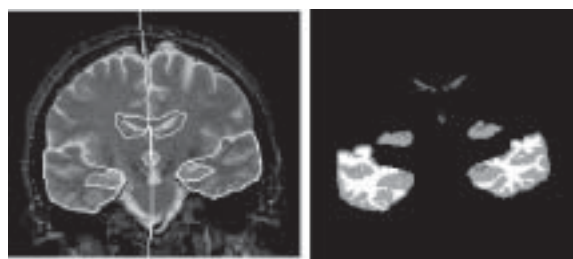
Left: Coronal late echo MR image displaying manual outlining of the hippocampi and temporal lobes and gross outlining of the lateral ventricles and third ventricle for segmentation analysis. Right: Each lateral region of interest after semi-automatic segmentation into compartments of gray matter, white matter, and CSF. Note that for illustration each hippocampus is displayed twice, once as it is integrated within the medial temporal lobe and again "excised" to emphasize the boundary outline.
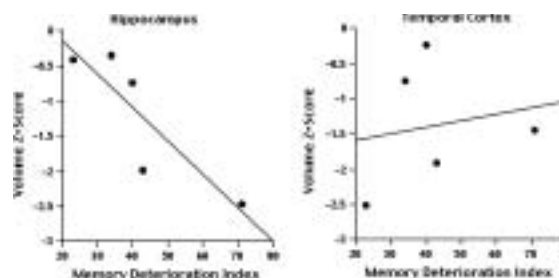
Correlations between memory deterioration index and bilateral hippocampal vs. bilateral temporal lobe gray matter volumes.

CONCLUSION

These results draw into question the traditional conceptualization of the neuropathological mechanism of the memory impairment in KS as being exclusive of hippocampal pathology. The KS patients studied herein exhibited substantial hippocampal volume shrinkage, the extent of which correlated with the degree of their declarative memory impairment. These findings have implications for identification of brain systems affected by nonalcoholic forms of KS, including anorexia, and indicate hippocampal dysmorphology and dysfunction as potential features (Sullivan and Marsh, 2003).

REFERENCES

Sullivan EV, Marsh L: Hippocampal volume deficits in alcoholic Korsakoff's Syndrome. Neurology 2003; 61:1716-1719

Preservation of Hippocampal Volume throughout Adulthood in Healthy Men and Women

Edith V. Sullivan,[1] Laura Marsh,[2] and Adolf Pfefferbaum[1,3]

[1]Department of Psychiatry and Behavioral Sciences, Stanford University; [2]Department of Psychiatry and Behavioral Sciences, Johns Hopkins University School of Medicine, Baltimore, [3]Neuroscience Program, SRI International, Menlo Park

INTRODUCTION

Brain tissue shrinkage is a common fate of normal aging, yet MRI studies have provided inconsistent evidence regarding shrinkage of the human hippocampus with age.

MATERIALS AND METHODS

This cross-sectional in vivo study used MRI to measure hippocampal volumes in healthy men and women, aged 20 to 85 years, rigorously screened to exclude dementia and other psychiatric and medical conditions.

All participants received a dual echo, spin echo MRI acquired in the coronal plane and perpendicular to the anterior commissure-posterior commissure plane (3 mm thick interleaved slices, no skip; TRB2800ms; TE=40ms and 80 ms). Operators, highly trained and blind to all subject identity, manually outlined the hippocampus, starting anteriorly from the first slice of fully volumed hippocampus distinct from the amygdala and ending posteriorly at the ascending tail. The borders of the temporal lobe were also determined manually and then each pixel was semi-automatically classified, on a slice-by-slice basis, as representing gray matter, white matter, or CSF.

RESULTS

Neither men nor women showed significant correlations between hippocampal volumes and age, despite significant age-related decline in temporal volumes. Absence of hippocampus-age relationships endured when restricting analysis to older individuals (B50 years) and considering menopause and hormone replacement therapy.

CONCLUSION

Even if hippocampal volume shrinkage does occur with normal aging, the current results indicate that it is insubstantial relative to volume shrinkage observed in surrounding tissue of temporal cortex. This *in vivo* finding of stability of hippocampal size with age is consistent with stereological cell count reports, evidence from animal models for modest hippocampal cell generation even in older adult age, and evidence for substantial environmental control over hippocampal size. Thus it is tempting to interpret the absence of hippocampal volume decline as arising, at least in part, from volume maintenance through neurogenesis in healthy adults.
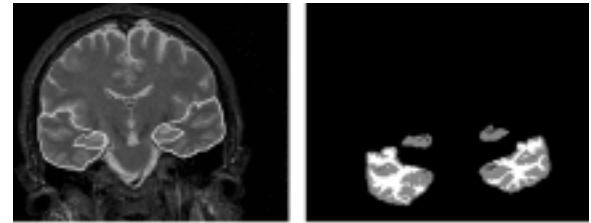
Left: Coronal late echo MR image displaying manual outlining of the hippocampi and temporal lobes and gross outlining of the lateral ventricles and third ventricle for segmentation analysis. Right: Hippocampi and temporal lobe ROIs after semi-automatic segmentation.
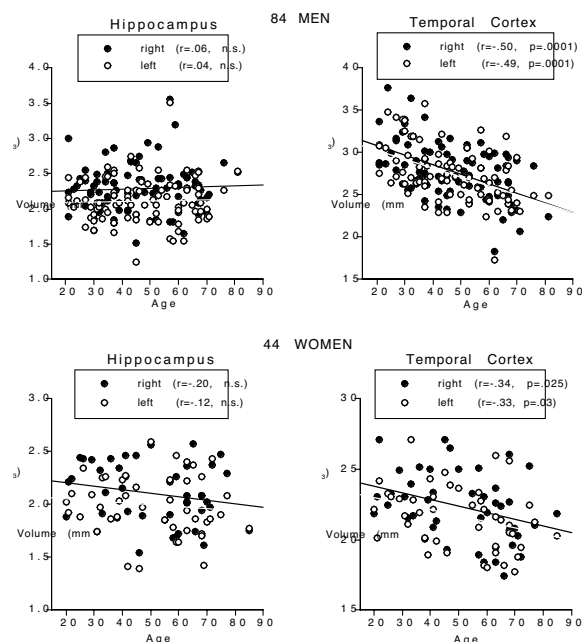
Correlations between volumes of the left (open circles and gray regression line) and right (closed circles and black regression line) hippocampus and temporal lobe gray matter and age displayed separately for men and women.

REFERENCES

Sullivan EV, Marsh L, Pfefferbaum A: Preservation of hippocampal volume with age in both healthy men and women (abs), Fourth Neurobiology of Aging Conference "Developmental Origins of Aging in the Brain and Blood Vessels". New Orleans, LA, 6-7 November, 2003

The Human Basal Forebrain Integrates the Old and the New

[1]Eve De Rosa, [2]John E. Desmond, [3]Adam K. Anderson, [1,4]Adolf Pfefferbaum, & [1]Edith V. Sullivan

[1]*Departments of Psychiatry & Behavioral Sciences,* [2]*Radiology, and* [3]*Psychology, Stanford University and* [4]*SRI International, Neuroscience Program, Menlo Park*

INTRODUCTION

Acquisition of new learning is challenged by the phenomenon of proactive interference (PI), which occurs when previous learning disrupts later learning. Whereas human neuroimaging studies have focused on the cortical contributions to interference resolution, animal studies demonstrate that efficient resolution of PI depends on cholinergic modulation from basal forebrain nuclei (BF). Whether the BF promotes PI resolution in humans is unknown.

MATERIALS AND METHODS

We used a PI paradigm in a functional MRI experiment testing 13 healthy men and 11 detoxified, non-amnesic men meeting DSM-IV criteria for alcohol dependence. For Baseline blocks, subjects were required to discriminate color pairs on which they had been trained prior to the scan. For PI blocks, the subjects learned a new color component for each color pair. To minimize fatigue and attention functional scanning was restricted to 12 minutes during which subjects attended 180 separate trials involving attend and rest for each condition with Baseline always shortly preceding each PI block.

Functional images were acquired continuously during task performance using T2*-weighted gradient echo spiral pulse sequence. Image spatial pre-processing and statistical analysis were performed using SPM99. In alcoholics and controls, areas of statistical significance were identified using random effects analysis with height threshold $p < 0.005$ uncorrected and extent threshold of 10 contiguous voxels (80 mm^3). Because we had an *a priori* hypothesis of BF activation, we also used small volume correction with a 3mm sphere radius centered at ($x = 8$, $y = 7$, and $z = -7$) in Talairach co-ordinates.

RESULTS

During PI resolution, control subjects recruited a BF system that included afferent anterior and posterior cortical sites associated with efficient memory acquisition and perceptual processing. Despite normal performance, alcoholic patients did not activate a BF network but instead invoked anterior cortical sites traditionally associated with executive function.
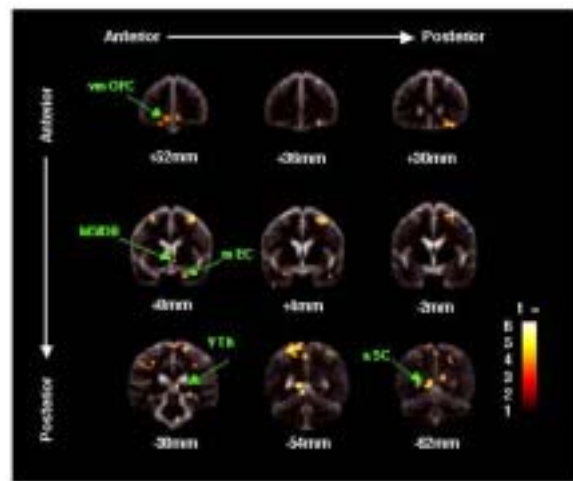
Control group activations superimposed on mean anatomical image for all controls. Panel 1: ventromedial orbitofrontal (vmOFC); Panel 2: the medial septum/diagonal band nuclei (MS/DB) and medial entorhinal cortex (mEC); Panel 3: pons, lateral geniculate and pulvinar nuclei of the thalamus (VTh), and lingual gyrus (LG)]. The y-values for each coronal section are provided under each frame.
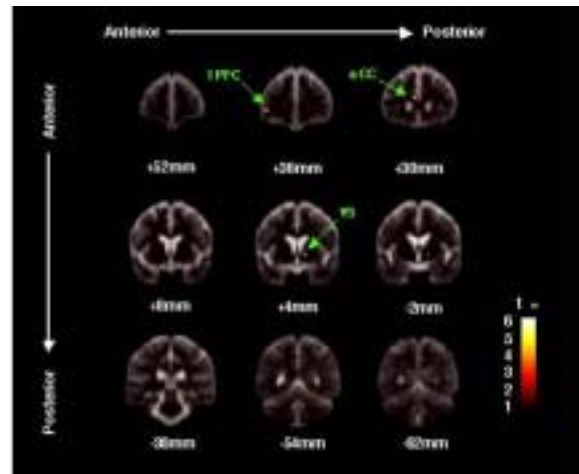
Comparable data for alcohol group. Panel 1: lateral prefrontal (lPFC) and anterior cingulate (aCC); Panel 2: ventral striatum (VS).

CONCLUSION

These results provide evidence for parallel neural systems, each with the potential to resolve interference in the face of competing information, but one better poised to integrate old with new memories (DeRosa et al., 2004).

REFERENCE

De Rosa E, Desmond JE, Anderson AK, Pfefferbaum A, Sullivan EV: The human basal forebrain integrates the new and the old. Neuron 2004; 41:825-837

Title Individual differences in pain-related fear and anxiety predict neural activation to pain

David H. Ludlow[1], Kevin N. Ochsner[3*], Kyle Knierim[1], Josh Hanelin[1], Tara Ramachandran[1], Gary C. Glover[2], & Sean C. Mackey[1]

*Departments of Anesthesia[1], Radiology[2], & Psychology[2] Stanford University; *Now at Department of Psychology, Columbia University*

INTRODUCTION

Individual differences in fear and anxiety have been known to modulate the pain response and may even cause more suffering than the initiating physical stimulus; however, little is known about the neural systems involved in this relationship. The present study sought to determine the neural correlates of individual differences in the tendency to 1) fear various types of physical pain, as measured by the fear of pain questionnaire (FPQ) and 2) feel anxious about the potentially negative implications of physical sensations, as measured by the anxiety sensitivity index (ASI).

MATERIALS AND METHODS

Conventional and functional magnetic resonance imaging data was collected on a 3T scanner (GE Lx rev VH3-M3.8, Milwaukee, WI) while a thermal stimulator applied alternating 30 second blocks of noxious heat (45-50C) and warmth stimuli (38C) to the lateral forearm of 13 healthy subjects (6 male, 7 female). Upon exiting the MR scanner, each participant completed a battery of questionnaires including the FPQ, ASI, and the State-Trait Anxiety Inventory (STAI-T). Scores from each questionnaire were correlated with individual brain regions through a regression analyses performed with the statistical brain analysis package, SPM99.

RESULTS

Regression analyses demonstrated that during the experience of pain, FPQ scores predicted activation of a ventral lateral frontal region associated with response regulation, and anterior and posterior cingulate regions associated with monitoring and evaluation of affective responses (Figure 1A), whereas ASI scores predicted activation of a medial prefrontal region associated with self-focused attention (Figure 1B). These functional relationships cannot be wholly explained by generalized anxiety (indexed by STAI-T scores), which did not significantly correlate with activation of any regions.

CONCLUSION

The present findings may help clarify both the impact of individual differences in emotion on the neural correlates of pain, and the roles in fear, anxiety, and pain processing played by medial and orbitofrontal systems.
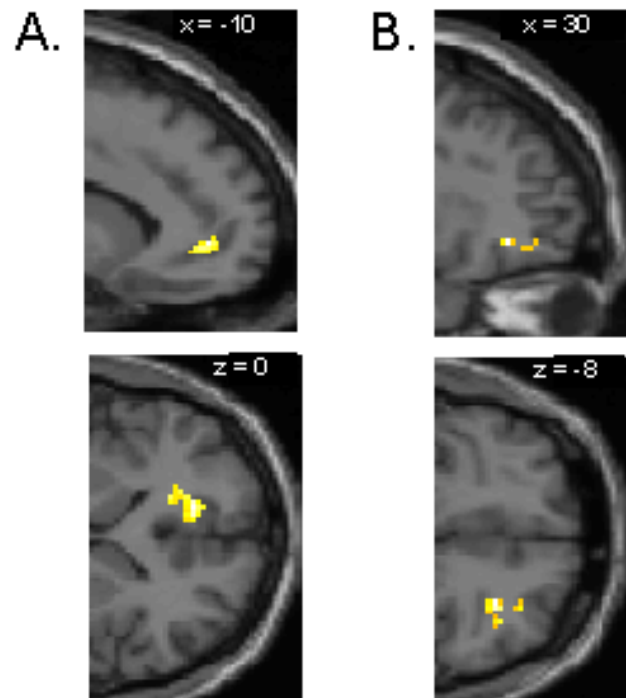

Figure 1. Regions identified in regression analyses (see Tables 2 and 3) whose activation during pain correlates p < .001 with individual differences in either anxiety sensitivity or fear of pain shown on canonical T1 anatomical images. A. Sagittal (top) and axial (bottom) views of left MPFC region correlated (r = .890) with ASI scores. B. Sagittal (top) and axial (bottom) views of right lateral orbital frontal region correlated (r = .912) with

REFERENCES

1. McNeil DW, Rainwater AJ, 3rd. Development of the Fear of Pain Questionnaire—III. Journal of Behav Med 1998; 21:389-410.
2. Reiss S, Peterson RA, Gursky DM, McNally RJ. Anxiety sensitivity, anxiety frequency and the prediction of fearfulness. Behav Research Ther 1986;24:1-8.
3. Spielberger CD, Gorsuch RL, Luschemne R, Vagg PR, Jacobs GA. Manual for the State-Trait Anxiety Inventory (FormY). Palo Alto, CA: Consulting Psychologist Press, 1983
4. Ochsner KN, Ray R, Cooper J, Robertson E, Chopra S, Gabrieli JDE. For better or for worse: Neural systems supporting cognitive down-and up-regulation of negative emotion. Stanford university manuscript 2003.
5. Gusnard DA, Akbudak E, Shulman GL, Raichle ME. Medical prefrontal cortex and self-referential mental activity: relation to a default mode of brain function. Proceedings of National Academy of Sciences USA 2001; 2:685-94.

Functional Magnetic Resonance Imaging of Pain Transmission in the Human Spinal Cord

Richard Shinaman, David Ludlow, Gary Glover, Sean Mackey

Departments of Anesthesia and Radiology

INTRODUCTION

Functional magnetic resonance imaging (fMRI) is a technique utilizing the blood oxygen level dependent (BOLD) signal to elucidate neuronal activity. This tool has been used extensively to examine areas of the brain responsible for cognition, emotion, and more recently; the perception of pain. Significant processing and transmission of pain also occurs in the spinal cord and brainstem, however few researchers have used fMRI for spinal cord imaging due to a variety of technical considerations. Image degradation occurs during spinal cord fMRI due to respiratory motion artifact, CSF pulsatility, magnetic field inhomogeniety and low overall signal magnitude. We previously were able to demonstrate that fMRI could be used to demonstrate somatotopic activations and lateralization of fMRI activations in the dorsal horn to noxious stimuli on the upper extremities. In order to further refine our previous data, we performed an additional study that utilized a number of strategies to optimize the localization and power of the functional activations.

MATERIALS AND METHODS

Healthy volunteers were recruited and subjected to a thermal pain task to determine a temperature which reliably produced 7/10 pain (0 = no pain and 10 = worst pain) in each of four sites. Subsequently, conventional and functional MRI scans were performed of their cervical spine. A 3T GE Signa whole body MR system was used to collect sagittal localizer, axial anatomic, and functional images. The subjects were imaged while experiencing 7/10 pain from a peltier heat thermode placed in right thenar, left thenar, right deltoid, and left deltoid positions. We utilized a gradient echo double-shot spiral acquisition sequence, with 12 contiguous 4mm axial slices prescribed either from C5 to C7 or C4 to C6. Other settings consisted of a 16 cm FOV, a 2000 msec TR, a 25 ms TE, and a 128 x 128 matrix. Retrospective correction for cardiac and respiration synchronized movement was performed with software created at the Stanford Center for Advanced MR Technology. All images were analyzed for activation patterns using Analysis of Functional Neuroimages (AFNI) and Brain Voyager software.

RESULTS

Simple regression analysis revealed statistically significant (p A 0.01) voxels of activation in several regions of the spinal cord. We were able to reliably demonstrate dorsal horn activation at the cervical level consistent with the dermatome of noxious stimulation. These areas were further examined by functional connectivity algorithms within AFNI in order
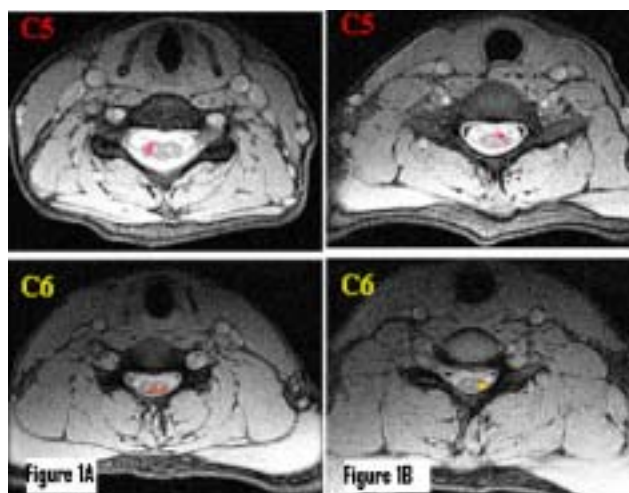

Figure 1A: Right Extremity (Top) Deltoid Nociception (Bottom) Thenar Nociception. 1B: Left Extremity (Top) Deltoid Nociception, (Bottom) Thenar Nociception.

to minimize artifact and areas of activation outside of the spinal cord. The resulting images revealed strong activation of the ipsilateral dorsal horn of C6 and C7 with noxious stimulation of the thenar eminence. Noxious stimulation of the lateral deltoid produced activations within the ipsilateral dorsal horn of C5 and C6. Activations correlated with ipsilateral transmission and both ascending and descending projections from the primary level of activation. Examples of the primary activation patterns can be seen in Figure 1.

CONCLUSION

This study provides additional evidence that fMRI can be used to create accurate representations of pain transmission and processing in the human spinal cord. The use of spiral k-space fMRI acquisitions combined with retrospective denoising alleviated some of the technical problems experienced in other studies. In addition, utilizing specific methods to increase homogeneity of the neck and limiting subject motion maximized the overall signal quality. Lastly, the application of functional connectivity algorithms to the raw data further refined the activation patterns. Our study was able to reveal consistent and accurate patterns of neuronal activity within the cervical spinal cord consequent to noxious stimulation. We believe that this data represents a significant improvement over previous studies involving fMRI of noxious stimulation in the human spinal cord. Overall, this study contributes to creating an objective analysis of pain transmission and can be used to further investigate central changes that occur in patients with acute and chronic pain.

REFERENCES

Stroman PW, Nance PW, Ryner LN. BOLD MRI of the human cervical spinal cord at 3 Tesla. Magn Reson Med 1999; 42:571-6

Madi S, Flanders AE, Vinitski S, Herbison GJ, Nissanov J. Functional MR imaging of the human cervical spinal cord. AJNR Am J Neuroradiol 2001; 22:1768-74

Dynamics of BOLD response to sinusoidal input

Thomas Ferree[1], Alexander Wade[2], Anthony Norcia[2], Michael Calvisi[3], Andrew Szeri[3], David Liley[4]

[1]Department of Radiology, University of California, San Francisco, [2]Smith-Kettlewell Eye Research Institute, San Francisco [3]Applied Science and Technology Graduate Group, University of California, Berkeley [4]School of Biophysical Sciences and Electrical Engineering, Swinburne University of Technology, Melbourne

INTRODUCTION

Better hemodynamic modeling means better statistical parametric maps. We study the dynamics of the BOLD response to sinusoidal input, to avoid the neural and hemodynamic transients associated with boxcars. We measure the amplitude and phase as a function of the stimulus period, and compare the results with theoretical predictions of the balloon model.

MATERIALS AND METHODS

Theoretical predictions of the amplitude and phase were computed using the balloon model, as implemented in Friston et al. (2001). Low-amplitude, sinusoidal input produces sinusoidal output, indicating this puts the model in its quasi-linear regime (Calvisi et al., 2004). Sinusoidal response time series were characterized in terms of their RMS amplitude and phase.

fMRI data were collected from a normal, adult subject, using the 3T MRI scanner at the Lucas Center. Four slices (1mm x 1mm x 1.3mm) were acquired with spiral acquisition sequence (TR = 250 msec). A horizontal grating (3 cycles/deg), reversing contrast at 9 Hz, was projected onto a vertical screen at the foot of the scanner. To elicit a dynamical response on the natural time scales of the BOLD response, the contrast was modulated sinusoidally between 0% and 40% with period T = 18 (slow), 9 (med), and 5.4 (fast) sec. Each condition (period) was repeated four times.

mrVista tools were used to select voxels for time series analysis. The four scans in the slow condition were averaged, and a region of interest (ROI) was defined to include voxels whose correlation with the stimulus was at least 0.25. The resulting ROI was limited to occipital cortex. The average time series within this ROI was computed for each scan. The RMS amplitude was computed directly, and the phase lag relative to the stimulus was estimated from the peak in the time-domain cross-correlation function.

RESULTS

Figure 1 shows the amplitude versus T. Open circles are for each scan; filled circles are for the average of the four scans. The thick solid line is the balloon model prediction. In both cases, the amplitude peaks near $T \Xi 10$ sec, and is nearly flat
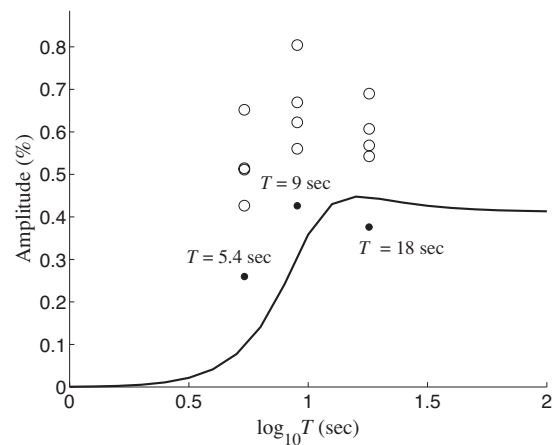

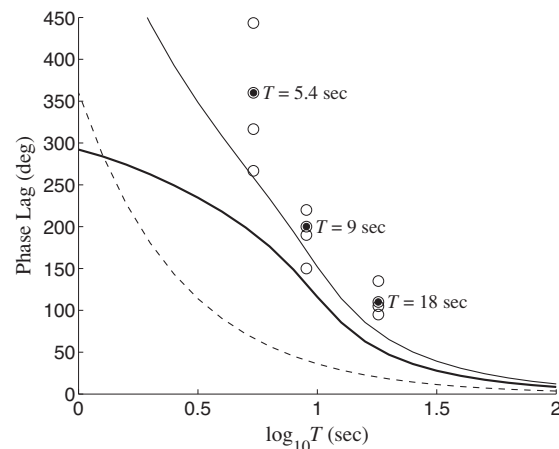*Fig.1. Amplitude of BOLD response to sinusoidal input with period T.*

Fig.2. Phase lag of BOLD response (relative to the stimulus) to sinusoidal input with period T.

for longer T, but falls off rapidly for shorter T.

Figure 2 shows the phase lag relative to the stimulus. The thick solid line is the balloon model prediction. Generally the data lie well above the theory. For comparison, the dashed line is the effect of a one-second delay, and the thin solid line is the sum of both.

CONCLUSION

The BOLD response to sinusoidal input provides a simpler context in which to test model predictions, by avoiding onset and offset transients. Our results show good qualitative agreement with the balloon model, with the largest discrepancy in the phase lag at T = 5.4 sec. Precise quantitative agreement will require more data and perhaps model re-parameterization.

REFERENCES

1. Friston KJ Mechelli A, Turner R, Price CJ (2000). NeuroImage 12: 466-477.
2. Calvisi ML, Szeri AJ, Liley DTJ, Ferree TC (2004). Proceedings of 25th Annual Conference of the IEEE Engineering in Medicine and Biology Society, in press.

SMITH-KETTLEWELL EYE RESEARCH INSTITUTE

Component Analysis of BOLD response

Lenny Kontsevich, Christopher Tyler

Smith-Kettlewell Eye Research Institute

INTRODUCTION

There are two major techniques for evaluating response in a block-design experiment on functional MRI: 1) magnitude estimation for the main harmonic, and 2) computing a scaling coefficient between the theoretically predicted temporal response to a particular stimulus and the actual response in the cortex. Both techniques are imperfect. The first one discards valuable information from the other response harmonics and makes the response components inseparable. The second is based on either inadequate linearity assumption or nonlinear balloon model, which has a limited scope since it does not explain the existence of a counter-phased BOLD response in un-stimulated parts of the cortex.

We propose an approach for deriving temporal response profiles for independent processes in the cortex based on Independent Component Analysis (ICA). This analysis is based on two assumptions: linear interaction of the components and non-Gaussian distributions of their responses. Both of these assumptions appear to be plausible for the BOLD response[1].

MATERIALS AND METHODS

The fMRI responses were collected with 2D spiral acquisition from a custom occipital surface coil in the Lucas GE Signa 3T scanner. There were 22 oblique coronal slices at 3 *s* TR with TE of 30*ms* and flip angle 90I, providing 1.72x1.72x3 *mm* voxels through the occipital cortex. Test and null stimuli alternated for 9 s each in 6 periods per scan.

In the test stimulus the central part of the visual field was filled by dynamic random noise while the rest was filled by the luminance-matched uniform gray. The null stimulus was always uniform gray. The observers were instructed to fixate a fixation mark in the center.

To simplify the analysis and make it more visual, we first performed the Principal Component Analysis (PCA) on the time sequences and then conducted ICA within 2-dimensional subspaces determined by pairs of the major principal components. The analysis was applied to the visual area V1 of primary visual cortex.

RESULTS

We found that the two major principal components contain independent components revealed by clusters along two (typically, oblique and non-orthogonal) axes. The components from the third one onwards did not produce such clusters. An example of the independent components (after they are made orthogonal) in the signal distribution across voxels is
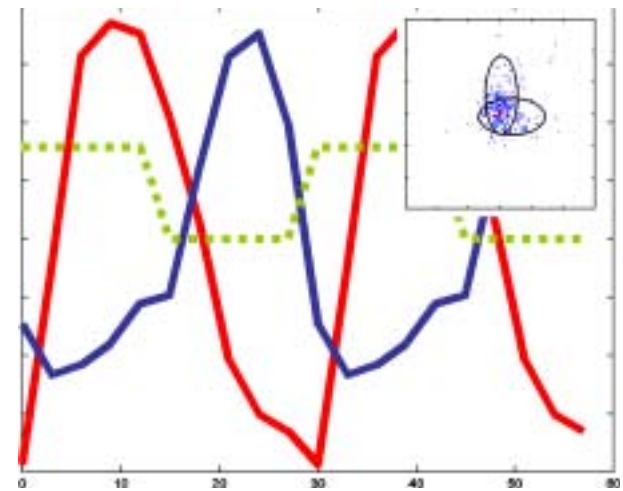

Figure 1. Two major independent components (red and blue), the stimulus profile (green) and distribution of the responses projected onto the plane defined by two major principal components. Notice that the responses are clustered along horizontal and vertical directions revealing the independent components.
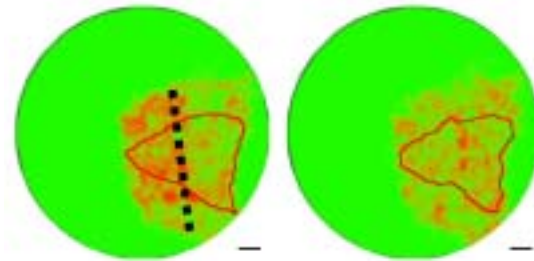

Figure 2. Magnitudes of the first (left) and second (right) independent components. The area outlined by red curve corresponds to the visual area V1.

shown in Fig. 1.

The magnitudes of the independent components from Fig. 1 across a region of interest covering V1 and V2 visual areas is shown in Fig. 2. The first, excitatory component shows higher magnitude in the left part of V1 area, which corresponds to central part of the visual field. The second, inhibitory component is distributed more uniformly across all eccentricities. This result suggests that the excitatory response component is local by nature. The inhibitory response component on the other hand, is global, and is present in the excited areas as well.

CONCLUSION

Independent Component Analysis reveals local inhibition and global excitation in the BOLD response.

REFERENCES

1. C.-C. Chen and C. W. Tyler, Statistical properties of BOLD magnetic resonance activity in the human brain. Neuroimage, 2003, 20(2):1096-1109

Stereomotion Perception: Is the hMT+/V5 Complex Involved?

Lora T. Likova, Christopher W. Tyler

The Smith-Kettlewell Eye Research Institute

INTRODUCTION

A basic problem for the visual system is to interpret the spatiotemporal events in the 3D world from the information provided by the two-dimensional retinal images. Binocular disparity is one of the strongest sources of 3D information, and disparity changes over time generate a percept of stereoscopic motion in depth - termed stereomotion. Stereomotion is a unique form of motion derived from stereoscopic cues that provides a natural paradigm for exploring the interactions between motion and stereo mechanisms. However, it is not known how stereomotion is processed by the human brain. To our knowledge, this study is the first fMRI study of stereomotion in human brain. We focused on the hMT+/V5 complex in the lateral occipital cortex, which is known to support both motion and disparity processing in primates. Does the motion complex process non-cyclopean stereomotion as well?

METHODS

Stimuli. The stereoscopic non-cyclopean stimuli were generated in the form of repetitive autostereograms. Stereoscopic Conditions. C1: Stereomotion contrasted to disparate lateral motion; C2: Stereomotion vs stationary disparate surface; C3: Stereomotion vs lateral motion at the horopter.

Control Non-Stereoscopic Condition. To test for potential monocular artifacts, the same displays for conditions C1 and C2 were observed non-stereoscopically in two control conditions – C4 and C5, respectively. Thus those control conditions did not produce stereomotion, but lateral motion with monocular images identical to the stereomotion conditions C1 and C3.

FUNCTIONAL MRI

The fMRI responses were collected on the Lucas GE Signa 3T scanner with a custom surface coil in 22 near-coronal slices spanning the posterior half of the brain at 3 sec TR, 2.5 x 2.5 x 3 mm voxels. The test-null stimuli were alternated for 9s each in 8 blocks. The retinotopic areas, as well as the hMT+/V5 were defined in separate scans.
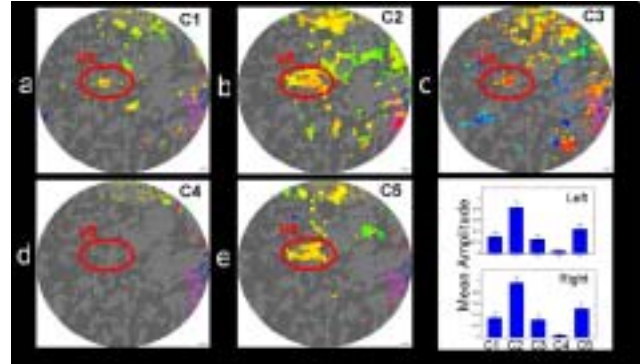
RESULTS

The basic results are summarized in Fig.1.

Figure 1. Comparison of the activation in hMT+/V5 during all stereoscopic (C1, C2, C3) and non-stereoscopic (C4,C5) conditions Notice the restricted subregion near the anterior border of the motion complex (panels a, c), which was found to be stereomotion selective locus.

CONCLUSION

The data analysis showed that there is a stereomotion- specific area around the anterior border of V5 (see C1 and C3 in panels a, c). Neither disparity per se (C3) nor lateral motion components (C1, C3) had any effect on the activation in this region, implying that it is responding to the stereomotion rather than to the disparities present in the stereomotion condition or to any lateral motion. The non-stereoscopic mode (C4) further demonstrated that that activation belongs entirely to stereomotion, and not to any lateral motion artifact. The stereomotion-specific response located near the anterior border of the hMT+/V5 complex contributes to the understanding of stereomotion perception and of the interactions between motion and stereo mechanisms, as well as to the understanding of the organization of overlapping functionally distinct neuronal subpopulations.

Representation of Coherent Flow Patterns in Human Visual Cortex

Alex Wade, Mark Pettet, Vladimir Vildavski, Anthony Norcia

Smith-Kettlewell Eye Research Institute, San Francisco

INTRODUCTION

Many types of motion stimuli have been shown to cause activation in human visual area hMT+: the human homologue of a macaque complex including MT and MST. These include real coherent and incoherent motion but also motion imagery (*1*) and static images showing "implied motion" (for example, javelin throwers, leaping animals) (*2*). hMT+ would seem to be an important part of the motion processing pathway. In this study we examine the response of hMT+ to 'Glass patterns'. Glass patterns are dot dipole patterns generated by taking a random dot field and adding to it a geometrically transformed (for example, rotated or translated) copy of itself. These patterns appear random at a fine spatial scale but have a coherent global structure with the appearance of 'frozen motion'. Surprisingly, we find that hMT+ shows little or no response to such patterns despite the strong percept of motion that they elicit.

MATERIALS AND METHODS

fMRI data were collected on 6 observers using the 3T Signa system at the Stanford Lucas Center. Semi-coronal functional data slices with a resolution of 2.5x2.5x3mm were prescribed over occipital cortex covering extending to parietal and temporal cortex. Data were acquired using a custom posterior-head surface coil to increase the local signal to noise ratio. Two types of stimuli were tested: 'Slow' Glass patterns (updating once per second) and 'Dynamic Glass patterns' (updating at roughly 10Hz). Control patterns were random dot dipole fields matched in contrast, luminance, dot density, update frequency, dot spacing and size. In addition, the response to true coherent motion patterns similar to the Glass patterns was measured for each subject. Subjects performed a demanding coherence discrimination task during all scans to eliminate attentional confounds. All data were analyzed and visualized using the Stanford VISTA toolbox (http://white.stanford.edu/software).

RESULTS

As expected, area hMT+ showed strong response to real coherent motion when compared to incoherent motion. How-
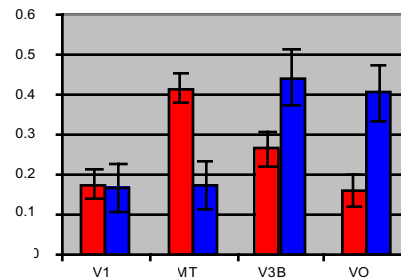

Figure 1: fMRI BOLD signal coherence levels in 4 visual areas in response to coherent motion (red) and dynamic Glass patterns (blue).

ever, the same region showed no responses to either slow or dynamic Glass patterns (fig 1). Although areas V1 through V3A did not show strong activation to this stimulus contrast, both types of Glass patterns generated strong focal activations outside hMT+ in both dorsal and ventral occipital cortex. The dorsal locus of activation is in a region corresponding to retinotopic area V3B while the ventral locus is in area VO anterior to area hV4.

CONCLUSION

The lack of response to dynamic Glass patterns in hMT+ is surprising. Firstly, dynamic Glass patterns have been shown to generate a psychophysical percept indistinguishable from real motion (*3*)and many studies show that activity in hMT+ is correlated with motion perception Secondly, it has been shown that adaptation to dynamic Glass patterns alters the response properties of neurons in macaque MT (*4*). From this study, it appears that a percept of directional motion without a defined polarity does not preferentially engage hMT+ relative to incoherent motion perception. We suggest that that activity changes in the neuronal population of MT may signal coherent motion direction polarity rather than motion *per se*. Finally, we demonstrate that coherent flow patterns preferentially activate two additional extrastriate areas (V3B and VO) not normally associated with the motion pathway. These areas support a percept of coherent and directional motion with ambiguous polarity.

REFERENCES

1. R. Goebel, D. Khorram-Sefat, L. Muckli, H. Hacker, W. Singer, *Eur J Neurosci* **10**, 1563-73 (May, 1998).
2. Z. Kourtzi, N. Kanwisher, *J Cogn Neurosci* **12**, 48-55 (Jan, 2000).
3. J. Ross, D. R. Badcock, A. Hayes, *Curr Biol* **10**, 679-82 (Jun 1, 2000).
4. B. Krekelberg, S. Dannenberg, K. P. Hoffmann, F. Bremmer, J. Ross, *Nature* **424**, 674-7 (Aug 7, 2003).

Cortical Area KO is Specialized for Depth Structure

Christopher W. Tyler, Lora T. Likova, Leonid L. Kontsevich, Alex R. Wade

Smith-Kettlewell Eye Research Institute, Fillmore Street, San Francisco CA 94115

INTRODUCTION

Functional MRI studies have identified a cortical area KO between retinotopic area V3A/B and motion area V5 in human cortex as particularly responsive to motion-defined, or kinetic borders (van Oostende et al., 1997). Zeki, Perry & Bartels (2002) have questioned this conclusion, finding responses in the same cortical region to static forms presented via color grating borders. To determine the response of the KO area to more general aspects of structure, we used stereoscopic depth borders and disparate planes with no borders, together with three stimulus types that evoked no depth percept: luminance borders, line contours and illusory-phase borders. Responses to these stimuli were compared with the responses in areas that have been variously associated with disparity processing in neurophysiological and fMRI studies.

MATERIALS AND METHODS

The fMRI responses were collected with 2D spiral acquisition from a custom occipital surface coil in a GE Signa 3T scanner. There were 23 coronal slices at 3 s TR, with TE of 30 ms and flip angle 90˚, providing 2 x 2 x 3 mm voxels through the occipital cortex. Test and null stimuli alternated for 9 s each in 18 blocks per scan. Other than fixation, no motor task was imposed, in order to limit the differential brain response to sensory processing signals and avoid confounding the perceptual responses with motor or decision processing.

RESULTS

The strongest responses in area KO were to stimuli containing depth structure from either disparity or motion cues, but it showed negligible responses to luminance-based contour stimuli and to edgeless disparity stimuli.

CONCLUSION

We conclude that area KO is best regarded as a primary center for the generic representation of depth structure rather than any kind of contour specificity.
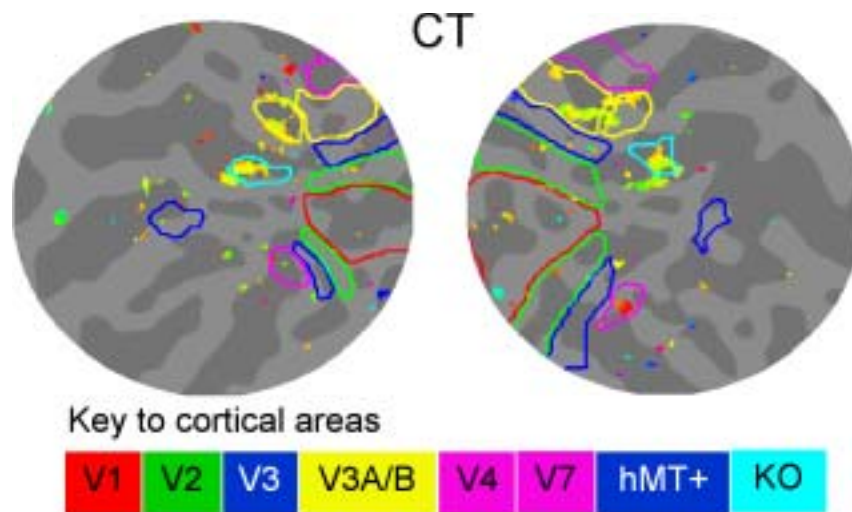

Fig. 1. Flatmaps of the posterior pole of the two hemispheres showing synchronized response to stereoscopic structure (yellowish phases) localized to V3A/B and KO

REFERENCES

Zeki, S., Perry R. J., & Bartels A. (2003) The processing of kinetic contours in the brain. Cereb. Cortex 13, 193-203.

Van Oostende S., Sunaert S., Van Hecke P., Marchal G. & Orban G.A. (1997) The kinetic occipital (KO) region in man: an fMRI study. Cereb. Cortex 7, 690-701.

CARDIOVASCULAR IMAGING

Generalized Reconstruction and Correction of Gradient Field Errors in Phase Contrast MRI

M. T. Alley[1], M. Markl[1], C.J. Elkins[2], N. J. Pelc[1]

Departments of [1]Radiology and [2]Mechanical Engineering

INTRODUCTION

Ideally, the gradients used in encoding spin information in MR imaging experiments are spatially uniform throughout the entire imaging field-of-view (FOV). In reality, any aberrations in the gradient uniformity cause geometric distortions in the image data. These distortions are most apparent near the edges of the FOV, and have been shown to affect the first moments used to encode flow or motion [1]. Any error in the strength or direction of the local gradient from its ideal value is directly reflected in the strength or direction of the first-order gradient moments and thus in the velocity encoding. Therefore, gradient field distortions can lead to considerable deviations between the designed encoding and the actual encoding in PC-MRI. We demonstrate the implementation of a set of tools to automate the correction of these errors in phase-contrast data.

METHODS AND MATERIALS

Data were acquired using a flow phantom oriented so that the direction of flow was along the axis of the main magnetic field. The flow tube was positioned at a radius of approximately 16 cm from the isocenter of the magnet in the axial plane. An imaging FOV of 36 cm was used in the acquisition. A computer controlled flow pump was used to provide constant laminar flow rates, and the tube length of 2 meters was chosen so that the velocity profiles were fully developed before entering the imaging volume. The phantom experiments were done using three-directional velocity encoding. To correct the phase contrast data the algorithm from Markl et al. [1] was implemented in our stand-alone reconstruction routine.

RESULTS

Figure 1 shows sample results from one phantom experiment. Because the flow tube was positioned at the edge of the FOV, the flow was subject to the pronounced distortions in the strengths of the imaging gradients. This is clearly apparent in the image of the uncorrected data where it is seen that the flow enters the tube at a nonphysical angle of approximately 45˚. The corrected data show that the expected flow pattern has been recovered.

CONCLUSIONS

Accurate reconstruction of velocities from PC-MRI data can be achieved if three-directional velocity encoding is performed and a matrix-based, generalized correction is applied. This is potentially a very important problem, as for fields-of-view of 40 cm^3, directional information can be off by as much as 45˚, and magnitude information can be off by as much as 67%. We have made it possible to correct these errors with a stand-alone program. This now makes it possible to correct any set of independently acquired phase-contrast data.

REFERENCES

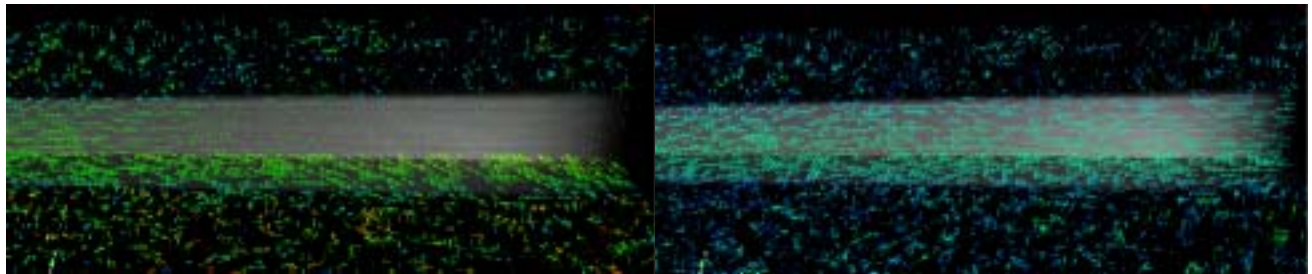[1] Markl M, et al., Magn Reson Med **50**:791-801 (2003).

Figure 1: Flow in the uncorrected and corrected velocity data. The flow travels from right to left in each image. The green arrows in the uncorrected phantom data on the left demonstrate that the errors in the directional information can be close to 45˚. The blue arrows in the corrected data on the right shows that the expected laminar flow pattern has been recovered.

Pulmonary and Caval Blood Flow Characteristics During Rest and Cycling Exercise Using Exercise-MRI

Christopher Cheng, Robert Herfkens, Charles Taylor, Jeffrey Feinstein

Departments of Mechanical Engineering, Radiology, and Pediatrics

INTRODUCTION

Medical imaging for diagnostic testing in patients with congenital heart disease are nearly always conducted while supine and at rest – conditions not representative of typical daytime hemodynamics. Upright exercise blood flow measurements may prove valuable in the assessment of these patients, but data from normal subjects is first required.

MATERIALS AND METHODS

Using the General Electric 0.5T interventional-magnet, a custom magnetic resonance-compatible exercise cycle and cine phase-contrast techniques, time-resolved blood flow velocities were measured in the right (RPA), left (LPA), and main (MPA) pulmonary arteries and superior (SVC) and inferior (IVC) vena cavae of ten healthy 10-14 year-olds. Measurements were made at seated rest and during cycling exercise (150% resting heart rate), and mean blood flow (L/min) and reverse flow index were computed from the velocity data.

RESULTS

With exercise, RPA and LPA mean flow increased from 2.0 ± 0.5 to 3.7 ± 0.7 L/min ($p<0.05$) and 1.6 ± 0.4 to 2.9 ± 0.8 ($p<0.05$) L/min, respectively, while SVC and IVC flow increased from 1.5 ± 0.2 to 1.9 ± 0.6 L/min ($p=0.054$, NS) and 1.6 ± 0.4 to 4.9 ± 1.3 L/min ($p<0.05$), respectively. Pulmonary reverse flow index (rest vs. exercise) decreased with exercise: MPA: 0.014 ± 0.012 vs. 0.006 ± 0.006 ($p=0.134$, NS), LPA: 0.041 ± 0.019 vs. 0.014 ± 0.016 ($p<0.05$), RPA: 0.005 ± 0.004 vs. 0.00 ± 0.00 ($p<0.05$).

CONCLUSION

While relative flow distribution between the right and left lungs (56% vs 44%) remained consistent, IVC flow increased about three times more than SVC flow from rest to upright cycling exercise. Also reverse flow observed in the MPA appears to originate predominantly from the LPA.

13-year-old subject pedaling a custom MR-compatible exercise cycle in the GE 0.5T interventional MRI during blood flow imaging in the pulmonary arteries and vena cavae.
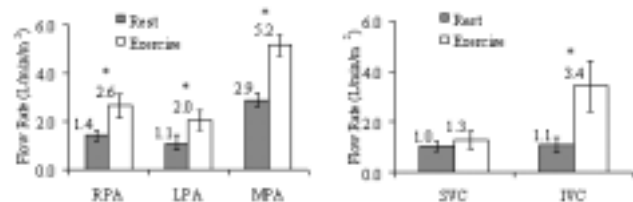
Average mean flow rate (scaled to body surface area) to the right, left, and main pulmonary arteries (RPA, LPA, MPA) and in the superior and inferior vena cavae (SVC, IVC) at rest and during exercise. * Denotes statistical significance between rest and exercise conditions ($p < 0.05$).

REFERENCES

Cheng CP, Herfkens RJ, Lightner AL, Taylor CA, Feinstein JA. Blood flow conditions in the proximal pulmonary arteries and vena cavae in healthy children during upright seated rest and cycling exercise, quantified with MRI. In press Am J Physiol Heart Circ Physiol

Computational Modeling of Blood Flow and Pressure in the Presence and Absence of Pulmonary Arterial Stenosis

Ryan L. Spilker, Mary T. Draney, Michael Markl, Robert J. Herfkens, Jeffrey A. Feinstein, Charles A. Taylor

Departments of Mechanical Engineering, Radiology, Pediatrics, Surgery

INTRODUCTION

Accurate simulations of blood flow in the pulmonary arteries will enable physicians to predict the outcomes of various treatments of cardiovascular diseases. We have applied a finite element method to solve the one-dimensional equations governing blood flow [1] in elastic vessels to the resolvable pulmonary arteries from a set of porcine MRA data. We compared simulations of blood flow in the presence and absence of a unilateral pulmonary arterial stenosis to experimentally measured values.

MATERIALS AND METHODS

Vascular anatomy and flow data were obtained using a 1.5T MRI system. A geometric model of the resolvable pulmonary arteries was created from a set of MRA data using custom image segmentation and geometric modeling software. Flow in the pulmonary arteries was quantified with 3D cine phase contrast (4D-Flow) imaging [2] and supplemented with 2D cine phase contrast acquisitions in the MPA, LPA, and RPA. Flow at the inlet of the model was set to equal that measured in the experiment. The relationship of the pressure and flow waveform at each outlet of the model was forced to satisfy the analytically derived impedance that represents flow in an arterial tree generated from a morphometric data set of human pulmonary arteries [3]. The size of each tree corresponded to the size of the outlet at which the impedance was applied. The result was a model that represented the entire pulmonary arterial tree. Energy losses caused by blood flowing through the stenosis not represented by the 1D equations were also accounted for in the simulation.

RESULTS

The fraction of flow to each lung was well predicted in the presence and absence of the stenosis. The left lung received 57% of the pulmonary blood flow when the RPA was left in its original state and 85% when a stenosis was induced. The simulations predicted values of 58% and 84%, respectively. The mean MPA pressure predicted by this simulation was 31 mmHg in the absence of a stenosis and 42 mmHg in its absence, while the measured values were 24 mmHg and 29 mmHg, respectively.

DISCUSSION

While the flow split measurements and predictions compared well, the pressure predictions showed significant error. Regarding these results, it should be noted that only the size of each outlet was used to initialize the generation of its downstream tree. Using only the anatomic characteristics of the pulmonary arteries, which can be resolved from the MRA data, does not seem to provide an accurate measure of the hydraulic resistance of the lungs. However, the change in pressure resulting from the correction of a stenosis is a clinically relevant measure of the success of a treatment. It should also be noted that the measured MPA flow waveform in the absence of a stenosis was prescribed for both simulations. In reality, the flow generated by the right ventricle decreased when the stenosis was introduced. Prescribing this flow at the inlet would result in a lower mean MPA pressure in the simulation including the stenosis. This shortcoming of neglecting the behavior of the heart may be remedied by the inclusion of a heart model in the simulation in place of the prescribed flow waveform. Further experiments and model developments are needed to demonstrate the clinical applicability of these methods.

REFERENCES

1. Wan J, Steele BN, Spicer SA, Strohband S, Feijoo GR, Hughes TJR, Taylor CA. A One-Dimensional Finite Element Method for Simulation-Based Medical Planning for Cardiovascular Disease. Comp Meth Biomech & Biomed Eng 2002; 5:195-206.
2. Markl M, Chan FP, Alley MT, Wedding KL, Draney MT, Elkins CJ, Parker DW, Wicker R, Taylor CA, Herfkens RJ, Pelc NJ. Time-Resolved Three-Dimensional Phase-Contrast MRI. J Magn Reson Imag 2003; 17:499-506.
3. Huang W, Yen RT, McLaurine M, Bledsoe G. Morphometry of the Human Pulmonary Vasculature. J Appl Physiol 1996; 81:2123-33.
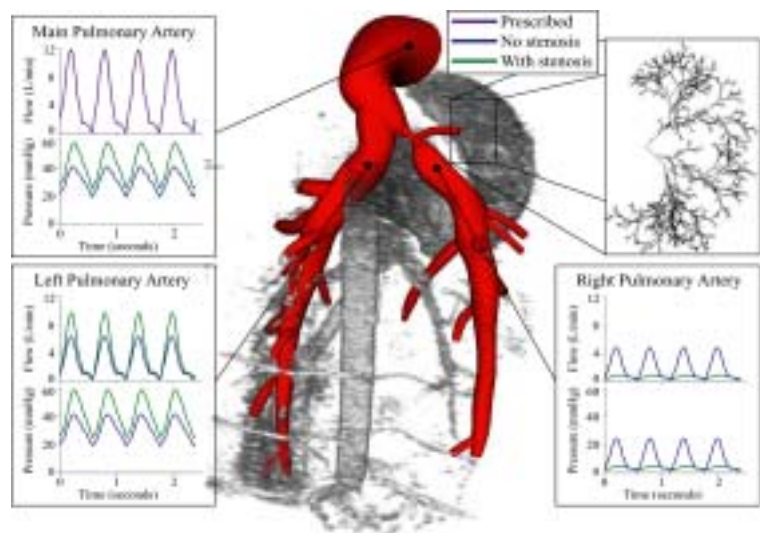
A simulation was performed in a model of the porcine pulmonary arteries shown in red by prescribing the flow in the MPA measured in the absence of stenosis.

Myocardial Infarct Imaging using a 3D SSFP Cine Sequence

M. T. Alley, R. Bammer, N. J. Pelc

Department of Radiology

INTRODUCTION

The prognosis and care of patients with acute myocardial infarction depends on the ability to assess the adequacy of reperfusion after injury. It has been shown that nonviable or infarcted tissue will exhibit delayed hyper-enhancement in the presence of contrast agents. The standard imaging protocol used today involves an inversion-recovery (IR) pulse in a fast, segmented 2D GRE-based sequence. The problems with this approach include patient fatigue, misregistration of the 2D slices, and the fact that the contrast concentration will change over the long time period necessary to complete the scan. We propose to address these issues by using an IR pulse in a 3D cine SSFP acquisition. The reconstructed images would then show both the temporal dynamics of cardiac motion at the same time as the T_1 recovery characteristics of the different tissues present.

METHODS AND MATERIALS

We have modified our 3D SSFP cine sequence by adding the ability to play out a non-slice selective IR pulse at the onset of every N RR intervals. The number N of cardiac cycles between IR pulses can be chosen by the user to assure adequate time for T_1 recovery.

RESULTS

Initial results from a normal volunteer are shown Figure 1. For this data set 16 5-mm sections were obtained with a TR of 4 ms, leading to a true temporal resolution in the dataset of 64 ms. The in-plane image matrix size was 256 by 160. Each IR pulse was separated by 2 cardiac cycles. The 3D image volumes were reconstructed at a temporal spacing of 35 ms. In the first frame, the artifacts from the disruption of the steady state are clearly visible. However, image quality is significantly improved after just 35 ms. The remaining frames show both the changing image contrast as the different tissues undergo T_1 relaxation, as well as the motional dynamics in the cardiac cycle.

CONCLUSIONS

An advantage of this approach is that a prep scan is no longer needed to determine an appropriate myocardial inversion time. Furthermore, the reconstruction can be carried out at user-selectable time points, thus providing the ability to fine-tune the image contrast. Finally, the volumetric acquisition is advantageous because of the reduced patient effort and interaction needed during the course of the scan.
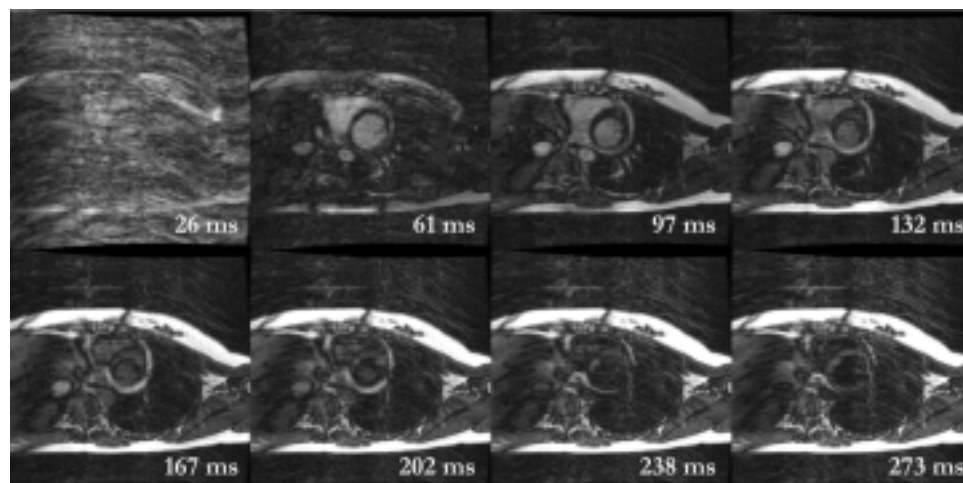

Figure 1: Eight frames from an IR-prepped 3D SSFP cine study. All images are at the same spatial location. The time since the onset of the R-wave is shown in the lower corner of each image. The first frame shows the initial disruption of the steady state, followed by the clearly visible T1 recovery patterns of the different tissues.

Parallel Cardiac CINE Imaging: Application to "Dixon" Water-Fat Separation and Steady-State Free Precession (SSFP)

S. B. Reeder[1], C. A. McKenzie[2], M. Markl[1], H. Yu[1], N. J. Pelc[1], J. H. Brittain[3]

[1]Radiology, Stanford University, [2]Radiology, Beth Israel Deaconess Medical Center and Harvard Medical School, [3]GE Medical Systems, Applied Science Lab-West, Menlo Park, CA

INTRODUCTION

SSFP is a rapid, short TR imaging technique well suited for cardiac imaging because of its high SNR and excellent blood-myocardial contrast (1,2). However, SSFP is limited by the fact that water and fat both appear bright and are difficult to distinguish. A recently described three-point "Dixon" water-fat separation technique has been applied to multi-coil cardiac SSFP CINE imaging (3), which, unfortunately, requires a threefold increase in the minimum scan time. This increase limits the achievable spatial and temporal resolution of this method. Parallel imaging methods (4,5,6) exploit differences in the spatial sensitivity profiles of multiple receiver coils to resolve aliasing ambiguities. The purpose of this work was to apply parallel imaging techniques to reduce the required minimum amount of data.

THEORY

In this work, we selected a TE increment of 0.9ms at 1.5T as a good compromise between maximizing SNR performance of the water-fat decomposition, and minimizing banding artifacts by maintaining a TR of 5ms or less. "Unwrapping" of under-sampled data obtained with the three-point method, as part of a parallel MRI acquisition must be performed for each of the three images. The reconstruction of full field of view (FOV) images must accurately preserve the phase of the three complex images.

MATERIALS AND METHODS

Image acquisition was performed at 1.5T (Signa CV/i, GEMS, Milwaukee, WI) with a retrospectively ECG-gated CINE SSFP sequence that acquires sequential sets of CINE images at 3 different echo times. 20 CINE phases were retrospectively reconstructed. A four-element phased array torso coil was used. Imaging parameters included: TRΞ5ms; TEΞ0.9, 1.8, 2.7ms; BW=±125kHz; FOV=32cm; Nx=256 (partial echo); views per segment ($Nseg$)= 16; temporal resolution=60-80ms. A first data set that was fully sampled in the phase encoding direction (FOV=32cm, Ny=128) was acquired in one breath-hold (27 heartbeats). An under-sampled data set (FOV=16cm, Ny=64) was acquired in a separate breath-hold (15 heartbeats). The multi-coil source images were reconstructed into combined full FOV images
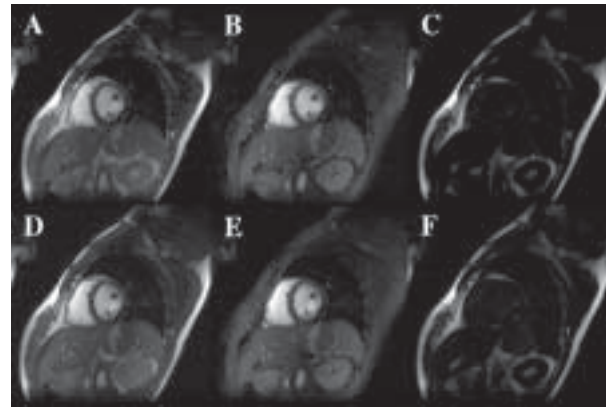

Figure 1: Short axis SSFP source (a), water (b) and fat (c) images reconstructed from under-sampled data with an acceleration factor of two. Source (d), water (e) and fat (f) images reconstructed from fully sampled data are shown for comparison.

with a hybrid generalized encoding matrix parallel imaging reconstruction (6). Separate water and fat images were calculated using the iterative decomposition method (3), and the process was repeated for all CINE phases and all slices.

RESULTS

Fig. 1 shows source (a), water (b) and fat (c) images (one of twenty phases) reconstructed from under-sampled data acquired in a normal volunteer. Source images reconstructed from under-sampled data had minimal artifact.

DISCUSSION AND CONCLUSION

The Dixon water-fat separation is a relatively efficient SNR method, with effective signal averaging close to three (3), so that losses in SNR from the parallel reconstruction are largely offset by the gains from the Dixon reconstruction method. Further work will be needed to clarify how to quantify SNR in the water and fat images. There are a number of ways in which the acquisition of low-resolution coil calibration data can be embedded into the acquisition of under-sampled data, such as variable k-space sampling directly into the pulse sequence acquisition to provide "self-calibrating" data sets (7). In addition, acquisition with phased array coils with a larger number of elements (e.g. 8) should permit acceleration factors such as 3 or higher.

Parallel imaging reduces the long minimum acquisition time needed for water-fat separation, while the high SNR efficiency of the "Dixon" decomposition offsets losses in SNR from the parallel imaging reconstruction.

REFERENCES

1. Oppelt, A. Electromedia 1986; 3:15-18.
2. Carr, JC et al Radiology 2001;219(3):828-834.
3. Reeder et al, MRM 2004; 51: 35-45
4. Sodickson, DK et al MRM 1997;38(4):591-603.
5. Pruessmann, KP et al MRM 1999; 4:952-62.
6. Sodickson DK et al. Med Phys 2001; 28:1629-43.
7. McKenzie, CA et al. MRM 2002; 47(3):529-38.

Asymmetric Echoes for Robust Fast Spin-Echo "Dixon" Water-Fat Separation

S. B. Reeder[1], Z. Wen[1], H. Yu[1], A. R. Pineda[1], A. Shimakawa[2], J. H. Brittain[2], G. E. Gold[1], C. F. Beaulieu[1], N. J. Pelc[1]

[1]Radiology, Stanford University, [2]GE Medical Systems, Applied Science Lab-West, Menlo Park, CA,

INTRODUCTION

Fat is bright with Fast Spin Echo (FSE) imaging and may obscure underlying pathology. "Dixon" water-fat decomposition method has gained popularity in combination with FSE, owing to its uniform fat-suppression and high signal to noise ratio (SNR) performance (1-4). Conventional Dixon methods acquire three echoes that are centered symmetrically about the spin-echo. We have recently shown that the noise performance of water-fat decomposition from symmetric acquisitions deteriorates when water and fat within a voxel are found in equal amounts (5). Such voxels commonly occur along water/fat interfaces as well as in normal or abnormal tissue such as fatty liver. We now demonstrate theoretically and with *in vivo* images that asymmetrically acquired echoes will prevent artifacts that degrade noise performance in locations where water and fat are equal.

THEORY

Fig. 1 plots the effective number of signal averages (NSA)(6,4), as a function of the echo shift (for 1.5T) with respect to the spin-echo for the first image (TE1) and the third image (TE3), when (a) water>>fat, and (b) water=fat. The second image (TE2) is acquired at the spin-echo (TE2=0). From Fig. 1b, it can be appreciated that there are many possible solutions that will provide estimates of water and fat with good SNR performance, and many combinations where decomposition performance will be poor. Symmetric echoes ($|TE1|=|TE3|$) lie along the dashed lines.

MATERIALS AND METHODS

Whole knee T2W FSE acquisition was performed at 1.5T (Signa TwinSpeed, GEMS, Milwaukee, WI) with approval of our IRB and informed consent. For a three-point symmetric acquisition, we used echo times of -1.2ms, 0, and 1.2ms. Based on Fig. 1b, asymmetric echo times of -1.8ms, 0, and 2.5ms, were chosen. Fat-saturated (NEX = 3) T2W FSE images were acquired for comparison. The same echo spacing was used for all imaging (15.6ms) for direct comparison.

RESULTS

Overall, image quality for both symmetrical and asymmetrical acquisitions was excellent, especially when compared
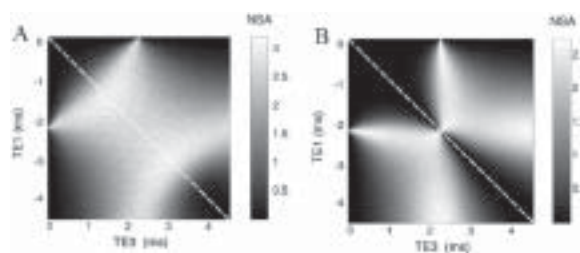

Figure 1: Effective NSA plotted against phase shift from TE_1 and TE_3 assuming the central echo occurs at the spin-echo and (a) water:fat=1:0, and (b) water:fat=1. The dashed lines represent symmetric echoes.
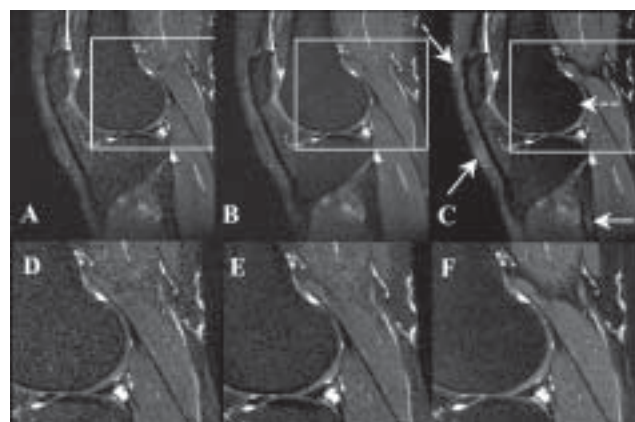

Figure 2: Calculated T2-weighed FSE water images for symmetric (a) and asymmetric (b) acquisitions, and FS-FSE (c) for comparison. Figs. 2d-f show magnified regions of Figs. 2a-c. Structured noise is seen in the marrow and soft tissue of the symmetric echo, and irregular interfaces between muscle and fat are best seen in (d). Failure of fat saturation is seen in the FS-FSE image (arrows), as well as shading within the posterior aspect of the lateral femoral condyle (dashed arrow).

with fat-saturated FSE. Closer inspection of these images (Figs 2d-f) shows structured noise within the bone marrow and subcutaneous tissues, and irregular borders between water and fat, in the symmetric echo image. These abnormalities are markedly improved with the asymmetric acquisition.

DISCUSSION

Future work will analyze different echo time combinations that maintain adequate noise performance at all proportions of water and fat, while minimizing echo spacing.

REFERENCES

1. Hardy et al, JMRI ;1995 Mar-Apr;5(2):181-5.
2. Rybicki et al, AJNR; 200; 22(9):1798-802.
3. Ma et al, MRM; 2002; 48(6):1021-7.
4. Reeder et al, MRM 2004; 51: 35-45
5. Wen et al, ISMRM, 2003, pg 483.
6. Glover et al, JMRI; 1991; 1:521-530.

"Dixon" Water-Fat Separation for Musculoskeletal Imaging with Fast Spin-Echo at 3T

S. B. Reeder[1], H. Yu[1], A. Shimakawa[2], J. H. Brittain[2], J. W. Johnson[2], N. J. Pelc[1], G. E. Gold[1]

[1]Department of Radiology, Stanford University; [2]GE Medical Systems, Applied Science Lab-West, Menlo Park, CA

INTRODUCTION

Fast spin-echo (FSE) imaging is used routinely for most musculoskeletal (MSK) imaging protocols. However, non-uniform fat-saturation is common because of Bo and B1 in-homogeneities with currently used spectrally selective fat-saturation pulses. This work compares the iterative least-squares "Dixon" method (4) combined with FSE with conventional T2W FS-FSE.

MATERIALS AND METHODS

Whole knee image acquisition was performed at 3.0T (Signa vH/i, GEMS, Milwaukee, WI) in 10 knees from 5 healthy volunteers (avg. age 32.8, range 26-40, 3 M, 2 F) with informed consent and approval by our IRB. We used a modified T2W fast-spin echo pulse sequence to acquire three images with echo shifts of –600us, 0, and 600us from the center of each spin-echo. A standard single element extremity coil was used for all imaging. Echo time shift was changed for each TR to interleave measurements.

For comparison, conventional fat-saturated (FS) T2W-FSE images were acquired at the same locations in all patients. Imaging parameters for both sequences included: TR=5s, BW=±31kHz, FOV=16cm, slice=2.5mm, Nx=512, Ny=256, echo train length=10. Total scan time for one knee was 5:05min with both sequences. The effective TE (TEeff) was 39ms for the Dixon acquisition and 42ms for conventional FS-FSE; differences in TEeff were caused by slight differences in echo spacing between the two sequences. Three signal averages (NSA) was used for the FS-FSE technique to facilitate comparison of SNR between the two sequences, for constant scan time. Of note, the lack of fat-saturation pulses in the Dixon approach allowed the acquisition of 10% more slices than in conventional FS-FSE, within the same scan time.

Images were reconstructed with an on-line program based on the iterative least-squares algorithm (4). For each method, we measured the SNR of cartilage and gastrocnemius muscle, and contrast-to-noise ratio (CNR) between cartilage and joint fluid. Images were scored by consensus by two experienced radiologists on 4-point scales (0-3) for both fat-suppression and diagnostic quality. A paired Student t-test was performed to compare quantitative measurements (SNR, CNR). Qualitative fat suppression and diagnostic quality scores were compared with a Wilcoxon paired signed rank test. To evaluate statistical significance $p<0.05$ was used for both quantitative and qualitative analyses.
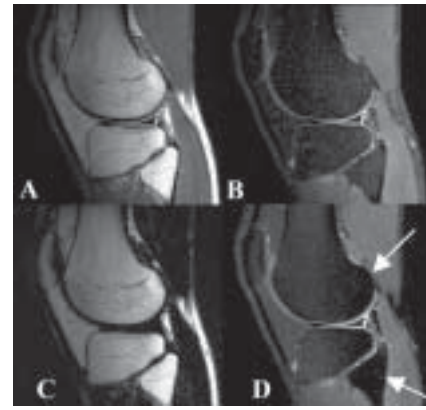

Figure 1: Source (a), calculated water (b), calculated fat (c) Dixon images, compared with a FS-FSE image (d) from the same slice. Excellent image quality is seen with; however, shading can be seen in the posterior aspect of the lateral femoral condyle and proximal fibula (arrows).

	SNR Muscle	SNR Cartilage	CNR Cart/Fluid	FS Score	DQ Score
Dixon-FSE	13.7±3.5*	13.7±3.7	22.4±7.3	2.8*	2.4
FS-FSE	12.0±3.9*	14.4±2.7	24.2±7.1	2.1*	2.7

Table 1: Comparison of SNR, CNR, Fat-Suppression (FS) Score, and Diagnostic Quality (DQ) Score for Dixon-FSE compared to FSFSE for 10 knees. *Statistically different (p<0.05).

RESULTS

Fig. 1 shows example images from one volunteer. Note the subtle shading of signal in the posterior aspect of the femur in the fat-saturated image. This effect is not seen on the calculated water image from the Dixon decomposition. Table 1 lists the SNR measurements for muscle, cartilage, and the CNR for cartilage and fluid, as well as the qualitative fat-suppression and diagnostic quality scores. All measurements were statistically similar except SNR of muscle and the FS score, both of which were higher for Dixon-FSE (p<0.05). Higher SNR in muscle was attributed to suppression of normal muscle by the fat-saturation pulse in regions of Bo inhomogeneity.

The average diagnostic quality was slightly lower for FSE-Dixon. The primary cause of this difference appears to be higher severity of flow related ghosting artifacts from the popliteal artery.

DISCUSSION

The Dixon method is highly SNR efficient and the additional scan time required for this method is reflected in the SNR of the calculated water and fat images; the two methods had comparable SNR performance. For high-resolution imaging, as was used in this study, standard clinical protocols often require NSA=3; in this scenario, no additional time is needed for the Dixon method. The effects of blurring from lengthened echo spacing was not observed in this study.

REFERENCES

1. Smith et al, JCAT, 1994; 18:209-213
2. Meyer et al, MRM,1990; 15:287–304
3. Hauger et al, Radiology, 2002; 224(3):657-63
4. Reeder et al, MRM 2004; 51: 35-45

Robust Field Map Estimation in a Dixon Water-Fat Separation Algorithm with Short Echo Time Increments

Huanzhou Yu[1,2], Scott B. Reeder[1], Ann Shimakawa[3], Jean H. Brittain[3], Norbert J. Pelc[1,2]

Departments of [1]Radiology and [2]Electrical Engineering, [3]ASL-West, GE Medical Systems, Menlo Park, CA

INTRODUCTION

In an extension of the 3-pt Dixon method [1], an iterative method is used to estimate the field map [2]. However, in certain circumstances the field map estimated may be incorrect, leading to imperfect water fat separation. The aim of this work is to propose a more robust field map estimation algorithm.

MATERIALS AND METHODS

We model the signals of each pixel at echo time TEn (n = 1, 2, 3) as: $S(TE_n) = (W + F\Delta e^{j2\pi Df TE_n})e^{j2\pi y TE_n}$, where W and F are water and fat components. *Df* is the off-resonance frequency of fat relative to water. *y* is the field map. It can be shown that if the pixel is purely water or fat, there are two solutions of the field map. If the true solution is (W_t, F_t, y_t), the other solution is described as $(F_t, W_t, y_a = y_t - Df)$ for a water pixel, or $(F_t, W_t, y_a = y_t + Df)$ for a fat pixel. If the initial value of the iterative field map estimation at a pixel is closer to y_a than to the true value y_t, the algorithm may converge to y_a. In that case, the estimated values for water and fat will be swapped. In general, when water and fat are mixed, y_a is in terms of either exact solution or local minimum.

In our improved method, we use a region-growing algorithm guided by a low-resolution Dixon reconstruction:

1) The source images are smoothed and down-sampled to a low-resolution set of source images.

2) The previous algorithm [2] is performed on the low-resolution source images to yield a low-resolution field map.

3) A signal threshold binary mask is generated from the low resolution source images and applied to the low-resolution field map.

4) A pixel with the median value is identified in the signal-thresholded low-resolution field map. This pixel corresponds to a small group of pixels in original resolution images. The pixel with the highest signal among this small group is selected as the starting pixel.

5) The field map *y* at this starting pixel is estimated using the result of the low resolution fit as the initial value for the iteration.

6) The field map term, *y,* of a pixel next to the starting pixel is estimated using the field map of the starting pixel as the initial value.

7) This procedure is repeated, growing the region by using the result of the previous pixel as the initial value for a neighboring pixel until all the pixels are estimated.

RESULTS

Figure 1 shows the reconstruction of a dataset using the original field map estimation method (b-d) and the new method (f-h). The data is from a FSE Dixon acquisition at 1.5T with echo times of [-1.5ms, 0, 1.5ms]. By comparison, the new method successfully resolves the ambiguity problem.
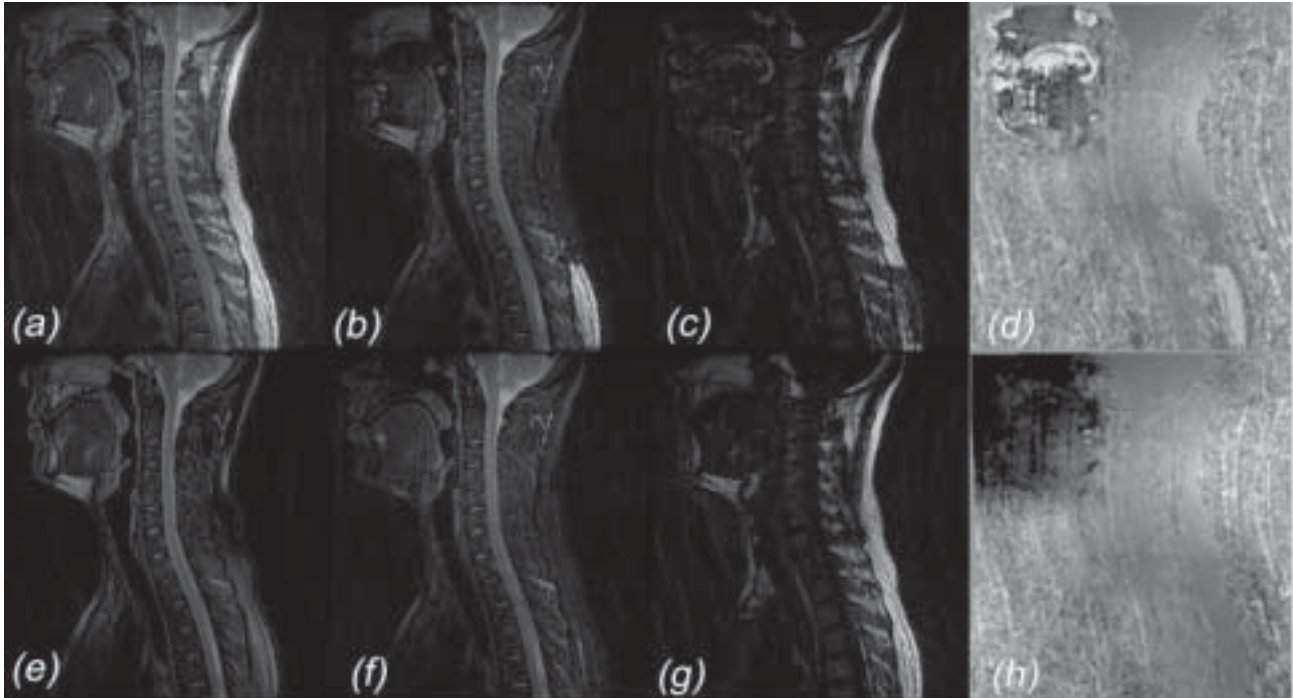

Figure 1: A sagittal slice of the cervical spine: (a) one of the source images; (b-d) water (b), fat (c) and field map (d) using original method; (e) fatsat image with NSA=4; (f-h) separated water (f), fat (g) and estimated field map (h) using the new method.

CONCLUSION

We have shown that an improved field map estimation method can increase Dixon method's immunity to ambiguity.

REFERENCES

[1] Glover et al, JMRI 1991; 1: 521-530.
[2] Reeder et al, MRM 2004; 51: 35-45
[3] Reeder et al, AJR 2003; 180: 357-362

Implementation and Noise Analysis of Chemical Shift Correction for Fast Spin Echo Dixon Imaging

Huanzhou Yu[1,2], Scott B. Reeder[1], Ann Shimakawa[3], Garry E. Gold[1], Norbert J. Pelc[1,2], Jean H. Brittain[3]

Departments of [1]Radiology and [2]Electrical Engineering, [3]ASL-West, GE Medical Systems, Menlo Park, CA

INTRODUCTION

The chemical shift artifact causes a spatial shift of fat tissues with respect to water in the readout direction. We will describe a method to obtain FSE chemical-shift free images during the Dixon water-fat separation algorithm [1].

MATERIALS AND METHODS

The reconstructed position of species with off-resonance frequency of Of is shifted in the readout direction by $Ox = Of \leftarrow Nx / (2 \leftarrow rBW)$. Nx is the number of pixels of the image matrix in the readout direction. rBW is the receiver bandwidth. To correct for chemical shift, the separated fat image is shifted back by $-Ox$ in the readout direction, by multiplying each of the k-space readout lines by a phase term $e^{j2 \leftarrow Ox k_x / Nx}$. The corrected fat image then is added to the water image to obtain the chemical shift free combined image.

To study the SNR of the combined image, consider a pixel with water and fat components W and F. The corresponding pixel in separated water image has signal W and noise of $\hat{\Uparrow}_w$, while in the fat image, it has signal F and noise of $\hat{\Uparrow}_f$. The values for $\hat{\Uparrow}^2_w$ and $\hat{\Uparrow}^2_f$ for symmetric Dixon imaging [1] are given in [2]. We define $r = \hat{\Uparrow}^2_f / \hat{\Uparrow}^2_w$. We assume the noise distribution in the real and imaginary channels of the separated water or fat images are zero mean Gaussian, which is

a good approximation even though the processing in the 3-point Dixon decomposition can be nonlinear. In the magnitude images, however, the noise standard deviation can be described as $m_f \leftarrow \hat{\Uparrow}_f$ or $m_w \leftarrow \hat{\Uparrow}_w$ for fat and water images respectively. The scale factors, m_f and m_w, are given in [3]. After the spatial translation for correction of chemical shift the noise in the fat and water signals in a single pixel are uncorrelated. Therefore, we can expect the noise in the pixel of the combined image has standard deviation of $\hat{\Uparrow}^2_c = \hat{\Uparrow}^2_w (m_w^2 + r \leftarrow m_f^2)$. Hence, $SNR_c/SNR_w = 1/(m_w^2 + r \leftarrow m_f^2)^{1/2}$ (SNR_c and SNR_w represent SNR of the combined and water images). For the optimal OTE (1.5ms at 1.5T) [1], and a purely water pixel with high SNR ($W >> \hat{\Uparrow}_w$, F = 0), $m_w \theta 1$, $m_f = 0.655$ [3] and $r = 2$ [2], thus SNR_c/SNR_w is 0.73. When a pixel contains approximately the same amount of two species, r, m_f and m_w all approach 1 [2, 3], and consequently SNR_c/SNR_w approaches 0.707.

RESULTS

Results from 2 volunteers are shown. Figure 1 compares a portion of source image to chemical shift corrected image of a wrist. The fat in has a chemical shift of 8.11 pixels in the read-out direction (vertical). Figure 2 shows images of a knee at 3T, with a chemical shift of 3.6 pixels in the read-out direction (vertical).

CONCLUSION

Chemical-shift corrected images are a useful side product of a Dixon FSE acquisition. The SNR of the combined image has a moderate approximately 30% loss from the separated images.

REFERENCES

[1]. Reeder et al, MRM 2004; 51: 35-45
[2]. Wen et al, ISMRM 2003; 483
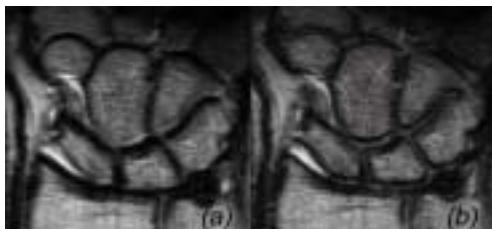[3]. Henkelman et al, Med. Phys. 1985; 12(2): 232-233

Figure 1: A FSE Dixon wrist slice at 1.5T with TEs=[-1.2, 0, 1.2]ms, rBW=6.94kHz and Nx=512. (a): the combined image without chemical shift correction; (b): with chemical shift correction.

Figure 2: A FSE Dixon knee slice at 3T with TEs= [-0.6, 0, 0.6]ms, rBW=31.25kHz and Nx=512. (a): the combined image without chemical shift correction; (b): with chemical shift correction; (c) separated water image

Cardiac CINE Imaging with "Dixon" Water-Fat Separation and Steady-State Free Precession (SSFP)

S. B. Reeder, M. Markl, H. Yu, J. C. Hellinger, R. J. Herfkens, N. J. Pelc1

Department of Radiology

INTRODUCTION

Conventional SSFP[1] is limited by the fact that water and fat both appear bright, possibly obscuring underlying pathology such as pericardial disease, fatty infiltration seen with arrhythmogenic right ventricular dysplasia (ARVD), or lipomatous myocardial neoplasms. Currently, fat suppression techniques used with other SSFP applications are impractical with cardiac SSFP imaging and are sensitive to field inhomogeneities.[2-4] "Dixon" methods achieve uniform separation of fat from water even in the presence of field inhomogeneities.[5] SSFP requires short TRs to prevent banding and flow artifacts caused by field inhomogeneities. To address this challenge, water and fat CINE cardiac images were decomposed from multi-coil SSFP images using an iterative least-squares algorithm, formulated for fitting data from images acquired at short TE values.[6]

MATERIALS AND METHODS

Image acquisition was performed at 1.5T (Signa CV/i, GEMS, Milwaukee, WI) with a retrospectively ECG-gated CINE SSFP sequence that acquires sequential sets of CINE images at 3 different echo times. A phased array torso coil was used in 3 volunteers except for one large patient (body coil). Informed consent was obtained and the study was approved by our IRB. Imaging parameters included: BW=±125kHz; FOV=32-38cm; Nx=224-256 (partial echo); Ny=128; $Nseg$=12-16, temporal resolution=60-80ms. 20 CINE phases were retrospectively reconstructed and breathhold time was 20-27 heartbeats per slice. In one volunteer, 3-point acquisitions were obtained with the TE increment varied from 0.3-1.4ms (TR=3.8-6.0ms), to measure the *NSA* behavior of the water-fat decomposition. In all other studies, the TE increment was 0.9ms and the three values of TE were approximately TE=0.8, 1.7, 2.6ms, with TR=4.7-5.2ms.

RESULTS

Fig. 1 plots the measured *NSA* for myocardium and subcutaneous fat, against TE increment. Measurements were averaged over all 20 cardiac phases, and are plotted with the theoretical *NSA* behavior,[5,6] demonstrating excellent agreement. Fig. 2 shows an example of water-fat separation in a patient with a pathology proven interventricular septal lipoma, and Fig. 3 shows a patient with chronic pericarditis on steroid therapy. Subjective evaluation found that images acquired with TR of approximately 5ms or less had acceptable levels of banding and flow artifacts.
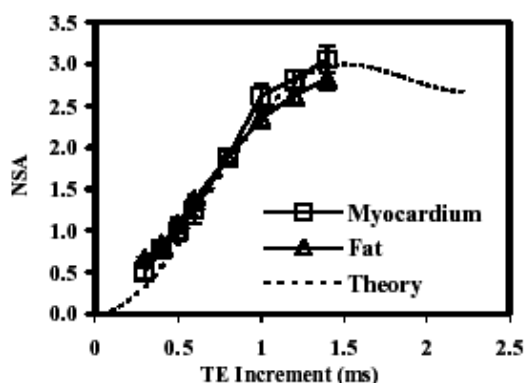

Figure 1: Measured NSA plotted against TE increment for myocardium and fat. Theoretical values are plotted as a dashed line.

Figure 2: Axial source (a), water (c), and fat (c) for one of 20 time frames from a patient with a pathology proven lipoma of the ventricular septum (arrow).
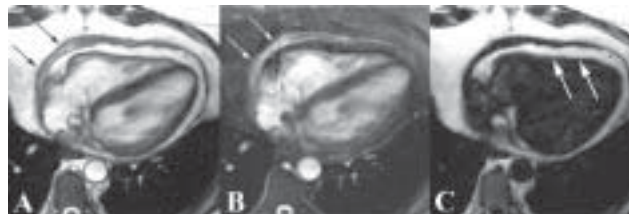

Figure 3: Axial source (a), water (c), and fat (c) images for one of 20 time frames from a patient with chronic pericarditis. Thick pericardium (small black/white arrows) separates pericardial fat (large white arrows) from epicardial fat.

DISCUSSION

Selection of TE increment was a trade-off between SNR performance and adequate image quality of the source images. It can be shown that a TE increment of 0.9ms decreases SNR by 17% from the maximum, and additional decreases lead to more substantial decreases in SNR.[5,6] At 1.5T, an increment of 0.9ms was a good compromise because it facilitated a TR of 5ms or less, to maintain low levels of artifact.

CONCLUSION

Multi-coil iterative "Dixon" techniques can be combined with SSFP cardiac CINE imaging to achieve excellent water-fat separation. This approach holds potential for clinical imaging applications that require uniform water-fat separation such as ARVD, lipomatous cardiac neoplasms, pericardial disease, and possibly coronary artery angiography.

REFERENCES

1. Oppelt, A. Electromedia 1986;3:15-18
2. Scheffler et al, 2001;45:1075-1080
3. Vasanawala et al, MRM,1999;42(5):876-883
4. Vasanawala et al, MRM, 2000;43(1):82-90
5. Glover et al, JMRI, 1:521-530.
6. Reeder et al, MRM 2004; 51: 35-4

Single Acquisition Water Fat Separation for SSFP Cardiac CINE Imaging: Feasibility Study

Huanzhou Yu[1,2], Scott B. Reeder[1], Michael Markl[1], Norbert J. Pelc[1,2]

Departments of [1]Radiology, [2]Electrical Engineering

INTRODUCTION

A recently proposed Dixon technique [1] has relieved the limitation of conventional Dixon [2] partially by allowing arbitrary echo time shifts. However, it still requires three acquisitions, which increases the scan time by three fold. We propose a single acquisition separation algorithm to achieve uniform fat-water separation with the ability to correct for field inhomogeneity with no increase in scan time.

MATERIALS AND METHODS

Water and fat spins rotate at different resonance frequencies. Let q_d denote the evolution of phase difference of water and fat at echo time TE. Therefore, the signal received can be modeled as: $S(TE) = (W + F \Delta e^{jq_d})e^{j2\pi(yTE + y_0)}$. W and F represent water and fat components in this pixel, and are real. y represents the local B0 field inhomogeneity, and y_0 denotes the initial phase of the signal at time zero. For SSFP, q_d at time TE is expected to be: *2pDf(TE – TR/2)*, where *Df* is the chemical shift of fat relative to water. In order to separate water and fat with only one acquisition, it is easily appreciated that when q_d is ±p/2, the separation will be optimal in terms of noise performance. Therefore, we will choose TE and TR such that q_d is close to ±p/2. Assuming that y and y_0 have been obtained, by demodulating the signals with the known y and y_0, the water and fat will be pushed into two orthogonal channels and thus can be separated.

To find y and y_0, we will perform a preliminary acquisition phase before the CINE imaging, where three echoes will be acquired and the method in [1] will be used. This set of y and y_0 then is repeatedly used in all other CINE phases, based on the assumption that both y and y_0 are slowly time varying over the cardiac cycle.

To demonstrate the feasibility of our method, we acquired four SSFP CINE slices using the method in [1], with TE = [0.8ms, 1.25ms, 2.6ms], TR = 4.7ms and 20 phases through the cardiac cycle per slice. The first phase was used as the preliminary phase. The proposed single acquisition water-fat separation then is conducted with the signals only from the 2nd echo.
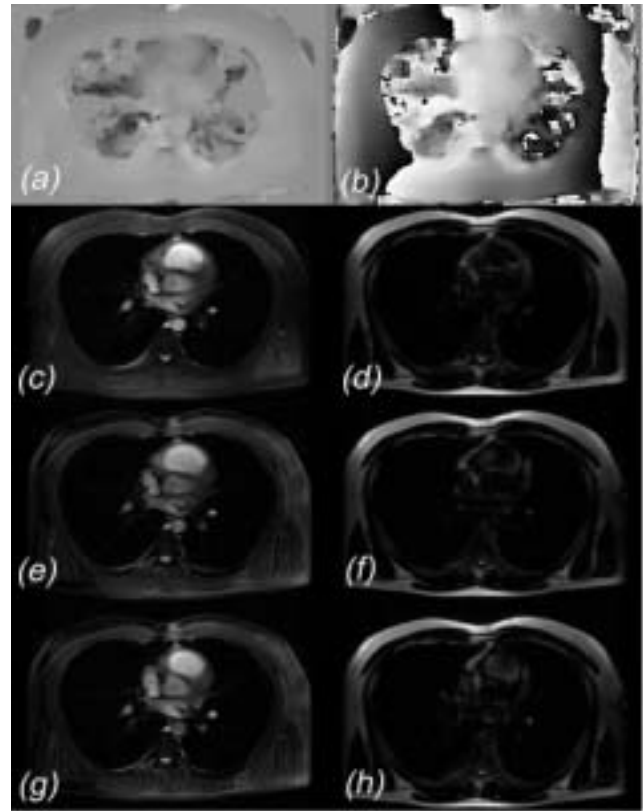

Figure 1: Separation results with a SSFP CINE data set. (a) and (b): field map and initial signal phase extracted from the 3-pt Dixon reconstruction at the first phase. (c) and (d): separated water and fat at the first phase using all three echoes. (e)-(h): separated water and fat using only the second echo at: (e) and (f), the first phase, and (g) and (h), the 11th phase.

RESULTS

Figure 1 shows the separation results from one of the slices. The 3-pt Dixon reconstruction at the first phase provided field map y (a) and signal initial phase y_0 (b). (c) and (d) show the 3-pt Dixon separation results at the first phase for comparison with single acquisition separation results (e), (f). It can be seen that the proposed method achieves successful separations with only 1/3 of the data. The separation results of a later phase (11th phase, (g) and (h)) show that the separation doesn't degrade from the first phase.

CONCLUSION

The proposed single acquisition water-fat separation scheme achieves successful separation on cardiac SSFP CINE data sets by using field map and phase information for all subsequent images in the acquisition.

REFERENCES

1. Reeder et al, MRM 2004; 51: 35-45
2. Glover et al, JMRI 1991; 1: 521-53

Cramer-Rao Bounds for 3-Point Dixon Imaging

Angel R. Pineda[1], Scott B. Reeder[1], Zhifei Wen[2], Norbert J. Pelc[1]

Departments of Radiology[1] and Physics[2]

INTRODUCTION

In most applications of MRI, the diagnostic information is contained in the signal coming from the water in tissue. The fat component of the signal can obscure underlying pathology. For this reason, it is important to suppress or separate the fat signal.

Dixon imaging uses images obtained at different times from the echo to separate the chemical species in each pixel. The most common application of this technique is the separation of fat and water using 3 measurements, i.e. 3-point Dixon imaging. The noise of the estimates for the magnitude of fat and water in 3-point Dixon imaging depends on many factors including the echo times, the field inhomogeneity, the fat-to-water ratio and the reconstruction algorithm[1].

The Cramer-Rao bound[2] (CRB) is the lower bound on the variance of any unbiased estimate. It provides a measure of the minimum uncertainty of the estimates for a given data acquisition which is independent of the reconstruction algorithm. We use the CRB to optimize the choice of echo times and compare performance of our least-squares estimation algorithm with this theoretical limit.

MATERIALS AND METHODS

The CRB was computed for estimating the magnitude of the fat and water from measurements at any 3 echo times. An optimization was carried out to find choice of echo times with the least imaging time that optimized the noise performance. As a measure of noise performance, we used the number of signals averaged (NSA) which is the ratio of the variance of the original images over the variance of the water estimate. In our case, an NSA of 3 is the maximum possible. An NSA of 0 says that the water cannot be estimated from the measurements.

To verify the theoretical result, an in-vitro experiment was carried out using a spherical phantom containing fat and water. By reconstructing an oblique slice with respect to the interface of the fat and water, we generated pixels with a range of fat-to-water ratios.

RESULTS

Figure 1. shows the results obtained by using the choice of echoes that was previously thought to provide the ideal noise performance. For pixels with all water, this is true but for pixels with equal amounts of fat and water, the NSA goes to zero. The variance of the water for pixels with all fat was less than those with all water.
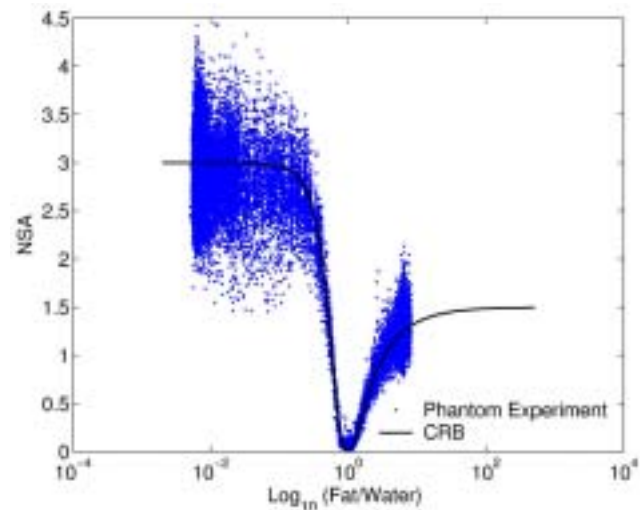

Fig. 1 NSA from in-vitro experiment and CRB over all fat:water ratios for a symmetric acquisition (-2p/3,0,2p/3).
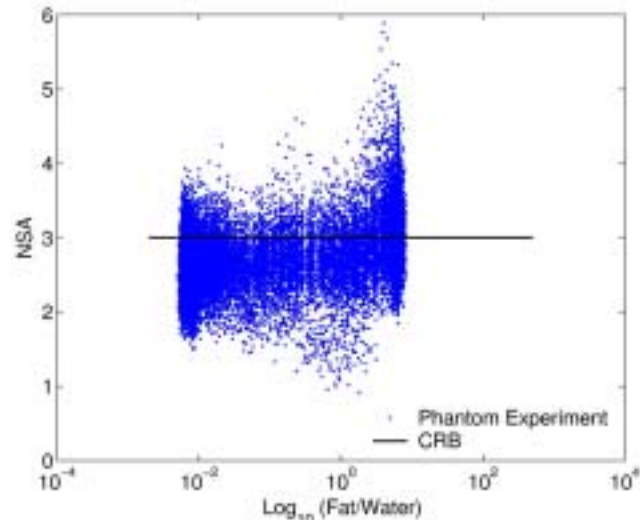

Fig. 2 NSA from in-vitro experiment and CRB over all fat:water ratios for an asymmetric acquisition (-p/6,p/2,7p/6).

The optimization based on the CRB lead to an asymmetric choice of echoes (Fig. 2). For this acquisition, we see that the noise is optimal for all fat-to-water ratios.

CONCLUSION

Cramer-Rao bounds provide a computationally efficient way to optimize the choice of echo times for Dixon imaging. Such an optimization was carried out to avoid the loss of NSA when a pixel contained equal parts fat and water. For this application, we have shown that the nonlinear least squares algorithm is efficient (since it achieves the CRB). By combining the use of the CRB to choose our echo times and a reconstruction algorithm that is efficient, we have obtained an imaging method that is ideal in terms of the variance of the reconstructed water and fat images.

REFERENCES

1. Reeder, et. al., submitted to MRM.
2. Pineda, et. al., to be submitted to TMI.

MR SPECTROSCOPY

In vivo detection of Citrate for Prostate cancer at 3T using 2D J-resolved spectroscopy

Donghyun Kim, Dirk Mayer, Lei Xing, Bruce Daniel, Daniel Margolis, Daniel Spielman

Department of Radiology, Department of Radiation Oncology

Introduction

Citrate is an important metabolite often used in Magnetic Resonance Spectroscopy and MR Spectroscopic Imaging to aid the detection of Prostate Cancer (PCa) along with the Choline and Creatine metabolites. To date, MRSI protocols for PCa detection have been well established at main field strength of 1.5 Tesla (T) (1). However, despite the potential advantage of increased SNR at 3T, strong coupling effects lead to echo time dependant signal characteristic, which needs consideration.

This work involves the study of using 2D J-resolved spectroscopy to determine the presence of Citrate metabolite. We show simulated and experimental results which illustrate the characteristics of Citrate when 2D J-resolved acquisitions are used.

Materials and Methods

Simulations and phantom measurements were also conducted for a 2D J-resolved acquisition. In both cases, the echo time spacing was adjusted to be 7.8 ms for a total of 64 steps from 35 ms to 534 ms for finer resolution in the F1 domain. This resulted in a 2 Hz spectral resolution with a bandwidth of 128 Hz in the F1 domain. The spectral bandwidth for F2 was 5000 Hz with 2048 data point acquisitions. For the actual 2D J-resolved measurements, a phantom composed of Citrate, Creatine, and Choline metabolites were used to emulate the existence of cancerous tissue.

Finally, in vivo data were collected from a subject suspicious of PCa using the 2D J-resolved technique. Single voxel
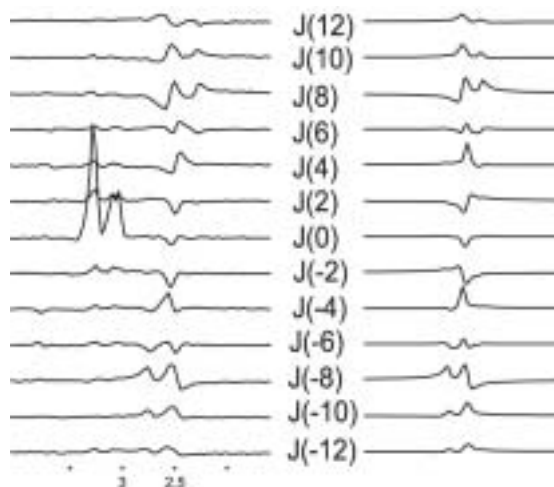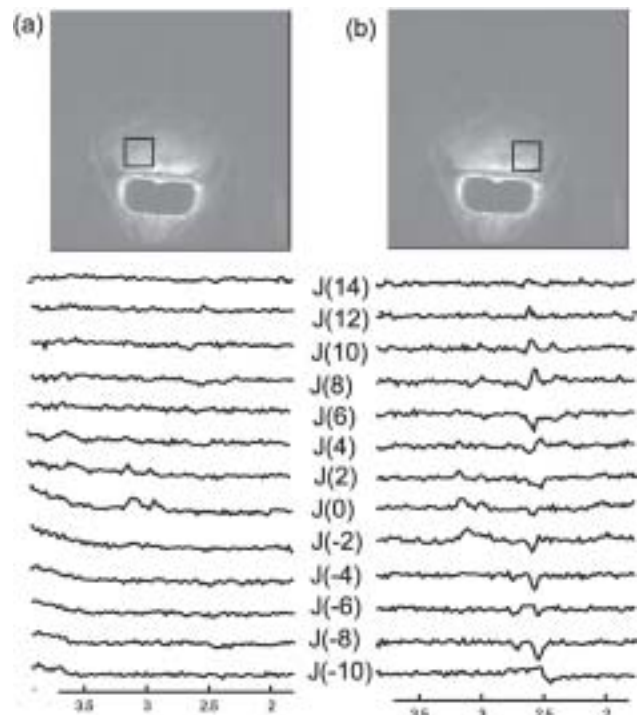

Figure 1

Figure 2

2D J-resolved spectroscopic data were acquired from two different regions at the peripheral zone of the prostate. The parameters were maintained as with the simulations. The voxel size chosen was 1cmx1.12cmx1.08 cm = 1.2 cc. Four acquisitions were averaged per echo time for a total scan time of 8 minutes (TR = 2 sec) for each voxel.

Results

Fig 1 shows 2D J-resolved spectra obtained from simulations (right) and phantom measurements (left). The echo time interval was 7.8 ms starting from 35 ms for 64 steps. For the phantom measurement, Choline and Creatine metabolites were added to mimic PCa. Due to modulations as a function of echo time, the J-resolved spectra show strong signal of the Citrate metabolite at lines outside of J(0). Simulated J-resolved spectra and phantom measured J-resolved spectra are shown with similar spectral patterns. In this respect, the detection of the Citrate resonance can be made robustly using J-resolved acquisitions.

Fig 2 shows single voxel 2D J-resolved spectroscopy results obtained from an in vivo subject suspicious of PCa. Two voxels were selected for the single voxel examinations as shown in the T2 weighted anatomical images. The corresponding J-resolved spectra are shown on the bottom of each image. In (a), even though the presence of Creatine and Choline metabolites are evident, there is no visible Citrate. As for the region shown in (b), the Citrate resonance is visible (2.6 ppm region from J(-10) to J(10) line) in the J-resolved spectra while other metabolites are also present. This shows the J-resolved spectroscopy can be useful for the detection of the Citrate metabolite as well as other metabolites of interest in the detection of PCa.

Conclusion

We have shown that 2D J-resolved spectroscopy provides an elegant method to detect the Citrate metabolite effectively. Strong coupling which leads to modulations as a function of echo time is easily observed using 2D J-resolved spectro-scopic sequences. In vivo measurements confirm the observation of Citrate with patterns similar to simulation and phantom studies.

References

1. J. Kurhanewicz, et al., Radiology, 213:473-480, 1999

Short Echo Time Spiral Chemical Shift Imaging

Donghyun Kim, Elfar Adalsteinsson, Daniel Spielman

Department of Radiology

Introduction

Increasing the information content of Magnetic Resonance Spectroscopy (MRS) in the brain can provide valuable clinical importance. Chemical Shift Imaging (CSI) can increase the spatial information content. Besides the conventional phase encoded CSI method, spiral based readout gradients have efficient k-space coverage allowing extended field of view (FOV). Therefore, the spatial information can be effectively increased using spiral based CSI [1]. As for the spectral component, various different methods can be used to achieve increased information. Of these methods, STEAM (Stimulated echo acquisition mode) excitation is frequently used with minimum echo time (TE) CSI [2], allowing observation of short T_2 metabolites. We used spiral readout gradients with STEAM excitation to increase the information content of MRS.

Methods

Spiral readout trajectories were built into a conventional STEAM sequence for use on a 1.5 Tesla GE whole body imaging scanner. Short echo (TE = 17 ms) three dimensional spectroscopic imaging data were collected. Spirals covering a 48cm FOV data were acquired over a 32x32 matrix with eight spatial interleaves which achieves a spectral bandwidth of 833 Hz. Phase encodes were implemented on the third dimension to collect volumetric data. Eight phase encodes over a FOV of 8cm were used. The effective voxel size was 2.25 cc and the total imaging time was 25 minutes.

Results

The figure shows the in vivo results. A sagittal scout image is shown in the middle with the selected excitation box. Each slice from this excited region is represented in the figure in different aspects. For slice (a), a FOV covering 24 cm is shown between the 4-1 ppm region. In this case, pixels with dominant metabolite signal correspond to the selected ROI region. It can be seen that small lipid contaminations are still present even after the spatial saturation pulses are applied. These are well resolved with the spiral acquisition due to the increased spatial coverage. For slice (b), the metabolite spectra within the 4-1 ppm region are given for the selected ROI region only. For slice (c), metabolite images are reconstructed for NAA, Cr, Cho, and mI. Finally, for slice (d), a representative spectrum within the selected ROI is given
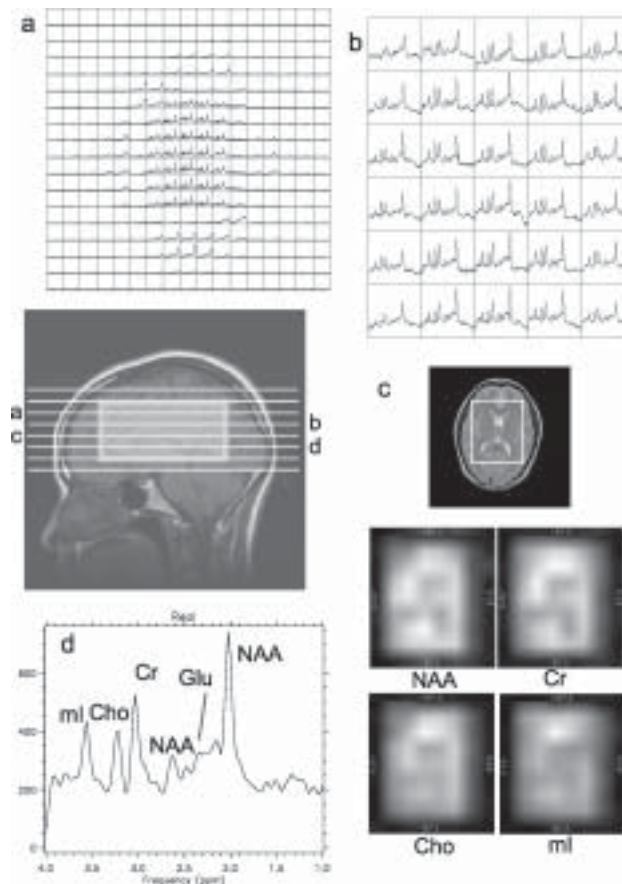
to illustrate the quality of data that has been acquired using the short echo spiral CSI sequence. As seen, good spectral quality is obtained ($SNR_{NAA} \approx 11$).

Increasing the information content can provide broader applications for CSI. Here we have demonstrated the increased spatial information content using spiral readouts and also increased spectral information content by applying a short echo STEAM sequence. For full volumetric coverage, spiral based readouts or echo planar readouts have merit since they require less minimum scan time. Although PRESS based spectroscopic sequences have been widely used due to increased signal to noise ratio compared with STEAM, at higher field strengths, the increased B_1 inhomogeneity may cause problems. STEAM based sequences that are relatively less vulnerable to RF inhomogeneities can potentially be used for application of short echo CSI at higher field strengths.

Conclusion

We have used short echo excitation combined with spiral based readout gradients. It is seen from in vivo brain exam that the increased spatial coverage offered by the spirals can

be effectively used for volumetric coverage and to separate lipid contamination from the subcutaneous fat while increased spectral content can be achieved with the short echo STEAM acquisition.

References

1. E. Adalsteinsson, et al., MRM, 39:889-898, 1998.
2. J. Frahm, et al. JMR, 72:502-508, 1987.

Lipid Suppression using Selective Inversion Recovery for 3D Spectroscopic Imaging at 3T

Meng Gu, Elfar Adalsteinsson, Daniel M. Spielman

Department of Electrical Engineering, Department of Radiology

Introduction

The most common approach for reducing lipid signals in ^{1}H brain chemical shift imaging (CSI) is the use of volume preselection via the PRESS technique. [1] This technique produces high quality metabolite spectra within a restricted brain volume. To achieve whole brain coverage, nonselective inversion recovery (IR) techniques are generally applied. [2] [3] At 1.5T, metabolite signal loss from IR is on the order of 30-40%. However, at higher fields, e.g. 3T, the increase in spectral separation between lipids and metabolites allows a frequency selective inversion. This paper discusses the design, implementation and results of an IR CSI pulse sequence that performs selective inversion for lipid suppression.

Method

The chemical shift between lipids and the closest metabolite (NAA) is 0.7 ppm. At 3T, these two spins are separated by 89 Hz. The design goals of the inversion pulse were a transition band less than 89 Hz, an inversion band wide enough to cover all of the lipid signals and a short enough pulse width to neglect relaxation effects during excitation. In the design, we chose a minimum phase RF pulse for a sharp transition band with 500 Hz inversion bandwidth and 20ms pulse width. The RF pulse synthesis was done using the Shinnar-Le Roux algorithm [4]. The ripple amplitudes were chosen such that the transition bandwidth was less than 89Hz. To test the effects of the selective IR, a 3T CSI imaging sequence was implemented with the following characteristics: spectral-spatial spin echo pulse for metabolite excitation and water suppression, TR/TI/TE=2000/170/144 ms, spiral readout gradients, single slice, 2.5 cc voxels and 2 minute acquisition. [5]

Results

The minimum phase RF pulse and its inversion profile are shown in Figure 1. The ripple amplitudes in the pass and stop bands are 1% and the transition bandwidth of the profile is 50 Hz, measured from 10% to 90% of inversion. Figure 2 shows spectra from two voxels with and without lipid inversion obtained from an in vivo study. The two representative voxels are chosen such that one is in the subcutaneous fat and the other is within the brain. The spectrum from the voxel in the subcutaneous fat clearly shows that the lipid
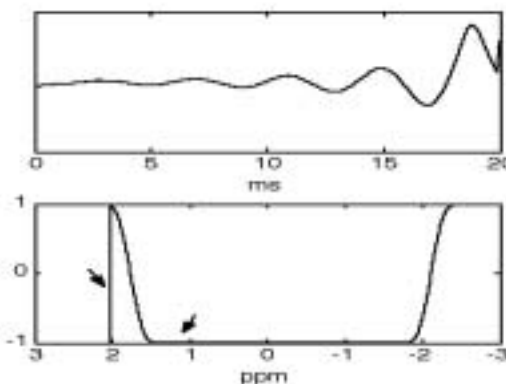

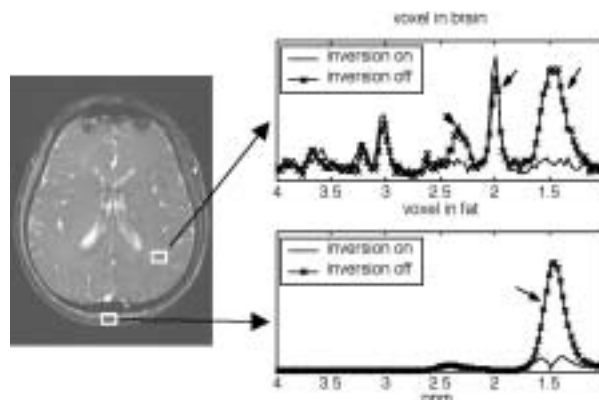*Fig. 1. Minimum phase RF inversion pulse and its inversion profile.*

Fig. 2. In vivo spectra of representative fat and brain voxels. Spiral CSI TR/TI/TE=2000/170/144ms, 2.5cc voxels, 2 minute acquisition.

signal is suppressed with the inversion on, and the measured suppression factor is on the order of 10. The spectra from the voxel in the brain show that the spectral artifacts due to lipid signal leakage is significantly reduced, and metabolite spectra are not disturbed by the inversion pulse.

Conclusion

We have designed and implemented a 3T frequency selective IR spiral CSI pulse sequence. The effectiveness of the selective inversion recovery is demonstrated on an in vivo scan showing a lipid suppression factor on the order of 10 while maintaining excellent quality metabolite spectra.

Acknowledgments

References

1 P.A. Bottomley, Ann N Y Acad Sci, 508, 333, 333-348, 1987
2 A. Ebel, et al, MRM, 49, 903-908, 2003
3 D. M. Spielman, et al., JMRM 2:253-262, 1992
4 J. Pauly, et al., IEEE Trans. Med. Imaging 10, 53-65, 1991
5 E. Adalsteinsson, et al., MRM, 39, 889-898, 1998

Fast CT-PRESS Based Spiral CSI at 3 T

Dirk Mayer, Dong-Hyun Kim, Elfar Adalsteinsson,
Daniel M. Spielman

Department of Radiology

Introduction

Even at a field strength of 3 T the detection of signals from scalar coupled metabolites in MR chemical shift imaging (CSI) is often hampered by spectral overlap due to the small dispersion of the chemical shift (CS) and line splitting caused by J-coupling. Constant Time PRESS (CT-PRESS) [1] has been introduced as a single voxel technique to detect coupled resonances with effective homonuclear decoupling and high signal-to-noise ratio (SNR). The aim of this work was to combine CT-PRESS with fast spiral CSI [2] as an alternative to short TE CSI.

Materials and Methods

The implemented sequence consists of five parts: (a) three CHESS pulses for water suppression, (b) an outer volume suppression module, (c) a PRESS module (TE/TR = 30/2000 ms) for slice(z)- and in-plane pre-selection, (d) an additional refocusing pulse for CS encoding in f_1, and (e) a spiral read-out gradient for combined spatial(xy)-spectral(f_2) encoding. The CS encoding pulse was shifted in increments of 6.4 ms in 17 steps leading to a spectral width SW_1 of only 78.125 Hz. Therefore, the 2D spectra are severely aliased in f_1. But as the signals occur close to the spectral diagonal in CT-PRESS the aliasing does not lead to signal overlap. The evolution time t_c (echo time at the central CS encoding step) was 151 ms. All refocusing pulses had flip angles of 167° due to RF peak power restrictions. Two spiral designs were tested: (a) 4 spatial interleaves with a FOV of 24x24 cm² for a 16x16 matrix and SW_2 of 1196 Hz (T_{meas} = 4:40 min), and (b) 12 spatial interleaves with an oversized FOV of 48x48 cm² for a 32x32 matrix and SW_2 of 1050 Hz (T_{meas} = 13:44 min). The spiral CSI module was shifted together with the

Fig. 2: Map of diagonal spectra (4 ppm Bf B1 ppm). All voxels are completely within the volume selected by the PRESS module

CS encoding pulse in order to increase the SNR.

The data post-processing comprised gridding, apodization in the spectral dimensions, and FFT. A t_1-dependent linear phase correction was performed along f.o correct for the differences of the start of data acquisition. After unwrapping the 2D spectra in f_1 diagonal spectra were calculated by integrating the signal along f_2 within a ±13 Hz interval around the spectral diagonal.

Results and Discussion

For the in viva application of the method a 20x92x108 mm³ volume (axial slice orientation) was selected above the ventricles of a healthy volunteer. The 2D con.r plot from a single voxel containing predominantly gray matter (Fig. 1, bottom) demonstrates the effect of the effective decoupling scheme as the line splitting due to J-coupling is suppressed in f_1. Therefore, all the signals appear as single lines in the corresponding diagonal spectrum (Fig. 1, top). Both the 2D contour plot and the diagonal spectrum show the good separation of the glutamate (Glu) C4 resonance at 2.35 ppm. Additionally, signals from NAA, total creatine (tCr), choline containing compounds (Cho) and *myoinositol* (mI) could be detected. Figure 2 shows a spatial map of diagonal spectra (4 ppm Bf B 1 ppm). All voxels are completely within the

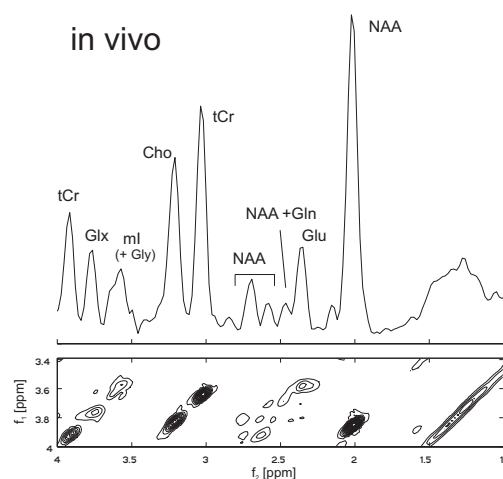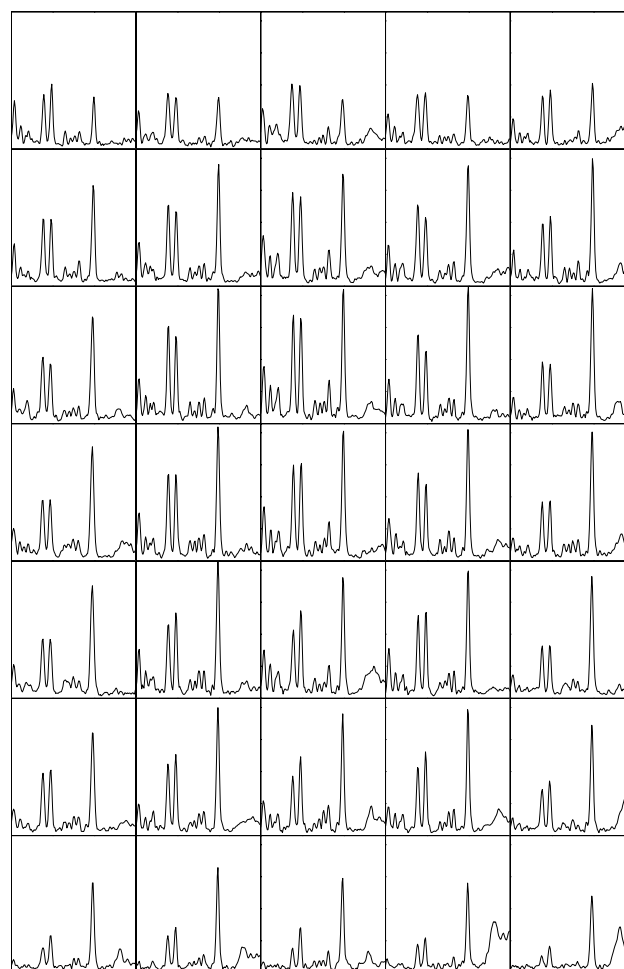*Fig. 1: 2D contour plot and diagonal spectrum from a single voxel containing mainly gray matter from a healthy volunteer (T_{meas} = 13:44 min, 2x1.5x1.5 cm³ nominal voxel size).*

volume selected by the PRESS module.

Conclusion

The presented data show the feasibility of combining CT-PRESS with a fast spiral based CSI technique. This allows the acquisition of multi-voxel spectroscopic data without line splitting. By using effective decoupling this work demon-strates that compounds such as Glu and mI can be reliably measured without water or lipid baseline artifacts which typically hamper short TE CSI.

References

1. Dreher, W., Leibfritz, D., Magn. Reson. Imag. 1999; 17: 141-150.
2. Kim, D.H., et al., Proc. ISMRM 2002, 2493.

Rapid *in vivo* Shimming with Current Constraints

Donghyun Kim, Gary Glover, Daniel Spielman

Department of Radiology

Introduction

Increasing number of MR systems now include shim coils. These include the higher-order shim coils as well as the linear gradients. In all these cases, a procedure involving current distribution to the individual coils is executed to produce a homogeneous field. However, depending on the region of interest (ROI), the required shim currents can overrange the power supply's capacity. In particular, this situation arises frequently when shimming over a localized region where the inhomogeneity is severe and especially at 3T since the inhomogeneity due to susceptibility has been doubled. For example, we have seen that this was often the case in the C-spine region. In this case, truncating the required shim currents does not necessarily achieve a good shim. A more elegant way to approach the problem is to solve the shim current values with boundary conditions [1]. Also, when iterations of the shim process are performed, care must be taken to take into account downloaded shim values existing from previous iterations.

W have implemented a rapid higher-order shimming method for 3 T which is targeted for arbitrary localized regions with constraints on the available shim currents. We show that by solving a contrained least squares, the homogeneity is improved compared to a simple truncation of the available currents.

Materials and Methods

A shimming procedure based on field mapping was used [2]. Spiral based readouts were used to rapidly acquire the field maps. From predetermined reference field maps of each shim coils, a least squares calculation with boundary conditions was used to determine the required shim currents from the region of interest selected by the user. For our 3 T system, the higher-order shim power supply had a upper/lower limit of ± 4 amps per channel. These values were used as the boundary conditions for solving the least squares problem. A built-in Matlab (Mathworks, Inc.) function was used which is based on a Newton algorithm [3] in searching for the minimum values.

Data were collected in vivo from the C-spine where the field inhomogeneity is severe and typically requested more current than available. First, we solved the least squares equation with no account of the maximum (minimum) current values of the shim supply. In this case, a truncated value of current was downloaded when overranges occur. Secondly, we solved a least squares algorithm with boundary conditions. Comparison of the RMS (root means square) field deviation was used to evaluate these two methods.

Results

Figure 1 shows the region of interest that was typically used for shimming the C-spine. In Fig. 2, a situation where the required current is overranged in the first iteration of the shimming process is given. In this case, the required current for the XY channel was 4.67 amps but the hardware could only supply 4 amps for the truncated method. As for the constrained least squares method, the algorithm took into account the boundary condition and resulted in different download currents for the other channels while achieving better RMS.
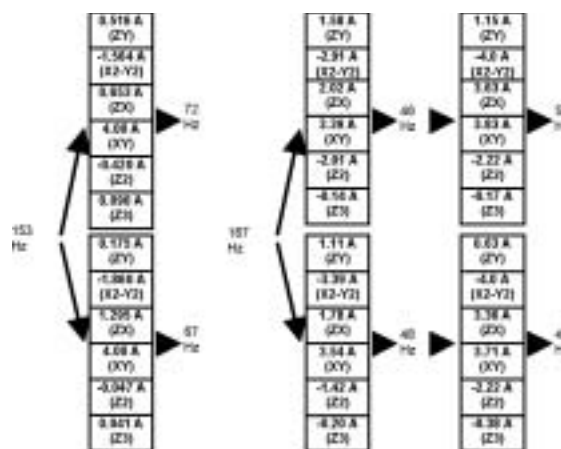

Figure 1

Figure 2   *Figure 3*

In Fig. 3, another example is given where the shimming process was iterated to further reduce the RMS field deviation. The top row shows the RMS value from the truncated method (167 ® 46 ® 53 Hz). In the second row, the RMS value obtained from the constrained least squares method is given (167 ® 48 ® 41 Hz). Here the least squares algorithm took into account the boundary conditions of each channel and therefore resulted in no truncation of current as evidenced in the decrease by the RMS value.

Conclusion

A fast higher-order shimming method for arbitrary regions is introduced. In this method, the available current values are taken into account by solving a least squares algorithm with boundary conditions.

References

1. H. Wen, et al., MRM, 34, 898-904, 1995. 2. D.H. Kim, et al., MRM, 48:715-722, 2002. 3. T.F. Coleman, et al., SIAM J Optim. 6(4): 1040-1058, 1996.

MRI-Guided Prostate Thermal Therapy with Catheter-Based Ultrasound Applicators

C.J. Diederich[1], W. H. Nau[1], A. B. Ross[1], K. Butts[2], V. Rieke[2], D. M. Bouley[2], H. Gill[2], B. Daniel[2], G. Sommer[2]

[1]Radiation Oncology Department, University of California, San Francisco; [2]Department of Radiology, Stanford

INTRODUCTION

High-temperature thermal therapy is emerging as a feasible treatment option for prostate cancer and benign prostatic hyperplasia. Previous investigations have demonstrated distinct advantages of catheter based ultrasound technology over other heating modalities for thermal ablation therapies, with significant potential for better spatial control and faster heating times. We are developing these ultrasound devices and techniques specifically for treating prostate cancer in conjunction with MR thermal imaging (MRTI) to monitor and control treatment progression.

MATERIALS AND METHODS

Directional transurethral applicators have been designed with arrays of narrow planar transducer segments, and integrated within a flexible delivery catheter with a cooling balloon. This applicator can be rotated within the prostatic urethra to target specific regions during treatment[1]. MRI compatible interstitial ultrasound applicators with 180˚ active acoustic sectors were developed specifically to treat the prostate[2]. These 2.4 mm diameter applicators may be implanted through the perineum into the posterior portion of the prostate (similar to HDR implant strategies), with their heating energy directed away from the rectum. Urethral and endorectal cooling was employed with both treatment strategies to provide further protection of the urethral mucosa and rectum from thermal damage. Both heating strategies were evaluated *in vivo* within canine prostate (n=5). During the *in vivo* studies, MRTI on the 0.5T GE interventional scanner was used to monitor treatment temperatures using the PRF technique. The cytotoxic thermal doses (t_{43}>240 min) and corresponding maximum temperature thresholds (T_{max}>52˚C) were monitored within 3 imaging planes simultaneously during the procedure.

RESULTS

Narrow zones of coagulation (~30˚ sector), extending up to 20 mm from the urethra to the periphery of the prostate gland, could be produced within 10-15 minutes using the planar transurethral applicators (Fig. 1a). Further, rotation of the applicator during treatment could be used to destroy larger regions in the prostate (Fig 1b). Modification of the endorectal imaging coil with a cooling bolus was effective at cooling the rec-
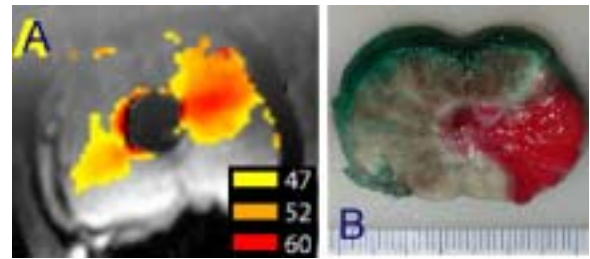

Fig. 1. (a) MRTI derived maximum temperature thresholds for two sequential shots with the planar transurethral applicator; (b) TTC stained section of prostate demonstrating 270 ˚ sweep of thermal ablation.
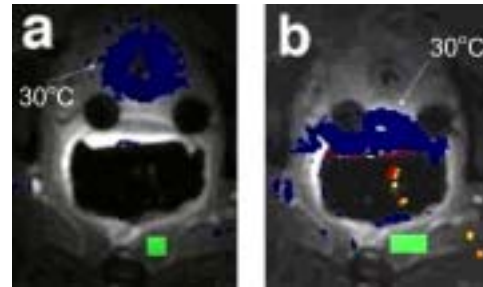

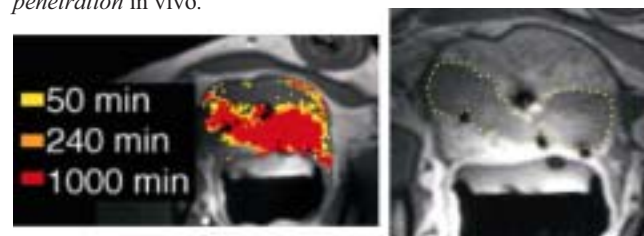*Fig. 2. MRTI of (a) urethral cooling and (b) endorectal cooling penetration in vivo.*

Fig. 3.(a) MRTI derived thermal dose levels and (b) resulting T1 contrast enhanced image demonstrating thermal coagulation with directional implant.

tal wall (Fig 2). Multiple interstitial directional applicators (~180˚ active sectors), implanted within the posterior margin of the prostate with the energy directed away from the rectum, produced contiguous zones of thermal coagulation which extended from the posterior prostate toward the anterior-lateral periphery of the gland (Fig 3).

CONCLUSION

Both transurethral and interstitial treatment strategies demonstrated significant potential for thermal ablation of localized prostate cancer, particularly when MRTI is used to guide and assess treatment.

REFERENCES

1. Ross AB, Diederich CJ, Nau WH, et al. Physics in Medicine and Biology 2004; 49:189-204.
2. Nau WH, Diederich CJ, Burdette EC. Medical Physics 2001; 28:1525-34

Temperature Mapping During Ultrasound Prostate Ablation Using Fat for Phase Reference

Viola Rieke[1], Anthony Ross[2], William Nau[2], Chris Diederich[2], Graham Sommer[1], Kim Butts[1]

[1]Department of Radiology and [2]Department of Radiation Oncology, UCSF

INTRODUCTION

High temperature thermal treatments are increasingly adopted for benign prostatic hyperplasia (BPH) and localized prostatic adenocarcinoma (CaP), due to their minimal invasiveness and low associated morbidities [1]. Spatial and temporal control of the tissue temperature is necessary during high temperature thermal therapy to ensure destruction of the targeted tissue and to avoid damage to surrounding normal structures. Accurate spatial control over thermal coagulation requires temperature monitoring of the treatment. Conventional magnetic resonance proton resonance frequency (PRF) shift thermometry is suitable to monitor the treatment, but it is inaccurate in the presence of tissue motion. We have investigated a referenceless method [2] that overcomes the motion sensitivity. This study expands the previous referenceless temperature reconstruction to allow background phase estimation from fatty tissue located around the prostate. A correction for distortions in the temperature map due to artifacts caused by the ultrasonic applicator is demonstrated. The method was evaluated during an *in vivo* canine prostate ablation experiment.

MATERIALS AND METHODS

For the background phase estimation a region of interest (ROI) in the fatty periprostatic tissue is selected, that partially surrounds the prostate, as seen in Fig. 1. The phase in the ROI is estimated by a low order polynomial in the least squares sense and the constant phase offset between water and fat is determined in a small ROI located in aqueous tissue outside the prostate (Fig. 1, yellow) which remains at body temperature. Using the estimated phase and the phase offset, the temperature change in the heated region can be calculated.
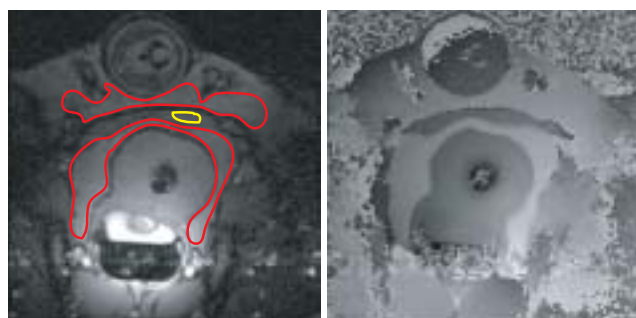

Figure 1: Magnitude image (left) of the canine prostate. The border of the ROI, used for the phase estimation is shown in red, the yellow ROI is used to determine the phase offset. The phase image (right) shows the phase offset between aqueous and fatty tissue.

Since the referenceless method only estimates the slowly varying background phase, it cannot distinguish between phase changes caused by a temperature change and those due to susceptibility changes introduced by the ultrasound applicator. To remove the phase contribution of the heating device, the artifact caused by the applicator is determined in an image prior to heating and subsequently subtracted from images acquired during heating.

In vivo prostate ablation was studied in a canine model using a transurethral ultrasound transducer [3]. Imaging was performed with an interventional 0.5T MRI scanner. Fifteen images were acquired during the experiment; three images before and 12 images during thermal treatment. Temperature maps inside the prostate were reconstructed with the referenceless method and compared to the conventional reconstruction method.

RESULTS

Figure 2 shows the temperature distribution in the prostate during thermal treatment, reconstructed with conventional baseline subtraction (left) and with referenceless reconstruction without (middle) and with (right) correction for the applicator artifact. Without correction, the temperature measurements close to the applicator are distorted by the artifact. The influence of the artifact decreases with increasing distance from the applicator, so that correct temperatures are measured at the periphery of the prostate gland. With artifact correction, the distortions are removed and the temperature maps of referenceless reconstruction and conventional baseline subtraction are very similar.
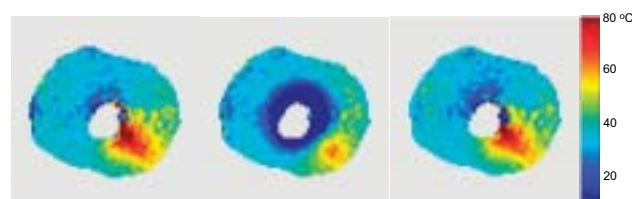

Figure 2: Temperature maps generated with conventional subtraction (left) and referenceless reconstruction without (middle) and with (right) correction for the applicator artifact.

CONCLUSION

The results show that reconstruction of temperature maps using an ROI in the fatty periprostatic tissue is feasible. After correction of the applicator artifact, referenceless reconstruction provides reliable temperature maps.

REFERENCES

1. Beerlage, HP, et al. Eur Urol. 37(1):2-13, 2000.
2. Rieke, V, et al. Magn Res Med. 51(6):1223-31, 2004
3. Ross, AB, et al. Phys Med Biol. 49(2):189-204, 2004.

Optimizing Spatial Resolution for MR Thermal Imaging of Transurethral Ultrasound Prostate Ablation

L. J. Pisani[1], A. B. Ross[2], C. J. Diederich[2], W. H. Nau[2], G. H. Glover[1], F. G. Sommer[1], K. Butts[1]

[1]*Radiology, Stanford University;* [2]*Radiation Oncology, University of California, San Francisco*

INTRODUCTION

Thermal ablation for local control of prostate cancer while sparing normal tissues may be facilitated by treatment with transurethral high-intensity ultrasound and concurrent guidance by magnetic resonance thermal imaging (MRTI). MRTI using the proton resonance frequency shift method differs from anatomical MRI, for which accurate depiction of sharp tissue boundaries demands high spatial resolution. In thermal ablation using these applicators the temperature distribution being imaged may vary slowly in space and may not tend to have the sharp edges commonly found in anatomical images. The goal of this work is to refine MRTI during thermal ablation by determining how high a spatial resolution is needed to accurately represent realistic temperature distributions, while still maintaining high signal to noise ratio (SNR).

MATERIALS AND METHODS

Temperature distributions of two transurethral high-intensity ultrasound applicators were simulated and measured in vivo in a canine prostate. Noise was added to the simulated data in order to generate the range of SNR levels measured in vivo. Both the simulated and in vivo data were reconstructed at different spatial resolutions (pixel sizes). The simulated data at each resolution were subsequently compared to the true temperature distributions. For the in vivo data, the cumulative equivalent number of minutes of heating to 43°C or thermal dose, t_{43}, was calculated from MRTI at each spatial resolution, where

$$t_{43} = I\, C^{43-T(t)}\, dt,$$

and C is 0.5 above 43°C and 0.25 below 43°C. The resulting dose maps were analyzed using contrast enhanced T1-weighted images that show the thermal lesions after ablation.

RESULTS

Figure 1 shows that the measured temperature distributions agree well with simulated temperature distributions for the tubular ultrasound applicator. For ultrasound planar and 90° sectored tubular transurethral applicators, the minimum root mean squared (RMS) error averaged over the measured SNR range is achieved by reconstructing to pixel sizes of 1.7 mm and 1.2 mm, respectively. Figure 2 is a post-therapy contrast enhanced image which shows the resulting lesion with thermal dose contour plots at different resolutions superimposed. Dose levels at $t_{43} = 10^0$, 10^2, and 10^4 are delineated for 1.67 and 5 mm pixels.
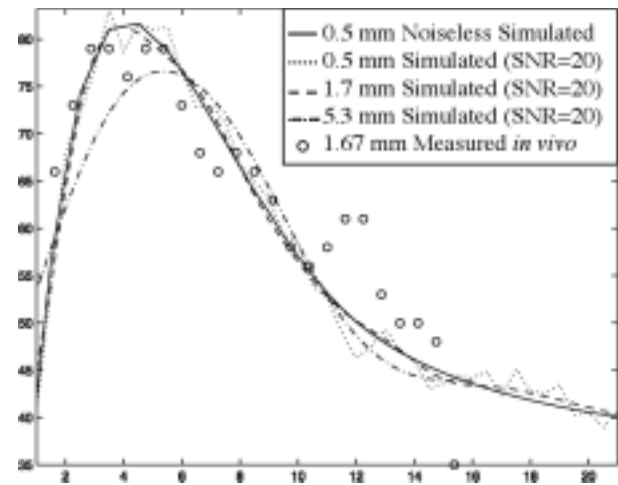

Figure 1: Center profile through the simulated temperature distribution, reconstructed at different resolutions and with noise added. The measured in vivo temperature profile for the same applicator is also shown.
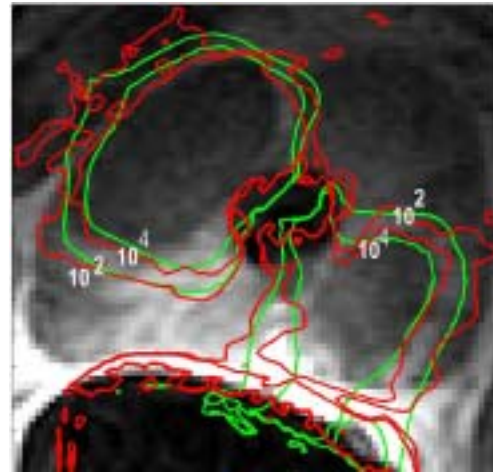

Figure 2: Contrast enhanced image showing canine prostate thermal lesions and superimposed $t_{43} = 10^2$ and 10^4 dose contour plots from MRTI with 1.67 and 5 mm pixels (red and green, respectively).

CONCLUSION

Determining MRTI optimal pixel size entails balancing the SNR gain of large pixel sizes with the accuracy in representing an underlying temperature distribution of small pixels. This is reflected in the smaller overall optimal pixel size of 1.2 mm for the narrow temperature distribution of the planar transurethral ultrasound applicator, as compared to the 1.7 mm optimal pixel size for the 90° sectored tubular applicator. The SNR advantage of larger pixels cannot be fully realized by retrospectively adjusting reconstruction parameters. Therefore, prospective analysis and optimization should direct MRTI data acquisition for a specific underlying temperature and expected SNR levels.

In vivo Porcine Liver Radiofrequency (RF) Ablation with Simultaneous Temperature Monitoring

Karl Vigen[1], Joan Frisoli[1], Viola Rieke[2], Bruce L. Daniel[1], Kim Butts[1]

Departments of [1]Radiology and [2]Electrical Engineering, Stanford University, Stanford CA 94305

INTRODUCTION

Recently, a modified radio-frequency (RF) generator was described (1) which allows MR imaging and temperature mapping during RF ablation. Here, we describe its use in 3 porcine livers *in vivo*. Post ablation imaging demonstrated the achievable size of the lesion.

MATERIALS AND METHODS

MR imaging and RF ablation tests were performed on a 0.5T MR system (Signa SP, GEMS, Milwaukee WI). Imaging was performed with a 2D GRE sequence (TR/TE/BW = 60ms/30ms/±8.93kHz; 64 time frames) with temperature maps calculated by the proton resonance frequency (PRF) method. One sagittal slice was imaged, placed approximately transverse to the RF electrode. An umbrella needle electrode (LeVeen, Boston Scientific) was attached to the filter/isolation network of the modified RF generator (1), and inserted percutaneously into the porcine liver. The pigs were anesthetized with atropine and telazol and maintained on isoflurane. One ablation was performed while the animal was manually ventilated to simulate variable respiratory motion, and images were reconstructed with a triggered, navigated, multi-baseline method (3), to simulate performing the procedure with only local anesthesia. The second ablation in each animal was performed with normal mechanical ventilation, using a simple respiratory-triggered sequence.

RESULTS

Temperature maps are shown for the case of variable respiratory motion with the triggered, navigated, multi-baseline reconstruction (Fig. 1a); and with mechanical ventilation and respiratory-triggered imaging (Fig. 1b). (An asymmetric heating area is seen in Fig. 1a due to the presence of nearby blood vessels). No noticeable RF interference was observed in the MR images. The shaft of the RF electrode (2) showed signal loss due to susceptibility effects near the probe. The last ten time frames during heating were evaluated for asymmetry of the heating spot and consistency in area of the +10°C contour between time frames. Gross asymmetry was evaluated by determining the distance between the center of the heating spot and the center of the probe; values ranged from 0.1±2.1 mm (little asymmetry) to 5.4±1.5 mm (high asymmetry). Heating spot areas averaged over the 10 time frames ranged from 7.7±1.2cm^2 for the smallest ablation size to 11.4±0.6cm^2 for the largest. The standard deviation of the heating spot area ranged from 0.6cm^2 to 1.5cm^2 over the ten time frames; more inconsistency was noticed when simu-
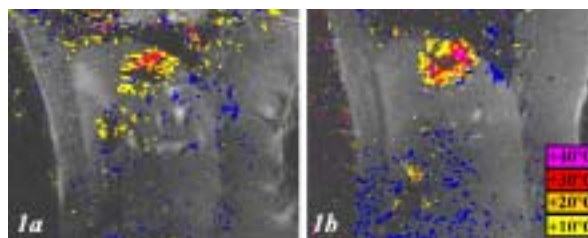

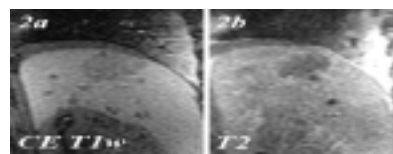*Figure 1: Temperature maps acquired during RF ablation.*

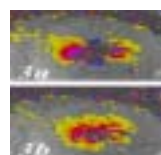*Figure 2: Post-ablation T1- and T2-weighted images.*

Figure 3: Temperature map artifacts due to air bubbles (a) return to a regular appearance after a few time frames (b).

lated variable breathing was used, compared with mechanical respiration. Post ablation T2-weighted and post-contrast T1-weighted images were acquired in the same plane, and showed the extent of the lesion (Fig. 2). The liver was sectioned post mortem, and a qualitative examination showed regions of complete necrosis with maximum diameters from 2.5" to 3.5". In some locations, nearby large blood vessels limited necrosis to small tissue volumes immediately adjacent to the electrode array tips.

In two procedures, artifacts in the temperature maps of some time frames appeared (Fig. 3a); the source was likely spherical gas bubbles with susceptibility different than tissue (4). These lasted for 105 and 225 seconds, respectively, but the temperature maps eventually returned to a regular appearance (Fig. 3b).

CONCLUSION

A modified radiofrequency (RF) generator was used to generate lesions in 3 porcine livers *in vivo*. RF interference in the MR images was not observed. Temperature maps showed the extent of heating, and post-ablation images demonstrated the extent of potential tissue destruction. Asymmetry of the heating spot was sometimes noted; it can be caused by presence of nearby blood vessels, or the relative orientation of the imaging plane with respect to the RF electrode. Temperature map artifacts caused by gas bubbles in several time frames of two ablations disappeared as heating progressed. In the future, this might be avoided with adjustment of the heating protocol.

REFERENCES

1. Vigen K, et al., Proc. 11th ISMRM, 685 (2003).
2. Daniel BL et al., Radiology, 205(P): 1555 (1997).
3. Vigen K, et al. Magn. Reson. Med., 50: 1003 (2003).
4. Schenck JF, Med. Phys., 23: 815 (1996).

An X-ray Compatible RF-coil for MR Imaging

Viola Rieke[1,2], Arundhuti Ganguly[1], Greig Scott[2], Bruce Daniel[1], John Pauly[2], Rebecca Fahrig[1], Norbert Pelc[1], Kim Butts[1]

Departments of [1]Radiology and [2]Electrical Engineering

INTRODUCTION

Magnetic resonance imaging and x-ray fluoroscopy are powerful tools for guiding interventional procedures. Both imaging modalities can be implemented in a hybrid system combining the advantages of each. However, certain restrictions are imposed from one modality on the other. For the reception of MR signals, an RF-coil has to be placed on or around the patient near the region of interest. X-ray fluoroscopic images on the other hand can become useless for image guidance if x-ray attenuating materials, located between the x-ray source and detector, obscure patient anatomy. Unfortunately, materials used in conventional RF-coils are highly x-ray attenuating. The purpose of this work was to design an x-ray compatible RF-coil with minimal x-ray attenuation such that x-ray fluoroscopic images are not degraded by the presence of the RF-coil in the FOV, while maintaining excellent MR image quality.

MATERIALS AND METHODS

For the design of an x-ray compatible RF-coil all coil components that potentially lie in the FOV of the x-ray image, i.e. in the path of the x-ray beam, should have minimal x-ray attenuation. To minimize the attenuation by the loop conductor, we used aluminum (Al) which has a significantly lower atomic number (Z=13) than the commonly used copper (Cu, Z=29). We compared the x-ray attenuation of a 50 mm thick Al strip and a 36 mm thick Cu strip by placing both strips directly on the x-ray detector for anode voltages ranging between 50 and 110 kVp. In a second experiment the strips were placed on 20 cm Lucite which yields a scatter behavior similar to that of the human body.

Using aluminum foil, we built a four element abdominal phased array (PA). Fig. 1 shows two elements of the x-ray compatible PA. The capacitors were placed in the loop outside the x-ray FOV, or moved into the detuning circuit.

Since the circuitry containing the detuning circuit, baluns, and cable connections can be easily designed to lie outside the x-ray FOV, the use of low x-ray attenuating material is not necessary for this. To evaluate the x-ray transparency of the coil, x-ray images of a porcine spine were taken with the coil in the FOV. MR image quality of the x-ray compatible PA was compared to a single
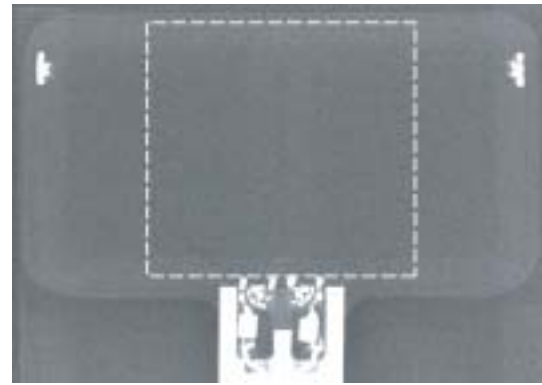

Figure 1: X-ray image of the x-ray compatible phased array coil. The approximate size and position of the x-ray detector is indicated by the white square.

channel receive-only coil, currently used in hybrid procedures (SPGR, TR/TE/flip/BW = 40ms/5.5ms/50/ 31kHz). MR Images were acquired on a 0.5T Signa SP MRI scanner (GE Medical Systems, Milwaukee WI) with an integrated x-ray fluoroscopy system [1,2].

RESULTS

Fig. 2a shows the x-ray attenuation of the aluminum (left) and copper (right) strip for 50 kVp anode voltage. The measured x-ray attenuation is 22% for the copper strip and 1.1% for the aluminum strip.

Figure 2b shows the x-ray attenuation of the strips placed on top of a 20 cm Lucite layer containing a guide wire phantom. The Al strip is not detectable while the Cu strip remains visible in the image. Fig. 3a shows an x-ray image of the porcine spine phantom. The x-ray compatible PA is placed around the phantom but is not detectable in the image. For comparison, the same image was taken with a conventional abdominal phased array in the FOV, seen in Fig. 3b. Copper traces and discrete elements (arrow) are visibly degrading the fluoroscopic image making this coil unusable in a hybrid system. The MR image SNR of the phased array improved by 60% compared to the single channel coil.

Figure 3: X-ray image of the spine phantom with the x-ray compatible PA (a) and the conventional PA(b) in the FOV.
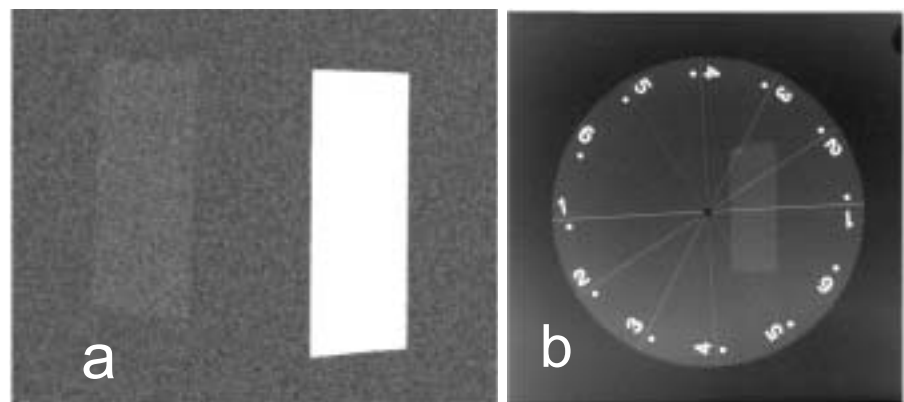
Figure 2: X-ray attenuation of the Al and Cu strip, placed directly onto the x-ray detector (a) and onto a 20 cm Lucite layer (b).

CONCLUSION

The use of x-ray compatible RF-coils in a hybrid system allows for x-ray fluoroscopic image acquisition with minimal or no impact by the RF-coil without compromising the MR image quality.

REFERENCES

1. Fahrig R., et al, JMRI 13:294-300 (2001).
2. Fahrig R., et al, Acad Radiol 8:1200-7 (2001).

MOLECULAR IMAGING

Changes in Genomic Expression Pattern in Contrast-Enhancing and Non-Enhancing Regions of Squamous Cell Carcinomas

Yi-Shan Yang[1], Yen Lin Chia[1,2], Mark Bednarski[1], Sylvia Plevritis[1], Samira Guccione[1]

Departments of [1]Radiology and [2]Statistics

INTRODUCTION

Molecular imaging (MI) is an important new technology with high temporal and spatial resolution for *in vivo* tracking of gene expression and protein synthesis. Its current focus has been on constructing new imaging agents and techniques that are sensitive to gene expression. This approach to MI is based on the development of probes for specific genes and proteins even though the materials being studied (e.g., VEGF) often have dramatic effects on changing many other factors *in vivo*. In this study, we report the gene expression profiles of samples from a mouse tumor model obtained from Gd(DTPA) contrast-enhanced and non-enhanced regions of tumors at different stages of tumor progression using MRI and functional genomics.

METHODS AND MATERIALS

The squamous cell carcinoma (SCC VII) cell line was used to initiate subcutaneous tumors in mice. This mouse model has been used as a model for human head and neck carcinomas. A total of 20 animals were imaged using CE-MRI in a clinical 3.0T GE Signa MR Scanner with a custom designed quadrature birdcage coil tuned to 127 MHz for signal reception. T1- and T2-weighted MR images were obtained using standard spin-echo (SE) and fast spin-echo (FSE) pulse sequences, respectively. Three different stages of tumor growth were defined based on changes in the T1 and T2-weighted MR imaging patterns. The contrast enhancing (CE) and non enhancing (NE) regions of the tumors were marked and biopsied for oligonucleotide microarray and histological analysis. SAM (Significance Analysis of Microarray) package was used to identify genes with significant expression level among different stages.

RESULTS

Three distinct temporal stages of tumor progression can be defined using both T1- and T2-weighted CE-MRI and microarray analysis. The early stage tumors (Stage 1) show a homogeneous contrast enhancement pattern in the T1-weighted image and is homogeneous in T2-weighted image (Figure 1A-C) The more advanced tumors (Stage 2) show discrete regions of contrast enhancement in the post contrast T1-weighted MR images (Figure 1D-F). The late stage tumors (Stage 3) show changes in T2-weighted MR signal intensity that corresponds to the post-contrast T1-weighted MR enhancement (Figure 1G-I). Histological analysis (H&E) showed that the samples obtained from the periphery and
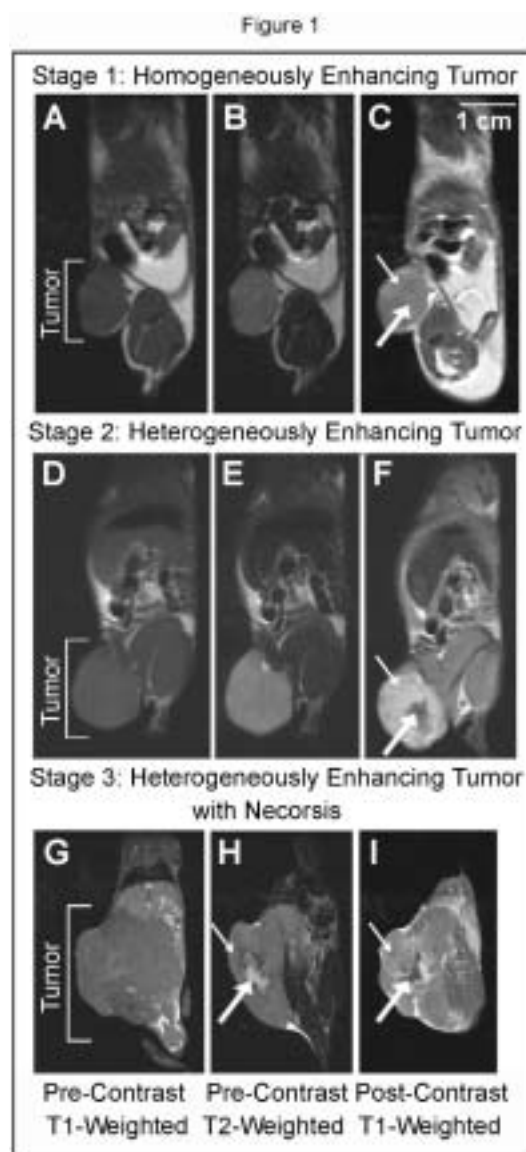

Figure 1

Figure 1. MRI of C3H/K mice with implanted subcutaneous squamous cell carcinoma VII tumors. Images A, D, G: pre-contrast T1-weighted, images B, E, H: pre-contrast T2-weighted, images C, F, I: contrast-enhanced T1-weighted images. The early stage of tumor growth (Stage 1): images A-C, tumors were homogeneously enhanced. The more advanced stage of tumor growth (Stage 2): images D-F, tumors were heterogeneously enhanced. The late stage of tumor growth (Stage 3): images G-I, tumors were heterogeneously enhanced with necrosis. The thick and thin arrows in images C and F indicate the central and peripheral regions of the tumors where the tissue samples were harvested for analysis. The thick and thin arrows in images H and I indicate regions with different T2-weighted MRI characteristics that were also obtained for tissue analysis. Scale bar=1 cm.

center of the Stage 1 tumors (Figure 2A-B), and the CE and NE regions from the Stage 2 tumors were similar (Figure 2C-D). In contrast, samples from the Stage 3 tumors show characteristic signs of tissue necrosis in histological analysis (Figure 2E-F).
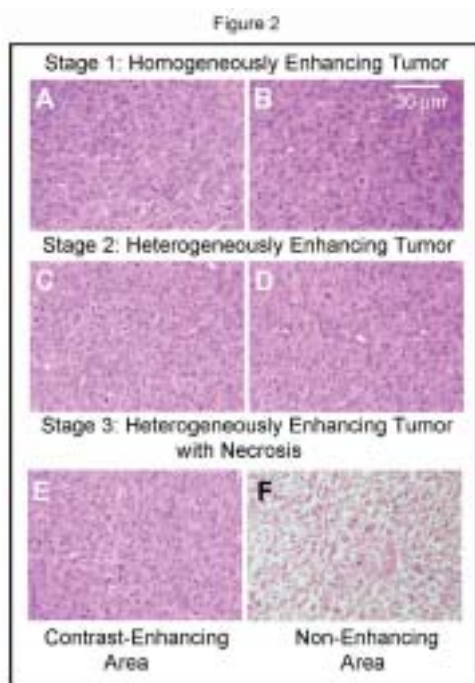
Figure 2: Hematoxylin and Hematoxylin and eosin (H&E) stained tissue samples obtained as marked by the arrows on Figure 1. Figure 2A is the peripheral and B the center areas of Stage 1 tumors. Figure 2C is the contrast enhancing and D the non-enhancing areas of Stage 2 tumors. Figure 2E is the contrast enhancing and F the non-enhancing areas of Stage 3 tumors. Figure 2A-E show viable tumor cells. Figure 2F shows characteristics that are indicative of necrosis. Scale bar=50 m .

Microarray analysis was performed on the periphery and center regions of Stage 1 tumors, and the CE and NE regions of Stages 2 and 3 tumors to obtain six distinct gene expression profiles. Statistical analysis was performed to obtain a list of genes with significant changes in the CE or periphery regions of the tumor, and a Fold Change (FC) value was calculated for each gene (Table 1). The same genomic analysis was performed for the NE and center regions of the tumor among the three stages (Table 2).

CONCLUSIONS

We have found that contrast enhanced MRI can serve as a tool for characterizing spatial heterogeneity through tumor progression for genomic analysis. Regions of increased contrast enhancement in the Stage 2 tumors seem to best correlate with changes in the mRNA of proteins strongly associated with the ECM and Stage 3 tumors show none of the genes up-regulated in the Stage 2 tumors. Five new classes of genes in these tumors now seem to be expressed in addition to genes with unknown function.

In conclusion, image-guided biopsies from these areas was used for genomic analysis to provide both characterization of tumor morphology and identification of potential targets for molecular imaging.

	Stage 2 vs 1 Fold Change	Stage 3 vs 2 Fold Change
Translation/Transcription Factors		
zinc finger, A20 domain containing 1	1.33	0.73
SWI/SNF related gene	0.31	2.00
striamin	2.49	0.32
RE1-silencing transcription factor	0.37	2.17
RIKEN cDNA 2610016F04 gene	0.52	2.04
myocyte enhancer factor 2C	0.52	1.87
zinc finger protein 148	0.43	1.53
splicing factor 3b, subunit 1	1.70	2.83
ion transport		
ATPase, H+ transporting, V1 subunit A, isoform 1	0.54	1.34
ATPase, Na+/K+ transporting, alpha 1 polypeptide	2.90	0.80
ATPase, Cu++ transporting, alpha polypeptide	0.35	2.10
Apoptosis		
CASP8 and FADD-like apoptosis regulator	0.39	1.72
metabolism: biosynthesis/proteolysis		
syndecan 4	4.05	0.20
superoxide dismutase 1, soluble	2.09	0.62
Cell proliferation/cell growth		
kinesin 2	0.77	0.80
cell line NK14 derived transforming oncogene	1.60	0.86
Signal transduction		
guanine nucleotide binding protein, alpha 13	0.41	3.87
complement component 3a receptor 1	0.57	2.29
casein kinase 1, delta	1.40	0.76
ras homolog gene family, member C	1.43	0.82
SNF related kinase	0.72	0.64
expressed sequence AI463719	2.40	0.68

Table 1. Summary of the microarray analysis of the peripheral region of Stage 1 tumors, and the contrast-enhancing regions of Stages 2 and 3 tumors. The table shows a list of genes identified from oligonucleotide microarray analysis to be statistically significant in both Stage 2 vs 1 and Stage 3 vs 2 comparisons using SAM, followed by Fold Changes to show their relative gene expression level.

	Stage 2 vs 1 Fold Change	Stage 3 vs 2 Fold Change
Translation/Transcription Factors		
ATPase, H+ transporting, V1 subunit A, isoform 1	0.45	2.43
splicing factor 3b, subunit 1	0.22	3.42
RIKEN cDNA 2610016F04 gene	0.60	2.18
myocyte enhancer factor 2C	0.48	1.67
RE1-silencing transcription factor	0.43	2.49
ion transport		
ATPase, Cu++ transporting, alpha polypeptide	0.46	2.32
chloride channel 3	0.44	1.77
metabolism: biosynthesis/proteolysis		
syndecan 4	3.84	0.19
NMDA receptor-regulated gene 1	0.21	0.62
KDEL (Lys-Asp-Glu-Leu) endoplasmic reticulum protein retention receptor 2	0.09	0.52
CASP8 and FADD-like apoptosis regulator	0.41	1.74
eukaryotic translation initiation factor 4E binding protein 2	0.39	0.67
Signal transduction		
RAN GTPase activating protein 1	1.54	0.51
cyclin-dependent kinase inhibitor 1A (P21)	1.98	0.69
guanine nucleotide binding protein, alpha 13	0.47	4.50
proviral integration site 1	0.65	1.39
IQ motif containing GTPase activating protein 1	1.46	1.61
complement component 3a receptor 1	0.47	2.61

Table 2. Summary of the microarray analysis of the center region of Stage 1 tumors, and the non-enhancing regions of Stages 2 and 3 tumors. The table shows a list of genes identified from oligonucleotide microarray analysis to be statistically significant in both Stage 2 vs 1 and Stage 3 vs 2 comparisons using SAM, followed by Fold Changes to show their relative gene expression level.

IMAGE ANALYSIS

Removal of folds in CT Colonography using physically based simulation: Proof of concept

Padmavathi Sundaram[+], David. S. Paik, Eftychis Dimitrios Sifakis[*], Chris Beaulieu, Sandy Napel

Departments of Radiology, Electrical Engineering[+], Computer Science[*]

INTRODUCTION

Colonic folds constitute majority of the false positives in computer-aided detection (CAD) of polyps in the colon. Removal of folds while preserving the polyps will not only improve visualization of the complex colon surface but also improve CAD specificity. We present a novel solution to this problem using physically based simulation.

MATERIALS AND METHODS

Our algorithm likens the thickened colon wall to a 3D volumetric sheet that can be stretched along the longitudinal direction, much like a carpet. In order to "shake off the folds," we start with a level set of the thresholded CT data. We then use the level set to build a tetrahedral volumetric mesh representing the thickened colon wall. Various physical properties, for example, Young's modulus, Poisson's ratio, hardening deformation and neo-hookean elasticity are attributed to this mesh. Stretching forces were then applied to two manually selected ends of the data.

The preliminary data used comprised of a small phantom (240 X 50 X 123) generated using MATLAB. The data contained 1 simulated fold and 2 simulated polyps. The surface curvature (K curvature) was measured at the fold and the polyps in the original and the stretched surface.

RESULTS

The surface curvature of the fold in the original unstretched surface was 0.0053 while that of the polyps was 0.0133. Af-

a

b

Stretching a colon phantom: (a) Colon phantom with 2 polyps and a fold (b) Phantom stretched out preserving polyps but flattening the fold

ter stretching the surface, the fold was completely flattened out with almost no curvature, while the curvature of the polyps remained the same. The output of our algorithm was still a 3D volume, except that the folds were suppressed by our simulation.

CONCLUSION

Using physically based approaches to stretch the colon surface free of folds is a novel approach that can change the way CTC data will be visualized. Removal of colonic folds will also improve specificity of CAD algorithms to find colonic polyps. Our preliminary results demonstrate the feasibility of this technique.

REFERENCES

1. Molino N, Bridson R, Teran J and Fedkiw R. A Crystalline, Red Green Strategy for Meshing Highly Deformable Objects with Tetrahedra. 12th International Meshing Roundtable, 103-114, 2003.
2. Teran J, Blemker S, Ng Thow Hing V and Fedkiw R. Finite Volume Methods for the Simulation of Skeletal Muscle. ACM SIGGRAPH/Eurographics Symposium on Computer Animation (SCA), 68-74, 2003.

Anatomically Selective Morphological Enhancement and Suppression in CT Colonography: Initial Experience with a Lagrangian Approach

David S. Paik, Padma Sundaram, Christopher Beaulieu, Sandy Napel

Department of Radiology

INTRODUCTION

CT colonography (CTC) has yet to gain widespread acceptance partially due to the difficulty in interpreting the complex morphology of the colon surface. We propose a new paradigm in CTC image interpretation by radically altering the 3D morphological appearance of the colon in order to entirely suppress and remove haustral folds while leaving polypoid features intact. This is a true departure from previous approaches to colon morphing in the literature in that the proposed algorithm takes advantage of some key observations about the morphology of folds vs. polyps to selectively change their appearance.

MATERIALS AND METHODS

The proposed algorithm is a physics-based simulation of haustral fold effacement by simulating "pulling" on the surface in the longitudinal direction. Unlike conformal mapping approaches that map to a flat plane, this algorithm produces a volumetric dataset that can be volume rendered and potentially processed by a CAD algorithm. Additionally, the degree of "pulling" can be continuously varied in order to infer some information from the dynamics of the colon surface.

A simulated CT phantom was created with 36 polyps from 5-10 mm in a variety of positions relative to haustral folds.
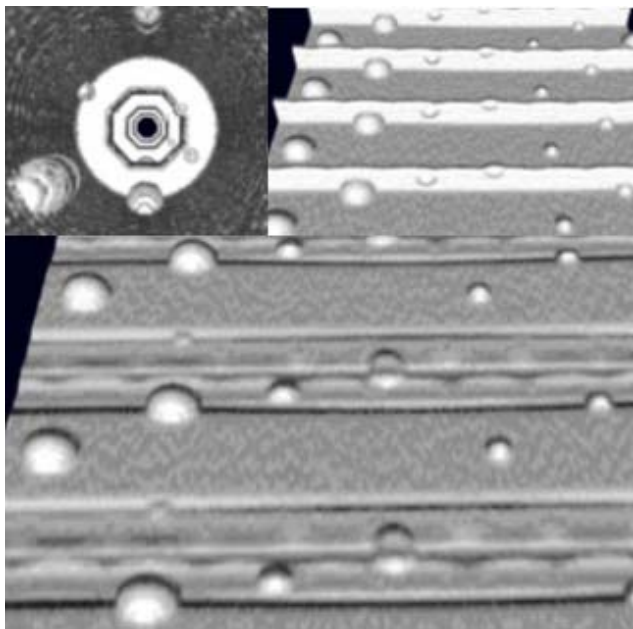
Figure 1 (above). Upper left: endoscopic view of colon phantom. Upper right: unrolled view with folds and polyps intact. Lower: flattened view with folds suppressed and polyps intact.

Simulated 1.25 mm collimation and 1.0 reconstruction intervals were used. As proof of concept, the algorithm was also tested using a 6.9 mm polyp in a patient CT scan. This particularly difficult polyp was chosen because it occurred on the side of a bulbous haustral fold in partially obscured area.

RESULTS

In the simulated phantom, the folds were completely effaced whereas the polyps were extremely well preserved. The folds were measured in the CT images and were reduced in height from 9.7 mm to less than 0.5 mm. The polyps did not change appreciably. In the patient scan, the haustral fold with the polyp on it was reduced from 14.6 mm to 1.8 mm while the polyp went from 9.7 mm to 10.0 mm in width and remained at 3.2 mm in height. Overall, there was a dramatic increase in polyp conspicuity due to the suppression of the haustral folds.
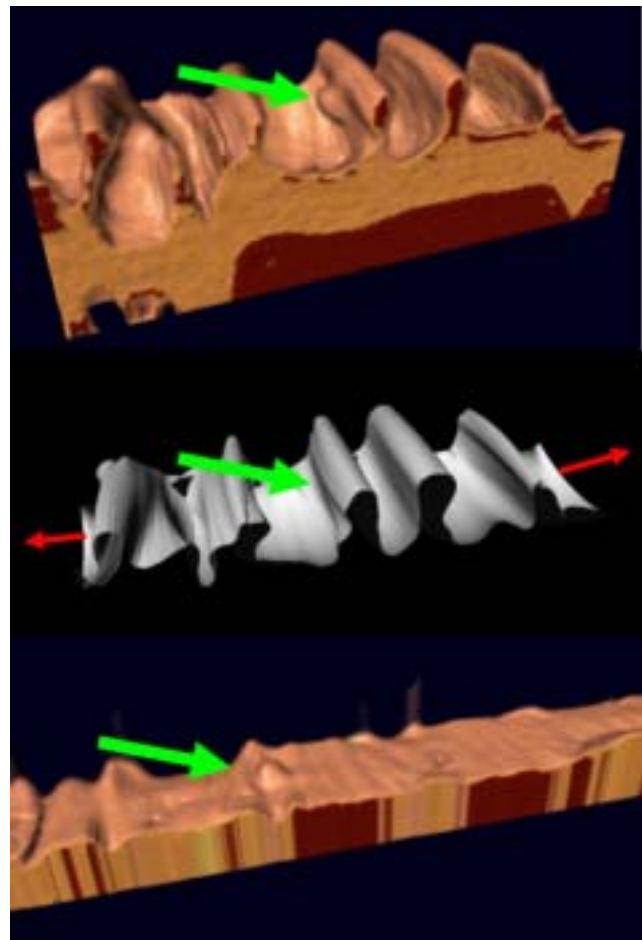

Figure 2 (right). Top: unrolled view of a portion of a human colon with polyp (green arrow) Middle: surface model being "pulled" (red arrows). Bottom: flattened colon with folds suppressed and polyp intact.

CONCLUSION

Although preliminary, these results demonstrate the feasibility of a physics-based simulation of haustral fold effacement in phantom and human data.

Computer Aided Polyp Detection in CT Colonography: Influence of Polyp Features and 3D Viewing on Acceptance or Rejection by Radiologists

Rong Shi, Daniel Margolis, R. Brooke Jeffrey, Jr., Eric Olcott, Pam Schraedley-Desmond, Christopher F. Beaulieu, Sandy Napel

Department of Radiology

INTRODUCTION

We sought to determine whether there are certain characteristics of polyps that impact radiologists' interpretation of computer-aided detection (CAD) results in CT Colonography (CTC) scans, and to investigate if 3D viewing has additional influence.

MATERIALS AND METHODS

In 11 CTC datasets (2.5 - 3 mm sections, 50% overlap, supine or prone position), two unblinded radiologists identified 38 true positive (TP) polyps based on knowledge of fiberoptic colonoscopy results. Each lesion was characterized by size, shape, segment, density, surface smoothness, local distension, and preparation quality. To these 38 lesions, we added 72 additional candidate lesions by supplementing with highly ranked false positive (FP) CAD hits or FP radiologist hits from earlier blinded reading. These potential FP lesions were categorized by their nature, such as thickened fold, stool, ileocecal valve (ICV), etc. Two other radiologists independently scored each candidate lesion (10 per CTC dataset) in terms of confidence that it represented a polyp (1-5 scale, 5 highest), first with axial and coronal tomograms,
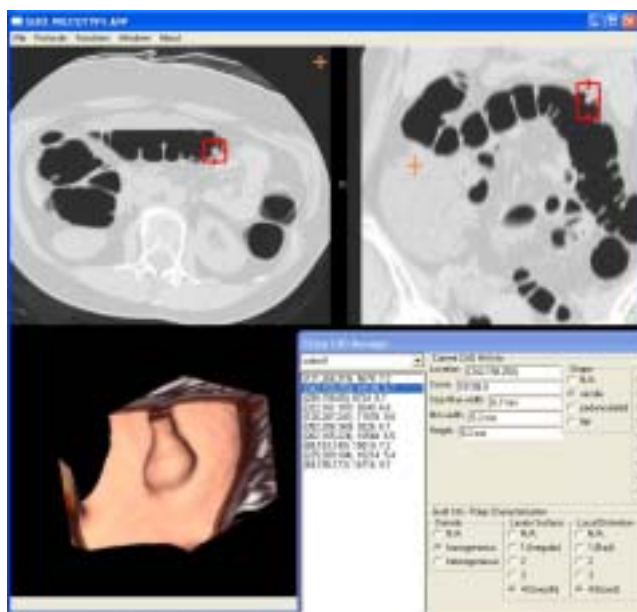
Figure 1: SURF interface displaying a candidate lesion in the center of the red box on transverse and coronal sections (top half). Volume rendering (left lower corner) of the voxels within the bounding box demonstrates that the opacity in question corresponds to a polyp on the edge of one haustral fold. Scoring box (right lower corner) is shown in greater detail in Figure 2.

then with the addition of targeted 3D volume rendering. SURF (Stanford University Radiology Framework) served as the main user interface; see Figs. 1 and 2.

RESULTS

For the 38 TPs, only size and segment influenced confidence levels. Lesions in the sigmoid were assigned lower confidence (mean 2.2) than in other segments (means 3.4-3.9, $p<0.05$). Larger maximum width ($p<0.05$), minimum width ($p<0.01$) and height ($p<0.01$) were associated with higher confidence. Adding 3D viewing increased confidence in smaller (<6mm) lesions ($p<0.05$), and may increase TP
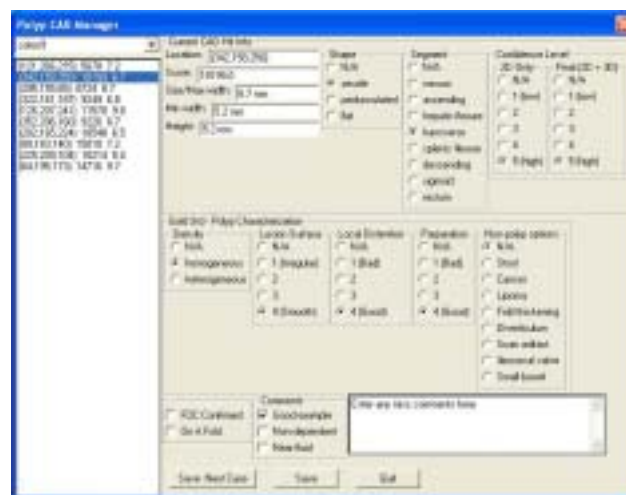

Figure 2: Polyp CAD Manager window of SURF. The list on the left represents polyp candidates to assess. Each TP lesion was characterized series of features including size, shape, segment, density, etc. The potential FP lesions were additionally categorized by their nature.

acceptance overall (2D, 75-89%; 3D, 86-93%). For the 72 FPs, the main variable affecting reader's confidence levels was the candidate's nature. The ICV contributed most of the highest confidence FPs, followed by stool and the small bowel. Thickened folds and scan artifacts were easier for readers to discard.

CONCLUSION

During directed reading of a CAD list of polyp candidates, polyp size and segment location most influenced radiologist judgment. 3D viewing aided interpretation in smaller lesions and may improve the accuracy of true polyp acceptance. Poor distension may be responsible for lower confidence in the sigmoid. Better algorithms and/or reader training to reduce FP caused by the ICV and the small bowel may be required to increase accuracy.

Atherosclerotic Calcium Distribution in Asymptomatic Patients – A Study in 22 patients.

Bhargav Raman, Raghav Raman, Sandy Napel, Geoff Rubin

Department of Radiology

INTRODUCTION

Vascular calcifications have been associated with the development of regional vascular disease. The severity of aortoiliac calcification as seen on chest x-ray studies has been correlated with atherosclerotic risk factors, coronary artery disease, peripheral arterial disease and with cardiovascular mortality. Aortoiliac calcification can be much more common that coronary calcification. The distribution of calcification in the aortoiliac system has been shown to vary significantly depending on age, sex and comorbidity. For ex-

ample, in this study, the occurrence of iliac calcification was also associated with an increased incidence of symptoms of intermittent claudication. Determining the quantity and distribution of calcium in each vessel could allow the investigation of the relationship between the distribution of vascular calcium and the occurrence of systemic vascular diseases including stroke, aneurysmal disease, mesenteric ischemia and lower extremity vascular disease.

MATERIALS AND METHODS

We quantified the amount and distribution of aortoiliac calcium in 21 prospectively obtained CT angiograms of asymptomatic patients (11 male, 10 female, mean age 60.3 years) using our previously developed algorithm. The aortic segments analyzed were: Ascending Aorta, Arch, Thoracic Aorta, Suprarenal Aorta, Infrarenal Aorta, Common Iliacs, External Iliacs, Femoral Arteries, Popliteal Arteries.
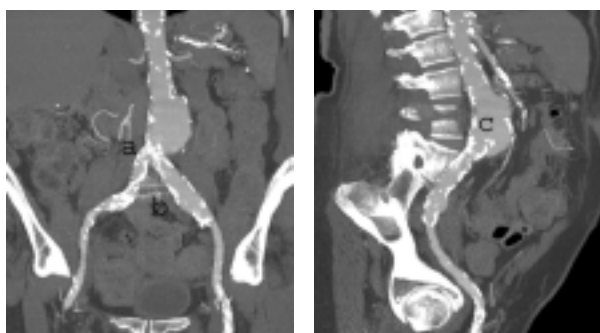
Maximum Intensity Projections (MIP) depicting calcium distribution in an abnormal symptomatic patient with abdominal and iliac aneurysms. The left image is a anterior view of the aorta and common iliacs and the right image is a sagittal view of the same. Notice the higher incidence of calcified deposits in the aortic (a) and iliac (b) bifurcations and near lumbar artery branches (c)

In addition to discrete segments of the aorta, we also focused on high and low shear zones areas near arteries branching off the aorta and areas of high curvature. Calcium mass was normalized to surface area, calcium in branch regions was compared to areas at a distance from a branch point, and the amount of calcium in high and low shear regions were compared to no-shear regions. All calcium fragments detected were reviewed by one of the authors (RR).

RESULTS

The infrarenal aorta had the largest amount of calcium mass (254 ± 392 mg, p < 0.05) followed by the thoracic aorta (79.3 ± 184 mg) and the common iliac arteries (65.9 ± 105 mg). The external iliacs (10.9 ± 26.9 mg) and the popliteal arteries (1.58 ± 6.30 mg) had the least amount of calcium (p < 0.05). When comparing branch regions to non-branch regions, branch regions exhibited on average 7.82 times more calcium per unit area than non-branch sectors. Low shear zones exhibited on average 16.8 times more calcium per unit area than non-shear zones. High shear zones exhibited on average 1.8 times more calcium per unit area than non-shear zones.

CONCLUSION

Preliminary results indicate that atherosclerotic plaque is most prevalent in the infrarenal aorta, thoracic aorta, and the common iliac arteries. These findings coincide with the locations of most aortic and aorto-iliac aneurysms. Branch areas and shear zones may be at increased risk of development of atherosclerosis. Further studies with more patients will need to be done to establish the predictive value of atherosclerotic plaque distribution with respect to the incidence and severity of future vascular disease.

Morphological Differences in Thoracic Aortic Aneurysms When Compared To Normal Aortas – A Comparative Study in 49 patients

Raghav Raman, Zhao Shaohung, Bhargav Raman, Sandy Napel, Geoff Rubin

Department of Radiology

INTRODUCTION

Aortic Aneurysms can potentially distort normal aortic anatomy by causing elongation, expansion and torsion, but this is especially pronounced with thoracic aortic aneurysms (TAA) because of the curve of the aortic arch. As a result, TAAs can cause difficulty during stent graft treatment planning and deployment. We aimed to characterize these morphological changes by comparing the shape and size profiles of the thoracic aorta in normal patients to patients with TAAs using Multi-Detector Row CT.

MATERIALS AND METHODS

We obtained preoperative CT Angiograms (CTAs) of 50 patients with TAAs and 17 controls scanned for other indications. Using our previously developed algorithm, we calculated an initial path through the lumen of the aorta to indicate its course. The path was then iteratively centralized to the center of mass of the aorta along its length. Using this central path, the diameter was calculated for each perpendicular cross-section of the aorta in each segment. Also, length and curvature (tortuosity) of the segments were quantified. These were compared with the corresponding segments in normal patients. Segments of the aorta were defined as the portions between the major branches of the aorta in this region. The segment nodes were the Aortic Root, Right Brachiocephalic Artery (RBCA), Left Common Carotid Artery (LCCA) and the Left Subclavian Artery (LSCA). Because normal patients do not have an aneurysm, we could not compare path lengths within the aneurysm itself. For curvature statistics, we compared the segment bounded by the proximal and distal necks of the aneurysm and the segment bounded by the LSCA and the proximal neck of the aneurysm with the segment bounded by the LSCA and the celiac artery bifurcation.

RESULTS

On average, the thoracic aorta was significantly larger in diameter in patients with aneurysms (34.8 vs 26.1 mm, p<0.01) with the largest difference being distal to the branch point of the left subclavian artery (LSCA) (34.7 vs. 25.3 mm, p<0.01). Patients with TAAs had thoracic aortas that were on average not significantly longer (p > 0.05). However the segments LCCA-LSCA and LSCA-end were significantly longer in abnormal patients (p< 0.01). There was no difference in overall average curvature (p=0.14). The segments Proximal-Distal Neck and LSCA-Proximal Neck had significantly higher curvature in abnormal patients than the segment LSCA-End in normal patients (p < 0.001 for both).
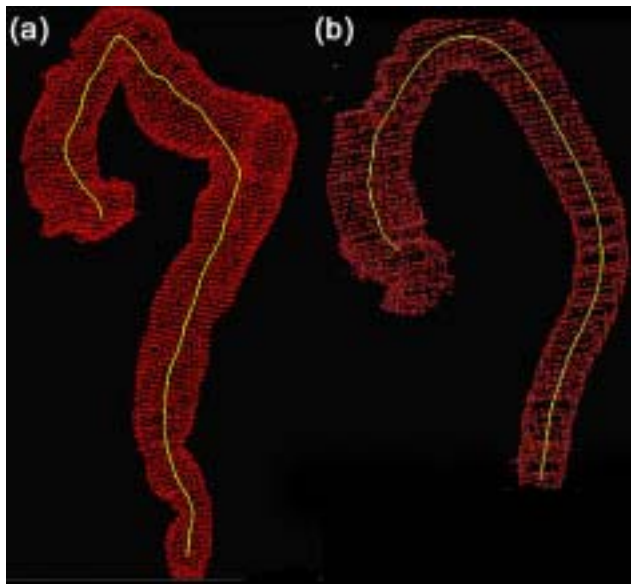
Table 1	Path Length (mm)		Curvature (mm⁻¹)	
	Normal	Abn.	Normal	Abn.
Total	289 ± 43.9	358 ± 71.9	14.8 ± 1.6151	15.6 ± 2.02
Root-RBCA	72.6 ± 18.5	71.9 ± 17.4	20.5 ± 4.12	19.6 ± 5.27
RBCA-LCCA	10.7 ± 5.38	10.88 ± 5.24	19.0 ± 4.26	19.1 ± 6.22
LCCA-LSCA	13.5 ± 5.94	18.9 ± 8.42	19.27 ± 5.36	19.27 ± 6.42
LSCA-End	192 ± 32.1	256 ± 68.4	13.74 ± 1.61	14.8 ± 2.60
Prox.- Dist. Neck	-	134 ± 73.7	-	17.2 ± 5.42
LSCA-Prox. Neck	-	47.3 ± 55.7	-	24.1 ± 8.25

Figure 1: (a) Abnormal and (b) normal luminal segmentations. Notice the significant kinking in the aorta caused by the aneurysm.

CONCLUSION

The morphological differences in aortas with thoracic aortic aneurysms were found in relatively specific areas. While the most well known effect of aneurysmal change is an increase in diameter, there is also a significant increase in length distal to the LSCA. We found significant curvature increase in abnormal patients only in the area of the aneurysm, indicating that the aneurysm causes significant kinking of the aorta (Fig. 1). Further studies to delineate the time course of these changes in morphology may be warranted to aid preoperative stent graft planning and deployment and improve follow-up for thoracic aortic aneurysms.

Knowledge Based Parameterization of the Arterial Tree using Principle Component Analysis

Tejas Rakshe[1], Dominik Fleischmann[2], Sandy Napel[2]

[1] Department of Electrical Engineering, [2] Department of Radiology

INTRODUCTION

Utilizing knowledge of the arterial system is essential for tackling the problems encountered while tracking partially or completely occluded blood vessels in radiological images, and for identifying normal and diseased arteries. Our goal is to find the optimum way of utilizing this prior knowledge, and we approach this using Principal Component Analysis (PCA).

MATERIALS AND METHODS

We studied 13 patients with normal lower extremity vascular structure obtained from CT-Angiographic data.

First, we extracted the medial axis of the vascular structure using a semiautomatic method. For consistency, the length of the femoral bone was used as a surrogate for the body size to normalize the data from different patients. In the next stage, we modeled the medial axis of each vessel as a parametric curve. Thus each 3-D curve was represented as a set of three functions. Each of the function represents the X, Y or Z co-ordinate of the curve as versus the distance traversed along the curve from a reference point, the reference point being the origin of the vessel segment. We used PCA on the patient data to find the eigenfunctions for each of the three functions for each vessel segment [1]. Thus, each eigencurve obtained is a set of three eigenfunctions. This analysis is done separately for each vessel of interest. As a result we have the most energy-efficient statistical description for each artery of interest.

RESULTS

Figure 1 shows two examples of the medial axis extracted from two typical patient data sets, and the first eigencurve computed for the same artery from all patients. The similarity between the typical artery shape and the most prominent eigencurve can be seen. Figure 2 plots the percentage cumu-
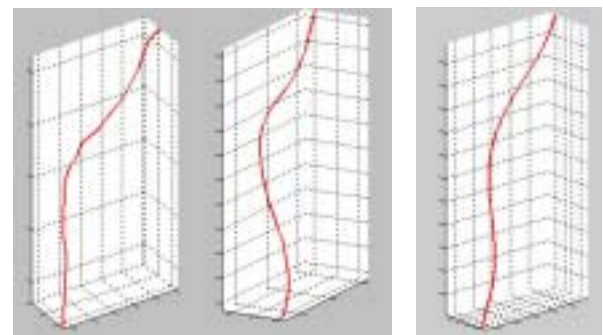

Figure 1: Left and middle: Medial axes of the right iliac (common and external) arteries from two typical patient data sets. Right: The first (most prominent) eigencurve for the medial axis of the right iliac (common and external) artery from all patients combined.

143

lative energy contained in a sequence of the first 4 ordered eigencurves for the right iliac vessel for all patients. In general, only the first 3 eigencurves were enough to capture over 95% of the energy for any of the medial axes.

CONCLUSION

The results confirm that the vascular tree has a highly correlated structure. The set of 13 vessels can be represented very accurately by a set of only 2 to 3 eigencurves for each. Such descriptions can be used in future for locating the medial axes of partially or completely occluded arteries, classifying unknown vessels based on their shapes, and classifying diseased arteries from the normal ones.

REFERENCES

1. K. Sam Shanmugan, Arthur M. Breipohl, "Random Signals: Detection, Estimation and Data Analysis", Wiley, 1988.
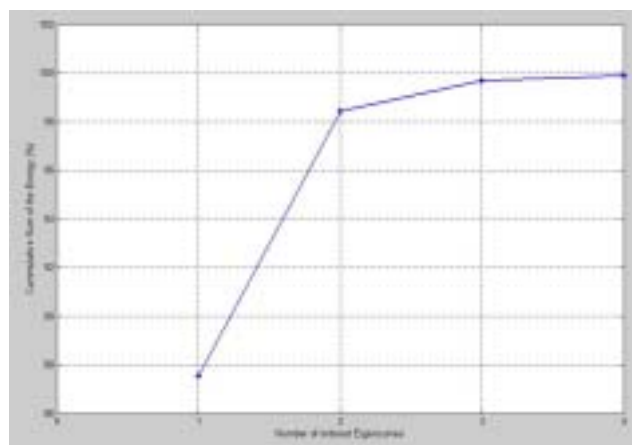
Figure 2: Cumulative sum of the energy in percent (for right common + external iliac artery), versus number of ordered eigencurves.

Investigation of Maximizing Mutual Information for Registration of 2D DSA images with 3D CTA as a Function of Vascular Filling

J. Dey, S. Napel

Department of Radiology

INTRODUCTION

To improve guidance of devices during interventional procedures, we aim to incorporate information from a preoperatively acquired 3D CT Angiogram (CTA), which requires registration of the 2D Digital Subtraction Angiogram (DSA) images with the CTA data. This study explores the robustness of our registration method as a function of different degrees of vascular filling (DVF) in the DSA images.
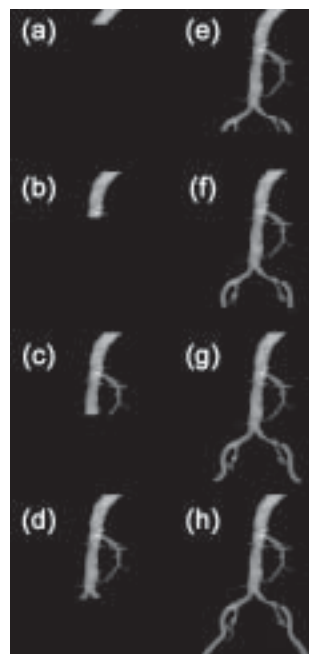

Figure 1: Sequence of DSA images simulated at different degrees of vascular filling: (a) 17%, (b) 33%, (c) 59%, (d) 60%, (e) 70%, (f) 76%, (g) 80%, and (h) 100%.

MATERIALS AND METHODS

We simulated anteroposterior 2D DSA images from a 3D CTA patient dataset consisting of 500 sections covering 450 mm acquired using multi-detector CT. The DSA images were simulated by segmenting the vasculature from the descending aorta to the bifurcations of the external and internal iliac arteries, including the celiac, hepatic, splenic and superior mesenteric arteries, and re-projecting through the segmented volume along divergent rays.

We simulated eight different DVFs by stopping the segmentation at different distances from an initial proximal seed point. We used Mutual Information (MI) as a similarity measure for our registration system, and tested it by computing, for each DVF, a stochastic estimate of the MI for each of 1000 random settings of 6 orientation parameters (3 angles and 3 translations, each on a range of ± 20° and ± 2 cm, respectively, from alignment) of the 3D CTA prior to re-projection.

We assessed convergability of the algorithm by a measure C defined as the (MI at alignment - mean MI away from alignment)/(standard deviation away from alignment), where away from alignment means at points in the range ±[4°-20°] for the 3 angles, and ±[0.4-2] cm for the three translations.

RESULTS

C was 3.2, 4.2, 5.9, 5.7, 7.5, 8.6, 9.7, and 12.3, at DVFs of 17%, 33%, 50%, 60%, 70%, 76%, 80% and 100%, respectively. Thus, while the amount of vascular filling affects the MI, complete vessel filling is not required.

CONCLUSION

In this preliminary example, even minimal vascular filling results in a visible peak above the noise in the MI vs. orientation parameters plot. This is encouraging for our DSA-CTA registration approach, and thereby warrants continued development and assessment with actual DSA and CTA data.

Three-Dimensional Characterization of the Normal Peripheral Arterial Tree

Tejas Rakshe[1], Dominik Fleischmann[2], Sandy Napel[2]

[1] Department of Electrical Engineering, [2] Department of Radiology

INTRODUCTION

Knowledge of normal anatomic parameters is a prerequisite for the development of an abstract vessel tree model. We attempted to determine the range of morphologic characterization of the lower extremity arterial tree (Figure 1) in patients without vascular disease.

MATERIALS AND METHODS

Eleven patients (6m/5f, 20-86y) without peripheral arterial occlusive disease underwent lower-extremity CT-Angiography (1.25mm/0.8mm STh/RI). A semi-automated algorithm was developed and used to identify the medial axes of the following anatomic segments: aorta (AO), common (CIA) and external (EIA) iliac arteries, femoropopliteal artery (FPA), anterior (ATA) and posterior tibial (PTA), and peroneal arteries (PEA). Individual arterial segmental diameters were measured. The lengths of the arterial segments were determined between branching points after polynomial smoothing of the medial axes. Arterial diameter and length measurements were correlated with the subject's femoral bone length as a surrogate for body size. Vessel curvature was expressed as the proportion of vessel length to the shortest distance between start/end points of the respective seg-
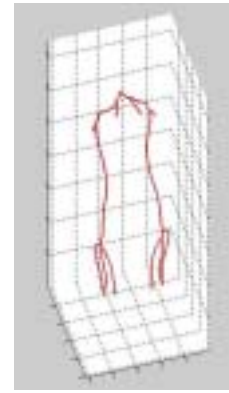

Figure 1: A typical lower extremity arterial tree.

ment. The initial 3 cm of the smoothed medial axes were used to determine the bifurcation angles in 3D.

RESULTS

Both diameters and lengths (Table 1) tended to increase with femur length (for FPA length: r=0.96, p<0.01) and were generally larger for men. Vessel curvatures (Table 1) were slightly greater in ATA than in FPA, and the CIA+EIA, with a tendency to increase with age. Aortic and popliteal artery bifurcation angles (Table 2) also increased with age.

CONCLUSION

The range of vessel diameters, lengths, curvatures, and branching angles of the normal peripheral arterial tree appears to be well predictable. An abstract, parameterized peripheral arterial tree model should account for gender, body size and subject age.

Artery	Mean diameter (mm)	SD diameter (mm)	Mean length (mm)	SD length (mm)	Mean curvature (mm^{-1})	SD curvature (mm^{-1})
CIA	9	1.3	80	26	1.013	0.02
EIA	7	1.3	179	30	1.021	0.017
FPA	5.2	0.7	661	83	1.079	0.041
ATA	2.8	0.7	295	111	1.092	0.066
PTA	2.7	0.9	265	104	1.083	0.075
PEA	2.6	0.7	258	114	1.082	0.091
CIA+EIA	-	-	-	-	1.03	0.03

Table 1: Main statistics for the arteries

Artery	Mean bifurcation angle (degrees)	SD bifurcation angle (degrees)
AO	34.7	8.0
CIA	38.4	15.4
EIA	17.3	3.8
FPA	35.1	7.6
TPT	20.1	5.1

Table 2: Angles of bifurcation at the lower end of the artery

Deep-Lumen: Medical Imaging Graphics Cluster

Anthony Sherbondy[1], Sandy Napel[2]

[1]Department of Electrical Engineering, [2]Department of Radiology

INTRODUCTION

Current medical imaging technology can produce CT or MR reconstructed volumes with sizes on the order of gigabytes. This is a daunting amount of information for radiologists to process in order to make their respective diagnosis.

Recently, inexpensive consumer desktop computers equipped with commodity video cards have been shown to be highly efficient architectures for medical image processing tasks including; high quality volume rendering, segmentation, image enhancement and registration operations. However, the utility of these algorithms has been limited by the modest amount of memory available on the commodity graphics cards.

While game developers do not seem to desire more memory on the cards they have continually pushed for architecture and speed improvements that would be useful for the previously mentioned medical image processing tasks. Therefore, Deep-Lumen was created to address the memory problem by providing a tightly linked cluster of computers that each contain a cutting edge video card while communication between nodes is handled with a fast interconnect.

MATERIALS AND METHODS

The Deep-Lumen cluster was designed to offer a scalable rendering and interaction platform for large medical datasets.

Deep-Lumen: This cluster has 8 nodes, each with an Infiniband interconnect and an ATI Radeon 9800Xt graphics card.

It specifically was designed in the short term to offer interactive volume rendering and manipulation of medical volumes up to 2 Gigavoxels. By relying on a cluster of the latest commodity graphics hardware, the cluster has the ability to upgrade its rendering capabilities at minimal costs. Currently, the cluster, provided by GraphStream, is comprised of the following:

- · Entire Configuration:
  - o 8 nodes
  - o 3U half depth of each node
  - o 16 2.4 GHz P4 Xeons CPUs
  - o 4 GB DDR RAM
  - o 600 GB hard disk
  - o Infiniband Interconnect
- · Node Configuration
  - o Dual 2.4 GHz P4 Xeons
  - o Intel E7505 chipset
  - o 512MB DDR memory
  - o ATI Radeon 9800XT graphics
  - o Infiniband 4X port
  - o GigE network port
  - o 80 GB IDE hard drive

RESULTS

Currently, we are able to execute a sort-last volume rendering algorithm on a 512x512x1024 volume at interactive rates (10 fps) across all 8 nodes. The volume rendering algorithm is a standard 3D texture based renderer with a common Levoy tent transfer function with lighting using a Blinn-Phong shading model.

CONCLUSION

We have shown that the volume rendering application is able to scale to Gigavoxel data sets at interactive display rates utilizing our graphics cluster. Volume rendering is an important benchmark application for processing large medical imaging data sets; however, there are other algorithms that will also be useful on our graphics cluster, such as segmentation, registration, reconstruction and computer automated detection and diagnosis algorithms. Future development should show these algorithms to benefit from deployment on the Deep-Lumen graphics cluster.

REFERENCES

1. Anthony Sherbondy, Mike Houston, and Sandy Napel, "Fast Volume Segmentation with Simultaneous Visualization Using Programmable Graphics Hardware," In Proceedings of *IEEE Visualization 2003,* pages 171-176.

Deep Lumen Display: A Large-Area High-Resolution Displays for Radiology Applications

Joong Ho Won[1], Anthony Sherbondy[1], and Sandy Napel[1,2]

[1]Departments of Electrical Engineering and [2]Radiology

INTRODUCTION

One promising solution to effectively handle large datasets in radiology is to visualize them at full-scale and at different levels of abstraction. High-resolution displays are crucial in presenting such information properly [1]. We developed a Deep Lumen Display (DLD) system that provides a large-area, high-resolution interactive display wall for radiology applications. This system uses only commodity hardware components and open-source software, providing an inexpensive solution for display of large-scale radiological imagery.

MATERIALS AND METHODS

The display cluster consists of two Linux workstations each of which has an ATI FireGL X1 graphics processing unit and dual Pentium 4 CPUs, and four 21-inch flat-panel LCD panels with 1600x1200 resolution each. For each workstation there are two panels attached, resulting in a 2x2 tiled display wall with 3200x2400 resolution. To provide a single uniform, seamless display wall, we use Distributed Multihead X (DMX) and Chromium.

DMX (http://dmx.sourceforge.net) is open-source software that provides X window functionality to run multiple displays (multi-head) attached to multiple physical workstations. Its Xinerama support provides a single unified screen, making a tiled display wall possible.

Multiple backend X servers run on physical workstations and a front-end proxy X server controls these servers, making up a large area display. The front-end server supports almost all of the X protocols and, therefore, existing X applications can run on the display wall without modification.

Chromium (http://chromium.sourceforge.net) [2] is also open-source software that provides distributed OpenGL processing functionality on a cluster of workstations. This software intercepts OpenGL calls from a client application and distributes them to the network so that servers to which displays are attached render their portion of a scene (tilesort). Chromium can run on DMX, providing 3D graphics support to the display wall.

In addition to the tilesort support, this software has various functionalities for distributed rendering. For example, a separate 8-node GraphStream cluster is used to render volume data for display on the DLD.

RESULTS

Most of the work so far has been devoted for tuning and debugging the open-source software to run on the DLD. As of June 2004, the display wall can render high-resolution 2D imagery and OpenGL applications without modification. Figure 1 shows two views of a CT angiogram runoff study

Figure 1: Volume rendering and MIP of a CTA runoff study on the 3200 x 2400 pixel display
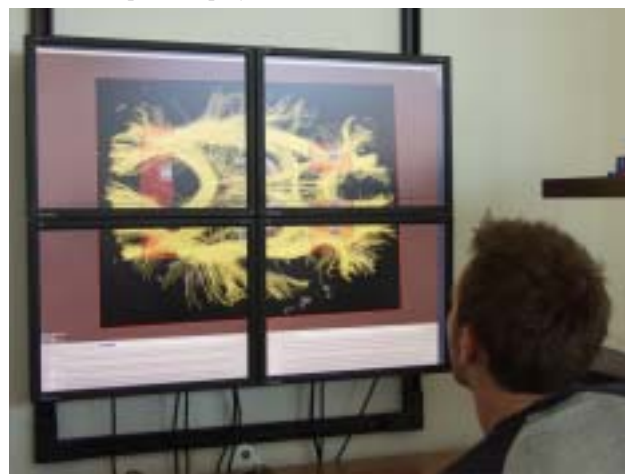

Figure 2: Brain DTI viewer rendered on DLD.

making use of the 3200x2400 resolution of the DLD. Figure 2 is an example of an OpenGL application, a Diffusion Tensor Imaging viewer developed by Akers and Sherbondy.

Also, many other Stanford University Radiology Framework (SURF) applications under development (e.g., CT colonography, Lung nodule detection) can take advantage of the physically extended display area and higher resolution.

CONCLUSION

Our work provides a new environment to visualize most of radiological application in a large-area, high-resolution display with minimum additional effort. We envision that this system can serve as a platform for testing and evaluating novel medical visualization methods.

REFERENCES

1. Wei B, Silva C, Koutsofios E, Krishnan S, North S, Visualization Research with Large Displays, IEEE CG&A, July/Aug 2000.
2. Humphreys G, Houston M, Ng R, Frank R, Ahern S, Kirchner P, Klosowski JT, Chromium: A Stream Processing Framework for Interactive Rendering on Clusters, ACM SIGGRAPH 2002.

A Voice-Controlled, Large Stereo Display for Improved Image Guidance in the Interventional Room

Markus Kukuk[1], Sandy Napel[2]

*[1]Siemens Medical Solutions; [2]Department of Radiology*

INTRODUCTION

During the past decade, the field of radiology has changed from a purely diagnostic to an also therapeutic field. Today, "interventional radiologists" perform a variety of minimally-invasive procedures such as "endovascular surgery" under radiological image guidance. Interventional radiology procedures are advances in medicine that have replaced many open surgical procedures. They are generally safer for the patient because they involve no large incision, and are associated with less pain and shorter recovery times.

The images are acquired in a dedicated operating room, generally called an "interventional room" using a fluoroscope system, which produces two-dimensional projection images in real-time, based on x-ray absorption. The lack of depth information in the acquired images makes introducing instruments, such as guidewires, into the vascular system a challenging task. Therefore, the goal of this project is to build a large in-room stereo display to help guiding procedures with particularly tortuous or abnormal vasculature. Voice control has been incorporated as a human-computer interface particularly suitable for sterile environments.

MATERIALS AND METHODS

The basic principle in which humans visually perceive their environment in three dimensions is well understood. The brain receives two images, one from the projection of a scene onto the back of each eye and creates depth information not previously included in the two input images. The resulting effect is also known as stereo vision. A prerequisite for stereo vision is "binocular disparity", which is the slight difference between the viewpoints of the left and right eye. In other words, the brain "sees" the world from two different viewpoints and "molds" this information into the perception of a three-dimensional scene.

The effect from binocular disparity has long been used to artificially create stereo vision for data viewing applications. Two images of a scene are generated from two different viewpoints and presented separately to the left and right eye. In the interventional room, stereo image pairs can be acquired using state-of-the-art fluoroscopy / c-arm systems. A c-arm consists of a source / detector pair, mounted on a c-shaped gantry, which can be rotated around the patient on an isocentric trajectory to acquire a series of projections, for example one projection per degree. From this acquisition, stereo pairs can be formed by selecting, for example, the 1st
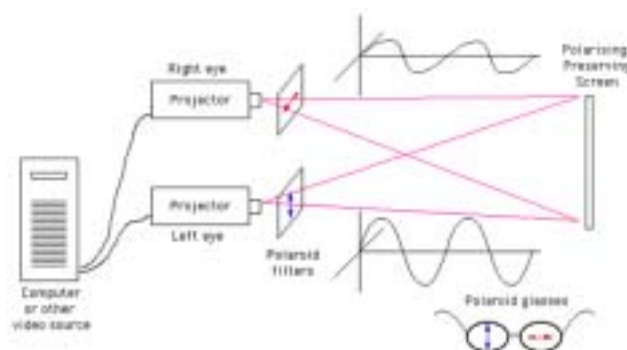
Top: Components of a passive stereo projection system. Bottom: Interventional room with our integrated large stereo display. Note the c-shaped gantry with the x-ray source (right) and flat panel detector (left) in the foreground.

and 4th, 2nd and 5th and so on, images for an eye distance of four degrees.

A passive stereo projection system (see figure below) was found to be the technology of choice for this application. It can produce large, high-quality images while requiring the user to only wear lightweight, passive glasses, similar to regular sun glasses. The images are in color and show high spatial and temporal resolution. In this technology, image separation is based on the principle of polarized light.

RESULTS

We built a passive stereo projection system and integrated it into an interventional room. The system can instantly display a series of projections in stereo without the need for time consuming 3D reconstruction. The display measures 6.4 x 4.0 feet and has a spatial resolution of 1024x768 pixels and a temporal resolution of 60Hz. Voice commands such as "loop", "rock" and "stop" can be used to navigate through the projections. Preliminary phantom studies suggest that the system may add value to the guidance of interventional procedures. Depth can be perceived from a static stereo image, which may facilitate the introduction of instruments into vessels with tortuous trajectories.

2D/3D Registration for Image Guidance in Interventional Radiology

Markus Kukuk[1], Sandy Napel[2]

[1]Siemens Medical Solutions; [2]Department of Radiology

INTRODUCTION

In interventional radiology, minimally invasive procedures, such as "endovascular stent grafting", are performed under image guidance. Currently, 2D fluoroscopic images based on X-ray absorption are acquired intraoperatively to visualize the introduced tools (guidewire, catheter, graft) inside the vascular system. The main problem with fluoroscopy as an intraoperative imaging modality is the lack of depth information. Therefore, numerous attempts have been made to incorporate information from preoperatively acquired 3D tomographic images (e.g., CT- and MR-Angiography). Incorporating images from other modalities requires registration (spatial alignment) of 2D projection images with 3D tomographic images. The goal of this project is to develop an experimental framework in which different 2D/3D registration algorithms can be tested and their performance be evaluated.

MATERIALS AND METHODS

For an initial evaluation, we simulated 2D fluoroscopic images corresponding to a 3D CT dataset by positioning a virtual camera and computing raysums (reprojection) along divergent rays. We then attempted to match these resulting Digitally Reconstructed Radiographs (DRR) to projections through the 3D dataset. This 3D-to-2D registration can be formulated as the problem of finding 6 parameters of a camera that produced the 2D image. The idea is to find the optimum value, over the 6D parameter space, of an image metric by comparing the original DRR to new projections through the 3D volume.

We measured the dissimilarity between the two images by means of the L1-norm and found the minimum by using a best-neighbor optimizer. To speed up the calculation of the L1-norm we implemented a stochastic approach called SSDA (Sequential Similarity Detection Algorithm). To increase the capture range and robustness we implemented a multi-resolution framework.

RESULTS

We produced a 2D DRR reference image and subsequently reoriented the camera by (37I, 43I, 44mm, 41mm, 51mm, 26I). The algorithm converged within 0.75I about all rotation axes and 1.3mm along all translation axes in 50 iterations (3 min. on an Intel P4/1GHz processor).
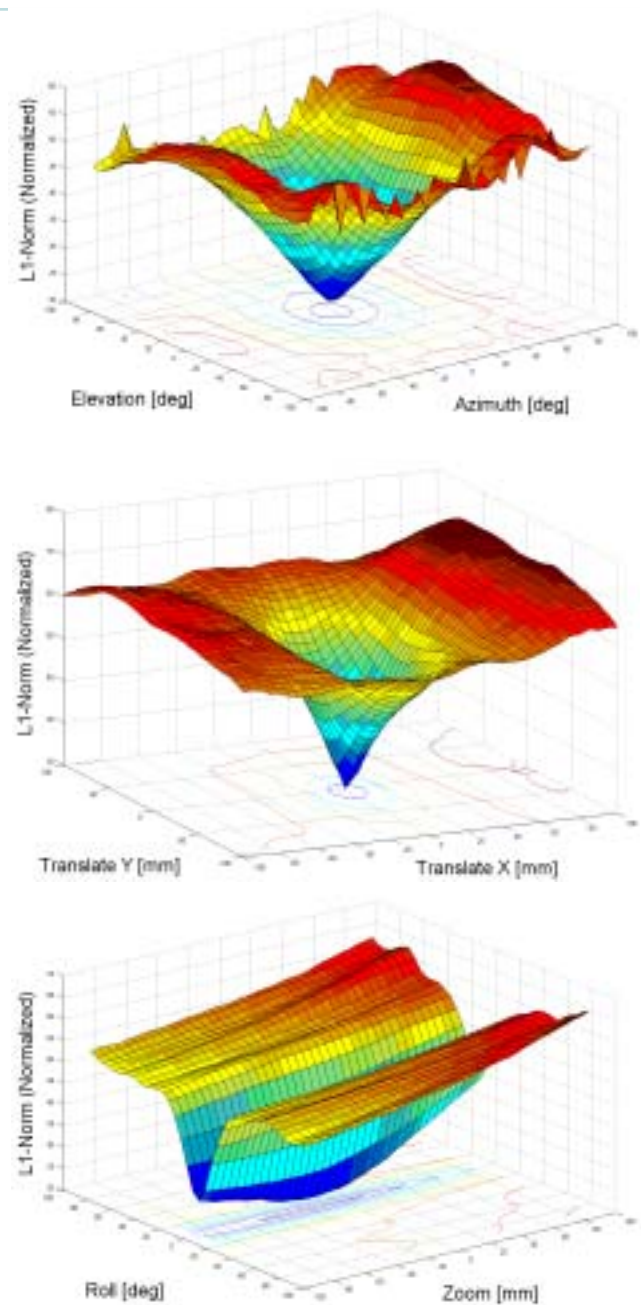

Image metric (L1-norm) over the 6D camera parameter space. Top: Azimuth and Elevation; Center: Translation X and Y; Bottom: Zoom and Roll

CONCLUSION

DRR-DRR registration by minimizing image dissimilarity exhibits a sharp and distinctive global minimum around the ground-truth for 5 of the 6 parameters, while "zoom" appears to cause slow convergence. The multi-resolution approach was found to significantly improve the speed, robustness and capture range. The capture range, on the order of 40I/mm, appears to be sufficient for most clinical applications. The next step will be to apply the algorithm to actual projection x-ray images.

Exploration of the Brain's White Matter Pathways with Dynamic Queries

Anthony Sherbondy[1], Dave Akers[2], Robert Dougherty[3], Sandy Napel[4], Brian Wandell[3]

[1]*Department of Electrical Engineering,* [2]*Department of Computer Science,* [3]*Department of Psychology,* [4]*Department of Radiology*

INTRODUCTION

Diffusion Tensor Imaging (DTI) provides a non-invasive way to measure properties of white matter pathways. Based on magnetic resonance imaging, DTI estimates the random diffusion of water molecules within biological tissue and, from that, infers the approximate local orientation of nerve fiber bundles.

We propose a new interaction technique to assist in the exploration and identification of the pathways suggested by DTI. We allow for the specification and interactive manipulation of box-shaped regions of interest within the brain, enabling researchers to selectively display pathways that pass through specific anatomical regions. Our key contribution is to precompute the pathways and their statistical properties and query the resulting database on-the-fly, allowing for easy exploration of pathway results using a direct-manipulation interface. This dynamic query approach enables researchers to answer specific questions about brain connectivity with far less time or effort than is required by existing approaches.

MATERIALS AND METHODS

Our direct manipulation interface (Fig. 1) allows one to identify and display pathways that satisfy statistical constraints, or that pass through specific volumes of interest (VOIs). Since data exploration involves making iterative adjustments to queries, one of our main goals has been to make the system immediately responsive when the investigator changes a query. One key to this interactivity is the preprocessing of the proposed pathways, but this preprocessing is not enough by itself to make our system interactive. At runtime, we also need to be able to interactively compute intersections between VOIs and pathways. To facilitate fast intersection tests, our program stores each pathway's geometry as a hierarchical oriented bounding box (or OBB) Tree. All VOIs and pathways are represented as sets of triangles that can be efficiently tested for intersection. The box-shaped VOIs are trivial to triangulate, and the pathways are triangulated as very small area (long and thin) triangles.

RESULTS

We acquired a DTI dataset from a single normal subject and experimented with queries that are especially useful to neuroscientists. In particular, we demonstrated how our system
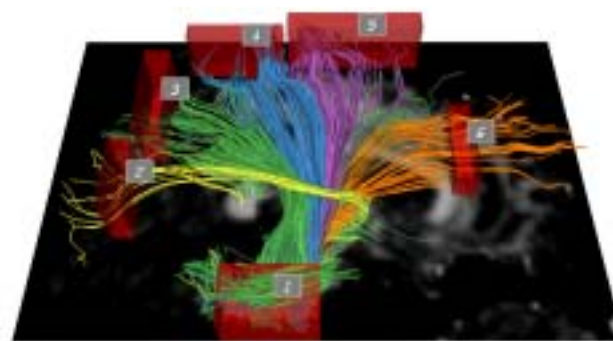

Figure 1: Exploring connectivity to the corona radiata. The user has placed VOI "1" in the brain stem and queried the computed database of pathways to discover distinct regions of the corona radiata connected to the VOI in the brain stem. Pathways stained yellow, e.g., connect VOI "1" to VOI "2", those stained green connect VOI "1" to VOI "3" and so on.

can be used to validate known white matter pathways, to explore previously unidentified pathways requiring future research, and to visually compare pathway tracing algorithms. All three query types were performed by a novice user of our system who is a neuroscientist specializing in brain imaging. Figure 1 demonstrates an example result where the user was able to isolate separate parts of the corona radiata connecting to the brain stem using our system.

Queries based on precomputed pathway properties take very little time. In our own benchmarks with 26,000 pathways, we are able to perform VOI queries at between 2 and 10 frames per second depending on the size of the VOI. Our technique will also allow us to implement more complex VOI shapes in the near future, without a major change in performance.

CONCLUSION

The fast interactivity provided by our system is the key to its utility. Our colleagues in psychology stressed the significance of this program as an exploratory tool - quickly browsing through connections in the brain could be invaluable in identifying areas of interest for future study. The system could serve as an interactive tool to help scientists explore anatomical structure and functional relationships in the brain. It could assist scientists investigating the neurological bases of disorders, as has been done with other methods for analyzing DTI data, or provide a diagnostic tool for such disorders. It could also be employed as an educational aid for students learning about neuroanatomy, as it allows for interactive viewing of the primary anatomical pathways.

REFERENCES

1. Akers, D., Sherbondy, A.J., Mackenzie, R., Dougherty, R.F., and Wandell, B. (2004). Exploration of the brain's white matter pathways with dynamic queries. Accepted for publication to IEEE Visualization, 2004.

A Simulated Annealing-based Algorithm for Lung Nodule Registration in CT Scans

Shaohua Sun[1], Geoffrey Rubin[2], Sandy Napel[2]

[1]Department of Electrical Engineering, [2]Department of Radiology

INTRODUCTION

Lung nodule growth over time is a strong indicator of malignancy. Thus, our purpose was to develop a system to facilitate matching lung nodules detected in serially-acquired CT scans.

MATERIALS AND METHODS

Lung registration is a non-rigid problem; most algorithms suffer from prohibitive computation and/or errors caused by unpredictable distortions at differing levels of inspiration. We propose to maximize the cross-correlation, using a modified very fast simulated annealing algorithm (MVFSRA), under a rigid transformation between data within small cube centered on a detected nodule in one scan and a second scan. The cube size is chosen large enough to include surrounding structures to be robust with respect to changes in nodule size/ shape between scans, but small enough to allow the rigid transformation assumption. We tested our method by simulating a second scan from a volumetric chest CT by re-sampling the first through known rigid (simulating transformation, rotation) and physiologically-based non-rigid (simulating varied inspiration points) transformations and comparing registration of 58 points uniformly distributed in the lungs with the known transformation. We also matched 70 nodules in pairs of scans acquired at different times from 5 patients and compared our results to a radiologist's visual determination. All patient data consisted of 1mm thick sections acquired with multi-detector helical CT.

RESULTS

For the experiment with a simulated second scan, the mean absolute error was 1.7±1.4 (s.d.) mm with a worst-case error of 4.9 mm. Poorest performance occurred when the nodule was close to the chest wall. For the experiments with the sequential patient data, the mean absolute error in nodule location compared to radiologist determination was 1.5±0.8 (s.d.) mm, with a worst error of 4.3 mm, and the mean absolute number of sections between the automatically- and radiologist-registered nodules was 0.7±0.7 (s.d.) mm, with a worst case of 3.0 mm. Poorest performance occurred when other disease processes altered the lung architecture near the nodule.

1. Segment lungs in both Cases
2. Find bounding boxes for left and right lungs in both cases
3. Compute initial registration of nodule chosen in Case 1 with Case 2 by affine transformation of respective boundingboxes
4. Apply MVFSRA optimization of 6 parameter rigid transformation (3 translation; 3 rotation) to maximize the cross-correlation of a small cube centered at nodule in segmented Case 1 with a transformed cube in segmented Case 2.
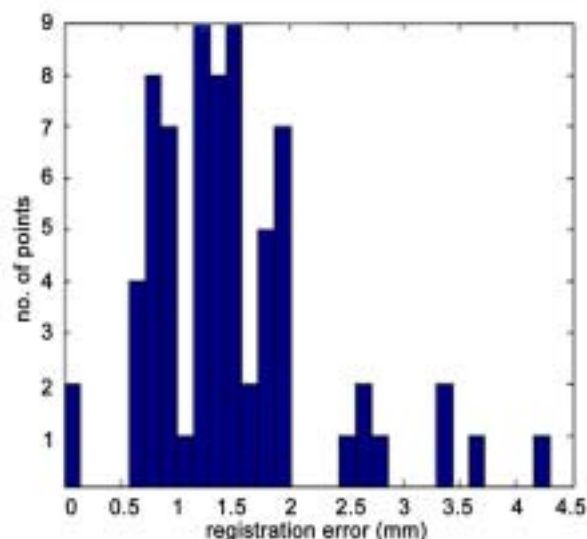
Figure 1: Registration algorithm steps

Figure 2: Histogram of registration error for the 5 patients in our database.

CONCLUSION

Our preliminary results suggest that accurate nodule matching can be achieved to aid qualitative and quantitative evaluation of nodule growth. Continued refinement and evaluation on a more extensive database are warranted.

ADVANCED X-RAY IMAGING

X-ray/MR Dual Visibility Contrast Agent Evaluation[1, 2]

Arundhuti Ganguly, Rebecca Fahrig, Mike Moseley, Dirk Mayer, Norbert J. Pelc

Department of Radiology, Lucas MRS Center

INTRODUCTION

Visibility of gadolinium (Gd) contrast enhanced MR images can be compromised by contamination from x-ray contrast agent such as iodine. This can be a significant problem while imaging with our truly hybrid x-ray/MR interventional unit. During image guided procedure using this system, often Gd injections follow that of iodine and pooling of residual iodine can affect the MR signal. Therefore for accurate image visualization and registration of say - tumor volume and adjacent blood vessels around liver cancer tumors, a contrast agent that is visible under both imaging modes would be ideal. We have studied the properties of mixtures of various concentrations of Gd and iodine to determine the nature of MR signal dropout.

MATERIALS AND METHODS

The characteristic MR relaxation time constants T1 and T2 were measured for several commonly used iodinated x-ray contrast agents (Hypaque, Omnipaque, Conray, and Renografin). The experiments were conducted in a 1.5T magnet (GE Signa, GE Medical Systems, Milwaukee, WI). The resulting T2:T1 ratios were compared with those measured for saline solutions of Gd-contrast agent (Magnevist, Berlex Lab., Wayne, MI). These MR time constants were also measured for solutions containing a range of concentrations of Hypaque-cysto (Amersham Health Inc., Princeton, NJ) mixed with Gd-contrast and saline. This was used to quantify the effect of iodine on Gd-contrast signal. Further, sodium iodide (NaI) solutions containing similar amounts of iodine as in Hypaque-cysto (141 mgI/ml) was mixed with Gd-contrast and saline and studied to isolate the effect of iodine from those of the large organic molecules in Hypaque.

RESULTS

The MR signal from Gd-contrast solution decreased with increasing iodine concentration (Fig. 1). The T2:T1 ratio for the iodine-contrast agents were found to be much smaller than the value of almost 1 for Gd-contrast as shown in Fig 2. These values for the different brands of iodine were: Hypaque = 0.21, Omnipaque = 0.19, Conray = 0.30, Renografin = 0.10. For the Hypaque/Gd solutions, the Gd-contrast relaxivity constants (R1 and R2 which are directly related to the inverse of T1 and T2) were found to be linear functions of the Hypaque concentration. The T2/T1 values were found to decrease with increasing Hypaque concentrations. This decrease in the ratio however was less drastic for increased Gd-contrast concentrations (72% decrease for 0 mM/ml Gd-solution
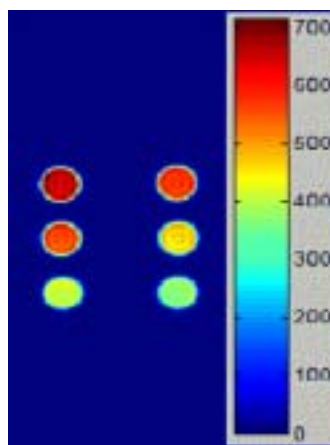

Fig.1 T2 weighted SE images of vials with 0.1% Gd and varying concentrations of Hypaque. Iodine concentration increasing top to bottom and left to right
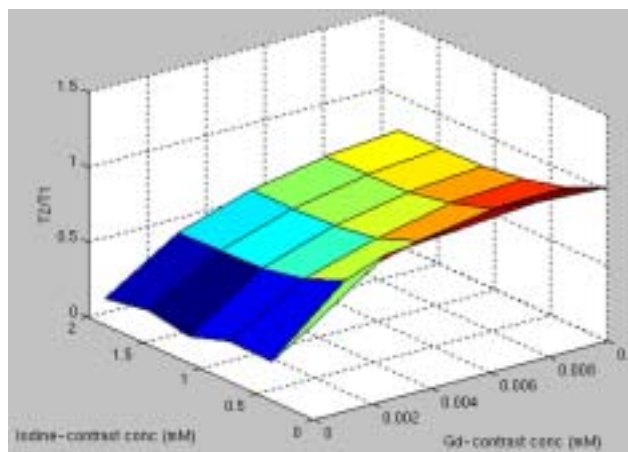

Fig.2 T2/T1 ratios for various concentrations of Hypaque for different Gd-contrast solutions in saline.

vs. 25% decrease for 1 mM/ml Gd-solution). This reduction in signal was however not observed for the NaI/Gd solutions. The Gd-contrast relaxivities for the NaI/Gd solutions were found to be independent of the NaI concentrations.

CONCLUSION

Iodinated x-ray contrast agents affect the MR signal in Gd-contrast enhanced images. This makes the presence of iodine particularly unsuitable for MR imaging in T2/T1 weighted pulse sequences such as SSFP. This effect however appears to be dependent on the size of the iodinated molecule with smaller molecules such as NaI showing no adverse effect on the Gd-contrast signal. Therefore, for an effective dual visibility contrast agent containing Gd, the iodine molecule selected should have smaller molecular size and shorter side chain if any. Other methods of isolation of iodine from Gd in the same solution are being investigated.

REFERENCES

1. A. Ganguly *et al*, "Contrast Agent Optimization for Imaging with MR/x-ray Hybrid system, abstract #2691, ISMRM 2004.
2. A. Ganguly *et al*, "Gadolinium Contrast Relaxivities in Presence of Iodinated Molecules: Contrast Agents for Hybrid Imaging, submitted to RSNA 2004.

Update on Permanent Magnet Shimming For A Detector Inside An iMRI

Zhifei Wen[1,2], Rebecca Fahrig[1], Norbert J. Pelc[1]

Departments of [1]Radiology and [2]Physics

INTRODUCTION

In our x-ray/MR hybrid system, a flat panel detector is placed under the patient cradle, where the magnetic field strength is ~0.5T. Because of the ferromagnetic components inside the detector, the MR field homogeneity is significantly degraded even after linear shimming of the scanner. Previously we proposed using a single permanent magnet to compensate for the high-order components of the additional field due to the detector[1]. Updated results are shown here with two shimming magnets optimized iteratively in a feedback process.

METHODS

Field maps were obtained using GRE images with two echo times in a cylindrical volume (f28x20cm). NdFeB magnets were calibrated in magnetic dipole strengths. Shimming of the detector was based on non-linear fitting of the measured field from the detector to the sum of a small number of dipole fields with the zeroth and first order terms removed. An iterative procedure to refine the placement of the shimming magnets was developed.

The correction approach was also evaluated qualitatively with an SSFP sequence (TR/TE= 11.64/5.56ms); this imaging method is important for interventional guidance and is very sensitive to field inhomogeneity.

RESULTS

In the absence of the detector, the peak-to-peak (p-p) deviation of the field map (DTE=2ms) was 46mG and the standard deviation (s) was 4.8mG. With the detector in place, these two parameters were 121mG and 14.7mG. Nonlinear least-squares fitting, optimizing both strengths and locations (on a plane available for placing the magnets) of the dipoles, predicted that two ideal dipoles would reduce the field inhomogeneity with the detector to 48mG (p-p) and 5.1mG (s). Two identical permanent magnets were chosen and placed at prescribed locations (F1). The field homogeneity was improved to 77mG (p-p) and 7.3mG (s), but not to the degree predicted.

In order to further improve the shim, the field map with the detector and the two magnets was fitted to the difference field between the field of two dipoles at known locations (F1) and that of two dipoles at new locations (F2). This feedback process accounted for the interaction between the detector and the magnets, and called for the magnets to be moved by 1-2cm. The field map with the shimming magnets at the new locations (F2), measured with DTE=3ms, showed a deviation of 54mG (p-p) and 5.3mG (s), compared to 41mG and 4.3mG for the baseline field (DTE=3ms). SSFP images show the severe impact of the inhomogeneity due to the detector and the improvement from the shimming magnets (Fig 1).

CONCLUSION

Properly selected permanent magnets, placed near the x-ray detector, can greatly diminish the degradation in the magnetic field homogeneity caused by the detector. This passive shimming approach of placing permanent magnets in proximity to objects that degrade field homogeneity may find other application in cases where such objects need to be placed inside the MR system.

REFERENCES

1. Wen Z, et al. Permanent magnet shimming for a detector inside an iMRI. Lucas Annual Report. 2003; p.123.
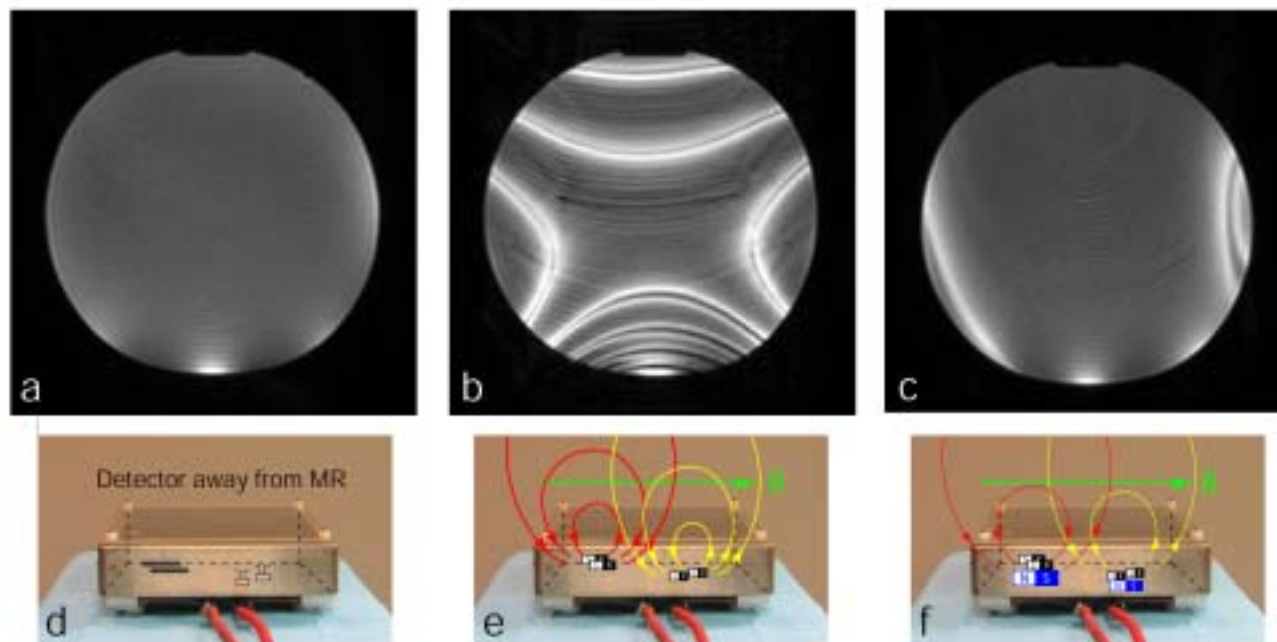

Figure 1 a,b,c) SSFP images with detector outside MR (d); detector inside MR but with no shimming magnets (e); and detector inside MR with shimming magnets (f).

A Fast and Accurate Tomosynthesis Simulation Model

Sungwon Yoon[2], Angel R. Pineda[1], Edward G. Solomon[3], Josh Starlack[3], Rebecca Fahrig[1]

Departments of [1]Radiology and [2]Electrical Engineering, Stanford University; [3]NexRay Inc, Los Gatos

INTRODUCTION

X-ray detection of lung nodules is a challenging task due to the complex over- and under-lying anatomical structures that confound the visualization. For this application, we are investigating the use of a tomosynthesis system that uses a large area scanned X-ray source and a small area digital detector array. To optimize the system for our purposes, many system parameters must be investigated via simulations. Simulations can be done using a physical model that uses ray-casting projection/back-projection algorithms. Although very accurate, the physical model requires long computational time to produce a reasonable quality reconstruction. This problem is especially severe for the SBDX geometry, which has many redundant rays. We present a faster image-based (analytical) model that produces equivalent tomosynthesis reconstructions at a fraction of the computational time.

METHODS

Tomosynthesis can be achieved by superimposing the focal plane of interest and the blurred versions of the over- and under-lying planes (of the volumetric data). In the traditional source-detector pair system, the amount of blur for each out-of-focus plane is a function of the distance from the focal plane and one single tomographic angle (which is determined by the trajectory of the source point). Applying this simple algorithm to the SBDX system geometry resulted in reconstructions that were not quite accurate compared to those obtained using the physical model. Analysis of the system geometry and its resulting projection/back-projection process show two major discrepancies from the traditional source-detector pair system - variable tomographic angle for each voxel and the effects of magnification. Variable tomographic angle is determined by the location of the voxel between the source and detector. Magnification is determined by the distance of the voxel to the focal plane. Using a 698x698x650 high-resolution (0:15mm isotropic resolution), low-noise CT volume data, 3 different variations of the analytical model were investigated; fixed tomographic angle for all planes with no magnification adjustments (FA), variable tomographic angle with no magnification adjustments (VA), and variable tomographic angle with magnification adjustments (VAM).

RESULTS

Figure of merit used for model comparison is the square root of the MSE divided by mean of the physical model reconstructed data. Figure 1 shows the comparison of the 3 different variations of the analytical model for the central 75% of the reconstructed data. Since the volume data was set up to be in a very slowing varying region and the volume thickness is
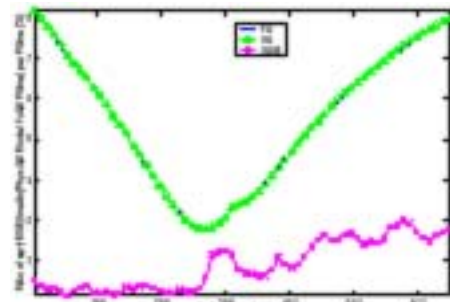

Figure 1: Model Performance Comparison. The analytical model with variable tomographic angle and magnification adjustments is within 3% of the very time-consuming physical model. (Definitions for FA, VA, and VAM models are in the Methods section)

(a) Sum of the Focal Plane and its Neighbors

(b) Conventional Projection Image

(c) Physical Model Tomosynthesis

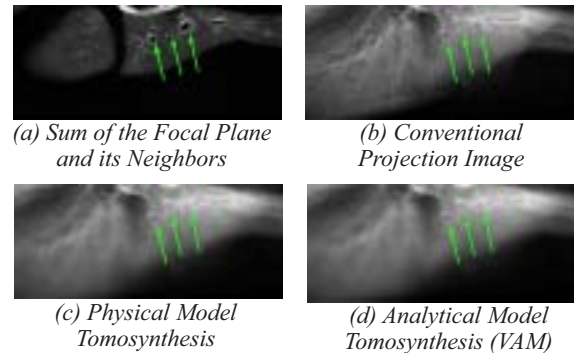*(d) Analytical Model Tomosynthesis (VAM)*

Figure 2: Different Reconstructions. The tomosynthesis reconstructions via the physical model (c) and the analytical model (d) are visually indistinguishable. The tomosynthesis results clearly exhibit the advantage over the conventional projection (b) in visualizing focal plane structures, as indicated by the green arrows.

about 10cm (resulting in smaller range of tomographic angle values), the simplified variable tomographic angle model does not show a significant improvement over the fixed tomographic angle model. On the other hand, the analytical model with magnification adjustment and variable tomographic angle results are shown to be within 3% of the physical model results. This result is verified by the quality of reconstruction images produced using the analytical model - example shown in Figure 2(d). In addition to the achieved accuracy, the analytical model simulations run more than 10 times faster than the physical model simulations on a modern desktop computer without any speedup optimization schemes.

DISCUSSION

The fast, accurate computation of the tomosynthesis images provides the groundwork for optimization of the SBDX system for our particular task of lung nodule detection. The analytical model separates the data and the system geometry, and the resulting tomosynthesis image is a superposition of the filtered out-of-focus planes. All the involved filtering is determined only by the geometry of the system, and the effects of the filtering on each out-of-focus plane can easily be investigated, whereas, for the physical model, such efficient, simple, and plane-by-plane analysis of the tomosynthetic effects is almost impossible. Furthermore, our approach can easily be generalized for any tomosynthesis system, including more classic linear or circular motion systems.

Modeling Human Observer Performance at Detecting Lung Nodules in Tomosynthetic Images

Angel R. Pineda[1], Sung-Won Yoon[1,2], David S. Paik[1] and Rebecca Fahrig[1]

Departments of Radiology[1] and Electrical Engineering[2]

INTRODUCTION

Detection in tomosynthetic and projection images is limited by the confounding anatomical structure. By using tomosynthesis, we hope to significantly improve the visibility of lung nodules.

Our goal is to use mathematical observers to model human observer performance at the task of detecting lung nodules in projection and tomosynthetic images. The mathematical observers will in turn be used to optimize a tomosynthesis system specifically for lung nodule detection.

MATERIALS AND METHODS

We consider a tomosynthetic angle of 3 degrees which is consistent with the current implementation of the scanned beam digital x-ray (SBDX) system. We used high resolution (0.15 mm isotropic) CT data of a dog-lung phantom to model noiseless projection and tomosynthetic images. Nodules were generated out of primitive volumes to mimic real nodules (Fig. 1). The nodule used has the volume equivalent to a sphere of radius 3.6 mm and has an attenuation of 40 HU. It was placed at locations in the lung parenchyma such that 46 non-overlapping subimages (64x64) of the projections could be generated.

The 46 images were generated with and without a nodule and used for a two alternative forced choice (2-AFC) experiment using the projection and tomosynthetic images (Figs. 2,3). The observers were presented two images with different backgrounds, one of which contained the lesion and the image of the lesion alone.

As a first attempt at modeling human performance, we used the non-prewhitening matched filter (NPW) as a mathematical observer. This observer correlates with human performance for detection tasks in uncorrelated noise.

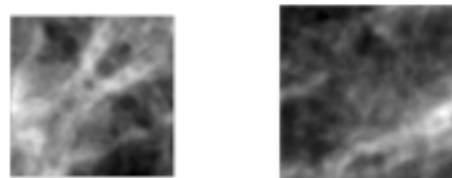*Figure 1. Lesion in tomosynthetic image (left) and projection (right).*

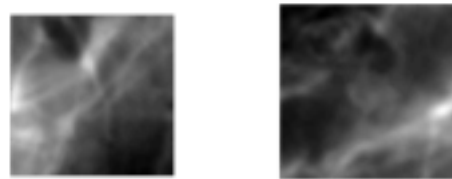*Figure 2. Projection images with (left) and without (right) the nodule.*

Figure 3. Tomosynthetic images with (left) and without (right) the nodule.

RESULTS

The average percent correct (PC) of four observers on the projection images was 74% and 95% in the tomosynthetic images showing a significant improvement in detectability by using tomosynthesis. The NPW observer had a PC of 58% for both the projection and tomosynthetic images.

CONCLUSION

This preliminary observer study quantifies the increase in detectability of lung nodules in anatomical backgrounds for tomosynthetic angles of 3 degrees. This result confirms previous subjective findings using spheres as nodules, The NPW observer underperforms the human observer and does not track the improvement seen in human performance in the tomosynthetic reconstructions. This is consistent with previous results for detection with structured backgrounds and a varying mean value in the image. We will improve the mathematical observer to account for channels in the visual system to better account for the background variation.

Noise Simulations for an Inverse Geometry Volumetric CT System

Taly Gilat Schmidt[1,2], Rebecca Fahrig[1], Norbert J. Pelc[1]

[1]Department of Radiology, [2]Department of Electrical Engineering

INTRODUCTION

The purpose of this work is to investigate the noise performance of an inverse geometry volumetric CT (IGCT) scanner through simulations. The first investigation compares the photon efficiency of the IGCT system to a 2D parallel ray system. The second investigation models the photon output of the IGCT source and calculates the expected noise.

MATERIALS AND METHODS

We have proposed an IGCT system to rapidly acquire volumetric data with negligible cone beam artifacts. The system uses a large array scanned source and a smaller array of fast photon counting detectors. During an acquisition, the electron beam, and thus the x-ray source, is rapidly steered across the area of the target as the gantry rotates about the patient.

The reconstruction algorithm rebins the acquired data into 2D parallel ray projections at multiple tilt angles and then reconstructs the volume using a 3D filtered backprojection algorithm. The IGCT system uses ray measurements that cross transverse planes and that may introduce a noise penalty. To study this potential effect, we used the metric of photon efficiency and modeled the same total number of photons in an IGCT acquisition and a multi-slice 2D parallel ray acquisition. The photon density was selected to give a noise level of 10 HU according to theoretical predictions. The 2D parallel ray geometry consisted of rays perpendicular to the axis of rotation, with sampling and resolution comparable to the IGCT geometry. For both cases, noise projections were simulated and the central axial slice reconstructed. In the second study, to investigate the noise in an IGCT system, the expected x-ray photon flux was modeled based on currently available components, although the photons were monoenergetic to avoid beam hardening. Projections were simulated through different ellipsoid phantoms. All simulations were compared to theoretical noise calculations.

RESULTS

In the photon efficiency study, the noise in the parallel ray and IGCT systems was 10.4 HU and 9.5 HU, respectively, as compared to the expected 10 HU noise. For a 6.5 cm diameter 4 cm thick ellipsoid water phantom, the calculated standard deviation was approximately 10 HU at the center of the ellipsoid. For the same size phantom with maximum attenuation equivalent to 30 cm of water, the calculated noise was approximately 140 HU. The theoretical noise predictions for these objects were 13 HU and 131 HU, respectively. These results are for a 0.16 second scan time and an isotropic resolution of 10 lp/cm.

CONCLUSION

The results of the photon efficiency simulations verify that the IGCT geometry is as efficient in photon utilization as a 2D parallel ray geometry. The simulations predict acceptable noise levels for the fast scan time and high resolution. Experiments with a table-top system are planned to verify these theoretical results.

First Images from a Table-top Inverse Geometry Volumetric CT System with a Large-area Scanned Source

Taly Gilat Schmidt[1,2], N. Robert Bennett[1], Samuel R. Mazin[1,2], Josh Star-Lack[3], Edward G. Solomon[3], Norbert J. Pelc[1]

[1]Department of Radiology, [2]Department of Electrical Engineering, [3]NexRay Inc

INTRODUCTION

A table-top inverse geometry volumetric CT (IGCT) system has been built and an initial dataset reconstructed in order to demonstrate feasibility of the new scanner geometry. The IGCT system acquires volumetric data in one circular scan with negligible cone-beam artifacts

MATERIALS AND METHODS

The prototype system consists of a C-arm gantry with a 25x25 cm scanned source opposite 2304 photon counting detectors in a 5x5 cm array (Nexray, Inc). During an acquisition an electron beam is rapidly steered across the transmission target, dwelling at an array of collimator holes. For each source position the entire detector array is read out. Ideally the source and detector would have the same axial extent, thus providing sufficient volumetric data. For the prototype system, this requirement is met by restricting the axial (z) FOV to 5 cm.

The C-arm gantry was positioned horizontally and a rotating stage placed between the source and detector. A phantom consisting of three, 2.3 mm diameter stainless steel beads mounted on a cardboard cylinder was scanned with the sys-
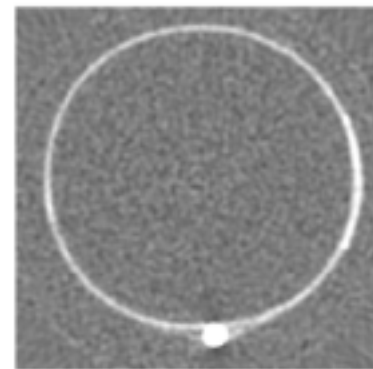

Figure 1: Axial slice of cardboard cylinder with stainless steel bead windowed from -1500 HU to -500 HU.
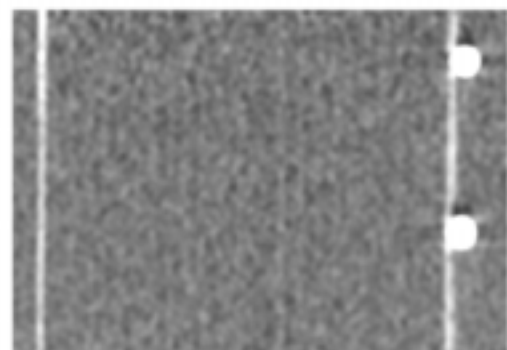
Figure 2: Sagital slice of cardboard cylinder with stainless steel beads windowed from -1500 HU to -500 HU.

tem operating in step and shoot mode. We acquired 125 "views" of the phantom equally spaced over 360 degrees, along with 110 flat-field views. Each view includes projections from all source spots. Additionally, eight lower noise views of the phantom were acquired and used to determine the geometric misalignment. The raw phantom dataset was normalized by the averaged flat-field views.

The data were reconstructed with a previously described algorithm. The algorithm first corrects for misalignment and rebins the data into 2D parallel ray projections at multiple tilt angles, followed by a 3D filtered backprojection.

RESULTS

The resulting axial and sagital images, Fig. 1 and Fig. 2, show the beads and cylinder reconstructed accurately without significant artifacts. The noise in the resulting 0.4 mm slices, with 0.4 mm in-plane resolution, was 48 HU compared to a theoretically predicted 47 HU.

CONCLUSION

The successful acquisition and reconstruction of the initial IGCT dataset indicates system feasibility. Future work is planned to further characterize the system, including MTF, noise performance and acquisition of anatomical data.

Inverse Geometry Cone-Beam CT with Multiple Detector Arrays

Samuel Mazin, Taly Gilat Schmidt, Norbert Pelc

Department of Radiology

INTRODUCTION

Volumetric CT imaging has been made possible in the last decade due to multiple-slice spiral CT scanners. However, spiral CT is still limited for high-resolution 3D cardiovascular imaging due to the need for many gantry rotations. Systems have been developed that employ a single rotation (cone-beam CT), but for large volumes they result in artifacts due to a fundamental sampling limit[1]. Gilat has proposed an inverse geometry system (IGCT) with a large scanned source array opposite a small detector array[2]. The system needs only a single rotation to acquire images that are free from cone-beam artifacts. However the IGCT system geometry may not be practical for clinical use due to a limited field-of-view (FOV). We are proposing to add more detector arrays to the IGCT system to achieve a cost-effective way to increase the FOV. This could lead to a CT scanner for cardiovascular imaging and other high performance applications.

MATERIALS AND METHODS

The system we are proposing has a large scanned source array opposite three small detector arrays spaced apart laterally to provide a large FOV.

Because there are large "gaps" between the detector arrays, there may not be adequate or uniform sampling of the entire FOV. We have developed a method to position the detector arrays so as to maximize the FOV while maintaining a uniform sampling criterion.

RESULTS

Each ray emanating from a source spot and hitting one of the detector elements of a detector array may be represented in Radon space as a pair (,) where is its distance to the axis of rotation and is its orientation. Each detector array contributes a set of points in Radon space that form a polygon-like shape. To achieve a uniform sampling of -values in this
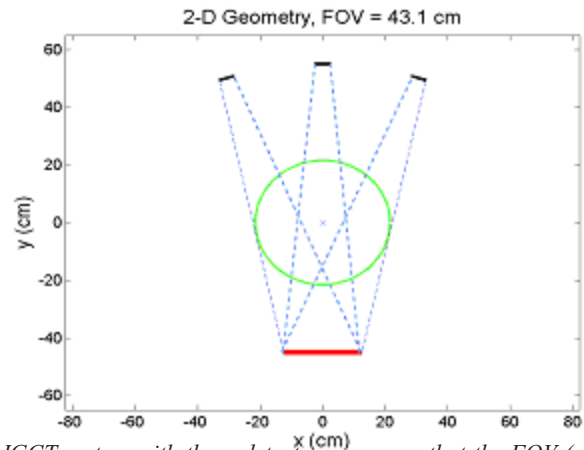
IGCT system with three detector arrays so that the FOV (circle) may be increased significantly without increasing the source size.
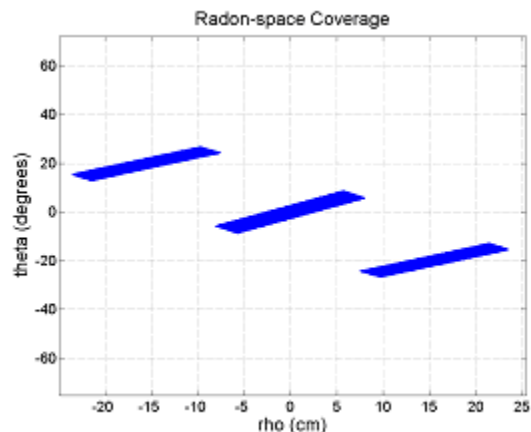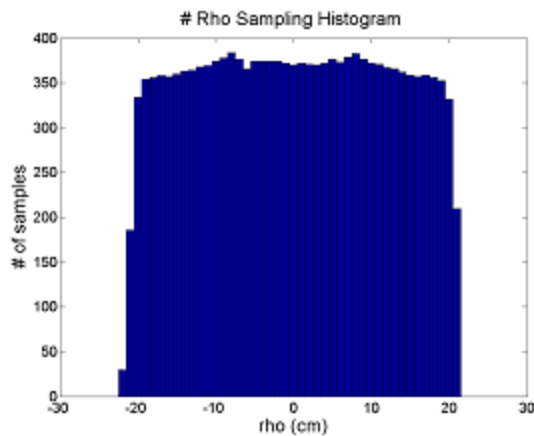

Radon space coverage for one view. Each polygon contains points from a single detector array.

space a constraint was derived that forced the polygons to overlap slightly so that the corresponding ⇐sampling histogram would be relatively uniform.

CONCLUSION

A 3X increase in the FOV was achieved without increasing the source size while maintaining uniform sampling in Radon space.

⇐sampling histogram corresponding to Radon space plot.

REFERENCES

1. B. D. Smith, "Cone-beam tomography: recent advances and a tutorial review,Ó Optical Engineering 29, pp. 524-534, 1990.
2. T. Gilat, R. Fahrig, N. Pelc, "Three-dimensional reconstruction algorithm for a reverse geometry volumetric CT system with a large array scanned source," in Medical Imaging 2003: Physics of Medical Imaging, Proc. SPIE 5030, pp. 103-111, 2003.

To Bin or Not to Bin? A Question Regarding the Noise Properties of CT Reconstructions with or without Binned Projections

Angel R. Pineda and Norbert J. Pelc

Department of Radiology

INTRODUCTION

High resolution flat panel detectors in computed tomography produce large amounts of data. In order to reduce the time required to extract the data from the panel and to reconstruct, the detector pixels are sometimes binned. We fix the desired resolution and study the noise variance resulting from using either the binned or unbinned projections to achieve it.

MATERIALS AND METHODS

For the theoretical result, we computed the CT image variance (assuming parallel-beam reconstruction for convenience) where the detector pixels are either not binned or binned in pairs in the limit of a large number of pixels and views. We consider an object which produces, after a bowtie filter, a fluence of x-rays that is uniform on the detector. In this case, both binned and unbinned data are uncorrelated and have equal variance.

We vary the reconstruction kernel of both data sets such that they have the same resolution. Our resolution goal is to undo the pixel blur of the binned system to accurately reconstruct the frequencies up to a given threshold. We assume quarter offset (or focal spot wobble) was used to double the sampling rate of the binned system. This system is said to be detector limited since the maximum frequency that can be estimated is the determined by the pixel.

We did a numerical simulation to verify the theoretical result. We generated projections from a 2-D disk and added noise using the Gaussian approximation to the Poisson distribution on the x-ray fluence measurements. We reconstruct after the log operation and reconstruct using the binned and unbinned projections such that the reconstructions have the same resolution. The variance was computed from the pixels in the center of a single image.
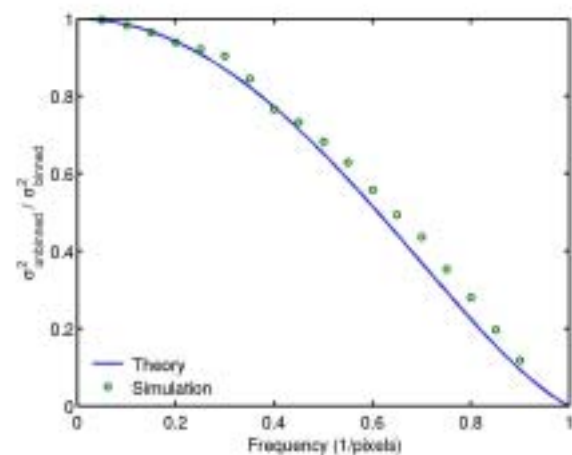
Fig.1 Relative increase in variance of CT reconstruction due to binning of projections.

RESULTS

Both systems have the same deterministic response but the variance with the unbinned system is always less. If we undo the pixel blur up to the Nyquist frequency of the binned system with no quarter offset (0.5/pixel), the ratio of the variances is 0.65 (Fig. 1). If we introduce quarter offset and require an accurate resolution up 0.9 of Nyquist of the unbinned system, the ratio is 0.1.

The noise amplification of the filtering process is magnified by binning the projections. The main difference comes from the correlation in the noise during the blurring process. When the pixels are binned, the noise remains uncorrelated. When the blurring occurs in the kernel, the noise is correlated. This difference in the correlation of the noise is what causes the differences in the variance of the reconstructions.

CONCLUSION

For a fixed resolution, binning the projections before reconstructing results in an increase in variance. As the resolution reaches that of a detector-limited system, the increase in the variance of the reconstructions is dramatic (in a non-Shakespearean way).

Electronic and Quantum Noise in a CT system

Jeff Dormo[2], Norbert J. Pelc[1]

[1]*Department of Radiology,* [2]*Department of Electrical Engineering*

INTRODUCTION

Current CT scanners use energy-integrating detectors, whose precision can be affected by electronic noise [1]. The purpose of this work is to identify the location where a CT image transitions from being electronic noise dominated to quantum noise dominated. The importance of the evaluation stems from the desire to reduce the radiation dose in CT, which can drive the detectors into electronic noise and the systems into poor performance. Two different approaches are used to address this problem. The first approach uses the variance in the images. This approach is simple, but the variance is also strongly determined by the reconstruction algorithm [2]. The second approach uses the Noise Power Spectrum [3], which should allow us to examine the noise performance independent of the reconstruction algorithm.

MATERIALS AND METHODS

Using the theoretically expected dependence of the noise in CT scanners [2], simulations were performed in Matlab modeling the noise and showing the transition from the electronic noise dominated region to a quantum noise dominated region, and its dependence on the characteristics of the detector and electronics. This provided motivation to experimentally determine where the change from electronic noise to quantum noise occurs. Two different polyethylene phantoms were used in this experiment. One was 48 cm in diameter and the other was 35 cm in diameter. The phantoms were scanned at four different slice thicknesses: 1, 3, 5 and 10 mm. At each slice thickness the mA setting was increased from 10 mA to 400 mA, and five images were acquired for each combination of slice thickness and mA setting. This provided images that ranged from extremely noisy to very low noise. Two approaches are used to analyze the images. The first approach focused on analyzing the signal-to-noise ratio (SNR) and the variance of the images. The signal strength and the variance within a specific region of interest in each image were found using Matlab. The size of the ROI was changed in order to view its effect on the behavior of the noise at different slice thicknesses and mA settings. Large regions are expected to provide more data but the measured variance could be affected by image shading. The second

approach to analyze the data was to use the Noise Power Spectrum (NPS) of each image. Noise images were formed by subtracting two images of the same phantom to remove signal from the object as well as any shading artifacts. The NPS was then calculated from the difference image using a Fourier Transform.

RESULTS

The simulations showed that the slope of a plot of variance vs. mA should be 2 when the image is dominated by electronic noise and 1 when dominated by quantum noise. In the images obtained on the 35 cm phantom for 5 mm and 10 mm slice thicknesses, the slope of the variances curve were 1.04 and 1.01, respectively. This indicates that in these scans the system is quantum noise limited, which is ideal. On the 48 cm phantom, the lowest mA settings were unreliable because the CT image values seem to become nonlinear. The CT number for polyethylene should be close to 930, but the CT numbers obtained at the lowest mA settings averaged 550.

The data spanning both phantoms and all slice thicknesses and mA settings suggest a transition to electronic noise at the low intensity settings. Ideally, the analysis should combine the data across all the images, but this requires us to take into account any reconstruction algorithm changes. Work on using the NPS to do this has just begun.

CONCLUSION

The results from the 35 cm phantom verify that at high SNR, the CT system is quantum noise dominated and the variance varies linearly with mA. Determination of the noise (or dose) level at which the system becomes electronic noise limited requires combining data across several phantoms and slice thicknesses. Analysis using the Noise Power Spectrum needs to be refined in order to do this. The NPS analysis should provide a more robust method of analyzing the data in high noise, low contrast images.

REFERENCES

1. Pelc NJ. Statistical aspects of digital x-ray imaging. In: G.D. Fullerton ea, editor. Electronic Imaging in Medicine. New York: Am. Inst. Phys.; 1984.
2. Chesler DA, Riederer SJ, Pelc NJ. Noise due to photon counting statistics in computed X-ray tomography. J Comput Assist Tomogr 1977;1(1):64-74.
3. Riederer SJ, Pelc NJ, Chesler DA. The noise power spectrum in computed X-ray tomography. Phys Med Biol 1978;23(3):446-454.

Monte Carlo Simulation in the Study of Cone-beam Scatter Correction Using Moving Blocker Array

Lei Zhu[1,2], Rebecca Fahrig[2]

Departments [1]Electrical Engineering and [2]Radiology

INTRODUCTION

Developing an effective scatter correction method is one of the major challenges in Cone beam computed tomography (CBCT) research field. Among the methods presented in the literature, direct measurement provides an accurate estimate of the scatter field using an array of lead blockers placed between the x-ray source and the object. Assuming small perturbation due to the presence of the blockers, the projection data in the shadows of the blockers on the detector are samples of the scatter profile and full field estimation can be obtained by low-pass filtering. In current literature, scanning with the blocker array is usually used to obtain the scatter estimation only, as a pre-calibration prior to the conventional scan without the blocker array. It inevitably prolongs the scanning time, causes more reconstruction errors due to object motion, and increases the patient dose. The goal of our study is to develop a scatter correction method using an array of moving blockers, such that the scatter estimation and the reconstruction can be done effectively in one step. Monte Carlo (MC) code (Geant4) has been verified and used as the major simulation tool to test the performance of the scatter correction algorithm.

METHODS

The geometric configuration of the CBCT system with the blocker array is shown in Fig.1. The blocker array moves at least one blocker diameter from projection to projection, so that each detector pixel will not be consecutively blocked during the rotational data acquisition. In every projection, the scatter correction consists of three steps: 1) estimate the full scatter field by low-pass filtering the sample data in the blocker shadows; 2) subtract scatter estimate from the total projection to obtain a primary estimate in the regions outside the shadows; 3) estimate the primary data in the shadows by interpolating the primary estimate obtained in step 2).

The system performance is tested using MC simulation (Geant4) on a software humanoid phantom. The RL fitting algorithm is used to speed up the simulation[1].

RESULTS

The reconstructed images of simulated chest scanning are shown in Fig 2. The results reveal that the blocker array modality effectively corrects the scatter corruption. The area of the reconstructed image which is within 5% of the ideal reconstruction increases from only ~6% to ~80% by applying the scatter correction algorithm, and the induced visual artifacts are mostly removed when using random blocker array trajectory.
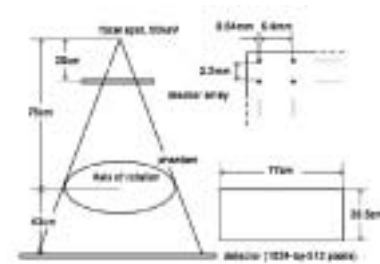

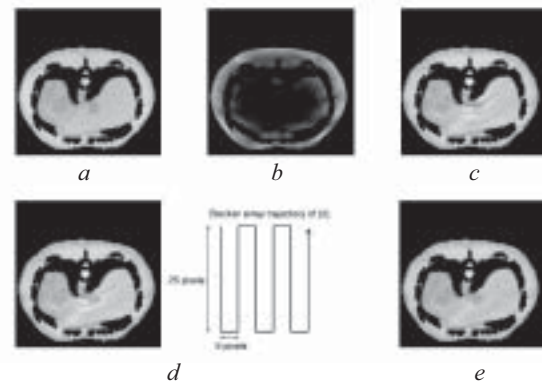*Fig 1. Geometric configuration of the CBCT system with the moving blocker array.*

Fig 2. Axial view of the reconstructed humanoid chest phantom with the scatter correction algorithm. a) use primary projections only; b) use scatter plus primary projections, without scatter correction; c) scatter corrected by stationary blocker array; d) scatter corrected by moving blocker array, the array moves one blocker diameter per projection, following the trajectory as shown; e) scatter corrected by randomly moving blocker array. In every projection, the array movement vector is uniformly distributed in [0,50] in x direction, [0,25] in y direction.

Another investigation is made by using the 'real' primary profile for the missing data in the blocker shadows in step 3). Interestingly, the images are not much different from those in Fig 2. This implies that the visual artifacts in the reconstructed images come from inaccurate scatter estimation.

FUTURE WORK

Future work will involve adjustment of the blocker array configuration, more testing of different blocker array trajectories, refinement of the estimation algorithm and experiment verification.

CONCLUSIONS

A new effective scatter correction method for CBCT with moving blocker array is proposed and tested using MC simulation on a software humanoid phantom. The results show that this method generates accurate reconstructions with scatter present in the projection data. It combines the scatter estimation and primary data acquisition into one step and makes the scatter field pre-computation unnecessary.

REFERENCES

1. A. P. Colijn, F.J. Beekman, "Accelerated simulation of cone beam x-ray scatter projections," IEEE Tran. on Med. Imaging, vol. 23, No.5, 584-590 (2004).

Extrapolating Truncated Projections using 0th and 1st Moment Constraints

Jared Starman[1], Norbert Pelc[1,2], Norbert Strobel[2], Rebecca Fahrig[2]

Departments of [1]Electrical Engineering and [2]Radiology

INTRODUCTION

C-Arm CT systems suffer from artifacts due to truncated projections caused by a finite detector size. The goal of this project is to determine a simple and computationally efficient method of extrapolating truncated projections to minimize reconstruction errors.

MATERIALS AND METHODS

Our proposed algorithm extrapolates truncated projections in two steps. First, truncated projections are extrapolated a small distance using an autoregressive linear predictor, similar to [1]. The linear predictor provides for a smooth transition into the extrapolated region. The second step of our algorithm is a further extrapolation that exploits the relationships between the object mass and object center of mass (COM) to the mass and COM of its projections. We assume a priori knowledge of the object mass and COM, which can be estimated from previous data or by other means. The truncated projections are linearly extrapolated from the end-point of extrapolation in step 1 down to zero. We add mass to both ends of the projections in keeping with the following constraints, also known as the two lowest order Ludwig-Helgason consistency conditions. 1.) The total mass of the final extrapolated projection must equal the image mass and 2.) The final COM of the extrapolated projection must be located where the image COM projects.

RESULTS

We tested our algorithm with simulated 2D head and thorax phantoms of our own design using parallel and fanbeam geometries. We compared the reconstructed images from: 1) full-width projections, 2) 40 % truncated projections 3) our moment-extrapolated projections, and 4) an extrapolation technique previously suggested by Ohnesorge et al [2] by taking a look at results inside the appropriate scan field of view associated with truncated projections. Results for our head phantom using parallel projections show a 95% reduction in reconstruction error using [2] and a 99% reduction in error using our technique, over simply reconstructing from truncated projections. For fanbeam geometry the reduction in errors is the same. Reconstructed images from projection
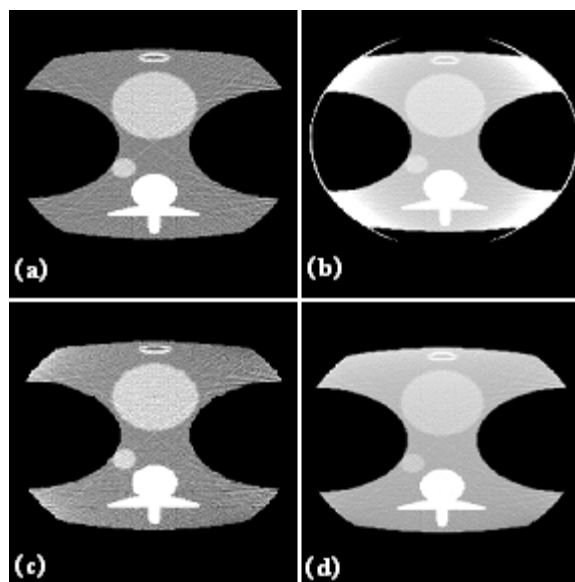

Figure 1: 2D reconstructions of our simulated thorax phantom inside the scan field of view. The four reconstructions shown are from (a) ROI from full-width projections, (b) 40% truncated projections with no extrapolation, (c) 40% truncation and extrapolated with our extrapolation algorithm, and (d) 40% truncation and extrapolated with symmetric mirroring.

sets 2) and 4) produced an offset error at the image center of 22% and 3% respectively, while our algorithm's bias was less than 1%. The reconstruction error reduction for the thorax phantom for parallel geometry was 96% using 3) and 70% using 4). For fanbeam the error reductions were 95% and 84% for 3) and 4), respectively. Our technique produced the smaller bias which was under 1%. Figure 1 shows the reconstructions over the scan field of view for the thorax phantom.

CONCLUSION

The proposed algorithm shows promise in reducing image artifacts due to truncated projections. The algorithm does not appear to introduce any significant bias at the reconstructed object center, which allows for accurate Hounsfield unit estimation.

REFERENCES

1. Galigekere RR, Holdsworth DW. 3D Reconstruction From Truncated Rotational Angiograms Using Linear Prediction. *MICCAI* 2003; 127-133
2. Ohnesorge B, Flohr T, Schwarz K, Heiken JP, Bae KT. Efficient correction for CT image artifacts caused by objects extending outside the scan field of view. *Med Phys* 2000;1:39-46

OUTCOMES ANALYSIS

Virtual Tumor Registry of the US Breast Cancer Population

Sylvia K. Plevritis[1], Bronislava M. Sigal[1], Peter Salzman[1], Peter Glynn[2], Jarrett Rosenberg[1]

[1]Department of Radiology, [2]Department of Management, Science and Engineering

INTRODUCTION

Breast cancer mortality rate is decreasing in the United States. The contributions of screening and treatment interventions to this decrease are difficult to quantify because the US does not have a comprehensive population-level database that captures patient demographics, screening, treatment and survival statistics for cancer statistics. The SEER database is the closest example of such a database, but it does not contain any information on screening history or even mode cancer detection (i.e. detection on screening examination versus physical examination versus symptomatic onset). To address the need for a single, all-inclusive national breast tumor registry, we have developed a simulation model that weaves together data from numerous national registries, such as SEER, PCOR and BCSC. SEERmainly contains information on patient and tumor characteristics at the time of diagnosis and vital status. PCOR contains information on the use of adjuvant therapy. BCSC contains information on compliance with screening mammography recommendations. We have combined these databases by building and validating mathematical and statistical models that synthesize known biological, epidemiological, clinical characteristics about breast cancer. Our virtual database information on the screening history, model of detection, tumor characteristic, treatment and survivorship for individual patients.

METHODS AND MATERIALS

Our virtual database is the output of a Monte Carlo simulation model that reproduces the life history of women in the United States who were born since 1890 and outputs population level statistics from 1975 onward. The simulation tracks the life history of individual women and records the following information for each breast cancer patient with invasive disease: her date of birth, her screening schedule (based on BCSC data), when and how she was detected, her tumor size and stage at detection stage, ER status at detection (based on SEER), what treatment she received (based on PCOR), and her survival time from diagnosis and her cause of death (based on SEER). While we used part of SEER to inform several components of our model, we did not use all of SEER. Components of the SEER database was left aside for model validation purposes. In particular, features such as the patient's age at detection, tumor size and stage at detection and mode at detection were outputs of the model and compared to SEER. In order to generate these outputs, we developed a natural history model of breast cancer that was presented and validated in earlier reports.
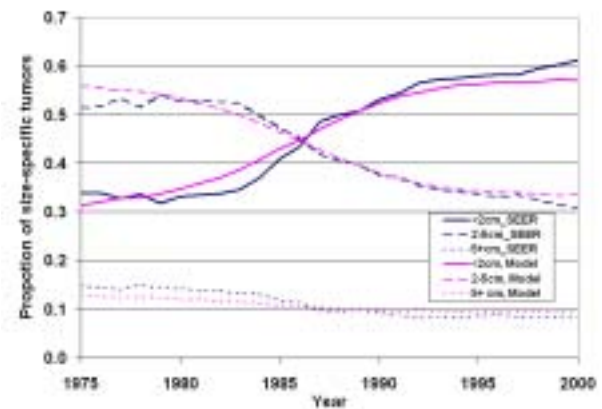

Figure 1: A comparison of SEER data and model prediction on the proportion of tumors in a specified size groups (<2cm, 2-5cm, 5+cm) over calendar year.
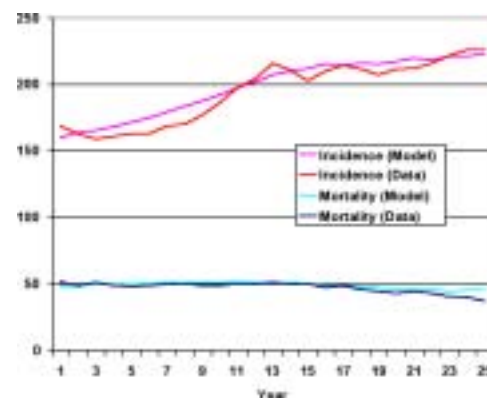
Figure 2: A comparison of data and model prediction for age-adjusted incidence and mortality of breast cancer.

RESULTS

Our virtual breast tumor registry closely reproduces population level trends observed in the SEER database that were not used in the model building process. Figure 1 show how well our model reproduces the tumor size distribution as a function of calendar year for all ages combined. Similar agreement was found by age group. We also found agreement between the model and the data on the proportion of tumor stage (local, regional, distant) by calendar year and age-group. Figure 2 shows good agreement between the model and data in terms of overall age-adjusted incidence and mortality.

CONCLUSION

We have generated a virtual tumor registry of the US breast cancer population that merges existing databases with assumptions about the natural history of breast cancer as the "glue.". Future work will show how this database can be used to decompose the separate and combined effects of screening and adjuvant treatment on breast cancer trends and determine what would have happened in the absence of screening and/or adjuvant treatment.

Predicting Future Trends in US Breast Cancer Mortality

Sylvia K. Plevritis[1], Bronislava M. Sigal[1], Allison Kurian[2], Peter Salzman[1], Peter Glynn[3], Jarrett Rosenberg[1]

[1]*Department of Radiology,* [2]*Division of Oncology,* [3]*Department of Management, Science and Engineering*

INTRODUCTION

The NIH and CDC have issued a report joint entitled "Healthy People 2010" that, among other national health goals, describes the goal of reducing breast cancer mortality to an age-adjusted level of 20.3 deaths/100,000 by the year 2010. This level would represent a 20% decline from breast cancer mortality levels in 1998. Even though breast cancer mortality has been on the decline since 1990, it is not known if the rate of decline will continue given the trend in incidence and current and future dissemination patterns of screening and treatment dissemination. We were asked by the DHHS to contribute to the HP2010 mid-course (calendar year 2005) evaluation of the breast cancer goals and help assess whether the nation would fall short/meet/exceed its 2010 breast cancer mortality goals given the efforts in prevention, early detection and treatment.

METHOD

Our CISNET population simulation model (described above) was modified. We have assumed 1999 levels for dissemination of mammography from 1999 to 2020 in one scenario. We also assumed a scenario where women ages 40 and 70 were undergoing annual mammography with 100% compliance. We dissemination of adjuvant therapy through 1999
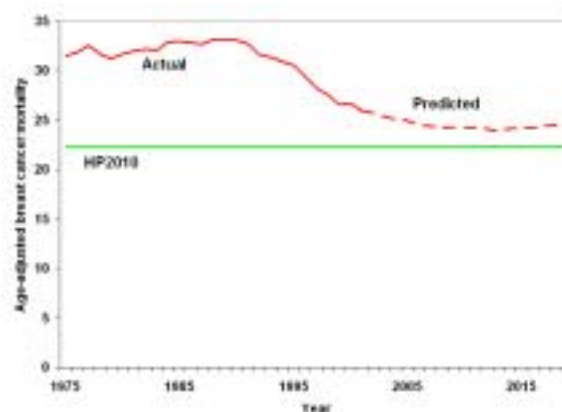

Figure 1. Age-adjusted breast cancer mortality from 1975 to 2020. Mortality rates from 1975 to 2001 are based on data and rates from 2001 to 2020 are predicted from a model.

for standard chemotherapy but incorporated a benefit due to a dose-dense schedule. We assumed the adoption of tazanes and aromatase inhibitors. From 2002 onward, taxanes where given to 15%, 80% and 100% of patients on chemotherapy if diagnosed in Stage I, Stage II-Stage III or Stage IV, respectively.

RESULTS

Our model predicts that the HP2010 goals will not be met. Breast cancer mortality is expected to level off starting 2005. Assuming women ages 40-79 years old are 100% compliant to annual screening starting 2005, the HP2010 goal may be reached by 2015.

CONCLUSION

Our model predicts that US breast cancer mortality rates will continue to decrease till 2005 and then level off. It is likely to fall short of the HP2010 goals. We are currently working to identify what efforts will be needed to meet the HP2010 goals.

Predicting the Magnitude in Lung Cancer Mortality Reduction Due to CT Screening

Sylvia K. Plevritis, Bronislava M. Sigal

Department of Radiology

INTRODUCTION

Helical CT screening examinations are detecting asymptomatic, early-stage lung cancer not seen on conventional chest radiographs. These findings have been fueling direct-to-consumer marketing of CT lung cancer screening; targeting individuals who are able to pay out-of-pocket costs for the hope of significantly reducing their risk of death from lung cancer. Lung cancer screening with CT has not been shown to reduce lung cancer mortality, but has been shown to generate unnecessary, life-threatening biopsies, and large downstream health care costs that are paid out by insurers. Even without evidence of the effectiveness of CT screening, policy makers are asking: Is lung cancer screening cost-effective?

This question is challenging for two primary reasons. First, the RCT trial designed to detect a lung cancer mortality reduction from CT screening started recruiting participants in September 2002 and is expected to produce data on mortality-specific endpoints in 2009. Secondly, CT screening is a moving-target, and interpretation criterion and practice patterns are in flux. Because of these challenges, a need exists to establish a framework for evaluating CT lung cancer screening that can absorb new information. We are developing this framework and report here preliminary results on the expected lung cancer mortality reduction due to CT screening.

METHODS

We estimate lung cancer mortality reduction due to CT screening in a cohort of 60 year old US smokers (55% men, 45% women). The cohort is offered annual CT screening examinations for 20 years. The annual non-compliance probability is 6.5%. All persons are followed till the age of 100.

We fit a natural history model of lung cancer to the SEER data. Data was obtained from SEER (9 registries), selecting only lung cancer cases detected after 1988 due to changes in tumor size coding. Figure 1 shows and 2 demonstrates how well the model matches the data on stage distribution and size distribution for females only. The results for males are similar. Overall, the data fit is reasonable. However, the model estimates a slightly greater proportion of smaller tumors. Also, it reproduces the stage distribution data more accurately for larger tumors than smaller tumors. This would suggest that the disease process for tumors that are clinically detected at smaller sizes is not fully captured by our modeling assumptions. Smaller tumors appear to advance to later stages faster than predicted by the model. Nevertheless, we proceeded to use this model for subsequent preliminary results. Our model requires two additional inputs, namely: the detection threshold for CT (assumed to be 5mm), and the mean doubling time of lung cancer (assumed to be 6 months).

RESULTS

Based on 1000 simulation runs, we estimate an increase of local disease from 26% to 64%. Our estimated mean lead time is 3.7 years. Our estimated mean percent overdiagnosis (i.e. number of overdiagnosed cases/number screen detected cases) is 8.2%. We estimate 8511 lung cancer deaths per 100,000 in non-screened group and 7731 deaths in screened group. Lung cancer mortality reduction due to CT screening is 9% after 40 years from the time of the initial exam, but the mortality reduction varies across the 40 year time horizon and reaches a maximum of 23%. Part of the reason for the rapid decrease in the mortality in later years is the increasing percentage of people who are not complying with screening due to the 6.5% annual nonadherence probability. If we reduced the nonadherence probability to zero, then the mortality reduction increases and is larger for a longer period as shown in Figure 3. It decreases due to increasing rates of other-cause death and because screening stops after 20 years. The temporal changes of the mortality reduction would be difficult to identify without a natural history model.

CONCLUSION

Our preliminary work predicts a reduction in lung cancer mortality due to CT screening.

Our framework that will have flexibility to be updated with an improved understanding of the disease, the technology and changes in interpretation criterion and practice patterns. Eventually, it will be applied to evaluate a variety of CT screening strategies that could not possibly be analyzed under a clinical trial setting.
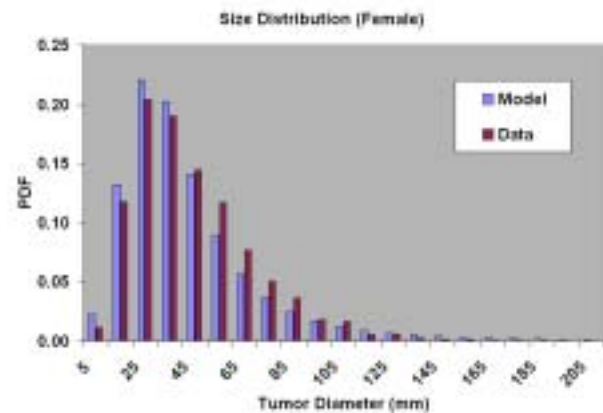

Figure 1. Comparison of model and data on the tumor size distribution (for females only).
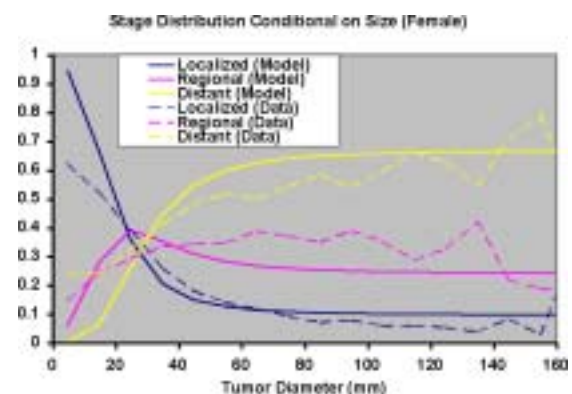

Figure 2. Comparison of model and data on the stage distribution conditioned on tumor size (for the females only).
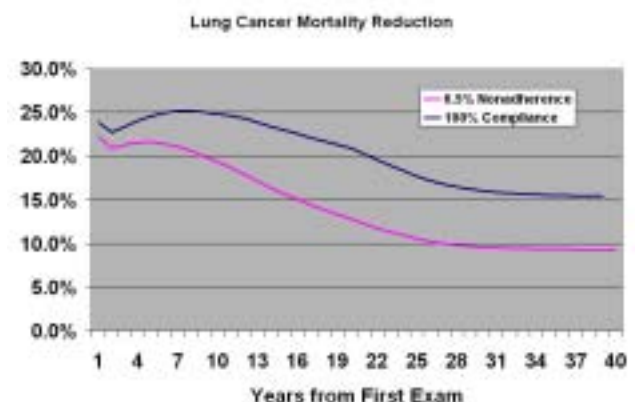

Figure 3. Lung Cancer Mortality Reduction due to annual CT screening for 20 years.

A Pilot Breast Cancer Screening Trial for Women at High Inherited Risk Using Clinical Breast Exam, Mammography, Breast Magnetic Resonance Imaging, and Ductal Lavage: Updated Results After Median Follow-up of Fourteen Months

Allison Kurian[2], Bruce Daniel[1], Kent Nowel[3], Kerry Kingham[2], Nicole Chun[2], Fred Dirbas[4], Sylvia K. Plevritis[1]

[1]*Department of Radiology,* [2]*Division of Oncology,* [3]*Department of Pathology,* [4]*Department of Surgery*

INTRODUCTION

Women who inherit mutations in BRCA1 or BRCA2 genes have a 50-85% risk of breast cancer. Options for management of this risk include screening (with mammography and clinical breast examination (CBE)) or prophylactic mastectomy. We have conducted a pilot study of adding breast magnetic resonance imaging (MRI) and ductal lavage (DL) to mammography and CBE for early detection of breast cancer, with an ultimate goal of decreasing breast cancer mortality. We report results after a median follow-up of 14.6 months.

METHODS

Eligibility criteria included a BRCA1 or BRCA2 mutation or an estimated greater than or equal to 10% risk of breast cancer over 10 years. Sixty-eight women entered a protocol requiring biannual CBE, and annual mammogram, breast MRI, and DL. Statistical analysis used Fisher's exact test, 2-tailed.

RESULTS

Mean age was 42 years. Seventeen biopsies were prompted by MRI, 2 by CBE, and 1 by mammography. Biopsy rate was significantly lower on subsequent, than on initial, MRI scans (4.5 vs. 23.9%; p=0.01). One 6.9 centimeter high-grade DCIS was MRI screen-detected and missed by mammography. Two cases of atypical lobular hyperplasia (ALH) and 2 cases of radial scar (RS) were screen-detected by MRI; one case of RS was detected by CBE. Atypia on DL was detected in 15 women, 8 (53.3%, 95% confidence interval (CI) 30.1-75.2%) of whom had abnormal MRIs, 2 (13.3%, 95% CI 2.5-39.1%) of whom had abnormal mammograms, and 1 (6.7%, 95% CI 0-31.8%) of whom had abnormal MRI-prompted biopsy (revealing ALH). Thirty-three (49.3%) women had had a bilateral salpingo-oophorectomy (BSO) and 12 (17.9%) women took tamoxifen or another selective estrogen response modulator (SERM). There was a lower abnormal biopsy rate among women with BSO and/or SERM than women with neither (2.6 vs.14.3%, p=0.15).

CONCLUSION

The low cancer incidence to date supports efficacy of risk reduction via BSO and tamoxifen, and suggests that yearly screening breast MRI might be less beneficial to genetically predisposed women after such interventions, although longer follow-up is necessary to confirm this. We are currently engaged in a prospective, multi-institutional study evaluating specificity, sensitivity, positive predictive value, negative predictive value, and cost-effectiveness of breast MRI compared to mammography for the detection of breast cancer in high-risk women, with a focus on subgroups risk-reduced by either BSO or SERMs. This study will also evaluate the clinical significance of ductal atypia and high-risk breast lesions in women genetically predisposed to breast cancer.

Table 1: Comprehensive Screening Results

	Abnormal Mammogram	Abnormal MRI	Ductal Atypia	Radial Scar or ALH	Cancer
BRCA1 N=36	3	22	8	3	1
BRCA2 N=11	1	5	1	0	0
No mutation N=21	4	15	6	1	0

Do K21, Parametric Mapping or Tumor Morphology on Contrast-Enhanced Breast Magnetic Resonance Imaging (MRI) Predict Tumor Response to Chemotherapy?

Daniel Margolis, Anthony Agoston, Robin Birdwell, Bruce Daniel, Gary Glover, Robert Herfkens, Sunita Pal, Sylvia Plevritis, Bronislava Sigal, Debra Ikeda

Department of Radiology

INTRODUCTION

A recent approach to treating women with large Stage T3 or T4 breast cancers, is the use of chemotherapy prior to surgery, or "neoadjuvant" chemotherapy. At this time, it is difficult to predict which breast cancers will respond to a specific chemotherapy regimen. Specific tumor features characterize cancer on contrast enhanced MRI of the breast. The shape of enhancement curves over time also helps to differentiate cancers (fast enhancement with a rapid washout or plateau of the curve shape) from benign tumors (slow enhancement with continued enhancement). One of the best enhancement parameters indicating cancer is K21, an estimate of the exchange rate of contrast concentrations between the intra- and extracellular fractions . It has been suggested that a combined analysis of both morphology and enhancement rate curves provides the most accurate diagnosis of malignancy

MATERIALS AND METHODS

We identified 5 patients in the radiology database who had pre- and post-adjuvant chemotherapy breast MRI followed by resection. All breast MRI was performed with dynamic contrast enhancement with identical parameters to those prospectively enrolled patients as described below. These MRI

scans were reviewed by two radiologists (BD, DI) and the tumors were characterized in terms of morphologic characteristics and enhancement contrast kinetics. We prospectively enrolled 19 patients who underwent dynamic contrast enhanced breast MRI after informed consent was obtained, followed by adjuvant chemotherapy and resection. All but one patient had a second MRI prior to resection.

We used the following parameters for each breast MRI: All MRI examinations used a four channel phased-array breast RF coil (MRI Devices) and all scans were obtained on a conventional 1.5 T GE Signa scanner. Patients were scanned employing a high resolution three dimensional spectral spatial magnetization transfer pulse sequence (3DSSMT) which provides high resolution morphologic data immediately following a rapid 3D spiral sequence which produces 3.5 minutes of kinetic data of breast lesion enhancement. In all cases intravenous gadolinium contrast was used at 1 mmol/kg, given as a bolus during the initial spiral sequences and flushed immediately with 20 cc of sterile saline.

The following morphologic parameters were evaluated for each scan: Enhancement Pattern (homogeneous, heterogeneous, or rim), Borders, Shape, and largest dimension. Additionally, regions-of-interest were chosen by the three reviewing radiologists and contrast kinetic parameters were recorded for the entire lesion, the worst portion, and the periphery.

Electronic patient charts were reviewed for each patient to document the duration of chemotherapy and date of surgery as well as excised tumor size, tumor histology, and for the presence of DCIS and LCIS. No patient with favorable tumor histologic subtype was included.

These data were utilized for the creation of a regression model based on covariates derived from the MR image, clinical parameters and pathology. The covariates most predictive of chemotherapy response were determined.

RESULTS

The histological type (tubular) and progesterone receptor (PR) status (positive) were found to correlate with lack of response to chemotherapy at surgery. Lesions with spiculated borders were also found to significantly be less likely to respond to chemotherapy. There was a correlation between one of the kinetic parameters, Kel, and poor response, but this did not reach significance. It was also found that extremely large values of another parameter, K21 were also associated with lack of response to chemotherapy at surgery. Interestingly, *negative* estrogen receptor was found to significantly correlate with poor clinical outcome at follow-up (metastasis). Positive PR status and high K21 values also correlated with poor clinical outcome but were not significant. Also, all patients who had a complete clinical response to chemotherapy at surgery were free of disease at last follow-up.

CONCLUSION

Dynamic contrast MRI provides information that correlates with outcomes at surgery and follow-up, and may determine which patients will benefit from neo-adjuvant chemotherapy.

REFERENCES

1. Leong CS, et al. Characterization of breast lesion morphology with delayed 3DSSMT: an adjunct to dynamic breast MRI. J Magn Reson Imaging 2000; 11:87-96.
2. Schwartz GF, et al. Neoadjuvant chemotherapy before definitive treatment for stage III carcinoma of the breast. Arch Surg 1987; 122:1430-4.

PUBLICATIONS & PRESENTATIONS

Published Papers, Book Chapter & Books

Adalsteinsson E, Hurd RE, Mayer D, Sailasuta N, Sullivan EV, Pfefferbaum A. In vivo 2D J-resolved magnetic resonance spectroscopy of rat brain with a 3-T clinical human scanner. Neuroimage 2004; 22:381-386.

Adalsteinsson E, Langer-Gould A, Homer RJ, et al. Gray matter N-acetyl aspartate deficits in secondary progressive but not relapsing-remitting multiple sclerosis. AJNR Am J Neuroradiol 2003; 24:1941-1945.

Arzoumanian Y, Mirmiran M, Barnes PD, et al. Diffusion tensor brain imaging findings at term-equivalent age may predict neurologic abnormalities in low birth weight preterm infants. AJNR Am J Neuroradiol 2003; 24:1646-1653.

Bammer R, de Crespigny AJ, Howard D, et al. A comparative evaluation of CH3-DTPA-Gd (NMS60) for contrast-enhanced magnetic resonance angiography. Magn Reson Imaging 2004; 22:619-624.

Bammer R, Markl M, Barnett A, et al. Analysis and generalized correction of the effect of spatial gradient field distortions in diffusion-weighted imaging. Magn Reson Med 2003; 50:560-569.

Bammer R, Moseley ME. Diffusion Weighted Magnetic Resonance Imaging. "Clinical Magnetic Resonance". editor. Edelman R. Saunders, 2004.

Beaulieu CF, Gold GE. Interactive and interventional sports medicine imaging. Top Magn Reson Imaging 2003; 14:115-130.

Bhaumik S, Lewis XZ, Gambhir SS. Optical imaging of Renilla luciferase, synthetic Renilla luciferase, and firefly luciferase reporter gene expression in living mice. J Biomed Opt. 2004; 9:578-86.

Bhaumik S, Walls Z, Puttaraju M, Mitchell LG, Gambhir SS. Molecular imaging of gene expression in living subjects by spliceosome-mediated RNA trans-splicing. Proc Natl Acad Sci U S A 2004; 101:8693-8698.

Birdwell RL, Jackman RJ. Clip or marker migration 5-10 weeks after stereotactic 11-gauge vacuum-assisted breast biopsy: report of two cases. Radiology 2003; 229:541-544.

Biswal S, Gambhir SS. Chapter 23: Gene and Cell Therapy, 2nd Edition. N. Templeton (Ed.). *Gene Therapy: Therapeutic Mechanisms and Strategies*. Marcel Dekker, Inc.: New York 2003; p. 447-480.

Biswal S. Molecular imaging of musculoskeletal diseases. Semin Musculoskelet Radiol 2003; 7:317-350.

Blankenberg F, Mari C, Strauss HW. Imaging cell death in vivo. Q J Nucl Med 2003; 47:337-348.

Blankenberg FG. Molecular imaging: The latest generation of contrast agents and tissue characterization techniques. J Cell Biochem 2003; 90:443-453.

Blankenberg FG. Recent advances in the imaging of programmed cell death. Curr Pharm Des 2004; 10:1457-1467.

Chan BK, Desser TS, McDougall IR, Weigel RJ, Jeffrey RB, Jr. Common and uncommon sonographic features of papillary thyroid carcinoma. J Ultrasound Med 2003; 22:1083-1090.

Chan FP, Chhor CM. Active lower gastrointestinal hemorrhage diagnosed by magnetic resonance angiography: case report. Abdom Imaging 2003; 28:637-639.

Chan FP. Cardiac multidetector-row computed tomography: principles and applications. Semin Roentgenol 2003; 38:294-302.

Chen IY, Wu JC, Min JJ, Sundaresan G, Lewis X, Liang Q, Herschman HR, Gambhir SS. Micro-positron emission tomography imaging of cardiac gene expression in rats using bicistronic adenoviral vector-mediated gene delivery. Circulation. 2004; 109:1415-20. Epub 2004 Mar 08.

Chow LC, Bammer R, Moseley ME, Sommer FG. Single breath-hold diffusion-weighted imaging of the abdomen. J Magn Reson Imaging 2003; 18:377-382.

Collisson EA, De A, Suzuki H, Gambhir SS, Kolodney MS. Treatment of metastatic melanoma with an orally available inhibitor of the Ras-Raf-MAPK cascade. Cancer Res. 2003; 63:5669-73.

Collisson EA, Kleer C, Wu M, De A, Gambhir SS, Merajver SD, Kolodney MS. Atorvastatin prevents RhoC isoprenylation, invasion, and metastasis in human melanoma cells. Mol Cancer Ther. 2003; 2:941-8.

Daniel BL, Gardner RW, Birdwell RL, Nowels KW, Johnson D. Magnetic resonance imaging of intraductal papilloma of the breast. Magn Reson Imaging 2003; 21:887-892.

De A, Gambhir SS. Chapter 50: PET in Imaging Gene Expression and Therapy. D. Bailey, D. Townsend, P. Valk, M. Maisey (Eds.). *Positron Emission Tomography: Basic Science and Clinical Practice*. Springer-Verlag 2003; p. 845-868.

Demers P, Miller DC, Mitchell RS, et al. Midterm results of endovascular repair of descending thoracic aortic aneurysms with first-generation stent grafts. J Thorac Cardiovasc Surg 2004; 127:664-673.

Desser TS, Sommer FG, Jeffrey RB, Jr. Value of curved planar reformations in MDCT of abdominal pathology. AJR Am J Roentgenol 2004; 182:1477-1484.

Do YS, Kao EY, Ganaha F, et al. In-stent restenosis limitation with stent-based controlled-release nitric oxide: initial results in rabbits. Radiology 2004; 230:377-382.

Do YS, Kao EY, Ganaha F, et al. In-stent restenosis limitation with stent-based controlled-release nitric oxide: initial results in rabbits. Radiology 2004; 230:377-382.

enhancement: what can we do? What should we do? Nat Rev Neurosci 2004; 5:421-5 (*Lead authors).

Fleischmann D. Future prospects in MDCT imaging. Eur Radiol 2003; 13 Suppl 5:M127-128.

Fleischmann D. High-concentration contrast media in MDCT angiography: principles and rationale. Eur Radiol 2003; 13 Suppl 3:N39-43.

Fleischmann D. MDCT of renal and mesenteric vessels. Eur Radiol 2003; 13 Suppl 5:M94-101.

Fleischmann D. Use of high-concentration contrast media in multiple-detector-row CT: principles and rationale. Eur Radiol 2003; 13 Suppl 5:M14-20.

Funabashi N, Kobayashi Y, Perlroth M, Rubin GD. Coronary artery: quantitative evaluation of normal diameter determined with electron-beam CT compared with cine coronary angiography initial experience. Radiology 2003; 226:263-271.

Gambhir SS, Deroose C, Wall Z. Cell Biology Fundamentals. P. Ell, Gambhir SS (Eds.). *Nuclear Medicine in Clinical Diagnosis & Treatment*. Churchill Livingstone Publishers, Third Edition 2004; p. 1687-1712.

Gambhir SS, Massoud TM. Molecular Imaging Fundamentals. P. Ell, Gambhir SS Eds.). *Nuclear Medicine in Clinical Diagnosis & Treatment*. Churchill Livingstone Publishers, Third Edition 2004; p. 1845-1870.

Gambhir SS, Schwimmer J, Decision Analysis Fundamentals. P. Ell, Gambhir SS (Eds.). *Nuclear Medicine in Clinical Diagnosis & Treatment*. Churchill Livingstone Publishers, Third Edition 2004; p. 1911-1924.

Gambhir SS. Molecular Imaging with Positron Emission Tomography. Discussions in PET Imaging, Diagnostic Imaging, 2003; 1-4, 2003.

Ganaha F, Kao EY, Wong H, et al. Stent-based controlled release of intravascular angiostatin to limit plaque progression and in-stent restenosis. J Vasc Interv Radiol 2004; 15:601-608.

Geraghty PR, Kee ST, McFarlane G, Razavi MK, Sze DY, Dake MD. CT-guided transthoracic needle aspiration biopsy of pulmonary nodules: needle size and pneumothorax rate. Radiology 2003; 229:475-481.

Glaser NS, Wootton-Gorges SL, Marcin JP, et al. Mechanism of cerebral edema in children with diabetic ketoacidosis. J Pediatr 2004; 145:164-171.

Glover GH, Thomason ME. Improved combination of spiral-in/out images for BOLD fMRI. Magn Reson Med 2004; 51:863-868.

Gold GE, Asakawa DS, Blemker SS, Delp SL. Magnetic resonance imaging findings after rectus femoris transfer surgery. Skeletal Radiol 2004; 33:34-40.

Gold GE, Asakawa DS, Blemker SS, Delp SL. Magnetic resonance imaging findings after rectus femoris transfer surgery. Skeletal Radiol 2004; 33:34-40.

Gold GE, Han E, Stainsby J, Wright G, Brittain J, Beaulieu C. Musculoskeletal MRI at 3.0 T: relaxation times and image contrast. AJR Am J Roentgenol 2004; 183:343-351.

Gold GE, McCauley TR, Gray ML, Disler DG. What's new in cartilage? Radiographics 2003; 23:1227-1242.

Gold GE, Reeder SB, Beaulieu CF. Advanced MR imaging of the shoulder: dedicated cartilage techniques. Magn Reson Imaging Clin N Am 2004; 12:143-159, vii.

Guccione S, Li KC, Bednarski MD. Vascular-targeted nanoparticles for molecular imaging and therapy. Methods Enzymol 2004; 386:219-236.

Gutierrez A, Do HM, Marks MP. Alteration in the venous drainage of a dural arteriovenous fistula following angioplasty. AJNR Am J Neuroradiol 2004; 25:1086-1088.

Hasegawa S, Choi JW, Rao J. Single-cell detection of transsplicing ribozyme in vivo activity. J Am Chem Soc 2004; 126:7158-7159.

Herneth AM, Philipp MO, Pretterklieber ML, Balassy C, Winkelbauer FW, Beaulieu CF. Asymmetric closure of ischiopubic synchondrosis in pediatric patients: correlation with foot dominance. AJR Am J Roentgenol 2004; 182:361-365.

Hildebrandt IJ, Gambhir SS. Molecular imaging applications for immunology. Clin Immunol. 2004; 111:210-24.

Hobbs SK, Shi G, Homer R, Harsh G, Atlas SW, Bednarski MD. Magnetic resonance image-guided proteomics of human glioblastoma multiforme. J Magn Reson Imaging 2003; 18:530-536.

Hope MD, Levin JM, Markl M, Draney MT, Alley M, Herfkens RJ. Images in cardiovascular medicine. Four-dimensional magnetic resonance velocity mapping in a healthy volunteer with pseudocoarctation of the thoracic aorta. Circulation 2004; 109:3221-3222.

Ikeda DM, Birdwell RL, O'Shaughnessy KF, Sickles EA, Brenner RJ. Computer-aided detection output on 172 subtle findings on normal mammograms previously obtained in women with breast cancer detected at follow-up screening mammography. Radiology 2004; 230:811-819.

Illes J, Kirschen MP. New prospects and ethical challenges for neuroimaging within and outside the health care system. Invited Editorial (Part II). AJNR Am J Neuroradiol 2003; 24:1932-4.

Illes J, Rosen A, Huang L, Goldstein RA, Raffin TA, Swan G, Atlas SW. Ethical consideration of incidental findings on adult MRI in research. Neurology 2004; 62:888-90.

Illes J. Medical Imaging: A hub for the new field of neuroethics. Acad Radiol 2004; 11:721-3.

Illes J. Neuroethics in a new era of neuroimaging. Invited Editorial (Part I). AJNR Am J Neuroradiol 2003; 24:1739-41.

Kim BS, Do HM, Razavi M. N-butyl cyanoacrylate glue embolization of splenic artery aneurysms. J Vasc Interv

Radiol 2004; 15:91-94.

Kim DH, Adalsteinsson E, Spielman DM. Spiral readout gradients for the reduction of motion artifacts in chemical shift imaging. Magn Reson Med 2004; 51:458-463.

Lane B. Practical imaging of the spine and spinal cord. Top Magn Reson Imaging 2003; 14:438-443.

Lee PY, Bazar KA, Yun AJ. Menstrual variation of autonomic balance may be a factor in exacerbations of certain diseases during the menstrual cycle. Med Hypotheses 2004; 63:163-167.

Lee PY, Yun AJ, Bazar KA. Acute coronary syndromes and heart failure may reflect maladaptations of trauma physiology that was shaped during pre-modern evolution. Med Hypotheses 2004; 62:861-867.

Leung AN. Case 63: hepatopulmonary syndrome. Radiology 2003; 229:64-67.

Liu C, Bammer R, Acar B, Moseley ME. Characterizing non-Gaussian diffusion by using generalized diffusion tensors. Magn Reson Med 2004; 51:924-937.

Loening AM, Gambhir SS. AMIDE: A Free Software Tool for Multimodality Medical Image Analysis. Journal of Molecular Imaging, 2003; 2:131-7.

Lu Y, Dang H, Middleton B, Zhang Z, Washburn L, Campbell-Thompson M, Atkinson MA, Gambhir SS, Tian J, Kaufman DL. Bioluminescent monitoring of islet graft survival after transplantation. Mol Ther. 2004; 9:428-35.

Mani A, Napel S, Paik DS, et al. Computed tomography colonography: feasibility of computer-aided polyp detection in a "first reader" paradigm. J Comput Assist Tomogr 2004; 28:318-326.

Mari C, Karabiyikoglu M, Goris ML, Tait JF, Yenari MA, Blankenberg FG. Detection of focal hypoxic-ischemic injury and neuronal stress in a rodent model of unilateral MCA occlusion/reperfusion using radiolabeled annexin V. Eur J Nucl Med Mol Imaging 2004; 31:733-739.

Markl M, Alley MT, Elkins CJ, Pelc NJ. Flow effects in balanced steady state free precession imaging. Magn Reson Med 2003; 50:892-903.

Markl M, Bammer R, Alley MT, et al. Generalized reconstruction of phase contrast MRI: analysis and correction of the effect of gradient field distortions. Magn Reson Med 2003; 50:791-801.

Markl M, Draney MT, Hope MD, et al. Time-resolved 3-dimensional velocity mapping in the thoracic aorta: visualization of 3-directional blood flow patterns in healthy volunteers and patients. J Comput Assist Tomogr 2004; 28:459-468.

Markl M, Reeder SB, Chan FP, Alley MT, Herfkens RJ, Pelc NJ. Steady-state free precession MR imaging: improved myocardial tag persistence and signal-to-noise ratio for analysis of myocardial motion. Radiology 2004; 230:852-861.

Massoud TF, Paulmurugan R, Gambhir SS. Molecular imaging of homodimeric protein-protein interactions in living subjects. FASEB J. 2004; 18:1105-7. Epub 2004 May 07.

Min JJ, Biswal S, Deroose C, Gambhir SS. Tetraphenylphosphonium as a novel molecular probe for imaging tumors. J Nucl Med 2004; 45:636-643.

Min JJ, Gambhir SS. Gene therapy progress and prospects: noninvasive imaging of gene therapy in living subjects. Gene Ther 2004; 11:115-125.

Napoli A, Fleischmann D, Chan FP, et al. Computed tomography angiography: state-of-the-art imaging using multidetector-row technology. J Comput Assist Tomogr 2004; 28 Suppl 1:S32-45.

Olafsen T, Cheung CW, Yazaki PJ, Li L, Sundaresan G, Gambhir SS, Sherman MA, Williams LE, Shively JE, Raubitschek AA, Wu AM. Covalent disulfide-linked anti-CEA diabody allows site-specific conjugation and radiolabeling for tumor targeting applications. Protein Eng Des Sel. 2004; 17:21-7. (Cover Article).

Ozduman K, Pober BR, Barnes P, et al. Fetal stroke. Pediatr Neurol 2004; 30:151-162.

Paik DS, Beaulieu CF, Rubin GD, et al. Surface normal overlap: a computer-aided detection algorithm with application to colonic polyps and lung nodules in helical CT. IEEE Trans Med Imaging 2004; 23:661-675.

Paulmurugan R, Massoud TF, Huang J, Gambhir SS. Molecular imaging of drug-modulated protein-protein interactions in living subjects. Cancer Res 2004; 64:2113-2119.

Raman B, Raman R, Raman L, Beaulieu CF. Radiology on handheld devices: image display, manipulation, and PACS integration issues. Radiographics 2004; 24:299-310.

Raman R, Napel S, Rubin GD. Curved-slab maximum intensity projection: method and evaluation. Radiology 2003; 229:255-260.

Ray P, De A, Min JJ, Tsien RY, Gambhir SS. Imaging trifusion multimodality reporter gene expression in living subjects. Cancer Res. 2004; 64:1323-30.

Ray S, Paulmurugan R, Hildebrandt I, Iyer M, Wu L, Carey M, Gambhir SS. Novel bidirectional vector strategy for amplification of therapeutic and reporter gene expression. Hum Gene Ther. 2004; 15:681-90.

Razavi MK, Lee DS, Hofmann LV. Catheter-directed thrombolytic therapy for limb ischemia: current status and controversies. J Vasc Interv Radiol 2003; 14:1491-1501.

Razavi MK, Lee DS, Hofmann LV. Catheter-directed thrombolytic therapy for limb ischemia: current status and controversies. J Vasc Interv Radiol 2004; 15:13-23.

Reeder SB, Herzka DA, McVeigh ER. Signal-to-noise ratio behavior of steady-state free precession. Magn Reson Med 2004; 52:123-130.

Reeder SB, Wen Z, Yu H, et al. Multicoil Dixon chemical species separation with an iterative least-squares estimation method. Magn Reson Med 2004; 51:35-45.

Rieke V, Vigen KK, Sommer G, Daniel BL, Pauly JM, Butts K. Referenceless PRF shift thermometry. Magn Reson Med 2004; 51:1223-1231.

Rubin GD. 3-D imaging with MDCT. Eur J Radiol 2003; 45 Suppl 1:S37-41.

Saket RR, Razavi MK, Padidar A, Kee ST, Sze DY, Dake MD. Novel intravascular ultrasound-guided method to create transintimal arterial communications: initial experience in peripheral occlusive disease and aortic dissection. J Endovasc Ther 2004; 11:274-280.

Saket RR, Sze DY, Razavi MK, et al. TIPS reduction with use of stents or stent-grafts. J Vasc Interv Radiol 2004; 15:745-751.

Saketkhoo RR, Razavi MK, Padidar A, Kee ST, Sze DY, Dake MD. Percutaneous bypass: subintimal recanalization of peripheral occlusive disease with IVUS guided luminal re-entry. Tech Vasc Interv Radiol 2004; 7:23-27.

Sato M, Johnson M, Zhang L, Zhang B, Le K, Gambhir SS, Carey M, Wu L. Optimization of adenoviral vectors to direct highly amplified prostate-specific expression for imaging and gene therapy. Mol Ther. 2003; 8:726-37.

Shiffman S, Rubin GD, Schraedley-Desmond P, Napel S. Semiautomated segmentation of blood vessels using ellipse-overlap criteria: method and comparison to manual editing. Med Phys 2003; 30:2572-2583.

Silverman D, Strommer J, Marseille D, Gambhir SS. Brain PET Atlas. P. Ell, Gambhir SS (Eds.). *Nuclear Medicine in Clinical Diagnosis & Treatment*. Churchill Livingstone Publishers, Third Edition 2004; p. 1475-1493.

Sommer G, Chow L, Pelc N. Measurement of renal extraction fraction using contrast-enhanced computed tomography. Med Phys 2004; 31:37-38.

Sood R. Off-resonance binomial preparatory pulse technique for high sensitivity MRI of H2O17. Magn Reson Imaging 2004; 22:181-195.

Su H, Forbes A, Gambhir SS, Braun J. Quantitation of cell number by a positron emission tomography reporter gene strategy. Mol Imaging Biol. 2004; 6:139-48.

Sundaresan G, Paulmurugan R, Berger F, Stiles B, Nagayama Y, Wu H, Gambhir SS. MicroPET imaging of Cre-loxP-mediated conditional activation of a herpes simplex virus type 1 thymidine kinase reporter gene. Gene Ther. 2004; 11:609-18.

Sundaresan G, Yazaki PJ, Shively JE, Finn RD, Larson SM, Raubitschek AA, Williams LE, Chatziioannou AF, Gambhir SS, Wu AM. 124I-labeled engineered anti-CEA minibodies and diabodies allow high-contrast, antigen-specific small-animal PET imaging of xenografts in athymic mice. J Nucl Med. 2003; 44:1962-9.A.

Sze DY, Razavi MK, Mitri RK, Regala AC, Dake MD. The "Y" stent: a technique using nitinol stents to treat bifurcations. J Endovasc Ther 2003; 10:780-787.

Toyokuni T, Walsh JC, Dominguez A, Phelps ME, Barrio JR, Gambhir SS, Satyamurthy N. Synthesis of a new heterobifunctional linker, N-[4-(aminooxy)butyl]maleimide, for facile access to a thiol-reactive 18F-labeling agent. Bioconjug Chem. 2003; 14:1253-9.

Vargas R, Nino-Murcia M, Trueblood W, Jeffrey RB, Jr. MDCT in Pancreatic adenocarcinoma: prediction of vascular invasion and resectability using a multiphasic technique with curved planar reformations. AJR Am J Roentgenol 2004; 182:419-425.

Vigen KK, Daniel BL, Pauly JM, Butts K. Triggered, navigated, multi-baseline method for proton resonance frequency temperature mapping with respiratory motion. Magn Reson Med 2003; 50:1003-1010.

Wong H, Gotway MB, Sasson AD, Jeffrey RB. Periaortic hematoma at diaphragmatic crura at helical CT: sign of blunt aortic injury in patients with mediastinal hematoma. Radiology 2004; 231:185-189.

Wu JC, Chen IY, Sundaresan G, Min JJ, De A, Qiao JH, Fishbein MC, Gambhir SS. Molecular imaging of cardiac cell transplantation in living animals using optical bioluminescence and positron emission tomography. Circulation. 2003; 108:1302-5. Epub 2003 Sep 08. (Cover Article).

Wu JC, Chen IY, Wang Y, Tseng JR, Chhabra A, Salek M, Min JJ, Fishbein MC, Crystal R, Gambhir SS. Molecular imaging of the kinetics of vascular endothelial growth factor gene expression in ischemic myocardium. Circulation. 2004; 110:685-91

Wu JC, Tseng JR, Gambhir SS. olecular imaging of cardiovascular gene products. J Nucl Cardiol. 2004; 11:491-505.

Yang YS, Guccione S, Bednarski MD. Comparing genomic and histologic correlations to radiographic changes in tumors: a murine SCC VII model study. Acad Radiol 2003; 10:1165-1175.

Yun AJ, Bazar KA, Lee PY. Autonomic dysfunction may be an under-recognized cause of female fertility disorders. Med Hypotheses 2004; 63:172-177.

Yun AJ, Lee PY, Bazar KA. Many diseases may reflect dysfunctions of autonomic balance attributable to evolutionary displacement. Med Hypotheses 2004; 62:847-851.

Yun AJ, Lee PY, Bazar KA. Modulation of autonomic balance by tumors and viruses. Med Hypotheses 2004; 63:344-351.

Yun AJ, Lee PY, Bazar KA. Modulation of host immunity by HIV may be partly achieved through usurping host autonomic functions. Med Hypotheses 2004; 63:362-366.

Yun AJ, Lee PY, Bazar KA. Temporal variation of autonomic balance and diseases during circadian, seasonal, reproductive, and lifespan cycles. Med Hypotheses 2004; 63:155-162.

Yun AJ, Lee PY. Maldaptation of the link between inflammation and bone turnover may be a key determinant of osteoporosis. Med Hypotheses 2004; 63:532-537.

Papers, Book Chapter & Books in Press

Bammer R, Moseley ME. A Comparitive Evaluation of CH3-DTPA-Gd (NMS60) for Contrast Enhanced Magnetic Resonance Angiography. Magn Reson Imaging.

Beaulieu CF, Paik DS, Napel S, Jeffrey RB. Advanced 3D Display Methods. In Fundamentals of Virtual Colonoscopy, Dachman AH (ed), Springer-Verlag, NY.

Chen KM, Bird L, Barnes PD, Barth RA, Hudgins L.Lateral Meningocele Syndrome: Vertical Transmission and Expansion of the Phenotype. Am J Med Genet.

Franc B, Yoshida E, Herfkens RJ, Goris M. Pericardial lymph node involvement in lymphoma as identified on PET. In press Clin Nucl MedIlles J (Ed.) 21st Century Neuroethics: Defining the Issues in Research, Practice and Policy, Oxford University Press, Oxford, UK.

Gambhir SS. Quantitative Assay Development for PET. IN Positron Emission Tomography. M.E. Phelps (Ed.). Raven Press.

Green LA, Nguyen K, Berenji B, Bauer E, Barrio J, Namavari M, Satyamurthy N, Gambhir SS. A Tracer Kinetic Model for FHBG for Quantitating Herpes Simplex Virus Type 1 Thymidine Kinase Reporter Gene Expression in Living Animals using Positron Emission Tomography. J Nucl Med.

Hope M, Herfkens RJ. Velocity mapping of thoracic aorta and pulmonary artery. In press N Engl J Med.

Illes J, Kann D, Karetsky K, Letourneau P, Raffin TA, Schraedley-Desmond P, Koenig BA, Atlas SW. Advertising, patient decision-making, and self-referral to CT and MR imaging. Arch Intern Med.

Illes J, Kirschen MP, Karetsky K, Kelly M, Saha A, Desmond JD, Raffin TA, Glover GH, Atlas SW. Discovery and disclosure of incidental findings on brain MRI in research. J Magn Reson Imaging.

Illes J. Imaging and imagining: Interpretation of Neuroimaging Data is a Key Ethical Challenge American Journal of Bioethics.

Iyer M, Bergara F, Lewis X, Zhang J, Carey M, Wu L, Gambhir SS. Non-invasive Imaging of Enhanced Prostate-Specific Gene Expression Using a Two-Step Transcriptional Amplification Based Lentivirus Vector. Mol Ther.

Iyer M, Gambhir SS. Molecular Imaging of the Lungs. D.P. Schuster and T. Blackwell (eds.). Marcel Dekker, Inc.

Kee ST, Ganguly A, Daniel BL, Wen Z, Shimikawa A, Butts K, Fahrig R, Pelc NJ, Dake MD. MR-Guided Transjugular Portosystemic Shunt Placement (TIPS) using a Hybrid X-Ray/MR System. The authors are:

Kim YP, Dubey P, Ray P, Gambhir SS, O. Witte. Multimodality Imaging of Lymphocytic Migration Using Lentiviral-based Transduction of a Fusion Reporter Gene. Mol Imaging Biol.

Li P, Napel S, Acar B, Paik DS, Jeffrey RB, Beaulieu CF. Automatic registration of colonic polyps between supine and prone scans in CT Colonography. Med Phys.

Liu C, Bammer R, Moseley ME. Characterizing Non-Gaussian Diffusion by Using Generalized Diffusion Tensors. Magn Reson Med.

Markl M, Draney MT, Levin JM, Williamson EE, Pelc NJ, Liang DH, Miller DC, Herfkens RJ. Time-Resolved 3D Magnetic Resonance Velocity Mapping of Aortic Flow in Normal Volunteers and Patients after Valve-Sparing Aortic Root Replacement. In press J Thorac Cardiovasc Surg

Na DG, Thijs V, G Albers, Moseley ME, Marks M. DWI in Acute Ischemia: TheValue of ADC and Signal Intensity Thresholds in Prediction of Tissue at Risk and Final Infarct Size. AJNR Am J Neurorad.

Rubin GD, Lyo J, Paik DS,Sherbondy A, Chow L, Leung AN, Mindelzun R, Zinck SE, Naidich DP, Napel S. Pulmonary nodules in MDCT scans: impact of computer-aided detection. Radiology.

Wu J, Gambhir SS. Gene Product Imaging. IN Clinical Nuclear Cardiology: State of the Art and Future Directions. B. Zaret & G. Beller (Eds.).

Yaghoubi SS, Barrio JR, Namavari M, Satyamurthy N, Phelps ME, Herschman HR, Gambhir SS. Imaging Progress of Herpes Simplex Virus Type I thymidine Kinase Suicide Gene Therapy in Living Subjects with Positron Emission Tomography. Cancer Gene Ther.

.

Peer-reviewed Presentations at Scientific Meetings

Alexander J, Bednarski M, Guccione S, Yao J, Menard C, Li KCP, Choyke P. Systemic prostate specific antigen (PSA) is a measure of vascular permeability: a study of dynamic contrast enhanced magnetic resonance imaging (DCE-MRI).

Chan FP, Lin W-T, Napel S. Correlative filtering to improve automated center path generation for MDCT coronary angiography

Ganguly A, Fahrig R, Wen Z, Pelc NJ. X-ray Image Quality Assessment in X-ray/MR Hybrid System

Gilat T, Fahrig R, Pelc NJ. A 3D Reconstruction Algorithm for an Inverse Geometry Volumetric CT System with a Large Array Scanned Source

Gold GE, Han E, Stainsby J, Wright GA, Brittain JH, Beaulieu CF. Relaxation Times and Contrast in Musculoskeletal MR Imaging at 3.0 Tesla

Gold GE, Pappas G, Blemker S, Whalen S, Campbell GT, Beaulieu CF. Abduction and External Rotation in Shoulder Impingement: An Open MRI Study

Hellinger JC, Draney MT, Markl M, Pelc NJ, Herfkens RJ. Application of Cine Phase Contrast Magnetic Resonance Imaging and SPAMM-Tagging for Assessment of Endoleaks and Aneurysm Sac Motion

Hellinger JC, Napoli A, Fleischmann D, Leung AN, Rubin GD. Multidetector Row CT (MDCT) Assessment of Thromboembolic Disease: Incremental Value of CT Venography (CTV) in 1240 Consecutive Exams

Li P, Napel S, Paik DS, Jeffrey RB Jr, Beaulieu CF. CT Supine and Prone Colon Data Registration: Algorithm Evaluations

Lo A, Song Y, Boyer AL, Pawlicki T, Xing L. Combining IMRT and MERT for Breast-Conserving Radiation Therapy

Nayak KS, Hargreaves A, Besier T, Delp S. High-Resolution Real-Time MRI of Knee Kinematics

Plevritis SK, Sigal BM, Salzman P. Estimating the stage shift and mortality reduction from CT lung cancer screening.

Raman B, Raman R, Carnethon C, Fortmann SP, Napel S, Rubin GD. Calcium Quantification In The Aortoiliac Arteries: Interscan Variability of Agatson Scoring vs. Automated Mass Quantification In Noncontrast and Contrast Enhanced Scans.

Raman R, Raman B, Raman L, Beaulieu CF. Handheld Computers: Potential use as a Portable Volumetric Workstation.

Reeder SB, Markl M, Hellinger JC, Yu H, Herfkens RJ, Pelc NJ. Multi-Coil Cardiac CINE Imaging with "Dixon" Fat-Water Separation and Steady-State Free Precession

Reeder SB, Shimakawa A, Brittain JH, Yu H, Pelc NJ, Gold GE. Multi-Point "Dixon" Fat-Water Separation with Steady-State Free Precession at 3T: Application to Musculoskeletal Imaging

Rieke V, Vigen KK, Daniel BL, Pauly JM, Butts K. Referenceless PRF Shift Thermometry: Feasibility for Liver Applications

Rubin DL, Desser TS. Building an Integrated Data Warehouse for Radiology Teaching, Process Improvement, and Research

Rubin GD, Lyo JP, Paik DS, Sherbondy AK, Naidich DP, Napel S. Impact of Computer-assisted Detection (CAD) Algorithm vs a Second Radiologist on Reader Sensitivity for Detecting Pulmonary Nodules in MDCT Scans

Rubin GD, Naidich DP, Sherbondy AJ, Lyo JP, Napel S. Inadequacy of Lung Nodule Reference Standard Based upon Standard Methods of Expert Consensus Review Using Cine-Paging of Transverse Thin-Section MDCT Lung Scans

Sherbondy A, Houston M, Napel S. Interactively Guided Volumetric Segmentation using Programmable Graphics Hardware.

Sommer G, Chow LC. Measurement of Renal Extraction Fraction Using Contrast-enhanced CT

Vasanawala SS, Hargreaves BA, Pauly JM, Nishimura DG, Beaulieu CF, Gold GE. Phase-Sensitive Steady-State Free Precession Musculoskeletal Imaging

Yun AJ, Lee P, Chao D, Schraedley-Desmond PK. The Lexicon Polemics in Radiology Reports: Disparity in Appreciated Probability Values Ascribed to Modifers Used in Dictations among Radiologists and Clinicians

Antonios VP, Silverman NH, Chan FP. Effectiveness of cardiac-gated MDCT for the diagnosis of congenital heart disease in small children with high heart rates,

Chan FP, Narayan G, Napoli A, Choi B, Chun SH, Pretreatment planning for biventricular pacemaker placement using MDCT: effectiveness and findings,

Desser TS, Kirkpatrick ID, Mindelzun RE. Dynamic MDCT Evaluation of Suspected Small Bowel Obstruction

Desser TS, Margolis D, Shelton A, Welton M, Jeffrey RB. MDCT for Local Staging of Rectal Cancer: Comparison with Endoscopic Ultrasound

Hiatt MD, Stockton CG. The Impact of the Flexner Report on the Fate of Medical Schools in North America after 1909

Hiatt MD. The Relationship between Physician Supply and Per Capita Income in Counties across the United States, 1920-1998

Hollingsworth C, Durham NC, Chan FP, Yoshizumi TT, Frush DP, Nguyen G, Lowry CR. Pediatric Gated Cardiac CT Angiography: What is the Radiation Dose?.

Jude C, Sherbondy AJ, Schraedley-Desmond P, Napel S, Rubin GD. Radiologist Characterization Of Lung Nodule Candidates Detected By Computer Aided Detection (CAD): Comparison Of Visualization Methods

Kirkpatrick ID, Desser TS, Nino-Murcia M, Jeffrey RB. Small Cystic Lesions of the Pancreas: Clinical Significance and Findings at Follow-up

Mazin SR, Schmidt T, Pelc NJ Collimator for a Multiple-Eye Inverse-Geometry Volumetric CT System

Nagle SK, Chan FP. Cardiac heterotaxy: emerging state-of-the-art evaluation using cardiac-gated MDCT and MRI,

Paik DS, Sundaram P, Beaulieu CF, Napel S. An Atomically Selective Morphological Enhancement And Suppression In CT Colonography: Initial Experience With A Lagrangian Approach

Reeder SB, Pineda AR, Y H, Wen Z, Shimakawa A, Brittain JH, Gold GE, Pelc NJ. Asymmetric Echoes for Optimal SNR Performance of "Dixon" Water-Fat Separation with Fast Spin-Echo Imaging

Reeder SB, Yu H, Johnson J, Shimakawa A, Brittain JG, Pelc NJ, Beaulieu CH, Gold GE. T1 and T2 Weighted Brachial Plexus Fast Spin-Echo Imaging with "Dixon" Fat-Water Separation: a Comparison with STIR and Fat Saturation

Rubin DL, Desser TS. Building an Open-Architecture Integrated Data Warehouse for Radiology Using Public Domain Tools

Rubin DL, Desser TS. Radbank: Evaluating an Integrated Data Warehouse for Radiology Research and Teaching

Sun S, Rubin GD, Napel S. A Simulated Annealing-Based Algorithm For Lung Nodule Registration In CT Scans

Sundaram P, Sifakis E, Paik DS, Beaulieu CF, Napel S. Physically based approach to removal of folds in CT Colonography: Proof of concept

Taira A, Herfkens RJ, Goris M, Kalinyak J; Gambhir SS, Quon A. Assessment of Integrated FDG PET/CT Imaging in the Detection of Bone Metastases

ISMRM 2004

12ᵀᴴ Scientific Session, Toronto, Ontario May 2004

Adalsteinsson E, Sullivan E, Mayer D. In vivo monitoring of alcohol uptake kinetics in rat brain

Atlas S, Harsh G, Guccione S, Lim M. The use of magnetic resonance imaging to guide the analysis of serum proteomic patterns in glioblastoma multiforme,

Bammer R, Moseley M, Liu C, Kim D-H.Self-Navigated Diffusion Tensor Imaging with Interleaved Variable Density Spiral Acquisition

Bammer R, Moseley M. Interleaved Dual-Echo Spiral-Out-Spiral-In DSC Imaging With Generalized SENSE,

Bangerter N, Cunningham C, Dicarlo J, Nishimura D, Lee JH. 3D High Resolution Skin Imaging,

Beatty P, Pauly J, Nishimura D. Fast Gridding Methods for 3D Reconstruction

Birdwell R, Daniel B, Hwang G, Ikeda D. Vacuum-assisted iMRI-guided percutaneous core biopsy of small breast lesions: first experience with a vertically open 0.5T scanner in the prone or supine position

Bouley D, Daniel B, Sommer G, Butts K. Correlation of real-time MRTI and post-treatment MRI with histologic depiction of prostatic ablation using high-intensity ultrasound

Busse R, Herfkens R. Evaluation of Respiratory Triggering Algorithms,

Butts K, Pisani L. Reduction of Blurring in View Angle Tilting MRI with Multiple VAT Readouts

Caffarelli A, Arai T, Kofidis T, Quertermous T, Yang P, McConnell M, Robbins R, Greve J. In vivo MR evaluation of the timing of mouse embryonic stem cell transplantation at 4.7 T

Chow L, Chang R, Bammer R. Diffusion weighted imaging in the assessment of renal dysfunction,

Conolly S, Nishimura D, Hargreaves B, Cunningham C. Time-Optimal VERSE Excitation for 3D Balanced SSFP Imaging

Cunningham C, Pauly J, Santos J. RF pulses with built-in saturation sidebands

Cunningham C, Pauly J. A Novel Approach for Reducing Chemical Shift Registration Error at 3T: Short TE CPRESS,

Cunningham C, Pauly J. High Resolution 3D MR Spectroscopic Imaging and J-resolved MRS of the Prostate at 3 Tesla

Cunningham C, Pauly J. Sequence Design Incorporating the LASER Technique for Prostate MRSI at High Field,

Cunningham C, Pauly J. Symmetric-sweep spectral-spatial RF pulses for spectral editing

Cunningham C, Pauly J. Ultra-Short TE Imaging with Single-Digit (8&[micro]s) TE

Cunningham C. Use of a Composite Spin Lock Pulse for Background Suppression with Applications to Angiography and Perfusion Imaging

Daniel B, Zakhour M, Vidarsson L, Pauly J. Dynamic Contrast Uptake Analysis in the Breast by Linear Combination,

De Charms C, Ress D, Miller K, Pauly J. High resolution BOSS fMRI at 1.5T

Dicarlo J, Nishimura D, Hu B, Scott G, Lee J, Conolly S, Hargreaves B, Bangerter N, Cunningham C. SNR Comparison of RF Coil Size for Ischemic Skin Imaging

Draney M, Hope M, Chan F, Alley M, Markl M, Pelc N, Herfkens R, Levin J. Time-Resolved 3D Velocity Mapping in the Thoracic Aorta: Three-Directional Blood Flow Patterns in Healthy Volunteers and Patients

F Adalsteinsson E, Spielman D, Mayer D, Kim, D-H. ast CT-PRESS Based Spiral CSI at 3 T,

Fahrig R, Pelc N, Ganguly A, Mayer D. Contrast Agent Optimization for Imaging with MR/x-ray Hybrid Systems

Frisoli J, Rieke V, Daniel B, Butts K, Vigen K. *In vivo* Porcine Liver Radiofrequency (RF) Ablation with Simultaneous Temperature Monitoring

Glover G, Foland L. Scanner Quality Assurance for Longitudinal or Multicenter fMRI Studies

Gold G, Besier T, Asakawa D, Draper C, Delp S, Beaupre G. Weight-bearing MRI of Patellofemoral Joint Cartilage,

Grafendorfer T, Macovski A, Conolly S, Scott G. A 180mT Pulsed Homogeneous Magnet for Prepolarized Knee MRI

Greve J, McConnell M, Arai T, Yang P, *In vitro* MR assessment of proliferating SPIO-labeled mouse embryonic stem cells

Gu M, Adalsteinsson E, Spielman D. Lipid Suppression using Selective Inversion Recovery for 3D Spectroscopic Imaging at 3T,

Guccione S, Wang Y, Lim M, Harsh G, Yang Y-S, Atlas S, Bednarski M, Homer R. Identification of serum protein profiles of glioblastoma multiforme patients: using image-guided microarray analysis of tumor samples to identify serum markers

Guccione S. Systemic prostate specific antigen (PSA) is a measure of vascular permeability and not malignancy: A Prostate Dynamic Contrast Enhanced Magnetic Resonance Imaging (DCE-MRI) Study

Gurney P, Hargreaves B, Nishimura D. Rapid Imaging using a 3D Cones Trajectory and Balanced SSFP,

Hargreaves B, Conolly S, Gold G, Scott G, Venook R. Comparison of Surface Coil and Automatically-tuned, Flexible Interventional Coil Imaging in a Porcine Knee

Hargreaves B, Nishimura D, Gurney P. Improved Fat Suppressed SSFP Imaging using 3DPR,

Hargreaves B, Vasanawala S, Nishimura D. Phase Sensitive SSFP Parallel Imaging,

Hsu J-J, Glover G. Localized Active Shimming for fMRI Signal Recovery

Hu Y, Glover G. Navigated 3D fMRI vs. 2D fMRI

Huang Y, Gurr D, Brittain J, Herfkens RJ, Merchant N, Wright G. Rotational projection contrast-enhanced MR angiography. ISMRM, May 2004

Hundt W, Yu E, Bednarski M. MRI - imaging, histological analysis and gene expression of a squamous cell carcinoma model treated with Focused ultrasound

Hyon MS, Kaneda H, Ikeno F, Nayak K, Yeung A, McConnell M. Magnetic Resonance Angiography Can Serially Evaluate Thrombolysis of In-stent Thrombus,

Kee S, Daniel B, Wen Z, Butts K, Fahrig R, Dake M, Pelc N, Ganguly A. TIPS using Truly Hybrid X-ray/MR Guidance

Kim D-H, Glover G, Spielman D. Rapid In Vivo Shimming with Current Constraints,

Kim D-H, Spielman D, Adalsteinsson E. Short Echo Time Spiral Chemical Shift Imaging

Larson P, Nishimura D. Robust Long-T_2 Suppression Pulses,

Larson P, Pauly J. Alternate Interpolators for rBURS without Deapodization,

Law C, Glover G. Statistical Combination of Partial k-Space EPI for BOLD fMRI

Lee D, Pauly J. Reducing Spurious Minima in Automatic Off-Resonance Correction for Spiral Imaging,

Levin J, Hope M, Markl M, Draney M, Wilson N, Herfkens R. Four-Dimensional Magnetic Resonance Velocity Mapping: Velocity Profile of Blood-Flow through the Thoracic Aorta in 10 Healthy Volunteers

Lew C, Bammer R, Spielman D. TurboSENSE: Phase Estimation in Temporal Phase-Constrained Parallel Imaging

Liu C, Bammer R Moseley M. The Effect of Gaussian Noise on Generalized Diffusion Tensor Imaging

Markl M, Moseley M, Bammer R, Vigen K. Self-Calibrating Radial Generalized SENSE,

Markl M, Pelc N, Yu H, Reeder S. Single Acquisition Water Fat Separation for SSFP Cardiac CINE Imaging: Feasibility Study,

Matter N, Conolly S, Scott G. Minimizing Field Inaccuracy in MRI Electomagnet Control Systems

Matter N, Conolly S, Scott G. Rapid Field Pulsing Circuit with Leakage Current Bypass for Pulsed Magnetic Coils in MR

Nguyen P, Cunningham C, Nishimura D, Hu B, McConnell M, Pauly JT, Yang P, Tsukiji M, Santos J. Real time MR Coronary Angiography at 3T,

Nguyen P, McConnell M, Terashima M. Carotid Plaque Imaging at 1.5T and 3T: Systematic SNR Comparison

Nishimura D, Hargreaves B, Vasanawala S, Bangerter N. 3D Fluid-Suppressed T2-Prep Flow-Independent Angiography using Balanced SSFP

Nishimura D, Lee JH, Delapp L. Assessment of Lower-Limb Perfusion using Rapid 3D Spiral Trajectories

Nishimura D, Santos J, Nayak K, Narayan G, Park J. Cardiac Output Measurement with Ungated Spiral Phase-Contrast and Triggered Real-Time SSFP Imaging

Pauly J, Hu B, Narayan G, Nayak K. Complete assessment of LV and RV function and volume in a single breathold using real-time, spiral, steady-state free precession

Pelc N, Gold G, Reeder S, Yu H. "Dixon" Water-Fat Separation for Musculoskeletal Imaging with Fast Spin-Echo at 3T

Pelc N, Gold G, Yu H, Reeder S. Implementation and Noise Analysis of Chemical Shift Correction for Fast Spin Echo Dixon Imaging

Pelc N, Pineda A, Reeder S, Yu H, Beaulieu C, Gold G, Wen Z. Asymmetric Echoes for Robust Fast Spin-Echo "Dixon" Water-Fat Separation,

Reeder S, Markl M, Yu H, Hellinger J, Herfkens R, Pelc N. Cardiac CINE Imaging with "Dixon" Water-Fat Separation and Steady-State Free Precession

Reeder S, Pelc N. Abdominal Three Point Dixon Imaging with Self Calibrating Parallel MRI,

Reeder S, Yu H, Pelc N, Beaulieu C, Gold G. Rapid Cartilage Morphology at 3.0T: Comparison of FS-SPGR, FS-SSFP, and "Dixon" SSFP Imaging,

Reeder S, Yu H, Yang P, McConnell M. Non-Contrast-Enhanced Angiography at 3T using SSFP and "Dixon" Fat-Water Separation

Ress D, Glover G, Wandell B. High-resolution functional MRI of retinotopic and laminar activation using a 3T scanner,

Santos J, Cunningham C, Pauly J. Excitation of Variable-Phase Profile for Efficient Saturation

Santos J. Integrated Real-time MRI User-Interface,

Schnitzer M, Jung J. Regional variations in BOLD Response during Transient Hemodilution in Rat

Schraedley-Desmond P, Desmond J, Kirschen M, Chen S. Increases in cerebro-cerebellar activation with increasing memory load and task practice: An fMRI study,

Scott G, Conolly S, Matter N, Macovski A, Ungersma S. MR Imaging with T_1 Dispersion Contrast

Scott G, Conolly S, Ungersma S. Magnet Design Considerations for Parallel Mouse Imaging

Scott G, Daniel B, Butts K, Rieke V, Ganguly A, Fahrig R, Pelc N, Pauly J. X-Ray Compatible RF-Coil for MR Imaging

Sommer FG, Butts K, Pisani L, Glover G. Optimizing Spa-

tial Resolution for MR Thermal Imaging of Transurethral Ultrasound Prostate Ablation

Spielman D, Mayer D, Hunjan S, Xing L, Kim D-H. Citrate Magnetic Resonance Spectroscopy at 3 T,

Taylor C, Feinstein J, Cheng C, Herfkens R. In Vivo Blood Flow Characteristics in the Proximal Pulmonary Arteries of Healthy Children and Adults at Seated Rest and During Cycling Exercise,

Terashima M, Nguyen P, McConnell M. High-resolution Black-blood MRI of Carotid Atherosclerotic Plaque at 3T: Optimization of Clinical Protocol

Thomason M, Foland L, Glover G. Calibration of fMRI Activation for the FIRST BIRN Project,

Vasanawala S, Hargreaves B, Pauly J, Nishimura D, Gold G, Beaulieu C. Musculoskeletal Imaging with PS-SSFP

Venook R, Scott G, Conolly S. Feasibility of Remote Polarization for Angiography Using Prepolarized MRI

Vidarsson L, Pauly J, Gold G. Myelin Imaging in the Brain of MS Patients via Linear Combination,

Vidarsson L, Pauly J, Gold G. T_2 Linear Combination Filtering in Patella Cartilage,

Vigen K, Conolly S, Scott G, Chen A. RF Ablation Electrode Current Imaging by MRI,

Wang Y, Yang Y-S, Bednarski M, Homer R, Shi G, Harsh G, Atlas S, Guccione S. Magnetic Resonance Image-Guided Proteomic Analysis of Human Glioblastoma Multiforme: A Two-Dimensional Gel Electrophoresis Study,

Wen Z, Fahrig R, Pelc N. Permanent Magnet Shimming for the X-ray Detector in a Hybrid X-ray/MR System,

Wen Z, Reeder S, Yu H, Pelc N, Pineda A. Cramér-Rao Bounds for 3-Point Dixon Imaging

Yang P, McConnell M. Rapid Comprehensive Cardiac Examination in an Integrated Real Time Suite,

Yu H, Pelc N, Reeder S, Markl M. Parallel Cardiac CINE Imaging: Application to "Dixon" Water-Fat Separation and Steady-State Free Precession,

Yu, Reeder S, Pelc N. Robust Field Map Estimation in a Dixon Water-Fat Separation Algorithm with Short Echo Time Increments

THE 2ND ANNUAL MEETING OF THE SOCIETY FOR MOLECULAR IMAGING

SAN FRANCISCO
AUGUST 15-18, 2003.

Bednarski M, Guccione S, Yang Y, Shi G, Wang Y, Homer R, Atlas S, Moes G, Harsh G. Search for Vascular Targets Using Contrast Enhanced MRI Guided Genomic and Proteomic Analysis in Human Glioblastoma Multiforme.

Shinde RR, Bednarski MD, Contag CH. Automated Synthesis of Novel Luciferyl-Derivatives for Use in In-Vivo Assays and Imaging.

Bhaumik S, Walls Z, Puttaraju M, Mitchell LG, Gambhir SS. Noninvasive Imaging of mRNA in Living Animals Using Spliceosome Mediated RNA *Trans*-Splicing. Molecular Imaging 2:282, 2003.

Burns SM, Wong RJ, Stevenson DK, Contag CH. Monitoring Heme Oxygenase-1 Expression in Infected Mice by In Vivo Bioluminescent Imaging.

Chen I, Wu J, Min JJ, Sundaresan G, Lewis X, Gambhir SS. MicroPET Imaging of Rat Cardiac Gene Expression Uisng Bicistronic Adenoviral Vector-Mediated Gene Delivery. Molecular Imaging 2:383, 2003.

Creusot R, Tarner IH, Nakajima A, Slavin AJ, Ermann J, Contag CH, Fathman CG. Retroviral Gene Therapy of Animal Models of Autoimmune Diseases by Local Delivery of Immunomodulatory Molecules Using AG-Specific T-Cells or Dendritic Cells

De A, Gambhir SS. Non-invasive Imaging and Quantitative Assessment of Bioluminescence Resonance Energy Transfer in Living Animal. Molecular Imaging 2:142, 2003.

Guccione S, Mari C, Yang YS, Bednarski M. Utility of Image-Guided Microarray Analysis in Identification of Targets for Molecular Imaging

Guccione S, Hood J, Frausto R, Cheresh D, Bednarski M. Imaging Tumor Angiogenesis for Developing Vascular Targeted Gene Therapy

Iyer M, Bergara F, Hildebrandt J, Lewis X, Zhang J, Le K, Carey M, Wu L, Gambhir SS. Optical Imaging of Amplified Firefly Luciferase Reporter Gene Expression in a Prostate-Specific Transgenic Mouse Model. Molecular Imaging 2:138, 2003.

Iyer M, Bergara F, Lewis X, Zhang J , De A, Carey M, Wu L, Gambhir SS. Optical Imaging in Living Mice of an Amplified Firefly Luciferase (*fl*) Reporter Gene Expression Strategy Using a Prostate-Specific Lentiviral Vector. Molecular Imaging 2:265, 2003.

Loening A, Gambhir SS. AMIDE: A Free Software Tool for Multimodality Image Analysis. Molecular Imaging 2:184, 2003.

Loening A, Paulmurugan R, Wu A, Gambhir SS. A Novel Renilla Luciferase/Epidermal Growth Factor Fusion Protein as an Optical Molecular Probe for Cancer Imaging. Molecular Imaging 2:155, 2003.

Massoud T, Paulmurugan R, Gambhir SS. Homodimeric Protein-Protein Interaction Imaging in Living Subjects. Molecular Imaging 2:224, 2003.

Min JJ, Biswal S, Hildebrandt I, Gambhir SS. Comparison of [3H]tetraphenylphosphonium (TPP) and [3H/18F]fluorodeoxyglucose (FDG) Accumulation in Cancer Cells in Culture and in Living Mice. Molecular Imaging 2:158, 2003.

Min JJ, Paulmurugan R, Gambhir SS. Reporter Gene Imaging for Singal Transduction Pathway of G-protein Coupled Receptor; Dopamine Type 2 Receptor. Molecular Imaging 2:220, 2003.

Mizobuchi M, Wong RJ, Zhao H, Vreman HJ, Stevenson DK, Contag CH. Effect of Dexamethasone on Heme Oxygenase-1 Transcription In Culture and In Vivo, as Assessed by Bioluminescent Imaging

Negrin RS, Edinger M, Beilhack A, Contag CH. Visualizing the Graft vs Host and Graft vs Tumor Reactions In Vivo

O'Connell-Rodwell CE, Shriver D, Simanovskii DM, McClure C, Cao Y, Zhang W, Bachmann MH, Jansen DE, Schwettman AH, Contag CH. Temporal Analysis of Cellular Response Across a Gradient of Thermal Stress: A Model for Laser Ablation Designs.

Patel M, Gambhir SS. Bioluminescence Imaging of T-cell Activation Using the Granzyme B Promoter. Molecular Imaging 2:346, 2003.

Paulmurugan R, Massoud T, Huang J, Gambhir SS. Modulation of a Split *Synthetic Renilla Luciferace* Complementation-Based Protein-Protein Interaction Using the Small Molecule Rapamycin in Cells and in Living Subjects. Molecular Imaging 2:221, 2003.

Ravindran J, Bachmann MH, Contag CH. In Vivo Imaging of BMP4-Expression in Mice Reveals a Spatiotemporal Shift During Early Neonatal Development

Ray P, De A, Min J, Tsien R, Gambhir SS. Multimodality Imaging of Reporter Gene expression in Single Cells and Living Mice Using a Novel Triple Fusion Reporter Gene Vector. Molecular Imaging 2:156, 2003.

Ray S, Paulmurugan R, Hildebrandt I, Iyer M, Wu L, Carey M, Gambhir SS. A Novel Bi-Directional Vector Strategy for Amplification of Reporter and Therapeutic Gene Expression. Molecular Imaging 2:140, 2003.

Shi G, Wang Y, Hobbs SK, Guccione S, Homer RJ, Harsh GW, Atlas SW, Bednarski MD. Image-Guided Proteome Analysis of Human Glioblastoma Multiforme by Two-Dimensional Differential Gel Electrophoresis

Strommer J, Gambhir SS. Mi-central.org: A Molecular Imaging Resource Website.

Subbarayan M, Sundaresan G, Gambhir SS. Noninvasive Imaging of 99mTc-Adenovirus and Reporter Gene Expression by Different Routes of Administration in Living Subjects. Molecular Imaging 2:138, 2003.

Sundaresan G, Murugesan S, Gambhir SS. MicroPET Imaging of 124I-Adenovirus Biodistribution and Optical Imaging of Reporter Gene Expression in Living Subjects. Molecular Imaging 2:302, 2003.

Venisnik KM, Olafsen K, Gambhir SS, Wu AM. A Bifunctional Antibody Fragment-Renilla Luciferase Fusion Protein for In Vivo Optical Imaging of Tumors Expressing CEA.

Wang TD, Mandella MJ, Chan NY, Kino GS, Contag CH. Confocal Fluorescence Microscope with Dual Axes Architecture for In Vivo Molecular and Cellular Imaging.

Wang Y, Iyer M, Wu L, Carey M, Gambhir SS. A Transgenic Mouse Model Incorporating a Two-Step Transcriptional Approach for Imaging of Vascular Endothelial Growth Factor (VEGF) Gene Expression. Molecular Imaging 2:276, 2003.

Wong RJ, Abate A, Vreman HJ, Dennery PA, Contag CH, Stevenson DK. Intestinal Absorption of Metalloporphyrins and Its Effects on Heme Oxygenase-1 Expression as Revealed by In Vivo Bioluminescent Imaging

Wu J, Chen I, Min JJ, Sundaresan G, De A, Qiao JH, Fishbein MC, Gambhir SS. Monitoring Engraftment and Survival of Transplanted Cells in Rat Myuocardium Using Optical and microPET Imaging. Molecular Imaging 2:382, 2003.

Wu Y, Kuge Y, Gobalakrishna S, Murray L, Gambhir SS. Use of FDG/FLT/NH3 PET and Optical Imaging to Evaluate the Efficacy of Tumor Treatment with an Angiogenesis Inhibitor. Molecular Imaging 2:286, 2003.

Yaghoubi S, Gambhir SS. Direct and Indirect Monitoring of Therapeutic Transgene Expression with the PET Reporter Probe [18F]FHBG. Molecular Imaging 2:291, 2003.

Yan Y-S, PhD, Samira Guccione, PhD, Mark D. Bednarski, MD, PhD. Comparing Genomic and Histological Correlation to Radiographic Changes Using a Squamous Cell Carcinoma Tumor Model.

Zhao H, Julie L. Prior, Tim Doyle, Stacy Burns, David Piwnica-Worms, Contag CH. Optimization of In Vitro and In Vivo Usage of Coelenterazine in Renilla Luciferase Reporter System

Dong D, Dubeau L, Bading J, Nguyen K, Luna M, Yu H, Gazit-Bornstein G, Gordon EM, Gomer C, Hall FL, Gambhir SS, Lee AS. Spontaneous and controllable activation of suicide gene expression driven by the stress-inducible grp78 promoter resulting in eradication of sizable human tumors. Hum Gene Ther. 2004; 15:553-61.

Edwards B, Ashcroft NW. Order in dense hydrogen at low temperatures. Proc Natl Acad Sci U S A 2004; 101:4013-4018.

Fahrig R, Heit G, Wen Z, Daniel BL, Butts K, Pelc NJ. First use of a truly-hybrid X-ray/MR imaging system for guidance of brain biopsy. Acta Neurochir (Wien) 2003; 145:995-997; discussion 997.

Farah M,* Illes J, * Cook-Deegan R, Gardner H, Kandel E, King P, Parens E, Wolpe PR, Sahakian B. Neurocognitive

THE 3RD ANNUAL MEETING OF THE SOCIETY FOR MOLECULAR IMAGING.

ST. LOUIS, MO
SEPTEMBER 9-12, 2004

Arai T, Caffarelli AD, Greve JM, Jacobs PM, Robbins RC, McConnell MV, Yang PC. In Vivo Magnetic Resonance Imaging of Inflammation in Myocardial Infarct Mouse Model

Arai T, Cunningham CH, McConnell MV, Conolly SM, Yang PC. In Vitro Quantitation of Cells Labeled with Magnetic Nanoparticles Using Off-resonance Sequence

Carey MF, Wu L, Gambhir SS. Two Step Transcriptional Amplification Vectors and Optical Imaging Applications.

Chen X, Liu S. 64Cu-Labeled Quinolone-Based Non-Peptide Vitronectin Receptor Antagonist For Tumor Imaging

Chen X, Moats R. Near-Infrared Fluorescence Imaging of Integrin Alpha(v)beta(3) Expression

Chen X, Sievers E, Hou Y, Park R, Tohme M, Bart R, Bremner R, Bading R, Conti P. MicroPET Imaging of Orthotopic Lung Cancer Integrin Expression with 64Cu-Labeled PEGylated Dimeric RGD Peptide

Conolly SM, Arai T, Yang P, McConnell M, Cunningham C. Instrumentation Considerations for In Vivo MRI of Targeted Cells

Contag CH. The Fate & Function of Individual Hematopoeitic Stem Cells

Cunningham CH, Arai T, Terashima M, McConnell MV, Pauly JM, Yang PC, Conolly SM. Positive Contrast MRI of Cells Labeled with Magnetic Nanoparticles

Graves EE, Sutphin PD, Chan DA, Giaccia AJ. Evaluation of Reporter Gene Expression and Protein Activity in Hypoxic Conditions

Guccione S, Mari C, Lee D, Bednarski M. Molecular Imaging of Platelet Derived Growth Factor Receptor in Gd-DTPA Contrast Enhanced Areas of Tumor as Determined by MR-Guided Functional Genomics Analysis

Guccione S, Yan Y-S, Chia YL, Wang Y, Lim M, Harsh G, Atlas S, Bednarski M. Identification of Genomic Targets of Glioblastoma Multiforme Patients Using Image-Guided Microarray Analysis

Hundt W, Guccione S, Mayer D, Bednarski M. In vivo assessment of gene expression ability after application of focused ultrasound

Hundt W, O'Connell-Rodwell C, Guccione S, Contag C, Bednarski M. Heat shock protein expression in 3 different tumor cells lines under exposure of heat. FACS analysis of cell survival.

Khanamiryan A, Toyokuni T, Nagichettiar S, Barrio G. A New Approach for COX-2 Inhibitor 18F-Fluorinated Radiotracers Development

Kopelman A, Bachireddy P, Giuriato S, Contag CH, Felsher DW. Bioluminescent Imaging As a Powerful Tool for Quantitatively Evaluating Tumor Regression

Lee S-W, Padmanabhan P, Biswal S. Using Molecular Imaging Techniques to Monitor Stem Cell-Based Therapy for Skeletal Injury

Loening AM, Wu AM, Gambhir SS. Alignment Guided Mutagenesis of Renilla Luciferase Increases Stability and Light Output.

McCaffrey AP, Pandey K, Huang Z, Kay MA, Salazar FH, Xu H, Nakai H, Marion PL. In Vivo Bioluminescence Imaging as a Tool for the Development of RNA Interference Inhibitors of Hepatitis Viruses

McDonald MA, Hunter F, Xie J, Frenkel V, Bryant H, Dewanjee MK, Guccione S, Bednarski M, Li K. Temperature-Sensative Nanoparticles for HIFU Mediated Gene delivery, MR and Optical Imaging

McDonald MA, Hunter F, Xie J, Frenkel V, Dewanjee MK, Guccione S, Bednarski M, Li K. Temperature-Sensitive Protein Nanospheres for HIFU Mediated Gene Delivery and Molecular Targeting

Padmanabhan P, Hoffman AR, Biswal S, Ulane GA. Non-Invasive Imaging of Human Telomerase Reverse Transcriptase (hTERT) Promoter Activity Using a Tri-Modality Fusion Reporter Construct

Ray P, Gambhir SS. Construction and Validation of Improved Version of Triple Fusion Reporter Gene Vectors

Ray S, Iyer M, Carey M, Wu L, Gambhir SS. A Single Vector System for Simultaneous Amplification and Monitoring of Transgene Expression

Shinde R, Perkins J, Contag C. In-Vivo Bioluminescence Protease Assay Using Aminoluciferyl Derivatives

Thorne SH, Tam B, Kuo CJ, Contag CH. Strategies for Combining a Replicating Oncolytic Virus and a Gene Therapy Vector in Order to Maximize the Levels and Duration of Gene Expression: Implications for Cancer Therapy

Venisnik K, Olafsen T, Loening AM, Gambhir SS, Wu AM. Optimization of Expression and Purification of a Diabody-Renilla Luciferase Fusion Protein for Localization of CEA Expressing Tumors

Wang DS, Bryant C, Greve J, Elkins CJ, Waugh JM, Kuo MD, Dake MD. Cell Labeling by Noncovalent Association of Gadolinium-DTPA with a Tat Peptide Derivative Carrier System

Wang DS, Lee J, Waugh JM, Dake MD. Transdermal Delivery of Blue Fluorescent Protein and A-Galactosidase Genes Using Tat Peptide Derivatives

Wang q, Contag CH, Ilves H, Johnston BH, Kaspar RL. Small Hairpin RNAs Efficiently Inhibit Hepatitis C IRES-mediated Gene Expression In A mouse Model.

Zhao H, Doyle TC, Coquoz O, Kalish F, Rice BW, Contag CH. Spectral characterization of firefly, click beetle and Renilla luciferases in mammalian cells and living mice

Other Conferences

Chen SA, Desmond JE. Cerebro-cerebellar circuitry of verbal working memory. Society for Neuroscience Abstracts, 2003.

Desmond JE, Chen SA, Shieh PB. Right cerebellar single-pulse transcranial magnetic stimulation (TMS) affects verbal working memory performance. Society for Neuroscience Abstracts, 2003.

Desmond JE, Chen SHA, Kirschen MP, DeRosa E, Pfefferbaum A, Sullivan EV. Cerebro-cerebellar circuitry in verbal working memory: Neuroimaging evidence from healthy and alcoholic populations. Eleventh Annual Meeting of the International Society for Behavioural Neuroscience, Prague, Czech Republic, June 2003.

Illes J. Neurocognitive enhancement, free will, human nature. Neuroscience Institute at Stanford, Annual Retreat, 2004, Asilomar, CA.

Illes J. Brain Imaging for bioethicists: Scientific and social dimensions, American Society for Bioethics and Humanities, 2004, Philadelphia, PA.

Illes J, Kelly M, Saha A, Kirschen M, Desmond JE, Glover GH, et al. Discovery and disclosure of incidental findings on brain MRI. Society for Neuroscience Abstracts, 2003

Kidwell CS, Leary M, Lai TC, Bammer R, Frew AJ, Villablanca JP, Saver JL, Alger JR. Calibration of contrast bolus passage magnetic resonance perfusion imaging with xenon computed tomography in human stroke. Brain, 2003.

Kirschen MP, Chen SA, Desmond JE. Modality specific cerebellar activation during verbal working memory: a fMRI study. Society for Neuroscience Abstracts. 2003

Kirschen M, Drazin D, Jaworska, Atlas SW, Raffin TA, Illes J. Participant expectations of incidental findings in neuroimaging research. Society for Cognitive Neuroscience, 2004, San Francisco, CA.

Lyons D, Boyett-Anderson J, Buckmaster C, Sood R, Moseley, ME Schatzberg A. Stress-related changes in white matter connectivity and neurocognitive decline. Society for Neurosciences 2004.

Mazin SR, Schmidt TG, Solomon E, Fahrig R, Pelc NJ. Geometry analysis of an inverse-geometry volumetric CT system with multiple detector arrays. Medical Imaging 2004: Physics of Medical Imaging, Proc. SPIE, 2004

Medina D, deToledo-Morrel L, Urresta1 F, Gabrieli JDE, Moseley ME, Turner DA, Fleischman D, Bennett DA, Stebbins GT. Imaging of white matter changes in mild cognitive impairment and alzheimer's disease. Society for Neurosciences meeting, 2004.

Racine E, Illes J. La neuro thique est-elle l'h rit re de l' thique de la g nomique? Une comparaison pour discuter des fondements de la neuro thique. Canadian Bioethics Society, 2004, Calgary, Alberta, Canada (Awarded "Best Student Paper")

Rieke V, Ross AB., Nau W.H., Diederich C.J., Sommer G., Butts K. MRI-temperature mapping during ultrasound prostate ablation using fat for phase estimation. To be presented at IEEE EMBS, San Francisco, 2004.

Stebbins GT, Carillo MC, Bangen, K Moseley ME, Katsamaki G, Stefoski D, Turner DA, Gabrieli JDE. Relationship of white matter integrity in multiple sclerosis with executive and non-executive cognitive functions: a DTI study. Society for Neurosciences 2004.

Stebbins GT, Nyenhuis DL, Freels S, Moseley ME, Turner DA, Gabrieli JDE, Gorelick PB. A diffusion tensor imaging study of normal appearing white matter integrity in recent ischemic stroke - relationship to cognitive function. Vascular Cognitive Society, Gothenburg, 2004.

Wang C, deToledo-Morrell L, Nyenhuis D, Freels S, Moseley ME, Turner DA, Gabrieli JDE, Gorelick RA, Stebbins GT. Longitudinal changes in anisotropic diffusion in ischemic stroke: relationship to initial motor impairment. Society for Neurosciences , 2004.

Wu JC, Chen IY, De A, Min JJ, Sundaresan G, Qiao JH, Fishbein MC, Gambhir SS. Positron Emission Tomography Imaging of Cellular Cardiomyoplasty. J Am Coll Cardiol. 41(6 Suppl B):446, 2003.